

# Development of highly accurate density functionals for H2 dissociation on transition metals

Smeets, E.W.F.

#### Citation

Smeets, E. W. F. (2021, June 29). *Development of highly accurate density functionals for H2 dissociation on transition metals*. Retrieved from https://hdl.handle.net/1887/3193529

Version: Publisher's Version

License: License agreement concerning inclusion of doctoral thesis in the

Institutional Repository of the University of Leiden

Downloaded from: <a href="https://hdl.handle.net/1887/3193529">https://hdl.handle.net/1887/3193529</a>

Note: To cite this publication please use the final published version (if applicable).

#### Cover Page



## Universiteit Leiden



The handle <a href="https://hdl.handle.net/1887/3193529">https://hdl.handle.net/1887/3193529</a> holds various files of this Leiden University dissertation.

Author: Smeets, E.W.F.

Title: Developement of highly accurate density functionals for H2 dissociation on

transition metlas

**Issue Date:** 2021-06-29

## Development of Highly Accurate Density Functionals for H<sub>2</sub> Dissociation on Transition Metals

Egidius Wilhelmus François Smeets

# DEVELOPMENT OF HIGHLY ACCURATE DENSITY FUNCTIONALS FOR H<sub>2</sub> DISSOCIATION ON TRANSITION METALS

#### Proefschrift

ter verkrijging van de graad van doctor aan de Universiteit Leiden, op gezag van rector magnificus prof.dr.ir. H. Bijl, volgens besluit van het college voor promoties te verdedigen op dinsdag 29 juni 2021 klokke 16:15 uur

door

Egidius Wilhelmus François Smeets geboren te Sittard in 1989

#### Promotiecommissie

Promoter: Prof. dr. G. J. Kroes Copromoter: Dr. M.F. Somers

Overige leden: Prof. dr. H. S. Overkleeft (voorzitter)

Prof. dr. E. Bouwman (secretaris) Prof. Em. dr. M. C. van Hemert

Prof. dr. D. J. Auerbach (MPI für Biophysikalische Chemie)

Prof. dr. J. Voss (Stanford University)

ISBN: 978-94-6423-288-2

The research reported in this thesis has been performed in the Theoretical Chemistry group at the Leiden Institute of Chemistry (Einsteinweg 55, 2333 CC, Leiden, the Netherlands). This work has been made possible by financial support by the Nederlandse Organisatie voor Wetenschappelijk Onderzoek (NWO) through an NWO/CW TOP Grant and by the European Research Council through an ERC-2013 advanced grant (Nr. 338580), and with computer time granted by the Physical Sciences division of NWO (NWO-EW).



## Contents

| 1 | Ger | ieral I                          | ntroduction  | 1  |  |  |
|---|-----|----------------------------------|--|----|--|--|
|   | 1.1 | Gas-s                            | urface reactions   | 1  |  |  |
|   | 1.2 | $H_2$ reacting on metal surfaces |  |    |  |  |
|   | 1.3 | Aims                             | and scope of this thesis   | 4  |  |  |
|   | 1.4 | Main                             | results  | 5  |  |  |
|   | 1.5 |                                  | ok   | 9  |  |  |
| 2 | The | eory ar                          | nd methods   | 27 |  |  |
|   | 2.1 | Electr                           | conic structure theory: density functional theory (DFT) .                      | 27 |  |  |
|   |     | 2.1.1                            | Exchange-correlation density functionals: LDA, GGA,                            |    |  |  |
|   |     |                                  | meta-GGA   | 29 |  |  |
|   |     | 2.1.2                            | Non-local correlation  | 30 |  |  |
|   |     | 2.1.3                            | The problem of obtaining accurate reaction barriers                            | 31 |  |  |
|   |     | 2.1.4                            | Specific reaction parameter approach to DFT                                    | 32 |  |  |
|   |     | 2.1.5                            | Periodic DFT   | 33 |  |  |
|   | 2.2 | Const                            | ructing potential energy surfaces  | 34 |  |  |
|   | 2.3 |                                  |  |    |  |  |
|   |     | 2.3.1                            | Quasi-classical trajectory method  | 35 |  |  |
|   |     |                                  | Langevin equation with energy dissipation                                      | 36 |  |  |
|   |     | 2.3.2                            | Quantum dynamics   | 37 |  |  |
|   | 2.4 | Comp                             | outation of observables  | 39 |  |  |
|   |     | 2.4.1                            | Molecular beam sticking  | 39 |  |  |
|   |     | 2.4.2                            | Rotational quadrupole alignment parameters                                     | 40 |  |  |
|   |     | 2.4.3                            | $E_{1/2}(\nu,J)$ parameters  | 41 |  |  |
|   |     |                                  | Method A1  | 42 |  |  |
|   |     |                                  | Method B1  | 42 |  |  |
|   |     | 2.4.4                            | Rovibrational state populations of H <sub>2</sub> and D <sub>2</sub> desorbing |    |  |  |
|   |     |                                  | from Au(111)   | 43 |  |  |

| 3  | $\mathbf{Spe}$ | cific r | eaction parameter density functional based on the            |     |  |
|--|----------------|---------|--|-----|--|
|  |                | _       | eralized gradient approximation:                             | 53  |  |
| Application to $\mathrm{H}_2 + \mathrm{Cu}(111)$ and $\mathrm{H}_2 + \mathrm{Ag}(111)$ |                |         |  |     |  |
|  | 3.1            | Introd  | luction  | 54  |  |
|  | 3.2            | Metho   | odology  | 56  |  |
|  |                | 3.2.1   | Dynamical model  | 56  |  |
|  |                | 3.2.2   | Made Simple meta-GGA density functionals                     | 56  |  |
|  |                | 3.2.3   | DFT calculations and representation of PESs                  | 59  |  |
|  |                | 3.2.4   | Quasi-classical trajectory method                            | 60  |  |
|  |                | 3.2.5   | Compation of observables                                     | 61  |  |
|  | 3.3            | Result  | ts and discussion  | 61  |  |
|  |                | 3.3.1   | Description of the metal                                     | 61  |  |
|  |                | 3.3.2   | Potential energy surfaces                                    | 63  |  |
|  |                | 3.3.3   | Dynamics results: molecular beam sticking                    | 69  |  |
|  |                | 3.3.4   | Dynamics results: initial-state selected reaction probabil-  |     |  |
|  |                |         | ities $Ag(111)$  | 78  |  |
|  | 3.4            |         | usions   | 78  |  |
|  | 3.A            |         | ndix: Details electronic structure calculations and interpo- |     |  |
|  |                |         | of the PESs  | 81  |  |
|  |                | 3.A.1   | Calculations on bulk metals and on slab relaxation           | 81  |  |
|  |                | 3.A.2   | 1 2 ' ( )  |     |  |
|  |                |         | and Ag(111)  | 81  |  |
| 4 Quantum dynamics of dissociative chemisorption of $H_2$ stepped $Cu(211)$ surface    |                |         |  |     |  |
|  |                |         |  | 91  |  |
|  | 4.1            | Introd  | luction  | 92  |  |
|  | 4.2            | Comp    | utational methods and simulations                            | 95  |  |
|  |                | 4.2.1   | Coordinate system  | 95  |  |
|  |                | 4.2.2   | Ab initio molecular dynamics simulations                     | 95  |  |
|  |                | 4.2.3   | Quasi-classical simulations                                  | 97  |  |
|  |                | 4.2.4   | Quantum dynamics simulations                                 | 98  |  |
|  |                | 4.2.5   | Computation of observables                                   | 96  |  |
|  | 4.3            | Result  |  | 103 |  |
|  |                | 4.3.1   | · -  | 103 |  |
|  |                | 4.3.2   |  | 104 |  |
|  |                | 4.3.3   | 1 0 1  | 111 |  |
|  |                | 4.3.4   | Classical molecular beam simulations                         | 118 |  |
|  |                | 4.3.5   | •  | 119 |  |
|  | 4.4            | Concl   | usions   | 122 |  |

| 5 |     |        | ning new SRP density functionals including non-local DF2 correlation for $H_2 + Cu(111)$ and their transfer- |       |  |  |  |
|---|-----|--------|--|-------|--|--|--|
|   |     |        | ${ m H}_2 + { m Ag}(111), \ { m Au}(111) \ { m and} \ { m Pt}(111)$  | 131   |  |  |  |
|   | 5.1 | -      | uction   | . 132 |  |  |  |
|   | 5.2 |        | dology   |       |  |  |  |
|   |     | 5.2.1  | Coordinate system  |       |  |  |  |
|   |     | 5.2.2  | SRP DFT  |       |  |  |  |
|   |     | 5.2.3  | Construction of the PESs   | . 138 |  |  |  |
|   |     | 5.2.4  | Quasi-classical dynamics   | . 138 |  |  |  |
|   |     | 5.2.5  | Quantum dynamics   | . 139 |  |  |  |
|   |     | 5.2.6  | Computation of observables   | . 139 |  |  |  |
|   |     |        | Simulating molecular beam sticking   | . 139 |  |  |  |
|   |     |        | Comparing to experimental $E_0(\nu, J)$ parameters   | . 142 |  |  |  |
|   |     |        | Rotational quadrupole alignment parameters   | . 145 |  |  |  |
|   |     |        | Rovibrational state populations of $H_2$ and $D_2$ desorbing   |       |  |  |  |
|   |     |        | from Au(111)   | . 145 |  |  |  |
|   |     | 5.2.7  | Computational details  | . 146 |  |  |  |
|   | 5.3 | Result | S  | _     |  |  |  |
|   |     | 5.3.1  | Electronic structure   |       |  |  |  |
|   |     |        | Description of the metal   |       |  |  |  |
|   |     |        | $H_2$ + metal surface PESs   |       |  |  |  |
|   |     |        | Van der Waals wells  |       |  |  |  |
|   |     | 5.3.2  | Molecular beam sticking probabilities  |       |  |  |  |
|   |     | 5.3.3  | Initial-state resolved reaction probabilities  |       |  |  |  |
|   |     | 5.3.4  | $E_{1/2}(\nu, J)$ parameters   |       |  |  |  |
|   |     | 5.3.5  | Rotational quadrupole alignment parameters Cu(111)   |       |  |  |  |
|   |     | 5.3.6  | Inelastic scattering of H <sub>2</sub> from Cu(111)  | . 164 |  |  |  |
|   |     | 5.3.7  | Rovibrational state populations of H <sub>2</sub> and D <sub>2</sub> desorbing                               |       |  |  |  |
|   |     | ъ.     | from Au(111)   |       |  |  |  |
|   | 5.4 |        | sion   |       |  |  |  |
|   |     | 5.4.1  | Metal properties   |       |  |  |  |
|   |     | 5.4.2  | Static PES properties  |       |  |  |  |
|   |     | 5.4.3  | Molecular beam sticking  | . 181 |  |  |  |
|   |     |        | Molecular beam sticking of $H_2$ ( $D_2$ ) + $Cu(111)$ : QCT   | 101   |  |  |  |
|   |     |        | results  |       |  |  |  |
|   |     |        | Molecular beam sticking in $H_2 + Cu(111)$ : QD results  |       |  |  |  |
|   |     |        | Molecular beam sticking in $D_2 + Pt(111) \dots \dots$   |       |  |  |  |
|   |     | F 4 4  | Molecular beam sticking in $D_2 + Ag(111) \dots$   |       |  |  |  |
|   |     | 5.4.4  | Associative desorption   |       |  |  |  |
|   |     |        | Comparing to experimental $P_0(\mathcal{V},J)$ parameters  | . 186 |  |  |  |

|   |     |        | Rovibrational state populations of $\Pi_2$ and $D_2$ desorbing  |        |
|---|-----|--------|---|--------|
|   |     |        | from $Au(111)$  | 192    |
|   |     |        | Initial-state resolved reaction probabilities for $D_2 + Ag(111)$   | .).194 |
|   |     |        | Rotational quadrupole alignment parameters: $H_2 + Cu(11)$  | 1).194 |
|   |     | 5.4.5  | Inelastic scattering of $H_2$ from $Cu(111) \dots \dots \dots$  | 195    |
|   |     | 5.4.6  | QD vs. QCT for $H_2 + Cu(111) \dots \dots \dots \dots$  | 196    |
|   |     | 5.4.7  | Overall description of systems  | 197    |
|   |     |        | $H_2 (D_2) + Cu(111) \dots \dots \dots \dots \dots \dots \dots$   | 198    |
|   |     |        | $\mathrm{D}_2 + \mathrm{Ag}(111) \ldots \ldots \ldots \ldots \ldots \ldots$   |        |
|   |     |        | $\mathrm{H_2} \; (\mathrm{D_2}) + \mathrm{Au}(111) \; \ldots \; \ldots \; \ldots \; \ldots \; \ldots \; \ldots \; \ldots$ | 199    |
|   |     |        | $\mathrm{D}_2 + \mathrm{Pt}(111) \ldots \ldots \ldots \ldots \ldots \ldots$   | 200    |
|   |     | 5.4.8  | Transferability   | 200    |
|   |     | 5.4.9  | Adiabatic description of $S_0$ and $E_{1/2}(\nu, J)$ , a possible   |        |
|   |     |        | fingerprint for ehp excitations   | 201    |
|   | 5.5 |        | usions  |        |
|   | 5.A |        | ndix: CRP interpolation of PESs   | 204    |
|   | 5.B |        | ndix: Methods for determining parameters describing initial-  |        |
|   |     |        | selected reaction probabilities from associative desorption   |        |
|   |     | -      | ments   |        |
|   |     |        | Method A1   |        |
|   |     |        | Method B1   |        |
|   |     |        |   | 206    |
|   | 5.C |        | ndix: The rotational hindering effect as obtained with the  |        |
|   |     | Dai-Zl | hang LEPS PES   | 207    |
| 6 | Don | formar | ace of made-simple meta-GGA functionals with ${ m rVV}$   | 710    |
| U |     |        | correlation for $\mathrm{H_2}+\mathrm{Cu}(111),\mathrm{D_2}+\mathrm{Ag}(111),\mathrm{H_2}$                                |        |
|   |     |        | and $D_2 + Pt(111)$   | 227    |
|   | 6.1 | . ,    | $\begin{array}{cccccccccccccccccccccccccccccccccccc$  |        |
|   | 6.2 |        | $\operatorname{pdology}$  |        |
|   | 0.2 | 6.2.1  | Coordinate system   |        |
|   |     | 6.2.2  | Combining Made Simple meta-GGA exhcange-correlation   | 201    |
|   |     | 0      | with rVV10 non-local correlation  | 231    |
|   |     | 6.2.3  | Construction of the PESs  |        |
|   |     | 6.2.4  | Quasi-classical dynamics  |        |
|   |     | 6.2.5  | Computation of observables  |        |
|   |     |        | Molecular beam sticking   |        |
|   |     |        | Rovibrational state populations of H <sub>2</sub> and D <sub>2</sub> desorbing  |        |
|   |     |        | from Au(111)  | 242    |
|   |     |        | $E_{1/2}(\nu, J)$ parameters  | 242    |
|   |     |        |   |        |

|         | 6.2.6                | Computational details  | 243       |  |
|---------|----------------------|--|-----------|--|
| 6.3     | Result               | s and Discussion   | 244       |  |
|         | 6.3.1                | Metal properties   | 244       |  |
|         | 6.3.2                | Static PES properties  | 245       |  |
|         | 6.3.3                | Molecular beam sticking  | 252       |  |
|         |                      | Molecular beam sticking of $H_2$ ( $D_2$ ) + $Cu(111)$                         | 252       |  |
|         |                      | Molecular beam sticking of $D_2 + Ag(111) \dots \dots$                         | 252       |  |
|         |                      | Molecular beam sticking of $D_2 + Pt(111) \dots \dots$                         | 254       |  |
|         | 6.3.4                | Associative desorption   | 256       |  |
|         |                      | 3.4.1 Initial-state resolved reaction probabilities $Ag(111)$                  | 256       |  |
|         |                      | $E_{1/2}(\nu, J)$ parameters Au(111)   | 257       |  |
|         |                      | Rovibrational state populations of H <sub>2</sub> and D <sub>2</sub> desorbing |           |  |
|         |                      | from Au(111)   | 259       |  |
|         | 6.3.5                | Transferability  | 262       |  |
| 6.4     | Concl                | usion  | 265       |  |
| C       | - 4 4 °              | 0.4 21 2.5 1.141   |           |  |
|         |                      | g: Ontwikkeling van zeer nauwkeurige dichtheids                                |           |  |
|         | ervlak               | en voor de dissociatie van ${ m H}_2$ aan overgangsmetaa                       | 1-<br>281 |  |
| opp     | erviak               | Kell   | 201       |  |
| Curric  | ulum v               | vitae  | 289       |  |
| T: d C  | 1. 1.                |  | 291       |  |
| List of | List of publications |  |           |  |

### 1 General Introduction

#### 1.1 Gas-surface reactions

In heterogeneous catalysis new products are formed through elementary reactions of molecules with surfaces. The chemistry of small molecules reacting on a surface are therefore an integral part of our everyday lives. Examples include the production of plastic and other everyday materials, the production of ammonia which enables the use of artificial fertilizer<sup>1</sup>, the polution reduction achieved by the use of a catalytic converter in a car<sup>2</sup>, or the steam reforming proces which is currently used to produce hydrogen (H<sub>2</sub>) and carbon monoxide (CO) gas from methane (CH<sub>4</sub>) and steam<sup>3</sup>. Gas-surface reactions are also not solely the preserve of human activity. A rusting bit of iron left outside in a humid environment is also an example of a gas-surface reaction: oxygen gas (O<sub>2</sub>) from the air has reacted with the metal surface of the iron forming rust. Chemical reactions that proceed using a catalyst are extremely important to the chemical industry. Improvements in the design of catalysts, either by allowing cheaper materials to be used as catalysts or reducing the energy cost of a given reaction, have a potentially huge impact on the chemical industry<sup>4</sup>.

In its simplest form a chemical reaction entails two reactants coming together with enough energy to overcome the energetic barrier to reaction and then reacting to form the product(s). A catalyst is a reaction partner that interacts with the reactants in order to provide an alternative reaction mechanism that can be more complicated but is energetically favorable. In general, a catalyst stabilizes the transition state of the reaction complex formed by the reactants coming together on a catalyst, thereby lowering the barrier to reaction and fascilitating the breaking of existing chemical bonds and the formation of new chemical bonds. After the reaction the resulting products move away from the catalyst, allowing the catalyst to go into a new catalytic cylce. Lowering the energetic barrier to a reaction by using a catalyst can thus not only increase the reaction rate but also allow the reaction to proceed under milder conditions (lower temperature and or pressure), reducing the cost. In some cases it is even possible to increase the selectivity of particular reaction such that the

formation of a desired reaction product is favored over an unwanted reaction product, reducing waste and polution.

In heterogeneous catalysis the reactants and the catalyst exist in different phases (plasma, gas, liquid, solid), while in homogeneous catalysis both the catalyst and the reactants are in the same phase. Another important type of catalysis that cannot go unmentioned is biocatalysis, in which proteins act as highly specialized catalysts for nearly all biochemical reactions underpinning life as we know it<sup>5</sup>.

Usually a heterogeneously catalysed process does not consist of a single reaction step. A reaction that takes place on a catalytic surface can be described as a complex process consisting of several elementary reaction steps. An example that includes some possible elementary reaction steps is a molecule that adsorbs on a surface and diffuses to a reaction site before dissociating. It thus goes through the elementary steps of adsorption, diffusion and dissociation at a reactive site. In 2007 Ertl was awarded the Nobel prize in chemistry for investigating elementary reaction steps in heterogeneous catalysis experimentally<sup>6</sup>.

The elementary reaction steps in heterogeneous catalysis form a complex network of reactions. The most important steps in such a network are called the rate-limiting steps. Creating a theoretical description of a complex reaction network ideally starts with the calculation of 'chemically accurate' barrier heights for elementary reaction steps<sup>7</sup>. Note that the calculation of chemically accurate reaction rates of reaction networks is also important to the search for extraterrestrial life in the solar system<sup>8</sup> and in the field of astrochemistry<sup>9-11</sup>. In heterogeneous catalysis the rate-limiting step is often the dissociative chemisorption of a molecule on a surface<sup>12,13</sup>. Calculating chemically accurate barrier heights for rate-controlling reactions to obtain accurate rates of the overall reaction network<sup>14</sup> is a rather complex task that not only needs to take into account the static electronic structures of both reactant and the catalytic surface at the transition state, but also dynamical effects such as the molecule's approach towards the transition state, the molecule's internal motion, as well as surface atom motion due to temperature<sup>15</sup>.

#### 1.2 H<sub>2</sub> reacting on metal surfaces

Metal surfaces from a group of effective catalysts for the reaction of small molecules such as  $H_2$ . The electrons of a metal are delocalized while the electrons of molecules are more localized around their constituent atoms<sup>16</sup>. The grouping of the metal electrons in bands, some of which are close to the Fermi level, allows the metal surface to readily donate to or accept an electron from

the molecule at hardly any energetic  $\cos^{17-19}$ . This possibility of electron exchange is what makes metal surfaces particularly effective catalysists.

The research presented in this thesis focussus on the reaction of  $H_2$  on metal surfaces. The dissociation of  $H_2$  is relevant to the industrial synthesis of methanol from  $CO_2$  over a  $Cu/ZnO/Al_2O_3$  catalyst, since in this process the dissociation of  $H_2$  is considered to be the rate-limiting step<sup>20–22</sup>.  $H_2$  dissociation on transition metal surfaces is an important process in hydrogenation catalysis<sup>23</sup>. Hydrogenation of unsaturated bonds in organic molecules through heterogeneous catalysis on solids has extensive uses in the chemical industry<sup>24–29</sup>. Although the basic elementary reaction steps of  $H_2$  dissociation and hydrogenation reactions have been elucidated long ago by Horiuti and Polanyi<sup>30</sup>, many open questions and research opportunities remain with respect to efficiency, selectivity, and catalytic particle or surface design and geometry<sup>23</sup>.

The kinetics of  $H_2$  dissociation, recombinative desorption, and scattering has predominantly been studied under ultra high vacuum (UHV) conditions<sup>31–71</sup>. However, very little is known about the dynamics of  $H_2$  dissociation at industrially relevant temperatures and pressures<sup>72,73</sup> (often denoted as the temperature and pressure gaps).

Scattering of  $H_2$  from reactive metal surfaces is also of interest for fundamental reasons, for the wealth of phenomena that have been investigated and uncovered by experiments on this topic. Reaction probability versus collision energy curves can be obtained from molecular beam experiments  $^{32,33,38,48,51-53,60-64,74}$  and associative desorption experiments  $^{32,34,38,50,75}$ . Associative desorption experiments also yield information on the effect of the initial rovibrational state  $^{32,34,38,50,75}$  and the alignment of the molecule relative to the surface normal on the reverse dissociative chemisorption reaction  $^{36}$ . Molecular beam experiments in which  $H_2$  scatters from a surface can provide final state resolved information on vibrational excitation  $^{40}$ , rotationally elastic  $^{31}$  and inelastic  $^{41}$  scattering, and vibrationally and rotationally inelastic scattering  $^{42,66}$  Elastic and inelastic diffractive scattering of  $H_2$  from metal surfaces can be adressed as well  $^{67-71,76-80}$ .

In order to improve the predictive power of theory with respect to the catalytic activity of small molecules reacting at metal surfaces, the way in which metal surfaces modify the potential energy of molecules needs to be understood at a fundamental level. The elementary reaction steps of a molecule interacting with a surface can be investigated experimentally using techniques that exert control over the various degrees of freedom of a molecule reacting on a cold metal surface. The work presented in this thesis is predominantly concerned with the description and simulation of supersonic molecular beam experiments <sup>32,33,38,48,51–53,60–64,74</sup> and associative desorption

experiments<sup>34,38,50,54,55,75,81–83</sup>. In the molecular beam technique, pioneerd by King and Wells<sup>84</sup>, a gas supersonically expands into a UHV chamber towards the target after being collimated by the use of skimmers. Initially the gas entering the target chamber will be blocked in some way until a steady state gas pressure is reached in the target chamber. Once the blockade between the collimated stream of supersonic gas (the molecular beam) and the target is removed the molecular beam will hit the target surface. Some molecules will react with the target causing the pressure in the target chamber to drop. The initial drop in pressure is directly proportional to the sticking probability of molecules in the molecular beam to the target surface in the zero coverage limit<sup>84</sup>. Various degrees of freedom of the molecules in the molecular beam can be controlled by adjusting the temperature of the nozzle through which the gas expands into to the UHV chamber, by adjusting the backpressure of the gas, or by changing the gas mixture. The importance of the molecular beam technique to catalysis research cannot be understated<sup>85–88</sup>.

Another approach to experimentally assess the potential energy landscape of a molecule interacting with a surface is conducting associative desorption experiments<sup>34,38,50,54,55,75,81–83</sup>, in which often state-specific information can be obtained by using the resonance-enhanced multi-photon ionization (REMPI) technique<sup>32,34,38,50,75</sup>. This bottom up approach allows for the disentanglement of the many competing effects present under real catalytic conditions, such as high temperatures and pressures.

#### 1.3 Aims and scope of this thesis

The main goal of the thesis is to improve the theoretical description of reactive scattering of  $H_2$  from various transition metal surfaces, such as Cu(111), Cu(211), Ag(111), Au(111) and Pt(111). The starting point for any theoretical description of the interaction of  $H_2$  with a metal surface presented in this thesis will be the time-dependent Schrödinger equation<sup>89</sup>. Specifically the aim will be to close the gap between theory and experiment with respect to the description of the reactivity and state-specific reaction dynamics, through the design of highly accurate density functionals.

In Chapter 2 the theory behind the dynamical methods used to simulate molecular beam experiments is discussed. First the solving of the electronic structure problem using DFT will be discussed, as well as how potential energy surfaces (PESs) can be constructed for relaxed ideal zero kelvin surfaces using the corrugation reducing procedure<sup>90</sup>. The two dynamics methods used in this thesis, namely the quasi-classical trajectory (QCT) method and the quantum dynamics (QD) method, will be introduced. The last section of Chapter 2

1.4. Main results 5

will deal with the calculation of observables that is needed to compare to experimental observations.

In Chapter 3 the aim is to determine whether, with a meta generalized gradient approximation (meta-GGA) functional constructed within the "made simple" approach, it is possible to get a chemically accurate description of the dissociative chemisorption of  $H_2$  on Cu(111), while at the same time obtaining a better description of the Cu lattice than possible with previous SRP functionals based on the generalized gradient approximation (GGA). A second goal is to determine whether with the meta-GGA "made simple" functionals constructed here it should be possible to also get a more accurate description of the dissociative chemisorption of  $H_2$  on and its associative desorption from Ag(111) than was previously possible with the SRP48 GGA functional for  $H_2 + Cu(111)$ .

In Chapter 4 the focus lies on the stepped nature of the Cu(211) unit cell and whether the dynamics of  $H_2$  impinging on Cu(211) can still be described by quasi-classical techniques. To this end a large number of time-dependent wave packet calculations are carried out for all rovibrational states populated in a molecular beam experiment according to the nozzle temperature.

In Chapter 5 new specific reaction parameter (SRP) density functionals at the GGA level that include non-local correlation are introduced for the  $\rm H_2$  +  $\rm Cu(111)$  system. Application of these newly designed functionals to the  $\rm H_2$  +  $\rm Ag(111)$ ,  $\rm Au(111)$  and  $\rm Pt(111)$  systems might allow for the identification of critical components of a density functional that make it transferable among systems in which the same molecule interacts with different metal surfaces.

In Chapter 6 the mGGA density functionals developed in Chapter 3 are combined with  ${\rm rVV10^{91}}$  non-local correlation. The effectiveness of the newly constructed density functionals is evaluated for the  ${\rm H_2+Cu(111)}$ , Ag(111), Au(111) and Pt(111) systems. Additionally the transferability of the newly constucted density functionals is assessed using the methodology first introduced in Chapter 5.

#### 1.4 Main results

The main results obtained during the research that resulted in this thesis are summarized in this section.

# Chapter 3: Specific reaction parameter density functional based on the meta-generalized gradient approximation: Application to $H_2 + Cu(111)$ and $H_2 + Ag(111)$

Three density functionals at the meta-GGA level have been constructed based on the "made simple" approach 92,93, namely the MS-PBEl, MS-B86bl and MS-RPBEl density functionals. Here the 'l' stands for 'like', in that the gradient enhancement factors of the functionals are based on PBE-like<sup>94</sup>, B86blike<sup>95</sup>, or RPBE-like<sup>96</sup> expressions but with  $\mu = \frac{10}{81}$  as is appropriate for metallic bonding<sup>97,98</sup>. In the made simple approach to constructing a meta-GGA density functional, a function of the kinetic energy density is defined that effectively allows one to vary the exchange functional according to whether the binding in a certain region is metallic or covalent. The three new MS meta-GGA functionals yield lattice constants that are in excellent agreement with zeropoint energy corrected experimental values. Likewise, the interlayer lattice spacing relaxations for the top two layers of Cu(111) and Ag(111) are in good agreement with experiment. The performance of the three new MS meta-GGA functionals was found to be comparable to PBEsol<sup>97</sup>, a density functional specifically designed for the solid state. The barrier heights and geometries obtained for  $H_2 + Cu(111)$  were in good agreement with those obtained earlier with the original SRP functional for  $H_2 + Cu(111)^{99}$ . More importantly, the sticking probability curves computed with the three MS functionals and the QCT method agreed with experiments of Rettner and Auerbach and co-workers and of Rendulic and co-workers to within chemical accuracy. Furthermore, the sticking probability curves computed with the MS-PBEl and MS-B86bl functionals for  $D_2 + Ag(111)$  agree slightly better with the molecular beam experiments of Hodgson and co-workers than dynamics calculations based on the SRP48 GGA functional designed for  $H_2 + Cu(111)$ . Good agreement is also obtained between initial-state selected reaction probabilities computed for  $H_2$  and  $D_2 + Ag(111)$  and the initial-state selected reaction probabilities extracted from associative desorption experiments of Hodgson and co-workers on these systems. Based on the obtained results it can be concluded that, (i) it is possible to construct non-empirical meta-GGA "made simple" functionals for these two  $H_2$ -metal systems that describe the dissociative chemisorption reaction as accurately as previous semiempirical functionals based on GGA functionals, while simultaneously giving a more accurate description of the metal lattice, and (ii) on the basis of these MS functionals (in particular, MS-PBEl and MS-RPBEl), an SRP-DF can be constructed for  $H_2 + Cu(111)$ , but not for  $H_2 + Ag(111)$ .

1.4. Main results 7

# Chapter 4: Quantum dynamics of dissociative chemisorption of $H_2$ on the stepped Cu(211) surface

A full quantum dynamical molecular beam simulation has been performed for the reaction of  $H_2$  on Cu(211). To the this end a large number of timedependent wave packet (TDWP) calculations have been performed to obtain fully initial-state resolved reaction probabilities for all rovibrational states that are relevant to the simulation of molecular beam sticking experiments. The main conclusion is that the reaction of  $H_2$  with Cu(211) is well described quasiclassically. This is especially true when simulating molecular beam experiments where one averages over a large number of rovibrational states and a wide velocity distribution. It has however been found that some small differences between QD and QCT calculations remain, most notably with respect to the extent to which the reaction depends on the alignment of  $H_2$ . The QD method predicts stronger alignment effects on the reactivity than the QCT method for low lying rotational states. A comparison to recent associative desorption experiments suggests and direct dynamics calculation that incorporate surface atom motion appear to show that the effect of surface atom motion and ehp's on the reactivity falls within chemical accuracy, even for the high surface temperature used in the associative desorption experiments. In contrast to the theoretical and experimental results for  $D_2$  reacting on Cu(111) and Cu(100), at low translational energy a sharp downturn of the rotational quadrupole alignment parameters is observed for vibrationally excited molecules. This downturn can be attributed to a site specific reaction mechanism of inelastic rotational enhancement. The results show that the stepped Cu(211) surface is distinct from its component Cu(111) terraces and Cu(100) steps and cannot be described as a combination of its component parts with respect to the reaction dynamics when considering the orientational dependence.

# Chapter 5: Designing new SRP density functionals including non-local vdW-DF2 correlation for $H_2 + Cu(111)$ and their transferability to $H_2 + Ag(111)$ , Au(111) and Pt(111)

New specific reaction parameter (SRP) density functionals that include non-local vdW-DF2<sup>100</sup> correlation have been constructed for the  $H_2$  ( $D_2$ ) + Cu(111) system, namely the B86SRP68-DF2 and SRPsol63-DF2 density functionals. The transferability of these density functionals to the  $H_2$  ( $D_2$ ) + Ag(111),  $H_2$  ( $D_2$ ) + Au(111) and  $H_2$  ( $D_2$ ) + Pt(111) systems has been investigated. All newly tested and developed density functionals are based on GGA-exchange and use non-local correlation to describe dissociative chemisorption of  $H_2$  ( $D_2$ ) on Cu(111) within chemical accuracy, and, to the extent that it can be assessed,

improve the transferability to the other systems discussed in this Chapter over the previously reported SRP48 and MS-B86bl SRP density functionals. Two SRP density functionals that include non-local correlation, namely B86SRP68-DF2 and PBE $\alpha$ 57-DF2<sup>101</sup>, are transferable from the highly activated late barrier  $H_2 + Cu(111)$  system to the weakly activated early barrier  $H_2 + Pt(111)$  system and vice versa. This feat could not be demonstrated with GGA and meta-GGA SRP density functionals that do not include non-local correlation. Assessing the transferability of the tested and developed SRP density functionals to H<sub>2</sub> + Ag(111) and H<sub>2</sub> + Au(111) is difficult due to the lack of well characterized molecular beam experiments for Ag(111) and their complete absence for Au(111). A detailed analysis of associative desorption experiments on Cu(111) suggests that accurate calculation of  $E_{1/2}(\nu, J)$  parameters requires an improvement of our dynamical model. Describing the surface degrees of freedom might close the gap between the excellent description of dissociative chemisorption and the good description of associative desorption, for molecules in the vibrational ground state. Any discrepancy in predicted reactivity between simulated associative desorption and dissociative chemisorption remaining after taking into account the effect of surface atom motion can then most likely be attributed to electronhole pair excitation. Lack of additional experiments for the  $H_2 + Au(111)$ system, specifically a well described dissociative chemisorption experiment, presently keeps us from disentangling the effects of surface reconstruction, surface temperature and ehp excitation for this system. Additionally a full molecular beam simulation using QD is presented for the  $H_2 + Cu(111)$  system using the B86SRP68-DF2 density functional, which is the best performing density functional for  $H_2 + Cu(111)$ , and which also gives a good description of the Van der Waals interaction in this system. Overall the  $H_2 + Cu(111)$  system is very well described quasi-classically when looking at molecular beam sticking probabilities or degeneracy averaged initial-state selected reaction probabilities.

# Chapter 6: Performance of made-simple meta-GGA functionals with rVV10 non-local correlation for $H_2$ + Cu(111), $D_2$ + Ag(111), $H_2$ + Au(111) and $D_2$ + Pt(111)

The three made simple mGGA density functionals designed in Chapter 3 have been combined with  $\rm rVV10^{91}$  in order to obtain the MS-PBEl-rVV10, MS-B86bl-rVV10 and MS-RPBEl-rVV10 density functionals. All three developed density functionals can describe the molecular beam dissociative chemisorption experiment of  $\rm D_2$  reacting on Ag(111) with chemical accuracy, and that the MS-B86bl-rVV10 density functional can describe two sets of molecular beam dissociative chemisorption experiments of  $\rm D_2$  reacting on Pt(111) with chemical

1.5. Outlook 9

accuracy. Additionally, by calculating  $E_{1/2}(\nu, J)$  parameters for the H<sub>2</sub> (D<sub>2</sub>) + Au(111) system and comparing to experimental  $E_0(\nu, J)$  parameters chemical accuracy is obtained with the MS-PBEl-rVV10 density functional. Assessing the performance of the three developed MS mGGA DFs for the H<sub>2</sub> (D<sub>2</sub>) + Au(111) system is difficult due the absence of well characterized molecular beam experiments and of calculations using a reconstructed Au(111) surface that incorporate surface motion, as also discussed in Chapter 5. Of the three developed density functionals MS-PBEl-rVV10 performs excellently with respect to the known Van der Waals well geometries. The MS-B86bl-rVV10 and MS-RPBEl-rVV10 density functionals yield Van der Waals well geometries that are somewhat too shallow. In a comparisson to initial-state resolved experiments on  $H_2$  ( $D_2$ ) + Ag(111) an excellent agreement with experiment is observed in the case of H<sub>2</sub>, for all three developed density functionals. With respect to the molecular beam sticking probabilities of  $H_2$  ( $D_2$ ) + Cu(111) the three developed density functionals yield sticking probabilities in line with sticking probabilities predicted by the PBE<sup>94</sup> density functional, which are too high. The three original made simple mGGA density functionals gave a description of the metal that was comparable to the PBEsol<sup>97</sup> density functional. We find that combining them with rVV10<sup>91</sup> non-local correlation comes at the cost of a slightly less good description of the metal. In general lattice constants become somewhat smaller than zero-point energy corrected experimental results. However, the slight underestimation of the calculated lattice constants is still smaller than the overestimation of calculated lattice constants generally found with the best current SRP density functionals that include vdW-DF2<sup>100</sup> nonlocal correlation. The three developed density functionals also predict that the interlayer distance of the top two layers of the six layer slabs that have been used tend to expand somewhat, in contrast to experimental observations. The obtained results show that climbing Jakob's ladder<sup>102</sup> yields increasingly more accurate results for most systems for the gas-surface systems of H<sub>2</sub> (D<sub>2</sub>) interacting with transition metals.

#### 1.5 Outlook

The development of (SRP) density functionals that can describe the reaction of  $H_2$  with multiple transition metal surfaces to within chemical accuracy is a good step forward in the theoretical description of such systems, however many open questions still remain. These questions are however difficult to answer without either additional experimental observations or improvements to the dynamical model, the implementation of which will lead to increased computational cost of the calculations. This section will highlight further research opportunities

that can potentially improve the theoretical description of H<sub>2</sub> interacting with transition metal surfaces.

Further development in theoretical descriptions of small molecules reacting with transition metal surfaces can be roughly segmented in three areas. One of these areas would be the improvement of the dynamical model, by taking into account thermal surface atom motion. Another of these research directions would be climbing Jacob's ladder<sup>102</sup> towards screened hybrid functionals. The third area can be described by approaches that attempt to go beyond the Born-Oppenheimer approximation<sup>103</sup>, thus beyond purely electronically adiabatic dynamics calculations.

The dynamics calculations presented in this thesis assume an ideal relaxed 0 K surface, thus surface atom motion according to the surface temperature is neglected. Adiabatic dynamics calculations on a ground state electronic PES and using the static surface approximation have been shown to work well for the activated reaction of  $H_2$  on cold transition metals<sup>15,104–108</sup>. Associative desorption experiments are however carried out on very hot surfaces<sup>34,38,50</sup>. In these experiments surface atom motion cannot be readily ignored.

Currently surface atom motion can be taken into account by performing direct dynamics calculations in which the forces are calculated on the fly using DFT<sup>107,109–112</sup>. This is however computationally very expensive, which makes it difficult to obtain accurate statistics. Another approach is to obtain a high dimensional PES that can accommodate surface atom motion using the Behler-Parrinello approach to construct a generalized neural network representation of a high dimensional PES<sup>113</sup>. The neural network approach allows for comparatively cheap quasi-classical dynamics calculations once the neural network has been trained to a large batch of electronic structure calculations for random geometries of H<sub>2</sub> above thermally distorted transition metal slabs. This method has now been succesfully applied to create high dimensional neural network potentials for the reaction of small molecules with transition metals<sup>114–117</sup>. Applying this method to the reaction of H<sub>2</sub> with transition metals would make it possible to test the assumption that molecular beam dissociative chemisorption experiments and associative desorption experiments are linked through detailed belance. As discussed in Chapter 5, when incorporating surface atom motion, the remaining difference between predictions made by theory and experiment can then be safely attributed to non-adiabatic effects such as electron-hole pair excitations. Additionally, if such a high dimensional neural network PES would be available, this would allow direct simulation of associative desorption experiments by running trajectories starting around the transition state using Metropolis sampling of the initial conditions 118-122. Although this has to some extent already been done, earlier work 119,120 used a PES that is an

1.5. Outlook 11

approximate fit<sup>123</sup> to unconverged DFT calculations<sup>124</sup> using the PW91 density functional<sup>125</sup>, and the statistical accuracy of the results of the later work<sup>122</sup> was limited by the number of trajectories that could be run due to the direct dynamics method employed. Performing such calculations with the highly accurate density functionals presented in this thesis might answer some of the open questions raised by earlier work<sup>118–122</sup>.

Note that high dimensional neural network potentials may be difficult to implement in QD calculations<sup>126</sup>. The static corrugation model (SCM)<sup>106,127</sup> in combination with the sudden approximation can potentially be used in QD calculations, where multiple QD calculations could be performed for differently initialized surface displacements.

A second way to improve the theoretical description of H<sub>2</sub> interacting with transition metal surfaces may be to climb Jacob's ladder<sup>102</sup>. The density functionals developed in the research that resulted in this thesis are based on the GGA or meta-GGA, a logical next step would be to move towards (screened) hybrid density functionals<sup>128</sup> combined with non-local correlation<sup>129</sup>. As the transferability of meta-GGA based density functionals that include non-local correlation developed in Chapter 6 has demonstrated, climbing to a higher rung on Jacob's ladder has the potential to yield more generally applicable density functionals. Some advances have been made using this approach with the notoriously difficult  $O_2 + Al(111)$  system<sup>130–132</sup> and other systems<sup>133</sup>. However, it is unclear whether hybrid density functionals will be better for H<sub>2</sub> late transition metal surface systems. For these systems,  $(\Phi - EA)$  tends to exceed 7 eV, where  $\Phi$  is the workfunction of the metal and EA the electron affinity of the molecule. For such systems semi-local exchange appears to work quite well<sup>132</sup>. Also, calculations with (screened) hybrid density functionals are computationally very demanding. It will therefore be difficult to go beyond the static surface approximation when using hybrid density functionals in the forseeable future.

The third area in which the theoretical description of  $H_2$  interacting with transition metal surfaces can be improved is by going beyond the Born-Oppenheimer approximation<sup>103</sup>. The lack of a band gap for electronic excitations in a metal allows for energy exchange of the molecule with the surface through electron-hole pair excitations. The effect of electron-hole pair excitations can be modelled as a classical friction force in molecular dynamics with electronic friction (MDEF) calculations<sup>134</sup>. In Chapter 4 this is done in the simplest possible way, by using the local density friction approximation (LDFA) together with the independent atom approximation (IAA)<sup>135,136</sup>. In this approach molecular properties are neglected, as the off-diagonal elements of the friction tensor expressed in Cartesian coordinates of the atoms are taken to

be zero. Therefore kinetic coupling between different degrees of freedom cannot be described in this model. To move beyond this limitation orbital-dependent friction (ODF) could be used in future dynamics calculations  $^{137-139}$ . However the effects of incorporating ODF in the reaction dynamics of  $H_2$  are small and require additional experiments for theoretical predictions to be verified  $^{139}$  and for proving that ODF should be better.

As suggested in Chapters 5 and 6 there is a need for more, more varied, and more accurately described experiments. Presently DFT is the only electronic structure method that is simultaneously computationally cheap and accurate enough to map out full PESs and make large comparative studies feasible. Within the SRP approach to DFT currently experimental observations are neccesary as a benchmark for density functional design. When looking at the  $H_2 + Ag(111)$  and  $H_2 + Au(111)$  systems considered in this thesis, one stark realization is that further development of chemically accurate density functionals for H<sub>2</sub> reacting on transition metal surfaces is still heavily stymied by a lack of experimental data. This is bad news as presently semi-empirical DFT seems to be the only path forward to extracting chemically accurate information on barriers to reaction. Relying on non-empirical constraints in density functional design is not guaranteed to yield better overall accuracy, as illustrated by the poor performance of the SCAN<sup>141</sup> density functional for H<sub>2</sub> +  $Cu(111)^{142}$ . For both the activated and non-activated reactions of  $H_2$  on transitions metals there is now only a single well studied system, namely H<sub>2</sub> + Cu(111) (and maybe  $H_2 + Pt(111)^{143}$ ) (see Chapter 5).

Finally, and this is best illustrated by the work on H<sub>2</sub> (D<sub>2</sub>) reacting on Ag(111) in Chapter 5, many density functionals predict roughly similar molecular beam sticking probabilities but different initial-state resolved reaction probabilities. Observations from new and more detailed experiments could lead the way, and show which theoretical model is more in line with reality. Initial-state resolved reaction probabilities, rotational quadrupole alignment parameters, vibrational efficacies, and inelastic scattering probabilities are more sensitive to the details of the PES<sup>144</sup>. However, accurately described measurements of these observables are sparse<sup>36,41,50,54,55</sup>.

#### References

(1) Ertl, G. Primary steps in catalytic synthesis of ammonia. *J. Vac. Sci. Technol.* **1983**, *1*, 1247–1253.

- (2) Bagot, P. A. J. Fundamental surface science studies of automobile exhaust catalysis. *J. Mater. Sci. Technol.* **2004**, *20*, 679–694.
- (3) Chorkendorff, I.; Niemantsverdriet, J. W., Concepts of modern catalysis and kinetics; John Wiley & Sons, Weinheim: 2017.
- (4) Park, G. B.; Kitsopoulos, T. N.; Borodin, D.; Golibrzuch, K.; Neugebohren, J.; Auerbach, D. J.; Campbell, C. T.; Wodtke, A. M. The kinetics of elementary thermal reactions in heterogeneous catalysis. *Nature Rev. Chem.* **2019**, *3*, 723–732.
- (5) Voet, D.; Voet, J. G., Biochemistry, 4th Edition; NewYork: John Wiley & SonsInc: 2011; Vol. 492.
- (6) Ertl, G. Reactions at surfaces: from atoms to complexity (Nobel lecture). *Angew. Chem. Int. Ed.* **2008**, *47*, 3524–3535.
- (7) Kroes, G.-J. Toward a database of chemically accurate barrier heights for reactions of molecules with metal surfaces. *J. Phys. Chem lett.* **2015**, 6, 4106–4114.
- (8) Sousa-Silva, C.; Seager, S.; Ranjan, S.; Petkowski, J. J.; Zhan, Z.; Hu, R.; Bains, W. Phosphine as a biosignature gas in exoplanet atmospheres. *Astrobiology* **2020**, *20*, 235–268.
- (9) Viti, S.; Holdship, J. In *Machine Learning in Chemistry: The Impact of Artificial Intelligence*; The Royal Society of Chemistry, Cambridge: 2020, pp 195–205.
- (10) Jørgensen, J. K.; Belloche, A.; Garrod, R. T. Astrochemistry during the formation of stars. *Annu. Rev. Astron. Astrophys.* **2020**, *58*, 727–778.
- (11) Yao, Y.; Giapis, K. P. Dynamic molecular oxygen production in cometary comae. *Nat. Comm.* **2017**, *8*, 1–8.
- (12) Wolcott, C. A.; Medford, A. J.; Studt, F.; Campbell, C. T. Degree of rate control approach to computational catalyst screening. *J. Catal.* **2015**, *330*, 197–207.
- (13) Sabbe, M. K.; Reyniers, M.-F.; Reuter, K. First-principles kinetic modeling in heterogeneous catalysis: an industrial perspective on best-practice, gaps and needs. *Catal. Sci. Technol.* **2012**, *2*, 2010–2024.

- (14) Stegelmann, C.; Andreasen, A.; Campbell, C. T. Degree of rate control: how much the energies of intermediates and transition states control rates. J. Am. Chem. Soc. 2009, 131, 8077–8082.
- (15) Kroes, G.-J.; Díaz, C. Quantum and classical dynamics of reactive scattering of H<sub>2</sub> from metal surfaces. *Chem. Soc. Rev.* 2016, 45, 3658– 3700.
- (16) Hoffmann, R. Building bridges between inorganic and organic chemistry (Nobel Lecture). Angew. Chem. Int. Ed. 1982, 21, 711–724.
- (17) Kiselev, V. F.; Krylov, O. V., Adsorption and catalysis on transition metals and their oxides; Springer Science & Business Media, New York: 2012; Vol. 9.
- (18) Hammer, B.; Nørskov, J. Electronic factors determining the reactivity of metal surfaces. *Surf. Sci.* **1995**, *343*, 211–220.
- (19) Hammer, B.; Nørskov, J. Why gold is the noblest of all the metals. *Nature* **1995**, *376*, 238.
- (20) Waugh, K. Methanol synthesis. Catal. Today 1992, 15, 51–75.
- (21) Grabow, L.; Mavrikakis, M. Mechanism of methanol synthesis on Cu through CO<sub>2</sub> and CO hydrogenation. *Acs Catalysis* **2011**, *1*, 365–384.
- (22) Behrens, M.; Studt, F.; Kasatkin, I.; Kühl, S.; Hävecker, M.; Abild-Pedersen, F.; Zander, S.; Girgsdies, F.; Kurr, P.; Kniep, B.-L., et al. The active site of methanol synthesis over Cu/ZnO/Al<sub>2</sub>O<sub>3</sub> industrial catalysts. *Science* **2012**, *336*, 893–897.
- (23) Zaera, F. The surface chemistry of metal-based hydrogenation catalysis. *ACS Catal.* **2017**, *7*, 4947–4967.
- (24) Rylander, P. N., *Hydrogenation methods*; Academic Press: London: 1990.
- (25) Veldsink, J. W.; Bouma, M. J.; Schöön, N. H.; Beenackers, A. A. Heterogeneous hydrogenation of vegetable oils: a literature review. *Cata. Rev.: Sci. Eng.* **1997**, *39*, 253–318.
- (26) Blaser, H.-U.; Malan, C.; Pugin, B.; Spindler, F.; Steiner, H.; Studer, M. Selective hydrogenation for fine chemicals: Recent trends and new developments. Adv. Synth. Catal. 2003, 345, 103–151.
- (27) Chen, B.; Dingerdissen, U.; Krauter, J. G. E.; Rotgerink, H. G. J. L.; Möbus, K.; Ostgard, D. J.; Panster, P.; Riermeier, T.; Seebald, S.; Tacke, T., et al. New developments in hydrogenation catalysis particularly in synthesis of fine and intermediate chemicals. *Appl. Catal. A* **2005**, *280*, 17–46.

(28) Mäki-Arvela, P.; Hájek, J.; Salmi, T.; Murzin, D. Y. Chemoselective hydrogenation of carbonyl compounds over heterogeneous catalysts. *Appl. Catal. A* **2005**, *292*, 1–49.

- (29) Hu, C.; Creaser, D.; Siahrostami, S.; Grönbeck, H.; Ojagh, H.; Skoglundh, M. Catalytic hydrogenation of C — C and C — O in unsaturated fatty acid methyl esters. Catal. Sci. Technol. 2014, 4, 2427–2444.
- (30) Horiuti, I.; Polanyi, M. Exchange reactions of hydrogen on metallic catalysts. *Trans. Faraday Soc.* **1934**, *30*, 1164–1172.
- (31) Gostein, M.; Parhikhteh, H.; Sitz, G. Survival probability of  $H_2$  ( $\nu = 1$ , J=1) scattered from Cu(110). *Phys. Rev. Lett.* **1995**, 75, 342.
- (32) Michelsen, H.; Rettner, C.; Auerbach, D.; Zare, R. Effect of rotation on the translational and vibrational energy dependence of the dissociative adsorption of D<sub>2</sub> on Cu(111). *J. Chem. Phys.* **1993**, *98*, 8294–8307.
- (33) Berger, H.; Leisch, M.; Winkler, A.; Rendulic, K. A search for vibrational contributions to the activated adsorption of H<sub>2</sub> on copper. *Chem. Phys. Lett.* **1990**, *175*, 425–428.
- (34) Kaufmann, S.; Shuai, Q.; Auerbach, D. J.; Schwarzer, D.; Wodtke, A. M. Associative desorption of hydrogen isotopologues from copper surfaces: characterization of two reaction mechanisms. *J. Chem. Phys.* **2018**, *148*, 194703.
- (35) Anger, G.; Winkler, A.; Rendulic, K. Adsorption and desorption kinetics in the systems  $H_2/Cu(111)$ ,  $H_2/Cu(110)$  and  $H_2/Cu(100)$ . Surf. Sci. 1989, 220, 1–17.
- (36) Hou, H.; Gulding, S.; Rettner, C.; Wodtke, A.; Auerbach, D. The stereodynamics of a gas-surface reaction. *Science* **1997**, *277*, 80–82.
- (37) Comsa, G.; David, R. The purely "fast" distribution of  $H_2$  and  $D_2$  molecules desorbing from Cu(100) and Cu(111) surfaces. Surf. Sci. 1982, 117, 77–84.
- (38) Rettner, C.; Michelsen, H.; Auerbach, D. Quantum-state-specific dynamics of the dissociative adsorption and associative desorption of H<sub>2</sub> at a Cu(111) surface. *J. Chem. Phys.* **1995**, *102*, 4625–4641.
- (39) Rettner, C.; Auerbach, D.; Michelsen, H. Dynamical studies of the interaction of D<sub>2</sub> with a Cu(111) surface. J. Vac. Sci. Technol. A **1992**, 10, 2282–2286.
- (40) Rettner, C.; Michelsen, H.; Auerbach, D. Determination of quantum-state-specific gas—surface energy transfer and adsorption probabilities as a function of kinetic energy. *Chem. Phys.* **1993**, *175*, 157–169.

- (41) Hodgson, A.; Samson, P.; Wight, A.; Cottrell, C. Rotational excitation and vibrational relaxation of  $H_2$  ( $\nu = 1$ , J = 0) Scattered from Cu(111). *Phys. Rev. Lett.* **1997**, 78, 963–966.
- (42) Watts, E.; Sitz, G. O. State-to-state scattering in a reactive system:  $H_2$  (v= 1, j= 1) from Cu(100). J. Chem. Phys. **2001**, 114, 4171–4179.
- (43) Michelsen, H.; Rettner, C.; Auerbach, D. On the influence of surface temperature on adsorption and desorption in the D<sub>2</sub>/Cu(111) system. Surf. Sci. **1992**, 272, 65–72.
- (44) Okazawa, T.; Takeuchi, F.; Kido, Y. Enhanced and correlated thermal vibrations of Cu(111) and Ni(111) surfaces. *Physical Review B* **2005**, 72, 075408.
- (45) Lindgren, S.; Walldén, L.; Rundgren, J.; Westrin, P. Low-energy electron diffraction from Cu(111): subthreshold effect and energy-dependent inner potential; surface relaxation and metric distances between spectra. *Phys. Rev. B* 1984, 29, 576–588.
- (46) Chae, K.; Lu, H.; Gustafsson, T. Medium-energy ion-scattering study of the temperature dependence of the structure of Cu(111). *Phys. Rev. B* **1996**, *54*, 14082.
- (47) Andersson, S.; Persson, M. Sticking in the physisorption well: influence of surface structure. *Phys. Rev. Lett.* **1993**, *70*, 202.
- (48) Cao, K.; Füchsel, G.; Kleyn, A. W.; Juurlink, L. B. Hydrogen adsorption and desorption from Cu(111) and Cu(211). *Phys. Chem. Chem. Phys.* **2018**, *20*, 22477–22488.
- (49) Harten, U.; Toennies, J. P.; Wöll, C. Molecular beam translational spectroscopy of physisorption bound states of molecules on metal surfaces.
  I. HD on Cu(111) and Au(111) single crystal surfaces. J. Chem. Phys. 1986, 85, 2249–2258.
- (50) Shuai, Q.; Kaufmann, S.; Auerbach, D. J.; Schwarzer, D.; Wodtke, A. M. Evidence for electron-hole pair excitation in the associative desorption of H<sub>2</sub> and D<sub>2</sub> from Au(111). *J. Phys. Chem. Lett.* **2017**, *8*, 1657–1663.
- (51) Luntz, A.; Brown, J.; Williams, M. Molecular beam studies of H<sub>2</sub> and D<sub>2</sub> dissociative chemisorption on Pt(111). *J. Chem. Phys.* **1990**, *93*, 5240–5246.
- (52) Groot, I.; Ueta, H.; Van der Niet, M.; Kleyn, A.; Juurlink, L. Supersonic molecular beam studies of dissociative adsorption of H<sub>2</sub> on Ru(0001). J. Chem. Phys. 2007, 127, 244701.

(53) Cottrell, C.; Carter, R.; Nesbitt, A.; Samson, P.; Hodgson, A. Vibrational state dependence of D<sub>2</sub> dissociation on Ag(111). *J. Chem. Phys.* **1997**, 106, 4714–4722.

- (54) Murphy, M.; Hodgson, A. Translational energy release in the recombinative desorption of H<sub>2</sub> from Ag(111). Surf. Sci. **1997**, 390, 29–34.
- (55) Murphy, M.; Hodgson, A. Role of surface thermal motion in the dissociative chemisorption and recombinative desorption of D<sub>2</sub> on Ag(111). *Phys. Rev. Lett.* **1997**, 78, 4458–4461.
- (56) Resch, C.; Berger, H.; Rendulic, K.; Bertel, E. Adsorption dynamics for the system hydrogen/palladium and its relation to the surface electronic structure. *Surf. Sci.* **1994**, *316*, L1105–L1109.
- (57) Beutl, M.; Riedler, M.; Rendulic, K. D. Strong rotational effects in the adsorption dynamics of H<sub>2</sub>/Pd(111): evidence for dynamical steering. *Chem. Phys. Lett.* **1995**, 247, 249–252.
- (58) Beutl, M.; Lesnik, J.; Rendulic, K.; Hirschl, R.; Eichler, A.; Kresse, G.; Hafner, J. There is a true precursor for hydrogen adsorption after all: the system H2/Pd (1 1 1)+ subsurface V. Chem. Phys. Lett. 2001, 342, 473–478.
- (59) Gostein, M.; Sitz, G. O. Rotational state-resolved sticking coefficients for H<sub>2</sub> on Pd(111): testing dynamical steering in dissociative adsorption. J. Chem. Phys. 1997, 106, 7378–7390.
- (60) Steinrück, H.-P.; Rendulic, K.; Winkler, A. The sticking coefficient of H<sub>2</sub> on Ni(111) as a function of particle energy and angle of incidence: A test of detailed balancing. *Surf. Sci.* **1985**, *154*, 99–108.
- (61) Robota, H. J.; Vielhaber, W.; Lin, M.-C.; Segner, J.; Ertl, G. Dynamics of interaction of H<sub>2</sub> and D<sub>2</sub> with Ni(110) and Ni(111) surfaces. *Surf. Sci.* **1985**, *155*, 101–120.
- (62) Hayward, D.; Taylor, A. The variation of the sticking probability of hydrogen and deuterium on Ni(111) with energy and angle of incidence. *Chem. Phys. Lett.* **1986**, *124*, 264–267.
- (63) Resch, C.; Zhukov, V.; Lugstein, A.; Berger, H.; Winkler, A.; Rendulic, K. Dynamics of hydrogen adsorption on promoter-and inhibitor-modified nickel surfaces. *Chem. Phys.* 1993, 177, 421–431.
- (64) Salmeron, M.; Gale, R. J.; Somorjai, G. A. Molecular beam study of the H<sub>2</sub>–D<sub>2</sub> exchange reaction on stepped platinum crystal surfaces: Dependence on reactant angle of incidence. *J. Chem. Phys.* **1977**, *67*, 5324–5334.

- (65) Gee, A. T.; Hayden, B. E.; Mormiche, C.; Nunney, T. S. The role of steps in the dynamics of hydrogen dissociation on Pt(533). *J. Chem. Phys.* **2000**, *112*, 7660–7668.
- (66) Gostein, M.; Watts, E.; Sitz, G. O. Vibrational relaxation of  $H_2$  ( $\nu=1$ , J=1) on Pd(111). Phys. Rev. Lett. **1997**, 79, 2891–2894.
- (67) Goncharova, L. V.; Braun, J.; Ermakov, A. V.; Bishop, G. G.; Smilgies, D.-M.; Hinch, B. J. Cu(001) to HD energy transfer and translational to rotational energy conversion on surface scattering. *J. Chem. Phys.* **2001**, *115*, 7713–7724.
- (68) Nieto, P.; Farías, D.; Miranda, R.; Luppi, M.; Baerends, E. J.; Somers, M. F.; van der Niet, M. J. T. C.; Olsen, R. A.; Kroes, G.-J. Diffractive and reactive scattering of H<sub>2</sub> from Ru(0001): experimental and theoretical study. *Phys. Chem. Chem. Phys.* 2011, 13, 8583–8597.
- (69) Whaley, K. B.; Yu, C.-f.; Hogg, C. S.; Light, J. C.; Sibener, S. J. Investigation of the spatially anisotropic component of the laterally averaged molecular hydrogen/Ag(111) physisorption potential. *J. Chem. Phys.* 1985, 83, 4235–4255.
- (70) Berndt, R.; Toennies, J. P.; Wöll, C. Evidence for coupled rotational and phonon quantum excitation in the scattering of a nearly monoenergetic HD beam from the Ni(001) surface. J. Chem. Phys. 1990, 92, 1468– 1477.
- (71) Laurent, G.; Barredo, D.; Farías, D.; Miranda, R.; Díaz, C.; Riviere, P.; Somers, M. F.; Martín, F. Experimental and theoretical study of rotationally inelastic diffraction of D<sub>2</sub> from NiAl(110). *Phys. Chem. Chem. Phys.* 2010, 12, 14501–14507.
- (72) Johansson, M.; Skulason, E.; Nielsen, G.; Murphy, S.; Nielsen, R. M.; Chorkendorff, I. Hydrogen adsorption on palladium and palladium hydride at 1 bar. *Surf. Sci.* **2010**, *604*, 718–729.
- (73) Fiordaliso, E. M.; Murphy, S.; Nielsen, R.; Dahl, S.; Chorkendorff, I. H<sub>2</sub> splitting on Pt, Ru and Rh nanoparticles supported on sputtered HOPG. *Surf. Sci.* **2012**, *606*, 263–272.
- (74) Rendulic, K.; Anger, G.; Winkler, A. Wide range nozzle beam adsorption data for the systems  $H_2/nickel$  and  $H_2/Pd(100)$ . Surf. Sci. **1989**, 208, 404-424.

(75) Sementa, L.; Wijzenbroek, M.; Van Kolck, B.; Somers, M.; Al-Halabi, A.; Busnengo, H. F.; Olsen, R.; Kroes, G.-J.; Rutkowski, M.; Thewes, C., et al. Reactive scattering of H<sub>2</sub> from Cu(100): comparison of dynamics calculations based on the specific reaction parameter approach to density functional theory with experiment. J. Chem. Phys. **2013**, 138, 044708.

- (76) Cowin, J. P.; Yu, C.-F.; Sibener, S. J.; Wharton, L. HD scattering from Pt(111): rotational excitation probabilities. *J. Chem. Phys.* **1983**, *79*, 3537–3549.
- (77) Yu, C.-f.; Whaley, K. B.; Hogg, C. S.; Sibener, S. J. Investigation of the spatially isotropic component of the laterally averaged molecular hydrogen/Ag(111) physisorption potential. *J. Chem. Phys.* **1985**, *83*, 4217–4234.
- (78) Nieto, P.; Pijper, E.; Barredo, D.; Laurent, G.; Olsen, R. A.; Baerends, E.-J.; Kroes, G.-J.; Farías, D. Reactive and nonreactive scattering of H<sub>2</sub> from a metal surface is electronically adiabatic. *Science* 2006, 312, 86–89.
- (79) Bertino, M. F.; Hofmann, F.; Toennies, J. P. The effect of dissociative chemisorption on the diffraction of D<sub>2</sub> from Ni(110). *J. Chem. Phys.* **1997**, *106*, 4327–4338.
- (80) Farías, D.; Díaz, C.; Rivière, P.; Busnengo, H.; Nieto, P.; Somers, M.; Kroes, G.; Salin, A.; Martín, F. In-plane and out-of-plane diffraction of H<sub>2</sub> from metal surfaces. *Phys. Rev. Lett.* **2004**, *93*, 246104.
- (81) Michelsen, H. A.; Auerbach, D. J. A critical examination of data on the dissociative adsorption and associative desorption of hydrogen at copper surfaces. *J. Chem. Phys.* **1991**, *94*, 7502–7520.
- (82) Wetzig, D.; Dopheide, R.; Rutkowski, M.; David, R.; Zacharias, H. Rotational Alignment in Associative Desorption of D<sub>2</sub> ( $\nu'' = 0$  and 1) from Pd(100). *Phys. Rev. Lett.* **1996**, 76, 463–466.
- (83) Darling, G. R.; Holloway, S. Vibrational effects in the associative desorption of H<sub>2</sub>. Surf. Sci. **1992**, 268, L305–L310.
- (84) King, D. A.; Wells, M. G. Molecular beam investigation of adsorption kinetics on bulk metal targets: Nitrogen on tungsten. *Surf. Sci.* **1972**, 29, 454–482.
- (85) Smith Jr, J. N. Molecular beam scattering from solid surfaces: A critical review. Surf. Sci. 1973, 34, 613–637.
- (86) D'Evelyn, M. P.; Madix, R. J. Reactive scattering from solid surfaces. Surf. Sci. Rep. 1983, 3, 413–495.

- (87) Libuda, J.; Freund, H.-J. Molecular beam experiments on model catalysts. Surf. Sci. Rep. 2005, 57, 157–298.
- (88) Zaera, F. Use of molecular beams for kinetic measurements of chemical reactions on solid surfaces. Surf. Sci. Rep. 2017, 72, 59–104.
- (89) Schrödinger, E. An undulatory theory of the mechanics of atoms and molecules. *Phys. Rev.* **1926**, *28*, 1049–1070.
- (90) Busnengo, H.; Salin, A.; Dong, W. Representation of the 6D potential energy surface for a diatomic molecule near a solid surface. *J. Chem. Phys.* **2000**, *112*, 7641–7651.
- (91) Sabatini, R.; Gorni, T.; De Gironcoli, S. Nonlocal van der Waals density functional made simple and efficient. *Phys. Rev. B* **2013**, *87*, 041108.
- (92) Sun, J.; Xiao, B.; Ruzsinszky, A. Communication: Effect of the orbital-overlap dependence in the meta generalized gradient approximation. *J. Chem. Phys.* **2012**, *137*, 051101.
- (93) Sun, J.; Haunschild, R.; Xiao, B.; Bulik, I. W.; Scuseria, G. E.; Perdew, J. P. Semilocal and hybrid meta-generalized gradient approximations based on the understanding of the kinetic-energy-density dependence. J. Chem. Phys. 2013, 138, 044113.
- (94) Perdew, J. P.; Burke, K.; Ernzerhof, M. Generalized gradient approximation made simple. *Phys. Rev. Lett.* **1996**, *77*, 3865–3868.
- (95) Becke, A. D. On the large-gradient behavior of the density functional exchange energy. J. Chem. Phys. 1986, 85, 7184–7187.
- (96) Hammer, B. H. L. B.; Hansen, L. B.; Nørskov, J. K. Improved adsorption energetics within density-functional theory using revised Perdew-Burke-Ernzerhof functionals. *Phys. Rev. B* 1999, 59, 7413–7421.
- (97) Perdew, J. P.; Ruzsinszky, A.; Csonka, G. I.; Vydrov, O. A.; Scuseria, G. E.; Constantin, L. A.; Zhou, X.; Burke, K. Restoring the density-gradient expansion for exchange in solids and surfaces. *Phys. Rev. Lett.* **2008**, *100*, 136406.
- (98) Hamada, I. van der Waals density functional made accurate. *Phys. Rev.* B **2014**, 89, 121103.
- (99) Díaz, C.; Pijper, E.; Olsen, R.; Busnengo, H.; Auerbach, D.; Kroes, G. Chemically accurate simulation of a prototypical surface reaction: H<sub>2</sub> dissociation on Cu(111). *Science* **2009**, *326*, 832–834.

(100) Lee, K.; Murray, É. D.; Kong, L.; Lundqvist, B. I.; Langreth, D. C. Higher-accuracy van der Waals density functional. *Phys. Rev. B* **2010**, 82, 081101.

- (101) Ghassemi, E. N.; Wijzenbroek, M.; Somers, M. F.; Kroes, G.-J. Chemically accurate simulation of dissociative chemisorption of D<sub>2</sub> on Pt(111). *Chem. Phys. Lett.* **2017**, *683*, 329–335.
- (102) Perdew, J. P.; Schmidt, K. In AIP Conf. Proc. 2001; Vol. 577, pp 1–20.
- (103) Born, M.; Oppenheimer, R. Zur quantentheorie der molekeln. Ann. Phys. 1927, 389, 457–484.
- (104) Díaz, C.; Olsen, R. A.; Auerbach, D. J.; Kroes, G.-J. Six-dimensional dynamics study of reactive and non reactive scattering of H<sub>2</sub> from Cu(111) using a chemically accurate potential energy surface. *Phys. Chem. Chem. Phys.* 2010, 12, 6499–519.
- (105) Wijzenbroek, M.; Somers, M. F. Static surface temperature effects on the dissociation of  $H_2$  and  $D_2$  on Cu(111). *J. Chem. Phys.* **2012**, *137*, 054703.
- (106) Spiering, P.; Wijzenbroek, M.; Somers, M. An improved static corrugation model. J. Chem. Phys. **2018**, 149, 234702.
- (107) Nattino, F.; Genova, A.; Guijt, M.; Muzas, A. S.; Díaz, C.; Auerbach, D. J.; Kroes, G.-J. Dissociation and recombination of D<sub>2</sub> on Cu(111): Ab initio molecular dynamics calculations and improved analysis of desorption experiments. J. Chem. Phys. 2014, 141, 124705.
- (108) Nieto, P.; Pijper, E.; Barredo, D.; Laurent, G.; Olsen, R. A.; Baerends, E.-J.; Kroes, G.-J.; Farías, D. Reactive and nonreactive scattering of H<sub>2</sub> from a metal surface is electronically adiabatic. *Science* **2006**, *312*, 86–89.
- (109) Füchsel, G.; Cao, K.; Er, S.; Smeets, E. W. F.; Kleyn, A. W.; Juurlink, L. B. F.; Kroes, G.-J. Anomalous dependence of the reactivity on the presence of steps: dissociation of D<sub>2</sub> on Cu(211). J. Phys. Chem. Lett. 2018, 9, 170–175.
- (110) Nattino, F.; Migliorini, D.; Kroes, G.-J.; Dombrowski, E.; High, E. A.; Killelea, D. R.; Utz, A. L. Chemically accurate simulation of a polyatomic molecule-metal surface reaction. J. Phys. Chem. Lett. 2016, 7, 2402–2406.

- (111) Migliorini, D.; Chadwick, H.; Nattino, F.; Gutiérrez-González, A.; Dombrowski, E.; High, E. A.; Guo, H.; Utz, A. L.; Jackson, B.; Beck, R. D., et al. Surface reaction barriometry: methane dissociation on flat and stepped transition-metal surfaces. J. Phys. Chem. Lett. 2017, 8, 4177–4182.
- (112) Gerrits, N.; Chadwick, H.; Kroes, G.-J. Dynamical study of the dissociative chemisorption of CHD<sub>3</sub> on Pd(111). *J. Phys. Chem. C* **2019**, 123, 24013–24023.
- (113) Behler, J.; Parrinello, M. Generalized neural-network representation of high-dimensional potential-energy surfaces. *Phys. Rev. Lett.* **2007**, *98*, 146401.
- (114) Gerrits, N.; Shakouri, K.; Behler, J.; Kroes, G.-J. Accurate probabilities for highly activated reaction of polyatomic molecules on surfaces using a high-dimensional neural network potential: CHD<sub>3</sub> + Cu(111). *J. Phys. Chem. Lett.* **2019**, *10*, 1763–1768.
- (115) Shakouri, K.; Behler, J.; Meyer, J.; Kroes, G.-J. Accurate neural network description of surface phonons in reactive gas-surface dynamics: N<sub>2</sub>+Ru(0001). J. Phys. Chem. Lett. **2017**, 8, 2131–2136.
- (116) Gerrits, N.; Geweke, J.; Smeets, E. W. F.; Voss, J.; Wodtke, A. M.; Kroes, G.-J. Closing the Gap Between Experiment and Theory: Reactive Scattering of HCl from Au(111). *J. Phys. Chem. C* **2020**, *124*, 15944–15960.
- (117) Zhu, L.; Zhang, Y.; Zhang, L.; Zhou, X.; Jiang, B. Unified and transferable description of dynamics of H<sub>2</sub> dissociative adsorption on multiple copper surfaces via machine learning. *Phys. Chem. Chem. Phys.* **2020**, 22, 13958–13964.
- (118) Perrier, A.; Bonnet, L.; Liotard, D.; Rayez, J.-C. On the dynamics of H<sub>2</sub> desorbing from a Pt(111) surface. Surf. Sci. **2005**, 581, 189–198.
- (119) Perrier, A.; Bonnet, L.; Rayez, J.-C. Dynamical study of  $H_2$  and  $D_2$  desorbing from a Cu(111) surface. J. Phys. Chem. A **2006**, 110, 1608–1617.
- (120) Perrier, A.; Bonnet, L.; Rayez, J.-C. Statisticodynamical approach of final state distributions in associative desorptions. *J. Chem. Phys.* **2006**, *124*, 194701.
- (121) Díaz, C.; Perrier, A.; Kroes, G. Associative desorption of  $N_2$  from Ru(0001): a computational study. *Chem. Phys. Lett.* **2007**, 434, 231–236.

(122) Galparsoro, O.; Kaufmann, S.; Auerbach, D. J.; Kandratsenka, A.; Wodtke, A. M. First principles rates for surface chemistry employing exact transition state theory: application to recombinative desorption of hydrogen from Cu(111). Phys. Chem. Chem. Phys. 2020, 22, 17532– 17539.

- (123) Dai, J.; Zhang, J. Z. Quantum adsorption dynamics of a diatomic molecule on surface: four-dimensional fixed-site model for H<sub>2</sub> on Cu(111). J. Chem. Phys. 1995, 102, 6280–6289.
- (124) Hammer, B.; Scheffler, M.; Jacobsen, K. W.; Nørskov, J. K. Multidimensional potential energy surface for H<sub>2</sub> dissociation over Cu(111). *Phys. Rev. Lett.* 1994, 73, 1400–1403.
- (125) Perdew, J. P.; Chevary, J. A.; Vosko, S. H.; Jackson, K. A.; Pederson, M. R.; Singh, D. J.; Fiolhais, C. Atoms, molecules, solids, and surfaces: Applications of the generalized gradient approximation for exchange and correlation. *Phys. Rev. B* 1992, 46, 6671–6687.
- (126) Manzhos, S.; Dawes, R.; Carrington, T. Neural network-based approaches for building high dimensional and quantum dynamics-friendly potential energy surfaces. *Int. J. Quant. Chem.* 2015, 115, 1012–1020.
- (127) Wijzenbroek, M.; Somers, M. Static surface temperature effects on the dissociation of H<sub>2</sub> and D<sub>2</sub> on Cu(111). *J. Chem. Phys.* **2012**, *137*, 054703.
- (128) Krukau, A. V.; Vydrov, O. A.; Izmaylov, A. F.; Scuseria, G. E. Influence of the exchange screening parameter on the performance of screened hybrid functionals. J. Chem. Phys. 2006, 125, 224106.
- (129) Berland, K.; Jiao, Y.; Lee, J.-H.; Rangel, T.; Neaton, J. B.; Hyldgaard, P. Assessment of two hybrid van der Waals density functionals for covalent and non-covalent binding of molecules. J. Chem. Phys 2017, 146, 234106.
- (130) Livshits, E.; Baer, R.; Kosloff, R. Deleterious effects of long-range self-repulsion on the density functional description of O<sub>2</sub> sticking on aluminum. *J. Phys. Chem. A* **2009**, *113*, 7521–7527.
- (131) Liu, H.-R.; Xiang, H.; Gong, X. First principles study of adsorption of O<sub>2</sub> on Al surface with hybrid functionals. *J. Chem. Phys.* **2011**, *135*, 214702.

- (132) Gerrits, N.; Smeets, E. W. F.; Vuckovic, S.; Powell, A. D.; Doblhoff-Dier, K.; Kroes, G.-J. Density functional theory for molecule–metal surface reactions: When does the generalized gradient approximation get it right, and what to do if it does not. J. Phys. Chem. Lett, 2020, 11, 10552–10560.
- (133) Mallikarjun Sharada, S.; Bligaard, T.; Luntz, A. C.; Kroes, G.-J.; Nørskov, J. K. Sbh10: A benchmark database of barrier heights on transition metal surfaces. J. Phys. Chem. C 2017, 121, 19807–19815.
- (134) Alducin, M.; Muiño, R. D.; Juaristi, J. Non-adiabatic effects in elementary reaction processes at metal surfaces. *Prog. Surf. Sci.* **2017**, *92*, 317–340.
- (135) Juaristi, J.; Alducin, M.; Muiño, R. D.; Busnengo, H. F.; Salin, A. Role of electron-hole pair excitations in the dissociative adsorption of diatomic molecules on metal surfaces. *Phys. Rev. Lett.* **2008**, *100*, 116102.
- (136) Puska, M. J.; Nieminen, R. M. Atoms embedded in an electron gas: Phase shifts and cross sections. *Phys. Rev. B* **1983**, *27*, 6121–6128.
- (137) Askerka, M.; Maurer, R. J.; Batista, V. S.; Tully, J. C. Role of tensorial electronic friction in energy transfer at metal surfaces. *Phys. Rev. Lett.* **2016**, *116*, 217601.
- (138) Maurer, R. J.; Jiang, B.; Guo, H.; Tully, J. C. Mode specific electronic friction in dissociative chemisorption on metal surfaces: H 2 on Ag (111). *Physical review letters* 2017, 118, 256001.
- (139) Spiering, P.; Meyer, J. Testing electronic friction models: vibrational de-excitation in scattering of H<sub>2</sub> and D<sub>2</sub> from Cu(111). *J. Phys. Chem. Lett.* **2018**, *9*, 1803–1808.
- (140) Doblhoff-Dier, K.; Meyer, J.; Hoggan, P. E.; Kroes, G.-J. Quantum Monte Carlo calculations on a benchmark molecule-metal surface reaction:  $H_2 + Cu(111)$ . J. Chem. Theory Comput. **2017**, 13, 3208–3219.
- (141) Sun, J.; Ruzsinszky, A.; Perdew, J. P. Strongly constrained and appropriately normed semilocal density functional. *Phys. Rev. Lett.* **2015**, 115, 036402.
- (142) Smeets, E. W. F.; Voss, J.; Kroes, G.-J. Specific reaction parameter density functional based on the meta-generalized gradient approximation: application to  $H_2 + Cu(111)$  and  $H_2 + Ag(111)$ . J. Phys. Chem. A **2019**, 123, 5395–5406.

(143) Ghassemi, E. N.; Somers, M. F.; Kroes, G.-J. Assessment of two problems of specific reaction parameter density functional theory: sticking and diffraction of H<sub>2</sub> on Pt(111). *J. Phys. Chem. C* **2019**, *123*, 10406–10418.

(144) Díaz, C.; Olsen, R. A.; Busnengo, H. F.; Kroes, G. J. Dynamics on six-dimensional potential energy surfaces for H<sub>2</sub>/Cu(111): Corrugation reducing procedure versus modified Shepard interpolation method and PW91 versus RPBE. J. Phys. Chem. C 2010, 114, 11192–11201.

# 2 Theory and methods

In this chapter the theory behind electronic structure calculations, the construction of potential energy surfaces (PESs), quasi-classical trajectory (QCT) calculations, and quantum dynamics (QD) calculations is introduced. The last section deals with the calculation of observables which can be used to compare to experimental observations.

Within the realm of quantum mechanics the wave function, usually denoted with the Greek letter  $\Psi$ , seems to take on the role of magical all-knowing oracle. There has been much discussion since its inception on whether the wave function is real object or a mathematical tool, and on whether it is a complete description of reality<sup>1–3</sup>. These sort of musings on the deep mathematical nature of reality are, however, far beyond the scope of this thesis.

From here on it is presumed that everything that can be calculated about a particular particle or system is described by the (non-relativistic) time-dependent Schrödinger equation for coupled electron-nuclei dynamics<sup>4,5</sup>. Throughout this chapter we shall assume that the Born-Oppenheimer approximation<sup>6</sup> (BOA) has been made. In practice this means that in QD calculations we first need to solve the electronic structure problem to compute the ground state PES. After the PES is obtained the time-dependent Scrödinger equation for the nuclear dynamics can be solved. With a quasi-classical approach we can also solve Hamilton's equations of motion instead. Alternatively forces can be obtained on the fly from an electronic structure method, and used to solve Hamilton's equations of motion in direct dynamics calculations.

# 2.1 Electronic structure theory: density functional theory (DFT)

Calculating a PES for  $H_2$  interacting with a metal surface in the static surface approximation involves solving the electronic problem for many different configurations of  $H_2$  relative to the surface. DFT is a particularly efficient method for solving the electronic structure problem<sup>7,8</sup>. DFT has its origin in the 1927 Thomas-Fermi model<sup>9,10</sup>, which tries to evaluate the energy of a system using only the three dimensional electron density of a system,  $n(\vec{r})$ , as opposed to

the wave function of a system which depends on the coordinates of all particles in the system. The lack of a rigorous foundation of the Thomas-Fermi model and the large errors it produces for molecular calculations made it a rather crude tool, not suited for quantum chemistry<sup>11</sup>.

Hohenberg and Kohn<sup>7</sup> provided the rigorous foundation by showing that for a system of electrons in an external potential (i.e. the potential generated by the nuclei) the ground state wave function is a unique, although unknown, functional of the electron density  $n(\vec{r})$ . It was also shown that the exact ground state corresponds to the global minimum of the unknown functional of  $n(\vec{r})$ , which makes it possible to apply the variational principle to obtain the minimum energy and ground state electron density for a given approximation. Thus the evaluation of the energy density functional on an electron density which is not the ground state electron density will yield a higher energy than the ground state energy.

A difficulty in DFT arises in calculating the electrons' kinetic energy from  $n(\vec{r})$ , which is the main constituent of the total energy of the system. A solution to this problem was given by Kohn and Sham<sup>8</sup> in the form of a ficticious system of non-interacting electrons in an effective external potential. The Kohn-Sham equations recast the many electron problem as a set of N single-electron equations:

$$\left[-\frac{\nabla^2}{2} + V_{KS}(\vec{r})\right]\phi_i(\vec{r}) = \epsilon_i \phi_i(\vec{r}) \tag{2.1}$$

In this equation and those below we will assume that atomic units are used. Here,  $\phi_i(\vec{r})$  is the single particle orbital (or Kohn-Sham orbital) for a ficticious non-interacting system. The electron density can then be retrieved by summing over all Kohn-Sham orbitals.

$$n(\vec{r}) = \sum_{i=1}^{N} |\phi_i(\vec{r})|^2$$
 (2.2)

The first term in equation 2.1 represents the kinetic energy of the non-interacting electrons, and the second term is the Kohn-Sham potential,  $V_{KS}(\vec{r})$ . The Kohn-Sham potential is given by

$$V_{KS}(\vec{r}) = V_{ext}(\vec{r}) + V_H(\vec{r}) + V_{xc}(\vec{r}),$$
 (2.3)

in which  $V_{ext}(\vec{r})$  is the external potential,  $V_H(\vec{r})$  is the Hartree (Coulomb) potential, given by

$$V_H(\vec{r}) = \int \frac{n(\vec{r}')}{|\vec{r} - \vec{r}'|} d\vec{r}', \qquad (2.4)$$

and the exchange-correlation potential is given by

$$V_{xc}(\vec{r}) = \frac{\partial E_{xc}[n(\vec{r})]}{\partial n(\vec{r})}.$$
 (2.5)

 $V_{xc}(\vec{r})$  represents the error made by ignoring many-body effects by using the kinetic energy of the system of non-interacting electrons and the Coulomb potential. Although Hohenberg and Kohn<sup>7</sup> proved that a universal exchange-correlation functional,  $E_{xc}$ , must exist, it is, presently, not known exactly. In any practical calculation it is therefore approximated. These approximations are discussed in section 2.1.1.

# 2.1.1 Exchange-correlation density functionals: LDA, GGA, meta-GGA

As discussed in section 2.1, the expression of the exact exchange-correlation functional is unknown. Many non-empirical density functionals have been constructed that recover some or all known exact constraints on the design of density functionals<sup>11,12</sup>. Some notable examples are the PBE<sup>13</sup>, PBEsol<sup>14</sup>, RPBE<sup>15</sup>, B86b<sup>16</sup>, TPSS<sup>17</sup>, revTPSS<sup>18</sup>, and SCAN<sup>19</sup> density functionals. In general semi-local approximations to the exchange-correlation functional, in a spin unpolarized framework, take the following form:<sup>20</sup>

$$E_{xc}(n(\vec{r})) = \int d^3\vec{r} n(\vec{r}) \epsilon_{xc}(n(\vec{r}), \nabla n(\vec{r}), \tau(\vec{r}))$$
 (2.6)

Here,  $\nabla n(\vec{r})$  is the gradient of  $n(\vec{r})$ , and  $\tau(\vec{r})$  is the kinetic energy density. Both  $\nabla n(\vec{r})$  and  $\tau(\vec{r})$  depend on  $n(\vec{r})$ . In equation 2.6 one can choose to only take into account  $n(\vec{r})$ , this is called the local density approximation (LDA)<sup>8</sup>. In the LDA the exchange-correlation energy is taken to be the exchange-correlation energy of the homegeneous electron gas of the same density as  $n(\vec{r})$ .

When one chooses to take into account not only  $n(\vec{r})$  but also  $\nabla n(\vec{r})$  this amounts to climbing Jacob's ladder<sup>21</sup> one rung up to the generalized gradient approximation (GGA)<sup>13,15,22</sup>. At the GGA level the exchange-correlation energy thus depends on both  $n(\vec{r})$  and its gradient. When  $n(\vec{r})$ ,  $\nabla n(\vec{r})$  and  $\tau(\vec{r})$  are taken into account in equation 2.6 one climbs another rung on Jacob's ladder<sup>21</sup> towards a meta-GGA exchange-correlation density functional<sup>18,19</sup>. Taking into

account higher orders in the expansion of  $n(\vec{r})$  amounts to taking into account more and more information about the local environment of each point in the three dimensional  $n(\vec{r})$ . So far only one density functional has been reported that statisfies all known exact constraints on a exchange-correlation functional, namely the SCAN density functional<sup>19</sup>. Statisfying all known exact constraints is however no panacea for describing the interaction of  $H_2$  with transistion metal surfaces, as will be discussed in chapter 3.

Many different functional expressions have been put forward as exchange correlation functionals. The work presented in this thesis focuses on the construction of density functionals at the GGA level (see chapter 5) and the meta-GGA level (see chapters 3 and 6).

#### 2.1.2 Non-local correlation

When an exchange-correlation functional is solely based on  $n(\vec{r})$ ,  $\nabla n(\vec{r})$  and/or  $\tau(\vec{r})$  it is inherently (semi-)local. Such exchange-correlation functionals cannot describe longe range electronic correlations such as Van der Waals interactions. As will be discussed in chapter 5, longe range electronic correlation is also important in the description of the interaction of  $H_2$  with transition metals.

So far, several methods have been proposed that introduce long range (non-local) correlation in DFT calculations<sup>23</sup>. The simplest method is the DFT-D3 method by Grimme<sup>24,25</sup> in which a pairwise potential is added based on  $C_6$  coefficients computed using time-dependent density functional theory (TD-DFT). A more general approach to incorporating non-local correlation in DFT calculations is based on the Rutgers-Chalmers formulation of non-local correlation by Lundqvist et al.<sup>26</sup>. One of the first generally applicable non-local exchange-correlation density functionals was the vdW-DF1 density functional proposed by Dion et al.<sup>27</sup>, and its later revision vdW-DF2<sup>28</sup>. Other implementations based on the same Rutgers-Chalmers formalism are the VV10<sup>29</sup> and rVV10<sup>30</sup> non-local exchange-correlation density functionals. The difference between the vdW-DF and VV10 based functionals is that the former consists of the local LDA correlation functional and a non-local correlation term, whereas the latter consists of a semi-local (beyond LDA) correlation functional plus a non-local correlation term.

The non-local term that is part of the vdW-DF and VV10 based non-local correlation functionals can be written as:

$$E_c^{\text{non-local}} = \int d\vec{r} n(\vec{r}) \left(\frac{\hbar}{2} \int d\vec{r}' \Phi(\vec{r}, \vec{r}') n(\vec{r}') + \beta\right). \tag{2.7}$$

Here  $\Phi(\vec{r}, \vec{r}')$  is the kernel describing density-density interactions<sup>31</sup>. The parameter  $\beta$  is not present in the vdW-DF non-local correlation functionals and is taken to be  $\beta = \frac{1}{32} (\frac{3}{b})^{\frac{3}{4}}$  in the VV10 group of non-local correlation functionals to ensure a zero non-local correlation energy for the homogeneous electron gas<sup>32</sup>. In the VV10 group of non-local correlation functionals the b parameter is optimized to avoid double counting of intermediate range correlation effects that might be present in the semi-local correlation functional that is part of the VV10 based correlation functionals.

In the context of plane wave DFT the method of Román-Pérez and Soler<sup>31</sup> has allowed for the vdW-DF1<sup>27</sup>, vdW-DF2<sup>28</sup>, VV10<sup>29</sup> and rVV10<sup>30</sup> non-local correlation functionals to efficiently evaluate the double integral over  $n(\vec{r})$  by use of an auxiliary function called the kernel which describes the density-density interactions. Note that apart from a convergence paramter C present in the integration kernel, only the vdW-DF1<sup>27</sup> non-local correlation functional is non-empirical<sup>23</sup>. In the construction of the vdW-DF2<sup>28</sup>, VV10<sup>29</sup> and rVV10<sup>30</sup> non-local correlation functionals at least one parameter is optimized to obtain better agreement with experimental observables.

#### 2.1.3 The problem of obtaining accurate reaction barriers

Currently no first principles electronic structure method exists that can compute molecule-metal interaction energies and barrier heights to within chemical accuracy (1 kcal/mol<sup>33</sup>). For the benchmark  $H_2 + Cu(111)$  system diffusion Monte-Carlo (DMC) calculations underestimate the best available value for the reaction barrier height by  $1.6\pm1.0$  kcal/mol<sup>34</sup>. The description of  $O_2$  scatttering from Al(111) was greatly improved by dynamics calculations employing an embedded correlated wave function (ECW) method, but chemical accuracy was not yet reached<sup>35</sup>.

In the absence of chemically accurate first principles methods describing the interaction of molecules with metals, validation of calculated barrier heights needs to be performed in relation to experimental measurements. However, a barrier height is not a direct observable. An alternative path to validating calculated results uses a dynamics method to compute a physical quantity that is an observable, such as the sticking probability as a function of the incidence energy. The sticking probability as a function of the incidence energy can be measured in supersonic molecular beam experiments<sup>36</sup>. The fact that such experiments can probe the reactivity of specific, well-defined Miller index metal surfaces at low temperatures make such experiments suitable for validation of calculated barrier heights<sup>33</sup>.

#### 2.1.4 Specific reaction parameter approach to DFT

The specific reaction parameter (SRP) approach to DFT is a semi-empirical method, originally proposed by Truhlar and coworkers<sup>37,38</sup>. Since the work presented in this thesis mostly focuses on reproducing molecular beam dissociative chemisorption experiments, the SRP method is applied by selecting a specific observable (here the zero coverage sticking probability,  $S_0$ ) of an experiment. In the present context a SRP density functional ( $E_{xc}^{\rm SRP}$ ) is then constructed by taking a weighted average of a density functional (e.g.  $E_{xc}^{\rm A}$ ) that overestimates the sticking probability, and one density functional (e.g.  $E_{xc}^{\rm B}$ ) that underestimates the sticking probability for the system of interest<sup>39</sup>.

$$E_{xc}^{\text{SRP}} = \alpha \cdot E_{xc}^{\text{A}} + (1 - \alpha) \cdot E_{xc}^{\text{B}}$$
(2.8)

Here  $\alpha$  is the SRP mixing parameter. This approach allows for the construction of chemically accurate SRP density functionals for specific systems<sup>33,39–43</sup>. A SRP density functional might be considered successful if it is fitted to reproduce one particular experiment, while also being able to describe another experiment on the same system the SRP density functional was not fitted to. Additionally, a SRP density functional can be considered transferable if it can reproduce experimental results for a system it was not fitted to, i.e. a molecular beam dissociative chemisorption experiment on the same molecule reacting with a different transition metal surface. Note that there exist also other approaches to creating a tunable density functional, one such example would be the PBE $\alpha$  density functional<sup>44</sup> in which  $\alpha$  can be adjusted, as was done for  $H_2 + Pt(111)^{40}$ .

So far SRP density functionals fitted to reproduce molecular beam dissociative chemisorption experiments for  $H_2$  and  $D_2$  were shown to be transferable among systems in which  $H_2$  interacts with different crystal faces of the same metal<sup>45,46</sup>, but not with different metals<sup>47,48</sup>. Transferability of SRP density functional among systems in which the same molecule interacts with different metals has only been reported for  $CH_4$  dissociation on  $Ni(111)^{42}$  to  $CH_4$  dissociation on  $Pt(111)^{49}$ . In chapters 5 and 6 it will be shown that this type of transferability can also be achieved for the reaction of  $H_2$  and  $D_2$  on low Miller index surfaces of transition metals, when using a non-local correlation functional such as vdW-DF1<sup>27</sup>, vdW-DF2<sup>28</sup> or  $vVV10^{30}$ .

In equation 2.8 a weighted average is taken of two exchange correlationfunctionals. In practice often only the exchange part of two density functionals is mixed in the creation of a SRP density functional. When creating SRP density functionals that incorporate a non-local correlation functional two expressions for the total exchange-correlation functional can be obtained, depending on whether the non-local correlation part stems from the vdW-DF or VV10 group of non-local correlation functionals:

$$E_{xc}^{\text{SRP}} = \alpha \cdot E_x^{\text{A}} + (1 - \alpha) \cdot E_x^{\text{B}} + \underbrace{E_c^{\text{LDA}} + E_c^{\text{non-local}}}_{\text{(r)VV10 non-local correlation}} (2.9a)$$

$$E_{xc}^{\text{SRP}} = \alpha \cdot E_x^{\text{A}} + (1 - \alpha) \cdot E_x^{\text{B}} + \underbrace{E_c^{\text{semi-local}} + E_c^{\text{non-local}}}_{\text{(r)VV10 non-local correlation}} (2.9b)$$

#### 2.1.5 Periodic DFT

Metal surfaces are often periodic. In this case it is advantageous to treat the metal surface as infinitely periodic in DFT calculations, since this naturally allows for performing calculations on only the atoms that are part of the repeating unit cell. Calculations using a finite metal slab would quickly spiral out of control with respect to computational cost due to the need to use large finite slabs in order to avoid 'edge' effects. An elegant way of introducing periodicity in DFT calculations is by applying Bloch's theorem<sup>50</sup>, which applies to the solution of the Schrödinger equation of an electron in a periodic potential, and to the Kohn-Sham orbitals of equation 2.1. Bloch's theorem states that eigenfunction for an electron in a periodic potential can always be written as a plane wave multiplied with a periodic function which obeys the periodicity of the system

$$\phi_{i,\vec{k}}(\vec{r}) = u_k(\vec{r})e^{i\vec{k}\cdot\vec{r}}.$$
(2.10)

Here  $\vec{k}$  is a wave vector in the first Brillouin zone, and i is an index running over all Khon-Sham orbitals. The function  $u_k(\vec{r})$  is a function that obeys the same periodicity as the potential of the surface  $(\vec{R})$ , i.e.  $u_k(\vec{r}) = u_k(\vec{r} + \vec{R})$ . When expanding  $u_{\vec{k}}(\vec{r})$  in a Fourier series (plane wave basis set) the Kohn-Sham orbitals can be written as

$$\phi_{i,\vec{k}}(\vec{r}) = N \sum_{G} c_{i,k}(\vec{G}) e^{i(\vec{k} + \vec{G}) \cdot \vec{r}},$$
(2.11)

where N is a normalization constant,  $\vec{G}$  is a reciprocal lattice vector and  $c_{i,k}(\vec{G})$  are the expansion coefficients.

In principle the Fourrier expansion is exact, in practice a maximum kinetic energy cut-off is used for the plane waves in the basis set according to:

$$\frac{1}{2}|\vec{k} + \vec{G}|^2 \le E_{\text{cut-off}} \tag{2.12}$$

Note that describing high energy core electrons using plane waves would require exceedingly high cut-off energies. To get around this problem one can replace the Coulomb potential set up by the bare nucleus and the core electrons by the potential of a pseudo atom. This pseudo atom would describe the nucleus, the core electrons, and the interactions between them, including relativistic effects<sup>51,52</sup>. Pseudo potentials are constructed in such a way that the pseudo wave function is as smooth as possible within a cut-off radius  $r_c$  close to the nucleus while simultaneously yielding almost exactly the same real potential and wave function outside of  $r_c$ . Given that the wave function describing the core of the atoms is much smoother when using pseudo potentials, calculations can be carried out using a lower cut-off energy (see equation 2.12). For the work presented in this thesis two types of pseudo potentials have been used, namely Vanderbilt's ultrasoft pseudo potentials<sup>51</sup> and the more general projector-augmented-wave potentials<sup>53</sup>.

# 2.2 Constructing potential energy surfaces

Obtaining a continuous representation of the six dimensional PES of a diatomic molecule interacting with a surface of which the surface atoms are fixed in their ideal lateral positions can be achieved by applying the corrugation reducing procedure (CRP)<sup>54,55</sup>. The CRP method is a rather efficient procedure to interpolate potential energies calculated on a grid and obtained from any electronic structure method. In the CRP method the molecule-surface PES is written as

$$V^{6D}(\mathbf{R}, \mathbf{r}) = I^{6D}(\mathbf{R}) + \sum_{i=1}^{2} V^{3D}(\mathbf{r}_i), \qquad (2.13)$$

where R are the coordinates of the molecule,  $r_i$  are the coordinates of the  $i^{\rm th}$  atom belonging to the molecule,  $V^{3D}$  is the atom-surface potential evaluated for each atom, and  $I^{6D}$  is the so-called interpolation function. Subtracting the atomic potentials from the six dimensional potential ensures that  $I^{6D}$  is a smooth function that can readily be interpolated without performing an excessive amount of electronic structure calculations. The atom-surface potential is constructed in a similar way as the molecule-surface potential. The atom-surface potential is written as

$$V^{3D}(\mathbf{r_i}) = I^{3D}(\mathbf{r_i}) + \sum_{j}^{N} V^{1D}(\mathbf{r_{ij}})$$
 (2.14)

where  $I^{3D}$  is the three dimensional interpolation function that needs to be interpolated over the atomic coordinates  $r_i$ ,  $r_{ij}$  is the distance between atom i and surface atom j, and  $V^{1D}$  is a one dimensional corrugation reduction function. For  $V^{1D}$  one usually takes the Z dependence of the interaction of an atom normally incident on a top layer surface atom.

Applying the steps outlined in equations 2.13 and 2.14 reduces the corrugation of  $I^{6D}$  in the  $X, Y, \theta$  and  $\phi$  degrees of freedom with respect to  $V^{6D54}$ . The number of electronic structure calculations that need to be performed can be further reduced by taking into account the symmetry of the surface during the interpolation. The way this is achieved is by generating symmetry adapted basis functions for the interpolation using a Fourier expansion that obeys the correct wallpaper group symmetry of the surface<sup>56</sup>. The way this is done specifically for the CRP PESs created for the work in this thesis has been documented in the PhD thesis of Wijzenbroek<sup>57</sup>.

# 2.3 Nuclear dynamics

After a six dimensional (i.e. depending on the six degrees of freedom of the  $H_2$  molecul are in relation to the metal surface) PES has been obtained, nuclear dynamics calculations can be performed either quasi-classically or quantum mechanically. Both methods can be used to calculate observables (see section 2.4) which in turn can be used to compare to experimental observations.

# 2.3.1 Quasi-classical trajectory method

In the quasi-classical trajectory method Newton's equations of motion are solved for the six degrees of freedom of the  $H_2$  molecule moving on the six dimensional PES.

$$M_i \frac{d^2 \mathbf{R}_i}{dt^2} = -\nabla_i V^{6D}(\mathbf{R}_i)$$
 (2.15)

Here i is the index that runs over the atoms in a diatomic molecule, and  $M_i$  is the mass of atom i. In all but chapter 4 the predictor-corrector method of Burlisch and Stoer<sup>58</sup> is used to integrate the equation of motion. Additionally, quasi-classical conditions are assumed<sup>59</sup> such that the quantum mechanical energies of impinging H<sub>2</sub> molecules in their initial rovibrational state are taken into account by imparting them to the molecule at time  $t_0$ . The energies of the rovibrational states of the H<sub>2</sub> molecule are obtained by using the Fourier grid Hamiltonian (FGH) method<sup>60</sup>.

The initial conditions of each trajectory are set up as follows. At the start of each trajectory the molecule is placed in the gasphase at  $Z = Z_{gas}$ , where

the potential does not depend on Z. The impact site in X and Y is randomly sampled, and an initial velocity vector for the center of mass of the molecule is constructed based on the chosen initial perpendicular and parallel translational energy ( $E_{\perp}$  and  $E_{\parallel}$ , respectively). The initial positions and momenta are further constrained by the the vibrational quantum number  $\nu$ , the rotational quantum number J and the magnetic rotational quantum number  $m_J$ . The orientation of the molecule with respect to  $\theta$  and  $\phi$  is choosen based on the rotational state. The initial angular momentum L is set by  $L = \sqrt{J(J+1)}\hbar$  and the orientation of L is randomly sampled with the constraint  $\cos\theta_L = m_J/\sqrt{J(J+1)}$ . Here  $\theta_L$  denotes the angle between L and the surface normal. The vibrational energy of a particular vibrational state is imparted to the molecule by randomly sampling positions and momenta obtained from a one dimensional classical dynamics calculations of the vibrating molecule of the same energy as the selected vibrational state.

Trajectories are considered to be reacted when the H-H distances becomes larger than some critical value  $r_c$ , and trajectories are considered to be scattered when Z becomes bigger than  $Z_{\rm gas}$  and has a momentum away from the surface. For practical reasons there is a maximum propagation time  $t_{\rm max}$  for all trajectory calculations. If neither reaction nor scattering has occurred the molecule is considered to be trapped. It should however be noted that when no energy is removed from the molecule during the trajectory, as is the case here, in principle no trapping should occur in the limit of an infinite simulation time. The reaction probability  $P_r$  is then calculated by dividing the number of reacted trajectories  $N_r$  by the total number of trajectories  $N_{\rm total}$ .

$$P_r = \frac{N_r}{N_{\text{total}}} \tag{2.16}$$

The standard error in  $P_r$ ,  $\sigma_{P_r}$ , can then be computed as

$$\sigma_{P_r} = \sqrt{\frac{P_r(1 - P_r)}{N_{\text{total}}}}.$$
(2.17)

#### Langevin equation with energy dissipation

In chapter 4 the Langevin equation is used instead of Newton's equations of motion in order to make it possible to carry out molecular dynamics calculations that incorporate electronic friction (MDEF). Disspative effects due to electron-hole pair excitations in MDEF calculations have been described phenomenologically by coupling the six-dimensional  $H_2$  molecule to a heat bath. The coupling is here realized by a  $(6 \times 6)$  frictional tensor  $\eta$ , which accounts

for the effect of electron-hole pair excitations during the dynamics $^{61-63}$ .

$$M_{i} \frac{d^{2} \mathbf{R}_{i}}{dt^{2}} = -\nabla_{i} V^{6D}(\mathbf{R}_{i}) - \underbrace{\sum_{k=1}^{N} \eta_{ik} \frac{d \mathbf{R}_{i}}{dt}}_{\text{friction force}} + F_{i}^{\text{random}}(T)$$
 (2.18)

Here  $\eta_{ik}$  is the frictional tensor element, and  $F_i^{\text{random}}(T)$  is a temperature dependent random force. The temperature dependent random force is calculated as discussed in references<sup>62,63</sup>, and is taken such that the fluctuation-dissipation theorem<sup>64</sup> can be taken into account<sup>65</sup>

$$\langle F_i^{\text{random}}(t) F_j^{\text{random}}(t') \rangle = 2k_B T_{el} \eta_{ii} \delta_{i,j} \delta(t - t').$$
 (2.19)

In equation 2.19  $k_B$  is the Boltzmann constant. In this way  $F_i^{\text{random}}(T)$  is taken to be correlated to a Gaussian white noise distribution which is implemented as discussed in reference<sup>62</sup>, and vanishes for T = 0K. The electronic temperature  $T_{el}$  is taken to be equal to the surface temperature. Equation 2.18 is integrated using the Ermak-Buckholz propagator<sup>66</sup>.

The local density friction approximation (LDFA) together with the independent atom approximation (IAA) is used to calculate the friction coefficients of equation  $2.18^{67,68}$ . Molecular properties are thus neglected in this approach and the off-diagonal elements of the friction tensor as expressed in the Cartesian coordinates of the atoms are zero. As a consequence kinetical coupling between different degrees of freedom cannot be described in this model. Whether the LDFA is a valid approximation in combination with the IAA is still under debate<sup>69–71</sup>, but it allows for a comparably simple incorporation of electronically non-adiabatic effects during the dynamics of  $H_2$  reacting on transition metal surfaces<sup>62,63,67,69,72,73</sup>.

# 2.3.2 Quantum dynamics

Six dimensial quantum dynamics (QD) calculations are performed by using the time-dependent wave packet (TDWP) method  $^{74-76}$  in order to solve the time-dependent nuclear Schrödinger equation:

$$i\hbar \frac{d\Psi(\vec{Q};t)}{dt} = \hat{H}\Psi(\vec{Q};t). \tag{2.20}$$

This is done using an in-house computer package<sup>77,78</sup>. Here,  $\Psi(\vec{Q};t)$  denotes the nuclear wave function of  $H_2$  at time t with  $\vec{Q}$  being the position vector. To describe motion in the six degrees of freedom of  $H_2$  the following Hamiltonian

is used:

$$\hat{H} = -\frac{\hbar^2}{2M} \nabla^2 - \frac{\hbar^2}{2\mu} \frac{\partial^2}{\partial r^2} + \frac{1}{2\mu r^2} \hat{J}^2(\theta, \phi) + V^{6D}(\vec{Q}). \tag{2.21}$$

Here, M and  $\mu$  are the mass and reduced mass of  $H_2$ , and  $\hat{J}^2(\theta,\phi)$  is the angular momentum squared operator. A discrete variable representation (DVR)<sup>79</sup> is used to represent the wave packet in the Z,r,X and Y degrees of freedom and a finite basis representation (FBR)<sup>80,81</sup> is used for the angular degrees of freedom. In order to transform the wave function from the DVR to the FBR and back, fast Fourier transforms<sup>82</sup> and discrete associated Gauss-Legendre transforms<sup>80,81</sup> are employed.

The initial wave packet is constructed as a product of a gas phase rovibrational eigenfunction of  $H_2$  characterized by the quantum numbers  $\nu, J$  and  $m_J$   $(\Phi_{\nu,J,m_J}(r,\theta,\phi))$  and a Gaussian wave packet with initial wave vector  $\vec{k}_0 = (k_0^X, k_0^Y, k_0^Z)^{\mathrm{T}}$  describing translational motion.

$$\Psi(\vec{Q}, t = 0) = \Phi_{\nu, J, m_I}(r, \theta, \phi) \psi(\vec{k}_0, t_0)$$
(2.22)

The initial translational motion is then described by the following wave function:

$$\psi(\vec{k}_0, t_0) = e^{i(k_0^X X_0 + k_0^Y Y_0)} \int_{-\infty}^{\infty} \beta(k_0^Z) e^{ik_0^Z Z_0} dk_0^Z$$
 (2.23)

Here,  $\beta(k_0^Z)$  is the initial Gaussian wave packet centered on  $Z_0$ , which is defined through the width parameter  $\sigma$  and average momentum  $\overline{k}$  according to:

$$\beta(k_0^Z) = \left(\frac{2\sigma^2}{\pi}\right)^{-\frac{1}{4}} e^{-\sigma^2(\overline{k} - k_0^Z)^2} e^{i(\overline{k} - K_0^Z)Z_0}. \tag{2.24}$$

Here,  $\sigma$  is the width of the wave packet centered around the wave vector  $\vec{k}_0$ . The width  $\sigma$  is chosen in such a way that most of the Gaussian wave packet is placed in a initial translational energy range of  $E_i \in [E_{min}, E_{max}]$ .

The wave function is propagated using the split operator (SPO) method<sup>83</sup> using a time step  $\Delta t$ . Reflections of the wave packet at large Z and r are avoided by the use of quadratic complex absorbing potentials<sup>84</sup>, which permits the use of short grids in order to reduce the computational cost. The scattered wave packet is analyzed using the scattering matrix formalism<sup>85</sup>. Scattering probabilities can then be obtained for the translational energy range present in the initial wave packet from the S-matrix elements. Subtracting the sum of the state-to-state scattering probabilities from unity yields the fully initial-state

resolved reaction probability.

$$P_r(\nu, J, m_J) = 1 - \sum_{\nu', J', m'_J, n, m} P_{scat}(\nu, J, m_J \to \nu', J', m'_J, n, m)$$
 (2.25)

Here  $P_{scat}(\nu, J, m_J \to \nu', J', m_J', n, m)$  are the state-to-state scattering probabilities, and  $\nu', J'$  and  $m_J'$  are the final vibrational, rotational and magnetic rotational quantum numbers. The quantum numbers for diffraction are denoted by n and m.

# 2.4 Computation of observables

#### 2.4.1 Molecular beam sticking

Calculation of molecular beam sticking probabilities from fully initial-state resolved reaction probabilities involves averaging over the rovibrational state distribution according to the nozzle temperature  $T_n$  as well as over the velocity distribution of the molecules in the molecular beam. The probability to find  $H_2$  with a velocity v in an interval v + dv and in a particular rovibrational state at a given  $T_n$  is denoted by

$$P(v_0, \alpha, \nu, J, T_n)dv = \underbrace{Cv^3 e^{-(v-v_0)^2/\alpha^2} dv}_{P_{flux}(v_0, \alpha)} \times P_{int}(\nu, J, T_n)dv$$
(2.26)

where C is a normalization constant,  $v_0$  is the stream velocity and  $\alpha$  is the width of the velocity distribution. In equation 2.26 the reactivity of each state is weighted according to its Bolzmann weight as:

$$P_{int}(\nu, J, T_n) = \frac{g_N f(\nu, J, T_n)}{Z(T_n)}$$
 (2.27)

with

$$f(\nu, J, T_n) = (2J+1) \times e^{(-(E_{\nu,0}-E_{0,0})/k_B T_{vib})} \times e^{(-(E_{\nu,J}-E_{\nu,0})/k_B T_{rot})}.$$
 (2.28)

Here, the factor  $g_N$  in equation 2.27 reflects the ortho/para ratio of hydrogen in the beam. For  $D_2$   $g_N = 2/3$  (1/3) for even (odd) values of J, while for  $H_2$   $g_N = 1/4$  (3/4) for even (odd) values of J.  $Z(T_n)$  is the partition function,  $k_B$  is the Boltzmann constant, and  $E_{\nu,J}$  is the energy of the rovibrational state characterized by the vibrational ( $\nu$ ) and rotational (J) quantum numbers. In equation 2.28 rotational cooling of the  $H_2$  molecules due to the supersonic expansion is taken into account by setting the rotational temperature to  $T_{rot}$  =

 $0.8 \cdot T_n^{86}$ . Degeneracy averaged reaction probabilities are computed from fully initial-state resolved reaction probabilities as:

$$P_{\text{deg}}(E,\nu,J) = \sum_{m_J=0}^{J} (2 - \delta_{m_J 0}) \frac{P_r(E,\nu,J,m_J)}{2J+1},$$
 (2.29)

where  $P_r(E, \nu, J, m_J)$  is the fully initial-state resolved reaction probability, with  $m_J$  being the magnetic rotational quantum number and E being the translational energy  $(\frac{1}{2}mv^2)$ . Note that calculations are only performed for positive J and  $m_J$ , since given the rotational symmetry of the surfaces used in this thesis the sign of the angular momentum is unimportant. Molecular beam sticking probabilities can then be computed as a function of the parameters describing a molecular beam:

$$S_0(\langle E_i \rangle, T_N) = \sum_{\nu, J} \int P(v_0, \alpha, \nu, J, T_n) P_{\text{deg}}(E, \nu, J) d\nu.$$
 (2.30)

Here,  $\langle E_i \rangle$  is the average incidence energy, which can be computed from  $v_0$  and  $\alpha$ ; usually the sticking probability is simply written as  $S(E_i)$  with the assumption that the reader knows that  $E_i$  then represents the average of  $E_i$  over the velocity distribution. A more exhaustive description of how molecular beam sticking probabilities can be computed can be found in ref.<sup>62</sup>

# 2.4.2 Rotational quadrupole alignment parameters

The extent to which the reaction of  $H_2$  with a transition metal surface depends on the alignment of the molecule relative to the surface normal can be calculated via the rotational quadrupole alignment parameter. The rotational quadrupole alignment parameter,  $A_0^{(2)}(E,\nu,J)$ , is computed from initial-state resolved reaction probabilities as follows:<sup>87</sup>

$$A_0^{(2)}(E,\nu,J) = \frac{\sum_{m_J=0}^{J} (2 - \delta_{m_J,0}) P_r(E,\nu,J,m_J) \left(\frac{3m_J^2}{J(J+1)} - 1\right)}{\sum_{m_J=0}^{J} (2 - \delta_{m_J,0}) P_r(E,\nu,J,m_J)}.$$
 (2.31)

A positive value for  $A_0^{(2)}(\nu,J)$  indicates a preference for reaction of molecules aligned parallel to the surface, a negative value indicates a preference for reactions of molecules aligned perpendicular to the surface, and zero means the reaction proceeds independent of independent of the molecule's alignment

relative to the surface. Here the orientation refers to the angle  $\theta$  between the H-H bond and the surface normal.

# **2.4.3** $E_{1/2}(\nu, J)$ parameters

Initial state-selected reaction probabilities can be obtained from  $H_2$  associatively desorbing from metal surfaces by applying the principle of detailed balance<sup>88</sup> to associative desorption experiments<sup>86,89–91</sup>. Typically the (unnormalized) state-resolved translational energy distributions of molecules desorbing from the surface is measured using resonance-enhanced multi-photon ionization (REMPI)<sup>46,86,89</sup> combined with time-of-flight techniques. The state resolved distributions of desorbing molecules,  $P_{\rm des}(E,\nu,J)$ , may be related to the degeneracy averaged initial-state resolved reaction probability, using:

$$P_{\text{des}}(E,\nu,J) \propto Ee^{-\frac{E}{k_b T_s}} P_{\text{deg}}(E,\nu,J). \tag{2.32}$$

The extracted reaction probabilities are usually fitted to a sigmoid function, in most cases an expression involving the error function:

$$P_{\text{des}}(E,\nu,J) = \frac{A_{\nu,J}}{2} \left[ 1 + erf\left(\frac{E - E_0(\nu,J)}{W_{\nu,J}}\right) \right]. \tag{2.33}$$

Here, the  $A_{\nu,J}$  values are the saturation values of the extracted degeneracy averaged reaction probabilities, and the effective barrier height  $(E_0(\nu,J))$  is the incidence energy at which  $P_{\text{deg}}(E,\nu,J)$  first becomes equal to  $\frac{1}{2}A_{\nu,J}$ .  $W_{\nu,J}$  represents the width of the reaction probability curve.

In an associative desorption experiment the exact state-selective flux is usually not measured  $^{86,89-91}$ , meaning that the proportionality factor in equation 2.32 cannot be obtained directly. In the absence of a measured proportionality factor it is still possible to make a comparison between theory and experiment. Chapter 5 will detail four different methods that can be used to make such a comparison, namely the methods A1 and A2 in which normalized proportionality factors are obtained from a wholly experimental procedure, and methods B1 and B2 in which normalized reaction probabilities are extracted with reference to theory. Given that methods A2 and B2 apply to a specific associative desorption experiment for the  $\rm H_2 + Au(111)$  system and the particular experimental conditions for that experiment, only methods A1 and B1 will be briefly discussed here.

#### Method A1

Method A1 assumes that the effective barrier heights  $(E_0(\nu, J))$  can be kept the same in the description of a molecular beam sticking experiment at a low surface temperature and an associative desorption experiment at a high surface temperature dependence of  $P_{\text{deg}}(E,\nu,J)$  is taken into account by allowing for larger  $W_{\nu,J}$  parameters in the description of the associative desorption experiments  $^{92,93}$ . Next, the  $A_{\nu,J}^{\text{A1}}$  parameters are determined assuming that they do not depend on the surface temperature by requiring that the measured molecular beam sticking probabilities can be computed as outlined in section 2.4.1. Generally the A parameters are taken to be independent of the initial rovibrational state, or to depend solely on the vibrational quantum number so that a fitting procedure can be followed with a properly constrained number of degrees of freedom. Method A1 was followed to extract initial-state resolved reaction probabilities in experiments on  $H_2$  and  $D_2$  desorbing from  $Cu(111)^{86,89,91}$ .

Calculated  $E_{1/2}(\nu, J)$  parameters can then be defined as the translational energy at which the computed reaction probability becomes equal to half the experimental saturation value<sup>39</sup>.

$$P_{deg}(E_{1/2}(\nu, J), \nu, J) = \frac{1}{2} A_{\nu, J}^{A1}$$
(2.34)

Method A1 is described in more detail in chapter 5.

#### Method B1

In method B1, the experimental sticking probability curve is normalized by equating the reaction probability at the maximum kinetic energy to which the experiment was sensitive  $(E_{\text{max}}(\nu, J))$  to the calculated value at that translational energy<sup>90,91</sup>.

$$P_{deg}(E_{1/2}(\nu, J), \nu, J) = \frac{1}{2} A_{\nu, J}^{B1} = \frac{1}{2} P_{deg}(E_{max}(\nu, J), \nu, J).$$
 (2.35)

Note that the maximum translational energy to which the experiment is sensitive is usually not high enough to equal the absolute saturation value A of the reaction probability. However, as will be discussed in chapter 5, as long as  $P_{\text{deg}}(E_{\text{max}}(\nu, J), \nu, J) \geq 0.9$ A the calculated  $E_{1/2}(\nu, J)$  parameters will be underestimated by no more than 0.09  $W_{\nu,J}$ .

# 2.4.4 Rovibrational state populations of $H_2$ and $D_2$ desorbing from Au(111)

The following expression is used to calculate state distributions of desorbing molecules:<sup>90</sup>

$$N(\nu, J) = \int_{0}^{E_{\text{max}(\nu, J)}} P_{int}(\nu, J, T_S) \sqrt{E} \, e^{\left(-\frac{E}{k_B T_S}\right)} \, P_{\text{deg}}(E, \nu, J) dE. \tag{2.36}$$

Here, E is the translational energy and  $T_S$  is the surface temperature. A comparison to experiment can be made by replacing  $P_{\text{deg}}(E, \nu, J)$  in equation 2.36 with reported error function fits obtained experimentally<sup>90</sup>. Note that it is critical for a valid comparison between theory and experiment that equation 2.36 is only integrated up to  $E_{\max(\nu,J)}$ . This is because the experimentally obtained error function fits for the reaction probability are only valid below  $E_{\max(\nu,J)}$ , and can yield reaction probabilities substantially bigger than one above  $E_{\max(\nu,J)}$ . Generally the obtained populations are normalized to the total  $\nu=0$  population according to:

$$N(\nu, J) = \frac{N(\nu, J)}{\sum_{J} N(\nu = 0, J)}$$
 (2.37)

The ratio  $\nu = 1 : \nu = 0$  can then calculated as:

$$\nu = 1 : \nu = 0 = \frac{\sum_{J} N(\nu = 1, J)}{\sum_{J} N(\nu = 0, J)}$$
 (2.38)

- (1) Einstein, A.; Podolsky, B.; Rosen, N. Can quantum-mechanical description of physical reality be considered complete? *Phys. Rev.* **1935**, *47*, 777–780.
- (2) Bell, J. S. On the Einstein Podolsky Rosen paradox. *Phys. Phys. Fiz.* **1964**, 1, 195–200.
- (3) Pusey, M. F.; Barrett, J.; Rudolph, T. On the reality of the quantum state. *Nat. Phys.* **2012**, *8*, 476–479.
- (4) Schrödinger, E. An undulatory theory of the mechanics of atoms and molecules. *Phys. Rev.* **1926**, *28*, 1049–1070.
- (5) Bohr, N., Niels Bohr Collected Works; Elsevier, Amsterdam: 1972-2008; Vol. 1-13.
- (6) Born, M.; Oppenheimer, R. Zur quantentheorie der molekeln. Ann. Phys. 1927, 389, 457–484.
- (7) Hohenberg, P.; Kohn, W. Inhomogeneous electron gas. *Phys. Rev.* **1964**, 136, B864–B871.
- (8) Kohn, W.; Sham, L. J. Self-consistent equations including exchange and correlation effects. *Phys. Rev.* **1965**, *140*, A1133–A1138.
- (9) Fermi, E. Un metodo statistico per la determinazione di alcune priorieta dell'atome. *Rend. Accad. Naz. Lincei* **1927**, *6*, 32–37.
- (10) Thomas, L. H. The calculation of atomic fields. *Math. Proc. Camb. Philos. Soc.* **1927**, *23*, 542–548.
- (11) Burke, K. Perspective on density functional theory. J. Chem. Phys. **2012**, 136, 150901.
- (12) Perdew, J. P.; Ruzsinszky, A.; Sun, J.; Burke, K. Gedanken densities and exact constraints in density functional theory. *J. Chem. Phys.* **2014**, 140, 18A533.
- (13) Perdew, J. P.; Burke, K.; Ernzerhof, M. Generalized gradient approximation made simple. *Phys. Rev. Lett.* **1996**, *77*, 3865–3868.
- (14) Perdew, J. P.; Ruzsinszky, A.; Csonka, G. I.; Vydrov, O. A.; Scuseria, G. E.; Constantin, L. A.; Zhou, X.; Burke, K. Restoring the density-gradient expansion for exchange in solids and surfaces. *Phys. Rev. Lett.* 2008, 100, 136406.

(15) Hammer, B. H. L. B.; Hansen, L. B.; Nørskov, J. K. Improved adsorption energetics within density-functional theory using revised Perdew-Burke-Ernzerhof functionals. *Phys. Rev. B* **1999**, *59*, 7413–7421.

- (16) Becke, A. D. On the large-gradient behavior of the density functional exchange energy. J. Chem. Phys. 1986, 85, 7184–7187.
- (17) Tao, J.; Perdew, J. P.; Staroverov, V. N.; Scuseria, G. E. Climbing the density functional ladder: Nonempirical meta-generalized gradient approximation designed for molecules and solids. *Phys. Rev. Lett.* 2003, 91, 146401.
- (18) Perdew, J. P.; Ruzsinszky, A.; Csonka, G. I.; Constantin, L. A.; Sun, J. Workhorse semilocal density functional for condensed matter physics and quantum chemistry. *Phys. Rev. Lett.* **2009**, *103*, 026403.
- (19) Sun, J.; Ruzsinszky, A.; Perdew, J. P. Strongly constrained and appropriately normed semilocal density functional. *Phys. Rev. Lett.* 2015, 115, 036402.
- (20) Perdew, J. P. Climbing the ladder of density functional approximations. *MRS Bull.* **2013**, *38*, 743.
- (21) Perdew, J. P.; Schmidt, K. In AIP Conf. Proc. 2001; Vol. 577, pp 1–20.
- (22) Perdew, J. P.; Chevary, J. A.; Vosko, S. H.; Jackson, K. A.; Pederson, M. R.; Singh, D. J.; Fiolhais, C. Atoms, molecules, solids, and surfaces: Applications of the generalized gradient approximation for exchange and correlation. *Phys. Rev. B* 1992, 46, 6671–6687.
- (23) Berland, K.; Cooper, V. R.; Lee, K.; Schröder, E.; Thonhauser, T.; Hyldgaard, P.; Lundqvist, B. I. Van der Waals forces in density functional theory: a review of the vdW-DF method. *Rep. Prog. Phys.* **2015**, *78*, 066501.
- (24) Grimme, S. Semiempirical GGA-type density functional constructed with a long-range dispersion correction. *J. Comput. Chem.* **2006**, *27*, 1787–1799.
- (25) Grimme, S.; Antony, J.; Ehrlich, S.; Krieg, H. A consistent and accurate ab initio parametrization of density functional dispersion correction (DFT-D) for the 94 elements H-Pu. J. Chem. Phys. **2010**, 132, 154104.
- (26) Lundqvist, B.; Andersson, Y.; Shao, H.; Chan, S.; Langreth, D. Density functional theory including van der Waals forces. *Int. J. Quant. Chem.* **1995**, *56*, 247–255.

- (27) Dion, M.; Rydberg, H.; Schröder, E.; Langreth, D. C.; Lundqvist, B. I. Van der Waals density functional for general geometries. *Phys. Rev. Lett.* **2004**, *92*, 246401.
- (28) Lee, K.; Murray, É. D.; Kong, L.; Lundqvist, B. I.; Langreth, D. C. Higher-accuracy van der Waals density functional. *Phys. Rev. B* **2010**, 82, 081101.
- (29) Vydrov, O. A.; Van Voorhis, T. Nonlocal van der Waals density functional: The simpler the better. J. Chem. Phys. **2010**, 133, 244103.
- (30) Sabatini, R.; Gorni, T.; De Gironcoli, S. Nonlocal van der Waals density functional made simple and efficient. *Phys. Rev. B* **2013**, *87*, 041108.
- (31) Román-Pérez, G.; Soler, J. M. Efficient implementation of a van der Waals density functional: application to double-wall carbon nanotubes. *Phys. Rev. Lett.* **2009**, *103*, 096102.
- (32) Peng, H.; Yang, Z.-H.; Perdew, J. P.; Sun, J. Versatile van der Waals density functional based on a meta-generalized gradient approximation. *Phys. Rev. X* **2016**, *6*, 041005.
- (33) Kroes, G.-J. Toward a database of chemically accurate barrier heights for reactions of molecules with metal surfaces. *J. Phys. Chem lett.* **2015**, 6, 4106–4114.
- (34) Doblhoff-Dier, K.; Meyer, J.; Hoggan, P. E.; Kroes, G.-J. Quantum Monte Carlo calculations on a benchmark molecule-metal surface reaction: H<sub>2</sub> + Cu(111). *J. Chem. Theory Comput.* **2017**, *13*, 3208–3219.
- (35) Yin, R.; Zhang, Y.; Libisch, F.; Carter, E. A.; Guo, H.; Jiang, B. Dissociative chemisorption of O<sub>2</sub> on Al(111): dynamics on a correlated wave-function-based potential energy surface. *J. Phys. Chem. Lett.* **2018**, *9*, 3271–3277.
- (36) King, D. A.; Wells, M. G. Molecular beam investigation of adsorption kinetics on bulk metal targets: Nitrogen on tungsten. Surf. Sci. 1972, 29, 454–482.
- (37) Chuang, Y.-Y.; Radhakrishnan, M. L.; Fast, P. L.; Cramer, C. J.; Truhlar, D. G. Direct dynamics for free radical kinetics in solution: Solvent effect on the rate constant for the reaction of methanol with atomic hydrogen. J. Phys. Chem. A 1999, 103, 4893–4909.
- (38) Chakraborty, A.; Zhao, Y.; Lin, H.; Truhlar, D. G. Combined valence bond-molecular mechanics potential-energy surface and direct dynamics study of rate constants and kinetic isotope effects for the H + C<sub>2</sub>H<sub>6</sub> reaction. J. Chem. Phys. **2006**, 124, 044315.

(39) Díaz, C.; Pijper, E.; Olsen, R.; Busnengo, H.; Auerbach, D.; Kroes, G. Chemically accurate simulation of a prototypical surface reaction: H<sub>2</sub> dissociation on Cu(111). *Science* **2009**, *326*, 832–834.

- (40) Ghassemi, E. N.; Wijzenbroek, M.; Somers, M. F.; Kroes, G.-J. Chemically accurate simulation of dissociative chemisorption of D<sub>2</sub> on Pt(111). *Chem. Phys. Lett.* **2017**, *683*, 329–335.
- (41) Smeets, E. W. F.; Voss, J.; Kroes, G.-J. Specific reaction parameter density functional based on the meta-generalized gradient approximation: application to H<sub>2</sub> + Cu(111) and H<sub>2</sub> + Ag(111). *J. Phys. Chem. A* **2019**, *123*, 5395–5406.
- (42) Nattino, F.; Migliorini, D.; Kroes, G.-J.; Dombrowski, E.; High, E. A.; Killelea, D. R.; Utz, A. L. Chemically accurate simulation of a polyatomic molecule-metal surface reaction. *J. Phys. Chem. Lett.* 2016, 7, 2402–2406.
- (43) Smeets, E. W. F.; Kroes, G.-J. Designing new SRP density functionals including non-local vdW-DF2 correlation for H<sub>2</sub> + Cu(111) and their transferability to H<sub>2</sub> + Ag(111), Au(111) and Pt(111). *Phys. Chem. Chem. Phys.* **2021**, 23, 7875–7901.
- (44) Madsen, G. K. Functional form of the generalized gradient approximation for exchange: the PBE $\alpha$  functional. *Phys. Rev. B* **2007**, 75, 195108.
- (45) Ghassemi, E. N.; Smeets, E. W. F.; Somers, M. F.; Kroes, G.-J.; Groot, I. M.; Juurlink, L. B.; Füchsel, G. Transferability of the specific reaction parameter density functional for H<sub>2</sub> + Pt(111) to H<sub>2</sub> + Pt(211). J. Phys. Chem. C 2019, 123, 2973–2986.
- (46) Sementa, L.; Wijzenbroek, M.; Van Kolck, B.; Somers, M.; Al-Halabi, A.; Busnengo, H. F.; Olsen, R.; Kroes, G.-J.; Rutkowski, M.; Thewes, C., et al. Reactive scattering of H<sub>2</sub> from Cu(100): comparison of dynamics calculations based on the specific reaction parameter approach to density functional theory with experiment. J. Chem. Phys. **2013**, 138, 044708.
- (47) Nour Ghassemi, E.; Somers, M.; Kroes, G.-J. Test of the transferability of the specific reaction parameter functional for H<sub>2</sub>+ Cu(111) to D<sub>2</sub> + Ag(111). J. Phys. Chem. C **2018**, 122, 22939–22952.
- (48) Tchakoua, T.; Smeets, E. W. F.; Somers, M.; Kroes, G.-J. Toward a specific reaction parameter density functional for H<sub>2</sub> + Ni(111): comparison of theory with molecular beam sticking experiments. *J. Phys. Chem. C* **2019**, *123*, 20420–20433.

- (49) Migliorini, D.; Chadwick, H.; Nattino, F.; Gutiérrez-González, A.; Dombrowski, E.; High, E. A.; Guo, H.; Utz, A. L.; Jackson, B.; Beck, R. D., et al. Surface reaction barriometry: methane dissociation on flat and stepped transition-metal surfaces. J. Phys. Chem. Lett. 2017, 8, 4177–4182.
- (50) Bloch, F. Über die quantenmechanik der elektronen in kristallgittern. Z. Phys. **1929**, 52, 555–600.
- (51) Vanderbilt, D. Soft self-consistent pseudopotentials in a generalized eigenvalue formalism. *Phys. Rev. B* **1990**, *41*, 7892–7895.
- (52) Laasonen, K.; Car, R.; Lee, C.; Vanderbilt, D. Implementation of ultrasoft pseudopotentials in ab initio molecular dynamics. *Phys. Rev. B* **1991**, *43*, 6796–6799.
- (53) Blöchl, P. E. Projector augmented-wave method. *Phys. Rev. B* **1994**, 50, 17953–17979.
- (54) Busnengo, H.; Salin, A.; Dong, W. Representation of the 6D potential energy surface for a diatomic molecule near a solid surface. *J. Chem. Phys.* **2000**, *112*, 7641–7651.
- (55) Olsen, R.; Busnengo, H.; Salin, A.; Somers, M.; Kroes, G.; Baerends, E. Constructing accurate potential energy surfaces for a diatomic molecule interacting with a solid surface: H<sub>2</sub> + Pt(111) and H<sub>2</sub> + Cu(100). *J. Chem. Phys.* **2002**, *116*, 3841–3855.
- (56) Verberck, B. Symmetry-adapted fourier series for the wallpaper groups. Symmetry **2012**, 4, 379–426.
- (57) Wijzenbroek, M. Hydrogen dissociation on metal surfaces, Ph.D. Thesis, 2016.
- (58) Stoer, J.; Bulirsch, R., *Introduction to numerical analysis*; Springer Science & Business Media, New York: 2013; Vol. 12.
- (59) Raff, L. M.; Karplus, M. Theoretical investigations of reactive collisions in molecular beams: K+CH<sub>3</sub>I and related systems. *J. Chem. Phys.* **1966**, *44*, 1212–1229.
- (60) Marston, C. C.; Balint-Kurti, G. G. The Fourier grid Hamiltonian method for bound state eigenvalues and eigenfunctions. *J. Chem. Phys.* **1989**, *91*, 3571–3576.
- (61) Head-Gordon, M.; Tully, J. C. Molecular dynamics with electronic frictions. J. Chem. Phys. 1995, 103, 10137–10145.

(62) Füchsel, G.; del Cueto, M.; Díaz, C.; Kroes, G.-J. Enigmatic HCl + Au(111) reaction: a puzzle for theory and experiment. *J. Phys. Chem. C* **2016**, *120*, 25760–25779.

- (63) Füchsel, G.; Klamroth, T.; Monturet, S.; Saalfrank, P. Dissipative dynamics within the electronic friction approach: the femtosecond laser desorption of H<sub>2</sub>/D<sub>2</sub> from Ru(0001). Phys. Chem. Chem. Phys. 2011, 13, 8659–8670.
- (64) Kubo, R. The fluctuation-dissipation theorem. Rep. Prog. Phys. 1966, 29, 255–284.
- (65) Springer, C.; Head-Gordon, M.; Tully, J. C. Simulations of femtosecond laser-induced desorption of CO from Cu(100). Surf. Sci. 1994, 320, L57–L62.
- (66) Ermak, D. L.; Buckholz, H. Numerical integration of the Langevin equation: Monte Carlo simulation. *J. Comput. Phys.* **1980**, *35*, 169–182.
- (67) Juaristi, J.; Alducin, M.; Muiño, R. D.; Busnengo, H. F.; Salin, A. Role of electron-hole pair excitations in the dissociative adsorption of diatomic molecules on metal surfaces. *Phys. Rev. Lett.* 2008, 100, 116102.
- (68) Puska, M. J.; Nieminen, R. M. Atoms embedded in an electron gas: Phase shifts and cross sections. *Phys. Rev. B* **1983**, *27*, 6121–6128.
- (69) Spiering, P.; Meyer, J. Testing electronic friction models: vibrational de-excitation in scattering of H<sub>2</sub> and D<sub>2</sub> from Cu(111). *J. Phys. Chem. Lett.* **2018**, *9*, 1803–1808.
- (70) Zhang, Y.; Maurer, R. J.; Jiang, B. Symmetry-Adapted High Dimensional Neural Network Representation of Electronic Friction Tensor of Adsorbates on Metals. *J. Phys. Chem. C* **2019**, *124*, 186–195.
- (71) Spiering, P.; Shakouri, K.; Behler, J.; Kroes, G.-J.; Meyer, J. Orbital-Dependent Electronic Friction Significantly Affects the Description of Reactive Scattering of N<sub>2</sub> from Ru(0001). J. Phys. Chem. Lett. 2019, 10, 2957–2962.
- (72) Luntz, A.; Makkonen, I.; Persson, M.; Holloway, S.; Bird, D.; Mizielinski, M. S. Comment on "Role of electron-hole pair excitations in the dissociative adsorption of diatomic molecules on metal surfaces". *Phys. Rev. Lett.* 2009, 102, 109601.
- (73) Juaristi, J.; Alducin, M.; Muiño, R. D.; Busnengo, H.; Salin, A. Juaristi et al. Reply. *Phys. Rev. Lett.* **2009**, *102*, 109602.

- (74) Kosloff, R. Time-dependent quantum-mechanical methods for molecular dynamics. J. Phys. Chem. C 1988, 92, 2087–2100.
- (75) Kosloff, R. In *Time-Dependent Quantum Molecular Dynamics*; Springer: 1992, pp 97–116.
- (76) Kosloff, D.; Kosloff, R. A fourier method solution for the time dependent Schrödinger equation as a tool in molecular dynamics. *J. Comput. Phys.* **1983**, *52*, 35–53.
- (77) Pijper, E.; Kroes, G.-J.; Olsen, R. A.; Baerends, E. J. Reactive and diffractive scattering of H<sub>2</sub> from Pt(111) studied using a six-dimensional wave packet method. *J. Chem. Phys.* **2002**, *117*, 5885–5898.
- (78) Kroes, G.-J.; Somers, M. F. Six-dimensional dynamics of dissociative chemisorption of H<sub>2</sub> on metal surface. *J. Theor. Comput. Chem.* **2005**, 4, 493–581.
- (79) Light, J.; Hamilton, I.; Lill, J. Generalized discrete variable approximation in quantum mechanics. J. Chem. Phys. **1985**, 82, 1400–1409.
- (80) Corey, G. C.; Lemoine, D. Pseudospectral method for solving the time-dependent Schrödinger equation in spherical coordinates. *J. Chem. Phys.* **1992**, *97*, 4115–4126.
- (81) Lemoine, D. The finite basis representation as the primary space in multidimensional pseudospectral schemes. *J. Chem. Phys.* **1994**, *101*, 10526–10532.
- (82) Kosloff, D.; Kosloff, R. A Fourier method solution for the time dependent Schrödinger equation as a tool in molecular dynamics. *J. Comput. Phys.* **1983**, *52*, 35–53.
- (83) Feit, M. D.; Fleck Jr, J. A.; Steiger, A. Solution of the Schrödinger equation by a spectral method. *J. Comput. Phys.* **1982**, *47*, 412–433.
- (84) Vibók, A.; Balint-Kurti, G. G. Parametrization of complex absorbing potentials for time-dependent quantum dynamics. *J. Phys. Chem.* **1992**, 96, 8712–8719.
- (85) Balint-Kurti, G. G.; Dixon, R. N.; Marston, C. C. Grid methods for solving the Schrödinger equation and time dependent quantum dynamics of molecular photofragmentation and reactive scattering processes. *Int. Rev. Phys. Chem.* **1992**, *11*, 317–344.
- (86) Rettner, C.; Michelsen, H.; Auerbach, D. Quantum-state-specific dynamics of the dissociative adsorption and associative desorption of H<sub>2</sub> at a Cu(111) surface. *J. Chem. Phys.* **1995**, *102*, 4625–4641.

(87) Zare, R. N.; Harter, W. G. Angular momentum: understanding spatial aspects in chemistry and physics. *Phys. Today* **1989**, *42*, 68–72.

- (88) Cardillo, M.; Balooch, M.; Stickney, R. Detailed balancing and quasi-equilibrium in the adsorption of hydrogen on copper. *Surf. Sci.* **1975**, 50, 263–278.
- (89) Michelsen, H.; Rettner, C.; Auerbach, D.; Zare, R. Effect of rotation on the translational and vibrational energy dependence of the dissociative adsorption of D<sub>2</sub> on Cu(111). *J. Chem. Phys.* **1993**, *98*, 8294–8307.
- (90) Shuai, Q.; Kaufmann, S.; Auerbach, D. J.; Schwarzer, D.; Wodtke, A. M. Evidence for electron-hole pair excitation in the associative desorption of H<sub>2</sub> and D<sub>2</sub> from Au(111). *J. Phys. Chem. Lett.* **2017**, *8*, 1657–1663.
- (91) Kaufmann, S.; Shuai, Q.; Auerbach, D. J.; Schwarzer, D.; Wodtke, A. M. Associative desorption of hydrogen isotopologues from copper surfaces: characterization of two reaction mechanisms. J. Chem. Phys. 2018, 148, 194703.
- (92) Michelsen, H.; Rettner, C.; Auerbach, D. On the influence of surface temperature on adsorption and desorption in the D<sub>2</sub>/Cu(111) system. Surf. Sci. **1992**, 272, 65–72.
- (93) Rettner, C.; Auerbach, D.; Michelsen, H. Dynamical studies of the interaction of D<sub>2</sub> with a Cu(111) surface. J. Vac. Sci. Technol. A **1992**, 10, 2282–2286.

3 Specific reaction parameter density functional based on the meta-generalized gradient approximation:

 $egin{array}{ll} {
m Application \ to \ H_2 + Cu(111)} \ {
m and \ H_2 + Ag(111)} \end{array}$ 

This Chapter is based on:

Smeets, E. W. F.; Voss, J.; Kroes, G.-J. Specific reaction parameter density functional based on the meta-generalized gradient approximation: application to  $H_2 + Cu(111)$  and  $H_2 + Ag(111)$ . J. Phys. Chem. A **2019**, 123, 5395–5406

# Abstract

Specific reaction parameter density functionals (SRP-DFs), which can describe dissociative chemisorption reactions on metals to within chemical accuracy, have so far been based on exchange functionals within the generalized gradient approximation (GGA), and on GGA correlation functionals or van der Waals correlation functionals. These functionals are capable of describing the molecule-metal surface interaction accurately, but they suffer from the general GGA problem that this can be done only at the cost of a rather poor description of the metal. Here we show that it is possible also to construct SRP DFs based on meta-GGA functionals, introducing 3 new functionals based on the "made-simple" (MS) concept. The exchange parts of the three functionals (MS-PBEl, MS-B86bl, and MS-RPBEl) are based on the expressions for the PBE, B86b, and RPBE exchange functionals. Quasi-classical trajectory (QCT) calculations performed with potential energy surfaces (PES) obtained with the three MS

functionals reproduce molecular beam experiments on  $H_2$ ,  $D_2 + Cu(111)$  with chemical accuracy. Similarly, QCT calculations performed on the MS-PBEl and MS-B86bl PESs reproduced molecular beam and associative desorption experiments on  $D_2$ ,  $H_2 + Ag(111)$  more accurately than was possible with the SRP48 density functional for  $H_2 + Cu(111)$ . Additionally, the three new MS functionals describe the Cu, Ag, Au en Pt metals with similar accuracy as the PBEsol functional. The only disadvantage we noted of the new MS functionals is that, for the example of  $H_2 + Cu(111)$ , the reaction barrier height obtained by taking weighted averages of the MS-PBEl and MS-RPBEl functionals is tunable over a smaller range (9 kJ/mol) than possible with the standard GGA PBE and RPBE functionals (33 kJ/mol).

### 3.1 Introduction

Dissociative chemisorption reactions often control the rate of heterogeneously catalyzed processes<sup>2,3</sup>, which are of large importance to the chemical industry<sup>4</sup>. Important examples include dissociative chemisorption of N<sub>2</sub> in ammonia synthesis<sup>5</sup>, and dissociation of methane in steam reforming<sup>6</sup>. Accurately simulating rate-controlling reactions is critical to the calculation of accurate rates of the overall catalyzed processes<sup>7</sup>.

The best method to obtain accurate results for dissociative chemisorption reactions is currently based on the specific reaction parameter (SRP) approach to DFT (SRP-DFT). In this approach, the density functional is taken as a weighted average of two functionals, using a mixing parameter that is typically fitted to obtain agreement with an experiment on dissociative chemisorption for the specific system considered. This method has now been applied successfully to four  $\rm H_2$ -metal systems<sup>8-11</sup>, and three  $\rm CH_4$ -metal systems<sup>12,13</sup>, in the sense that it was possible to describe the sticking probability as function of incidence energy with chemical accuracy (to within better than 1 kcal/mol). (Note that the terms dissociation, dissociative chemisorption, and sticking are used interchangeably in this work).

So far, the SRP density functionals (SRP-DFs) that have been developed were based<sup>8,9,14</sup> on exchange–correlation functionals within the generalized gradient approximation (GGA)<sup>15–17</sup>, or they were based<sup>10–12</sup> on GGA exchange functionals<sup>16–18</sup> and Lundqvist–Langreth van der Waals correlation functionals<sup>19,20</sup>. Unfortunately, GGA functionals are not good at giving a simultaneously accurate description of molecule–surface interaction energies (and therefore reaction barriers) and metal surfaces (surface energies and lattice constants)<sup>21</sup>. Specifically, GGA functionals that are good at describing adsorption underestimate metal surface energies and overestimate metal lattice

3.1. Introduction 55

constants, while GGA functionals that are good at describing metals overestimate adsorption energies<sup>21</sup>, in spite of efforts to design GGA functionals<sup>22</sup> or nonseparable gradient approximation functionals<sup>23</sup> that perform equally well on both properties. The problem is often, but not always, exacerbated, in the sense that lattice constants are increased further<sup>24</sup>, if a Lundqvist–Langreth correlation functional describing the attractive van der Waals interaction<sup>19,20</sup> is used with a GGA exchange functional to arrive at an SRP-DF<sup>10,12,13</sup>. A description of the metal that is fair at best may pose a problem for an SRP-DF if it is to describe sticking over a large range of surface temperatures  $(T_s)$  or sticking (often measured at low  $T_s$ )<sup>25,26</sup> and associative desorption (often measured at high  $T_s$ )<sup>8,25,26</sup>. The reason is that the reaction barrier may depend on the interlayer spacing in the top two metal layers<sup>14,27,28</sup> as well as the amplitude of motion of the metal atoms in the top layer<sup>29,30</sup>, both of which are properties of the metal and depend on  $T_s$ .

A specific advantage of meta-GGA functionals is that their additional dependence on the kinetic energy density  $\tau$  allows one to distinguish between regions of electron densities describing single (covalent) bonds, metallic bonds, and weak bonds<sup>31</sup>. A particularly elegant way is to introduce a dimensionless parameter  $\alpha$  that is a function of  $\tau$  such that  $\alpha = 0$  corresponds to covalent bonding,  $\alpha = 1$  to metallic bonding, and  $\alpha \gg 1$  to weak bonding<sup>31</sup>. This parameter has been employed in the construction of several much used meta-GGA functionals, such as the TPSS<sup>32</sup>, the revTPSS<sup>33</sup>, the RTPSS<sup>34</sup>, the SCAN<sup>35</sup>, and the mBEEF<sup>36</sup> functionals. More recently, meta-GGA exchange functionals have been constructed on the basis of a function  $f(\alpha)$  such that the exchange functional can be interpolated between the  $\alpha = 0$  and  $\alpha = 1$ limits and extrapolated to the  $\alpha = \infty$  limit. Examples of such methods include the meta-GGA made simple (mGGA-MS)<sup>37,38</sup> and the meta-GGA made very simple (mGGA-MVS) functionals<sup>39</sup>. A good simultaneous description of adsorption energies and lattice constants<sup>36,40,41</sup> or more generally of energetics and structure<sup>37–39,42,43</sup> has now been reported by several groups using meta-GGA functionals.

Here, a new variant of the meta-GGA functional of the mGGA-MS type  $^{37,38}$  is tested. The use of mGGA-MS functionals, in which exchange functionals are used with Perdew–Burke–Ernzerhof (PBE)-like  $^{17}$  and RPBE-like  $^{16}$  expressions and with a B86b-like expression  $^{44}$  will be explored. It is shown that the three meta-GGA MS functionals provide a chemically accurate description of several molecular beam experiments for a benchmark system  $^{8,25,26,45-47}$ , that is, dissociative chemisorption of  $H_2$  on Cu(111), while yielding a much more accurate description of the Cu lattice and of other metals than the previous SRP-DFs for this system. The results imply that an SRP-DF can be constructed

for  $H_2 + Cu(111)$  on the basis of the two MS functions with PBE-like and RPBE-like expressions (MS-PBEl and MS-RPBEl), just like it was possible to do on the basis of the actual RPBE<sup>16</sup> and PBE<sup>17</sup> (or almost equivalently PW91<sup>48</sup>) functionals<sup>8,13</sup>. The MS-PBEl functional also gives a slightly better description of experiments on sticking of  $D_2$  to  $Ag(111)^{49}$  than achieved<sup>50</sup> with the previous SRP48 functional for  $H_2 + Cu(111)$ , but a chemically accurate description was not yet achieved for this system. It is suggested that SRP-DFs for specific systems can be based on mixtures of the MS-PBEl and the MS-RPBEl MS meta-GGA density functionals. However, reaction barriers are tunable over a range that is smaller than the range obtained with the original PBE and RPBE functionals. Therefore, it may be necessary to replace one of the two MS functionals with a more attractive or repulsive meta-GGA functional to obtain a meta-GGA SRP-DF for other specific systems, such as  $H_2 + Ag(111)$ .

# 3.2 Methodology

#### 3.2.1 Dynamical model

The model used is the Born–Oppenheimer static surface model, assuming the surface atoms to be in their ideal surface lattice positions. In this model, the effect of electron–hole pair excitation, of surface phonon motion, and of  $T_s$  on reaction is neglected. In view of the low  $T_s$  employed in the molecular beam experiments on  $H_2 + Cu(111)^{25,51}$ ,  $D_2 + Cu(111)^{26}$ , and  $D_2 + Ag(111)^{49}$  that we compare to, these approximations should be reasonable, as discussed for instance in ref.<sup>47</sup> Note in particular that recent theoretical work shows only a modest influence of electron–hole pair excitation on sticking of  $H_2$  to  $Cu(111)^{52}$  and  $Ag(111)^{53}$ . The six degrees of freedom in which the motion is explicitly modeled are the coordinates of  $H_2$ . The center-of-mass position of  $H_2$  is described by its Cartesian coordinates X, Y, and Z, where Z is the distance to the surface. The orientation of the molecule is specified by the polar angle  $\theta$  and the azimuthal angle  $\phi$ , and r is the H–H distance. The coordinate system and the (111) surface of face-centered cubic (fcc) metals such as Cu and Ag are shown in figure 1.

### 3.2.2 Made Simple meta-GGA density functionals

Aiming at a more flexible functional with the potential for a simultaneously good description of lattice structure and surface adsorption, we extend beyond the GGA space used for the SRP functional to the meta-GGA functional space.

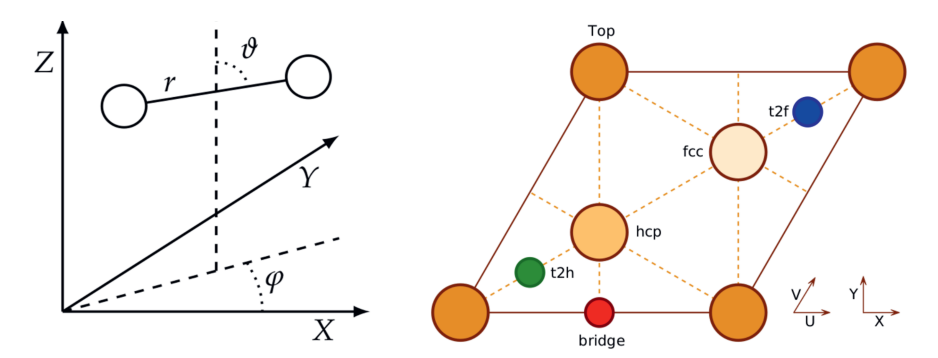


FIGURE 3.1: (a) Center-of-mass coordinate system used for the description of  $H_2$  molecule relative to the (111) face of an fcc metal (with ABCA... stacking). (b) Surface unit cell and the sites considered for the (111) face, and the relationschip with the coordinate system chosen for  $H_2$  relative to the (111) surface. The origin (X,Y,Z)=(0,0,0) of the center of mass coordinates is located in the surface plane at a top site. Polar and azimuthal angles  $\theta$  and  $\phi$  are chosen such that  $(\theta=90^\circ,\phi=0^\circ)$  corresponds to molecules parallel to the surface along the X (or equivalent U) direction. The hexagonal close packed (hcp) and fcc hollow sites correspond to atoms in layers 2 and 3, respectively.

In general, this can be done by making the density functional depend also on the kinetic energy density  $\tau$ , in addition to the density and its gradient. Sun et al.<sup>37</sup> are followed in expressing the meta-GGA in the so-called "made-simple" (MS) form as an interpolation between the exchange part of two GGAs for two extreme scenarios: the uniform electron gas (UEG) (a limit that describes metallic bonding rather well) and a single-orbital system (as in covalent bonds). The exchange enhancement factor describing the increase of exchange relative to the UEG then reads:

$$F_x^{MS}(p,\alpha) = F_x^1(p) + f(\alpha)(F_x^0(p;c) - F_x^1(p)). \tag{3.1}$$

 $F_x^1(p)$  and  $F_x^0(p;c)$  are the gradient only dependent exchange-enhancement factors for the UEG and single-orbital cases, respectively. The exchange enhancement factor is used in GGA and meta-GGA functionals to obtain the exchange part of the exchange-correlation energy. The numerical parameter c will be discussed below. In eq. 3.1,  $p = s^2$ , where s is the reduced density gradient, which is proportional to the gradient of the electron density divided by  $n^{\frac{4}{3}}$ , n being the electron density (the exact expression is given in ref<sup>37</sup>). The interpolation  $f(\alpha)$  depends on the Kohn-Sham kinetic energy  $\tau$  through the

inhomogeneity parameter<sup>37,38</sup>

$$\alpha = \frac{\tau - \tau^W}{\tau^{\text{unif}}}.\tag{3.2}$$

Here,  $\tau^W$  is the von Weizsäcker kinetic energy density, which is equal to the kinetic energy density associated with a single-orbital electron density<sup>41</sup>. Furthermore,  $\tau^{\text{unif}}$  is the kinetic energy density of the UEG. The expressions of  $\tau^W$  and  $\tau^{\text{unif}}$  may be found in for instance ref.<sup>38</sup>. Crucial points are that for a slowly varying electron density as found in metals,  $\alpha$  approaches 1 as  $\tau \approx \tau^{\text{unif}}$  and  $\tau^W \ll \tau^{\text{unif}}$ , whereas for a single-orbital electron density as found in covalent bonding  $\alpha = 0$ , because  $\tau = \tau^{W41}$ . The MS functionals take advantage of this by defining a function  $f(\alpha)$  that equals 0 for  $\alpha = 1$  and that equals 1 for  $\alpha = 0$ :<sup>38</sup>

$$f(\alpha) = \frac{1 - \alpha^2}{1 + \alpha^3 + b\alpha^6} \tag{3.3}$$

Interpolation between the exchange enhancement factor  $F_x^{\mathrm{MS}}(p,\alpha)$  describing the UEG and a single orbital can then be enforced by taking  $F_x^1(p) = F_x^{\mathrm{MS}}(p,\alpha=1)$  from a GGA functional accurately describing metallic bonding, and  $F_x^0(p;c) = F_x^{\mathrm{MS}}(p,\alpha=0)$  from a GGA functional accurately describing single-orbital systems, as in covalent bonds<sup>31</sup>. It is noted that in the present chapter b is simply taken to be equal to 1, as in ref.<sup>37</sup>

In this work, for the functional describing metallic bonding, the following PBE-like<sup>17</sup>, RPBE-like<sup>16</sup>, or B86b-like<sup>44</sup> expressions are used:

$$F_{x,\text{PBE}}^{1}(p) = 1 + \kappa - \frac{\kappa}{1 + \frac{\mu p}{\kappa}}$$
(3.4)

$$F_{x,\text{RPBE}}^{1}(p) = 1 + \kappa \left(1 - \exp\left(\frac{-\mu p}{\kappa}\right)\right)$$
 (3.5)

$$F_{x,\text{B86b}}^{1}(p) = 1 + \frac{\mu p}{\left(1 + \frac{\mu p}{\kappa}\right)^{\frac{4}{5}}}$$
 (3.6)

In equations 3.4-3.6, for  $\kappa$ , we use the value 0.804 used in the original expressions, which corresponds to imposing a Lieb–Oxford bound on the exchange–correlation energy in equations 3.4 and 3.5<sup>16,17</sup>. A crucial point is that to make the functionals defined in equations 3.4-3.6 describe metallic bonding we always take  $\mu = \frac{10}{81}$ , as appropriate for metallic bonding 54,55 and as opposed to the actual value used in the PBE and RPBE functionals. This way, with the PBE-like expression the PBEsol exchange functional 54 is recovered, which was designed to accurately describe elastic properties of metals.

To obtain the corresponding functionals describing covalent bonding,  $F_x^0$ , in line with the MS strategy,  $\mu p$  is replaced everywhere by  $(\mu p + c)$  in equations 3.4-3.6, with c > 0. We then optimize c for each functional to reproduce the exchange energy exactly for the hydrogen atom by cancelling the spurious self-interaction present in the Hartree energy in this atom. The strategy of hydrogen self-interaction correction is adopted in several meta-GGAs, for instance in MS functionals<sup>38</sup>, and in the TPSS<sup>32</sup> and SCAN<sup>35</sup> functionals. The spurious interaction arises because in DFT an electron interacts with itself through the use of a classical expression for the Coulomb interaction of electron densities, and this anomalous self-interaction even occurs for the one-electron H-atom, for which it can be computed and corrected for (in the exchange-correlation energy) exactly<sup>56</sup>. We choose to follow this strategy and c can be determined straightforwardly by numerical quadrature over the analytical nonrelativistic hydrogen atom density. This can be expected to lead to a reasonable GGA  $F_x^0(p;c)$  for further single-orbital densities in general, importantly suppressing otherwise significant self-interaction errors in for example covalent bonds. Tuning the functional form of the made simple exchange functionals depending on the inhomogeneity of the density thus allows for more accurate general-purpose functionals than possible at the pure GGA-level, in particular with the capability of accurately describing interactions within the metal where  $\alpha \approx 1$  as well as in the inhomogeneous scenario of covalent and surface bonds.

For the  $F_x^0(p,c)$  counterparts in equations 3.4-3.6, the following values of c were obtained by numerical integration: 0.1036 (equation 3.4), 0.07671 (equation 3.5), and 0.08809 (equation 3.6). For the correlation functional, we used the variant of the PBE correlation (vPBEc) used in revTPSS<sup>33</sup>, as was also done in the MS functionals of refs.<sup>37,38</sup>. The three MS functionals described in this way are called MS-PBEl, MS-RPBEl, and MS-B86bl, where the "l" stands for "like" to emphasize that we use a different value of  $\mu$  and a different correlation functional than in the original PBE, RPBE, and B86b expressions. It is emphasized that the expressions 3.4-3.6 are non-empirical, like the original PBE, B86b, and RPBE expressions, and that no empirical fitting was performed for the b and  $\kappa$  parameters, as was done in ref.<sup>38</sup> Finally, note that the PBE-like expression (equation 3.4) was used before with MS functionals<sup>37,38</sup>, but with different values of  $\kappa$ , and/or c, and/or b.

# 3.2.3 DFT calculations and representation of PESs

All PESs used here were constructed from self-consistent, periodic DFT calculations carried out with a user modified version of the 5.4.4 version of the VASP program<sup>57–60</sup>, using the three functionals described above in Section

Application to  $H_2 + Cu(111)$  and  $H_2 + Ag(111)$ 

3.2.2, as well as other functionals. All calculations used projected augmented wave pseudopotentials from the VASP database<sup>61</sup>. All calculations used a  $(2 \times 2)$  surface unit cell, a  $(11 \times 11 \times 1)$   $\Gamma$ -centered Monkhorst–Pack k-point grid, a plane wave cut-off of 600 eV, 6 metal layers, a smearing of 0.2 eV using the Methfessel–Paxton method of order 1, and a vacuum distance between the slabs of 16 Å. Additional details, including details of how the metal lattice was computed and on the interlayer relaxation of the slab, are presented in appendix 3.A.

To obtain all PESs described here, the DFT data obtained with a particular functional were interpolated with the corrugation reducing procedure (CRP)<sup>62,63</sup>. In the CRP, the six-dimensional PES  $V_{6D}$  is written as a sum of a 6D interpolation functional  $I_{6D}$  and two 3D potentials  $V_{3D,i}$ , describing the interaction of the H-atoms with the surface:

$$V_{6D}(\mathbf{R}, \mathbf{r}) = I_{6D}(\mathbf{R}) + \sum_{i=1,2} V_{3D,i}(\mathbf{r}_i)$$
(3.7)

Here, the 6D functional  $I_{6D}$  is easier to interpolate than the full 6D potential because its "corrugation" has been reduced by subtracting the two 3D atom–surface potentials<sup>62</sup>. A similar trick is used in the interpolation of the atom–surface potentials<sup>62</sup>. The details of how we interpolated the PESs are mostly the same as described in ref.<sup>64</sup> for  $H_2 + Ru(0001)$  and ref.<sup>65</sup> for  $H_2 + Cu(111)$ ; where these details deviate, this is described in appendix 3.A.

# 3.2.4 Quasi-classical trajectory method

To compute observables, the quasi-classical trajectory (QCT) method<sup>66</sup> was used. The QCT method gives a very good description of initial-state resolved reaction probabilities for activated  $\rm H_2$ -metal surface systems in general<sup>67,68</sup> and for  $\rm H_2 + Cu(111)$  in particular (see Figure 5 of ref.<sup>69</sup>). The QCT method would be expected to perform even better for sticking probabilities simulating the results of molecular beam experiments on  $\rm H_2 + Cu(111)$ , which are highly averaged quantities, involving averages over collision energy and  $\rm H_2$  internal states distributions. Specifically, results for the very similar, but slightly less reactive  $\rm H_2 + Cu(211)$  system<sup>70</sup> show that QCT sticking probability curves accurately reproduce quantum dynamical sticking probabilities down to probabilities of 0.002 (see chapter 4). In all calculations, we model scattering at normal incidence. Reaction and scattering probabilities are calculated by counting how many trajectories result in a particular outcome and dividing by the total number of trajectories. The  $\rm H_2$  is initially placed at a distance from the surface where it no longer interacts with the surface ( $Z=8\rm{\AA}$ ). It is

considered to have dissociated when r > 2.25 Å, and the molecule is considered to have scattered when Z becomes > 8 Å and the molecule is moving away from the surface. The initial conditions are simulated using standard Monte Carlo methods as described in ref.<sup>65</sup>. To obtain accurate statistics, for each incidence condition at least 100.000 trajectories were propagated. To integrate the equations of motion, the method by Stoer and Bulirsch<sup>71</sup> was used. In the trajectories, the maximum propagation time was taken as 22 ps.

# 3.2.5 Compation of observables

The initial (clean surface) sticking probability  $S_0$  can be computed from initialstate resolved reaction probabilities with appropriate averaging over the velocity distribution of the molecular beam and the rovibrational state distribution of the molecules in the beam<sup>72,73</sup>. The way this is done is described in section 2.4.1.

# 3.3 Results and discussion

# 3.3.1 Description of the metal

Equilibrium lattice constants computed with the three MS functionals are compared with the experimental values and the values computed with other functionals in table 3.1, for the noble metals Cu, Ag, Au, and Pt. To facilitate the comparison with theory, the experimental lattice constants were corrected by subtracting a contribution due to zero-point vibrations<sup>74</sup>. The comparison clearly shows the advantage of the MS functionals that we already anticipated: the mean signed deviations (MSDs) from the experiment computed with the MS-PBEl (0.008 Å) and MS-B86bl (0.009 Å) functionals are considerably lower than that obtained with the all-purpose functional PBE<sup>17</sup> (0.015 Å), with only a GGA specifically designed for the solid state (PBEsol<sup>54</sup>) performing better (MSD = 0.002 Å, table 3.1). For the MS-PBEl functional this was to be expected as its exchange part equals that of the PBEsol<sup>54</sup> functional in the metallic limit (see section 3.2.2). All MS functionals perform much better for lattice constants than the RPBE<sup>16</sup> functional, which consistently overestimates lattice constants, with a mean absolute deviation (MAD) equal to the MSD = 0.127 Å (table 3.1).

The performance of the PBE and RPBE functionals is relevant for the description of dissociative chemisorption: in many cases, PBE (or the very similar<sup>17</sup> PW91<sup>15</sup> functional) overestimates and RPBE underestimates the reactivity<sup>8,64,75</sup>, and an SRP functional or in any case an improved functional

Table 3.1: Equilibrium lattice constants, the MSD, and MAD with respect to experiment (all in Å) computed with the MS functionals in this work are compared to zero-point energy corrected experimental values and values computed with other density functionals<sup>74</sup>.

| metal               | Expt. | MS-PBEl | MS-B86bl | MS-RPBEl | $\mathrm{PBE}^{74}$ | $PBEsol^{74}$ | RPBE        |
|---------------------|-------|---------|----------|----------|---------------------|---------------|-------------|
| Cu                  | 3.596 | 3.585   | 3.583    | 3.590    | 3.632               | 3.570         | $3.68^{43}$ |
| Ag                  | 4.062 | 4.091   | 4.092    | 4.099    | 4.152               | 4.058         | $4.23^{43}$ |
| Au                  | 4.062 | 4.084   | 4.087    | 4.092    | 4.154               | 4.081         | $4.23^{80}$ |
| $\operatorname{Pt}$ | 3.913 | 3.906   | 3.908    | 3.912    | 3.985               | 3.932         | $4.00^{43}$ |
| MSD                 |       | 0.008   | 0.009    | 0.015    | 0.015               | 0.002         | 0.127       |
| MAD                 |       | 0.017   | 0.018    | 0.019    | 0.019               | 0.017         | 0.127       |

Table 3.2: Relaxations of the interlayer lattice spacing between the top two layers relative to the bulk, in %, for Cu(111) and Ag(111)

| $_{\rm metal}$ | MS-PBEl | MS-B86bl | MS-RPBEl | Expt.                      |
|----------------|---------|----------|----------|----------------------------|
| Cu             | -1.0%   | -1.0%    | -1.6%    | $-1.0\%^{76}, -0.7\%^{81}$ |
| Ag             | -0.4%   | -0.5%    | -0.5%    | $-2.5\%^{78}, -0.5\%^{77}$ |

can be constructed by taking a weighted average of the PBE and RPBE functionals<sup>8,9</sup>. Table 3.1 suggests that such GGA functionals should yield too large lattice constants (0.017 Å  $\leq$  MSD  $\leq$  0.127 Å). This arises from the need to achieve a good description of the molecule–surface interaction energy: in the construction of a GGA functional, this comes at the cost of a good description of the metal lattice<sup>21</sup>. Finally, the good performance of the three MS functionals shown here is consistent with findings of earlier studies using a MS functional<sup>37</sup>.

Table 3.2 shows the interlayer contractions (in %) computed for Cu(111) and Ag(111), for the interlayer distance between the first two top layers, also comparing with experiments. For Cu, especially the MS-PBEl and the MS-B86bl functionals yield good agreement with experiments, especially with the medium energy ion scattering experiments<sup>76</sup>. For Ag, all three MS functionals yield good agreement with the low-energy electron diffraction (LEED) experiments of Soares et al. Ti is not clear to us what the source of discrepancy is between these experiments and the energy ion scattering experiments of Statiris et al. However, we note that the LEED results of Soares et al. Ti are in good agreement with results obtained recently with the SCAN functional and other functionals. It is important that a functional gives a good description of the interlayer contractions between the top two layers of a given surface, as this may have an important effect on the dissociation barrier height, as found for both  $H_2 + Cu(111)^{14,28}$  and  $Cu(100)^{27}$ .

## 3.3.2 Potential energy surfaces

Figure 3.2 shows elbow plots of the MS-B86bl PES (i.e., plots of the dependence of the potential on r and Z for specific orientations and center-of-mass projections on the surface of  $\rm H_2$ ) for four configurations in which  $\rm H_2$  is parallel to the  $\rm Cu(111)$  surface. Table 3.3 shows the associated geometries and barrier heights, comparing to the previous values of the SRP PES, which gave dynamics results in agreement with experiments to chemical accuracy<sup>8</sup>. Analogous results for the MS-PBEl and MS-RPBEl functionals are given in figures 3.3 and 3.4 and tables 3.4 and 3.5.

The barrier heights  $E_b$  computed with the MS-B86bl functional are in good agreement with the previous SRP results, overestimating the SRP barriers by 0.4-5.3 kJ/mol (table 3.3). This already suggests that the MS-B86bl functional should give a quite good description of dissociative chemisorption of  $H_2$  on Cu(111): the molecular beam sticking probabilities computed with the SRP functional slightly overestimated the experimental values, although agreement was achieved to within chemical accuracy. The barrier geometries obtained with the MS-B86bl functional are in quite good agreement with the SRP barrier geometries (table 3.3), except perhaps for the high barrier fcc geometry considered, for which the PES is quite flat in r around the barrier geometry (see figure 3.2c). Note that the barriers tend to be a bit earlier (i.e., they occur at a smaller H-H distance) for the MS-B86bl PES than for the SRP PES. Finally, the MS-PBEl barrier heights are in even better agreement with the SRP results (see table 3.4, comparing to table 3.3).

Finally, an important issue for the construction of semiempirical functionals is the tunability of the barrier height that can be achieved with them. With an SRP functional that is a weighted average of the GGA functionals PW91 (which is very similar to PBE<sup>17</sup>) and RPBE, the minimum barrier height for  $H_2 + Cu(111)$  can be tuned between 46.8 and 78.9 kJ/mol (see table 3.6), that is, over quite a large range of 33 kJ/mol. However, with a trial SRP functional based on the MS-PBEl and MS-RPBEl functionals (which of the three MS functionals tested yield the lowest respectively the highest barriers, comparing tables 3.3, 3.4, and 3.5) the minimum barrier height can only be tuned between 60.7 and 69.6 kJ/mol (table 3.6), a range of only 9 kJ/mol. The present results thus suggest that semi-empirical functionals based on the made simple mGGA approach with equations 3.4-3.6 can yield a much better description of the metal lattice, but at the cost of a reduced tunability of the reaction barrier height. Our finding for meta-GGA functions based on PBE-like and RPBE-like expressions is analogous to results of Garza et al. for the TPSS<sup>32</sup> (incorporating a PBE-like expression for the exchange enhancement factor)

TABLE 3.3: H–H distance at the barrier  $(r_b, \text{ in Å})$ , the molecule–surface distance at the barrier  $(Z_b, \text{ in Å})$ , and the barrier height  $(E_b, \text{ in kJ/mol})$  as computed for  $H_2 + Cu(111)$  with the MS-B86bl functional. Values in parentheses are the SRP values from ref<sup>8</sup>. The values are given for four different dissociation geometries (see figure 3.1). In all cases,  $H_2$  is parallel to the surface.

| dissociation route         | $E_b$        | $r_b$       | $Z_b$       |
|----------------------------|--------------|-------------|-------------|
| bth                        | 65.9 (60.6)  | 1.00 (1.03) | 1.21 (1.16) |
| ttb                        | 86.4 (86.0)  | 1.35(1.40)  | 1.39(1.39)  |
| $t2f (\phi = 120^{\circ})$ | 78.1 (74.4)  | 1.22(1.27)  | 1.28(1.27)  |
| fcc $(\phi = 0^{\circ})$   | 101.1 (97.7) | 1.34(1.59)  | 1.27(1.27)  |

and their RTPSS functional (incorporating an RPBE-like expression)<sup>34</sup>. To obtain a better agreement with molecular chemisorption energies (and greater tunability between TPSS and RTPSS), they relaxed the constraint that their RTPSS functional should reproduce the exact energy of the H-atom (i.e., that it should correct for self-interaction of this atom exactly)<sup>34</sup>.

Figure 3.5 shows elbow plots of the MS-B86bl PES computed for four configurations in which  $H_2$  is parallel to the Ag(111) surface. Table 3.7 shows the associated geometries and barrier heights, comparing to the previous values of the SRP48 PES<sup>50</sup>, which gave sticking probabilities that were shifted to higher incidence energies by 6.6–7.6 kJ/mol with respect to results of molecular beam experiments<sup>49</sup> (note that the SRP48 functional is an SRP functional for  $H_2 + Cu(111)^{14}$  but not for  $H_2 + Ag(111)^{50}$ ). The results for the MS-PBEl functional are given in figure 3.6 and table 3.8.

The barrier heights  $E_b$  computed with the MS-B86bl functional are lower than the previous SRP48 results, underestimating the SRP48 barriers by 3.6-10.2 kJ/mol. This might be taken to suggest that the MS-B86bl functional should give a quite good description of dissociative chemisorption of  $D_2$  on Ag(111), as the SRP48 functional gave sticking probabilities that were shifted to higher incidence energies by 6.6-7.6 kJ/mol<sup>50</sup> with respect to experiment<sup>49</sup>. However, although the barrier geometries obtained with the MS-B86bl functional are in reasonable agreement with the previous SRP48 barrier geometries (table 3.7), as for  $H_2 + Cu(111)$  (see table 3.3), the barriers for  $H_2 + Ag(111)$  tend to be a bit earlier (occur at smaller H–H distance) for the MS-B86bl PES. As discussed below, this is relevant also to the reaction dynamics<sup>82,83</sup>, and dynamics calculations are required to see whether the MS-B86bl PES leads to higher sticking probabilities for  $D_2 + Ag(111)$  than the SRP48 PES used earlier<sup>50</sup>, as would be needed for better agreement with the experiment.

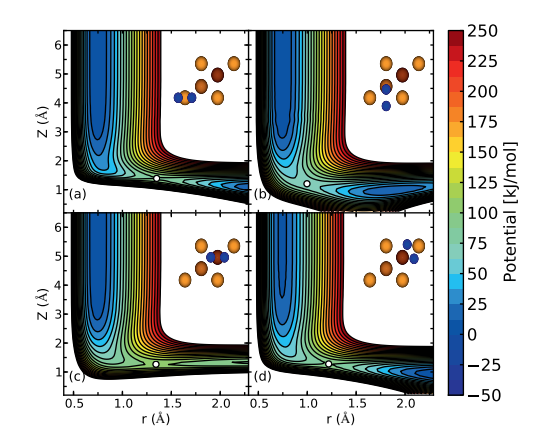


FIGURE 3.2: Elbow plots (i.e. V(Z,r)) resulting from the H<sub>2</sub> + Cu(111) PES computed with the MS-B86bl functional and interpolated with the CRP method for four high symmetry configurations with the molecular axis parallel to the surface  $(\theta = 90^{\circ})$  as depicted by the insets, for (a) top site and  $\phi = 0^{\circ}$ , (b) bridge site and  $\phi = 90^{\circ}$  (the bridge-to-hollow global minimum barrier geometry), (c) fcc site and  $\phi = 0^{\circ}$ , and (d) t2f site and  $\phi = 120^{\circ}$ . Barrier geometries are indicated with white circles, and the corresponding barrier heights are given in table 3.3.

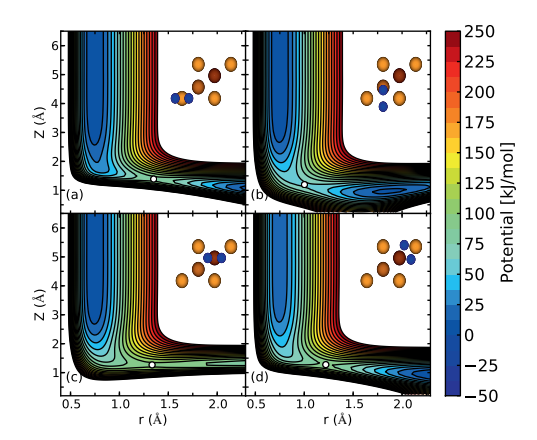


FIGURE 3.3: Elbow plots (i.e. V(Z,r)) resulting from the H<sub>2</sub> + Cu(111) PES computed with the MS-PBEI functional and interpolated with the CRP method for four high symmetry configurations with the molecular axis parallel to the surface  $(\theta=90^\circ)$  as depicted by the insets, for (a) top site and  $\phi=0^\circ$ , (b) bridge site and  $\phi=90^\circ$  (the bridge-to-hollow global minimum barrier geometry), (c) fcc site and  $\phi=0^\circ$ , and (d) t2f site and  $\phi=120^\circ$ . Barrier geometries are indicated with white circles, and the corresponding barrier heights are given in table 3.4.

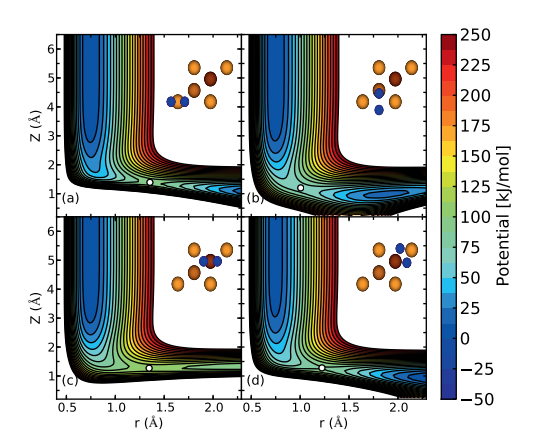


FIGURE 3.4: Elbow plots (i.e. V(Z,r)) resulting from the  $H_2 + Cu(111)$  PES computed with the MS-RPBEl functional and interpolated with the CRP method for four high symmetry configurations with the molecular axis parallel to the surface  $(\theta = 90^{\circ})$  as depicted by the insets, for (a) top site and  $\phi = 0^{\circ}$ , (b) bridge site and  $\phi = 90^{\circ}$  (the bridge-to-hollow global minimum barrier geometry), (c) fcc site and  $\phi = 0^{\circ}$ , and (d) t2f site and  $\phi = 120^{\circ}$ . Barrier geometries are indicated with white circles, and the corresponding barrier heights are given in table 3.5.

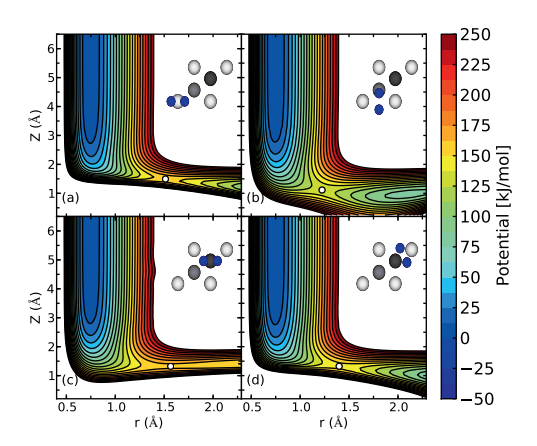


FIGURE 3.5: Elbow plots (i.e. V(Z,r)) resulting from the  $H_2+Ag(111)$  PES computed with the MS-B86bl functional and interpolated with the CRP method for four high symmetry configurations with the molecular axis parallel to the surface  $(\theta=90^\circ)$  as depicted by the insets, for (a) top site and  $\phi=0^\circ$ , (b) bridge site and  $\phi=90^\circ$  (the bridge-to-hollow global minimum barrier geometry), (c) fcc site and  $\phi=0^\circ$ , and (d) t2f site and  $\phi=120^\circ$ . Barrier geometries are indicated with white circles, and the corresponding barrier heights are given in table 3.7.

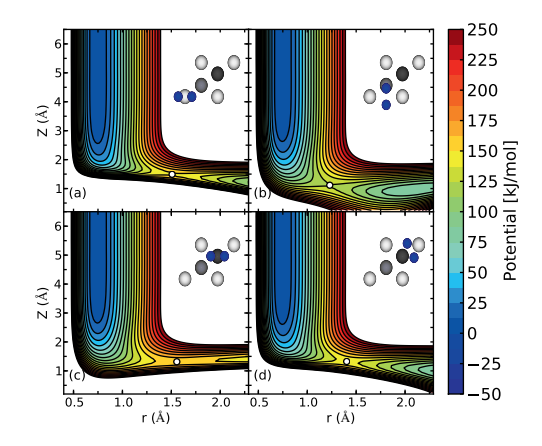


FIGURE 3.6: Elbow plots (i.e. V(Z,r)) resulting from the H<sub>2</sub> + Ag(111) PES computed with the MS-PBEl functional and interpolated with the CRP method for four high symmetry configurations with the molecular axis parallel to the surface  $(\theta = 90^{\circ})$  as depicted by the insets, for (a) top site and  $\phi = 0^{\circ}$ , (b) bridge site and  $\phi = 90^{\circ}$  (the bridge-to-hollow global minimum barrier geometry), (c) fcc site and  $\phi = 0^{\circ}$ , and (d) t2f site and  $\phi = 120^{\circ}$ . Barrier geometries are indicated with white circles, and the corresponding barrier heights are given in table 3.8.

TABLE 3.4: H–H distance at the barrier  $(r_b, \text{ in Å})$ , the molecule–surface distance at the barrier  $(Z_b, \text{ in Å})$ , and the barrier height  $(E_b, \text{ in kJ/mol})$  as computed for  $H_2 + Cu(111)$  with the MS-PBEl functional. Values in parentheses are the SRP values from ref<sup>8</sup>. The values are given for four different dissociation geometries (see figure 3.1). In all cases,  $H_2$  is parallel to the surface.

| dissociation route         | $E_b$       | $r_b$       | $Z_b$       |
|----------------------------|-------------|-------------|-------------|
| bth                        | 60.7 (60.6) | 1.00 (1.03) | 1.20 (1.16) |
| ttb                        | 81.7 (86.0) | 1.35(1.40)  | 1.39(1.39)  |
| $t2f (\phi = 120^{\circ})$ | 73.2(74.4)  | 1.22(1.27)  | 1.28(1.27)  |
| fcc $(\phi = 0^{\circ})$   | 96.3 (97.7) | 1.34(1.59)  | 1.27(1.27)  |

TABLE 3.5: H–H distance at the barrier  $(r_b, \text{ in Å})$ , the molecule–surface distance at the barrier  $(Z_b, \text{ in Å})$ , and the barrier height  $(E_b, \text{ in kJ/mol})$  as computed for H<sub>2</sub> + Cu(111) with the MS-RPBEl functional. Values in parentheses are the SRP values from ref<sup>8</sup>. The values are given for four different dissociation geometries (see figure 3.1). In all cases, H<sub>2</sub> is parallel to the surface.

| dissociation route         | $E_b$        | $r_b$       | $Z_b$       |
|----------------------------|--------------|-------------|-------------|
| bth                        | 69.6 (60.6)  | 1.01 (1.03) | 1.20 (1.16) |
| $\operatorname{ttb}$       | 89.7 (86.0)  | 1.35(1.40)  | 1.39(1.39)  |
| $t2f (\phi = 120^{\circ})$ | 81.6 (74.4)  | 1.22(1.27)  | 1.28(1.27)  |
| fcc $(\phi = 0^{\circ})$   | 104.8 (97.7) | 1.39(1.59)  | 1.28(1.27)  |

TABLE 3.6: Minimum barrier height ( $E_b$ , in kJ/mol) as computed for H<sub>2</sub> + Cu(111) with the three different MS functionals, and with the PW91 and RPBE functionals, for bridge-to-hollow dissociation. In all cases, H<sub>2</sub> is parallel to the surface.

| functional | $E_b$      |
|------------|------------|
| PW91       | $46.8^{8}$ |
| MS-PBEl    | 60.7       |
| MS-B86bl   | 65.9       |
| MS-RPBEl   | 69.6       |
| RPBE       | $78.9^{8}$ |

TABLE 3.7: H–H distance at the barrier  $(r_b, \text{ in Å})$ , the molecule–surface distance at the barrier  $(Z_b, \text{ in Å})$ , and the barrier height  $(E_b, \text{ in kJ/mol})$  as computed for  $H_2 + Ag(111)$  with the MS-B86bl functional. Values in parentheses are the SRP values from ref<sup>50</sup>. The values are given for four different dissociation geometries (see figure 3.1). In all cases,  $H_2$  is parallel to the surface.

| dissociation route         | $E_b$         | $r_b$      | $Z_b$       |
|----------------------------|---------------|------------|-------------|
| bth                        | 129.5 (133.1) | 1.22(1.27) | 1.12 (1.10) |
| ttb                        | 152.9 (163.1) | 1.51(1.57) | 1.50(1.51)  |
| $t2f (\phi = 120^{\circ})$ | 145.9 (152.4) | 1.40(1.45) | 1.33(1.34)  |
| fcc $(\phi = 0^{\circ})$   | 159.4 (164.0) | 1.57(1.67) | 1.32 (1.34) |

TABLE 3.8: H–H distance at the barrier  $(r_b, \text{ in Å})$ , the molecule–surface distance at the barrier  $(Z_b, \text{ in Å})$ , and the barrier height  $(E_b, \text{ in kJ/mol})$  as computed for  $H_2 + Ag(111)$  with the MS-PBEl functional. Values in parentheses are the SRP values from ref<sup>50</sup>. The values are given for four different dissociation geometries (see figure 3.1). In all cases,  $H_2$  is parallel to the surface.

| dissociation route         | $E_{b}$       | $r_b$       | $Z_b$       |
|----------------------------|---------------|-------------|-------------|
| bth                        | 124.3 (133.1) | 1.23 (1.27) | 1.12 (1.10) |
| ttb                        | 148.0 (163.1) | 1.51(1.57)  | 1.49(1.51)  |
| $t2f (\phi = 120^{\circ})$ | 139.8 (152.4) | 1.40(1.45)  | 1.33(1.34)  |
| fcc $(\phi = 0^{\circ})$   | 154.5 (164.0) | 1.56(1.67)  | 1.32 (1.34) |

# 3.3.3 Dynamics results: molecular beam sticking

The  $S_0$  values computed with the three new MS functionals and with the SRP48 functional are compared to experimental values for  $H_2 + Cu(111)^{25,51}$ and  $D_2 + Cu(111)^{26}$  in figure 3.7. As can be seen, the  $S_0$  values computed with the three new MS functionals are in excellent agreement with all experiments shown. The best agreement with the experiments of Auerbach and Rettner and co-workers<sup>25,26</sup> (figure 3.7a–e) is obtained with the MS-B86bl functional, except perhaps for the lowest incidence energy. At the lowest incidence energies, the MS-PBEl functional would seem to give better results, but this may be an artifact of the use of the QCT method (reaction probabilities computed with the MS-B86bl PES being smaller than 0.002 in these cases), as the QCT method ignores tunneling contributions. The best agreement with the experiment of Rendulic and co-workers<sup>51</sup> (figure 3.7f) is obtained with the MS-PBEl functional, of which the overall performance is very similar to the performance of the SRP48 functional. However, these are details, and the main message is that the three MS functionals all yield excellent agreement with the molecular beam experiments, while also giving a very good description of the metal lattice.

To obtain a measure of the quality of the functionals for  $H_2 + Cu(111)$ , one can compute the mean distance along the incidence energy axis from the computed  $S_0$  to the interpolated experimental values. In figure 3.8, the MS-B86bl results are shown comparing to those experiments for which enough data were available to perform cubic spline interpolation of the experimental data points. Computing the MAD (i.e., the mean of the calculated distances), we obtain MAD values of 0.3 kJ/mol for the experiment of Rettner et al.<sup>25</sup> using pure H<sub>2</sub> beams (figure 3.8a), 1.7 kJ/mol for the experiment using seeded  $D_2$  beams for a nozzle temperature of 2100 K of Michelsen et al.<sup>26</sup>, and 2.0 kJ/mol for the pure H<sub>2</sub> beam experiment of Rendulic and co-workers<sup>51</sup>. This illustrates that the MS-B86b yields a chemically accurate description (MADvalues less than 4.2 kJ/mol) of the sticking of H<sub>2</sub> and D<sub>2</sub> on Cu(111). The same is true for the MS-PBEl functional (MAD values of 3.2, 4.1, and 0.3 kJ/mol, see figure 3.9) and for the MS-RPBEl functional (MAD values of 1.2, 3.2, and 3.0 kJ/mol, see figure 3.10), although the MS-B86bl functional gives a slightly better overall performance. Therefore, all three non-empirical MS functionals used individually yield agreement with these  $H_2 + Cu(111)$ experiments to within chemical accuracy. These results also imply that it is possible to construct an SRP-DF on the basis of these functionals, for instance, an SRP-DF that is a weighted average of the MS-PBEl (lowest barriers) and the MS-RPBEl functional (highest barriers).

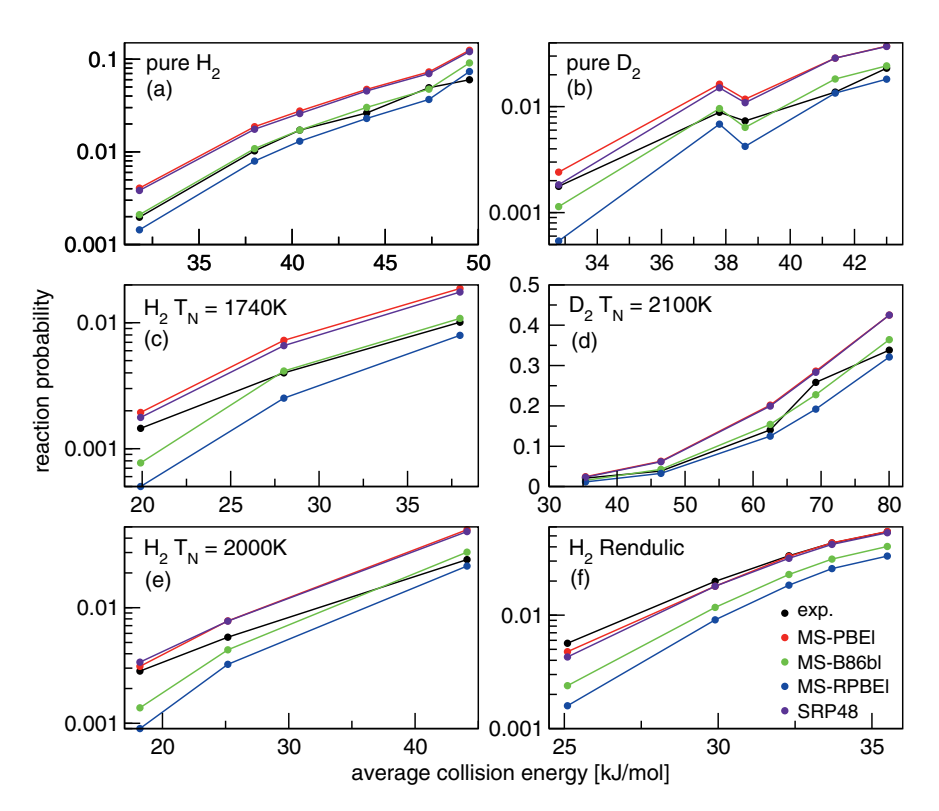


FIGURE 3.7:  $S_0$  values computed with the three new MS functionals and with the SRP48 functional are compared to experimental values for  $H_2 + Cu(111)$  measured in ref.<sup>25</sup> (panels a-c),  $D_2 + Cu(111)$  measured in ref.<sup>26</sup> (panels d,e), and  $H_2 + Cu(111)$  measured in ref.<sup>51</sup> (panel f). Experimental results are presented in black, and computational results in red (MS-PBEl), green (B86bl), blue (MS-RPBEl), and purple (SRP48).

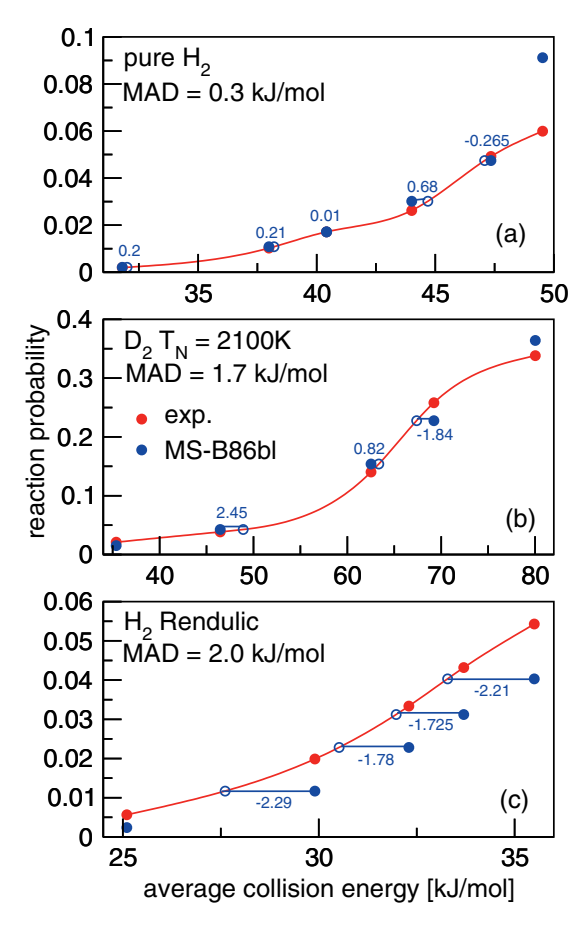


FIGURE 3.8:  $S_0$  values computed with the MS-B86bl functional (blue symbols) are compared to experimental values (red symbols) for  $H_2 + Cu(111)$  measured in ref.<sup>25</sup> (panel a),  $D_2 + Cu(111)$  measured in ref.<sup>26</sup> (panel b), and for  $H_2 + Cu(111)$  measured in ref.<sup>51</sup> (panel c). Horizontal lines indicate the distances along the energy axis between the computed  $S_0$  and the cubic-spline interpolated experimental curve, and the MAD is the mean value of these distances (in kJ/mol).

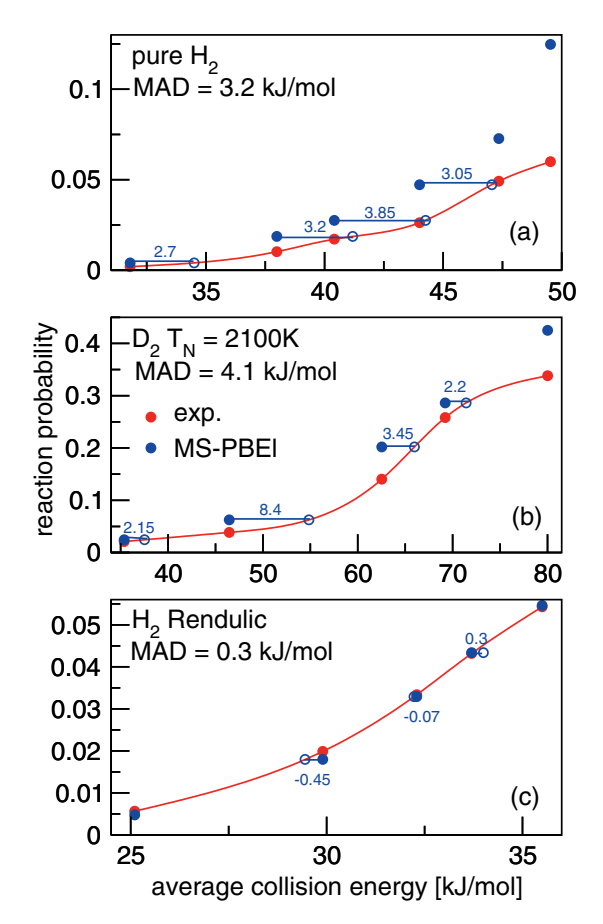


FIGURE 3.9:  $S_0$  values computed with the MS-PBEl functional (blue symbols) are compared to experimental values (red symbols) for  $H_2 + Cu(111)$  measured in ref.<sup>25</sup> (panel a),  $D_2 + Cu(111)$  measured in ref.<sup>26</sup> (panel b), and for  $H_2 + Cu(111)$  measured in ref.<sup>51</sup> (panel c). Horizontal lines indicate the distances along the energy axis between the computed  $S_0$  and the cubic-spline interpolated experimental curve, and the MAD is the mean value of these distances (in kJ/mol).

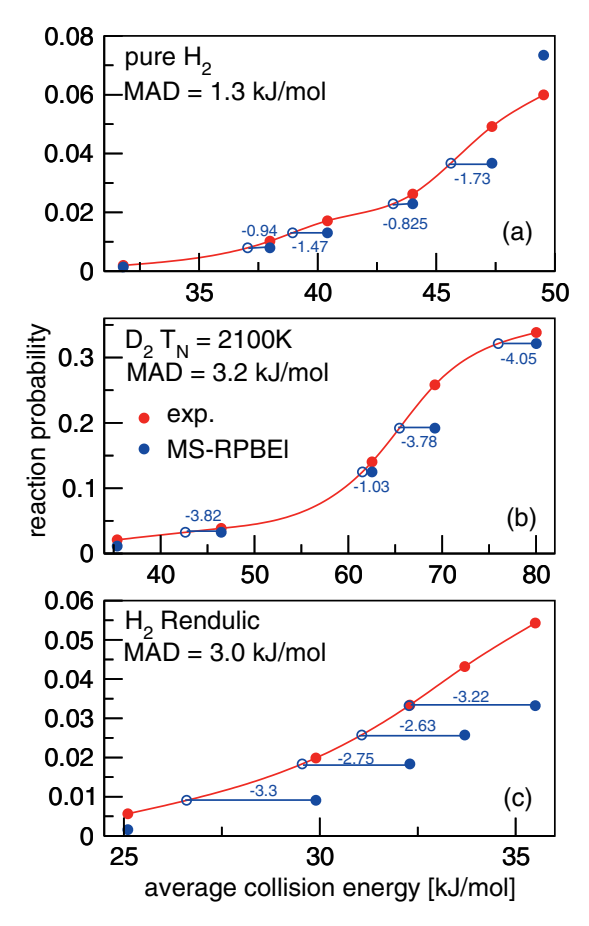


FIGURE 3.10:  $S_0$  values computed with the MS-RPBEl functional (blue symbols) are compared to experimental values (red symbols) for  $H_2 + Cu(111)$  measured in ref.<sup>25</sup> (panel a),  $D_2 + Cu(111)$  measured in ref.<sup>26</sup> (panel b), and for  $H_2 + Cu(111)$  measured in ref<sup>51</sup> (panel c). Horizontal lines indicate the distances along the energy axis between the computed  $S_0$  and the cubic-spline interpolated experimental curve, and the MAD is the mean value of these distances (in kJ/mol).

To put the performance of the three MS meta-GGA functionals in perspective, in figure 3.11 we compare the seeded beam  $D_2 + Cu(111)$  experimental results of Michelsen et al.  $^{26}$  to the  $S_0$  computed with two standard GGA functionals (PBE<sup>17</sup> and RPBE<sup>16</sup>) and three standard meta-GGA functionals (TPSS<sup>32</sup>, revTPSS<sup>33</sup>, and SCAN<sup>35</sup>). The PBE and RPBE results straddle the experimental  $S_0$  over a rather large energy interval, in agreement with the large tunability of SRP functionals taken as weighted averages of these functionals. As previously observed for  $H_2 + Ru(0001)^{64}$ , the revTPSS functional improves over the performance of PBE, which is consistent with the design purpose of the former being to function well for both condensed matter physics (metals) and quantum chemistry (molecules). For  $H_2 + Cu(111)$  the improvement of revTPSS over PBE is more substantial than for  $H_2 + Ru(0001)^{64}$ . We also see an improvement going from PBE to TPSS, but not as much as with revTPSS. The SCAN functional gives the worst performance of all. This functional obeys a maximum number of known exact constraints and performs better than PBE for thermochemical data, gasphase reaction barriers, and for lattice constants of solids<sup>35</sup>. Our finding that it performs more poorly than PBE for dissociative chemisorption may seem surprising but it is consistent with studies that find that SCAN overbinds more than PBE for chemisorption on  $metals^{34,84}$ . The reasons for this are presently not fully understood. Garza et al. have speculated that the result that the most constrained non-empirical meta-GGA (i.e., SCAN) performs poorly at describing chemisorption on metals is due to inherent limitations of the form of semilocal functionals<sup>34</sup>. They seem to have based their suggestion partly on their finding that a meta-GGA functional (RTPSS) that performs quite well at describing molecular chemisorption on metals can be obtained by relaxing a constraint, that is, the constraint that the H-atom should be described exactly by correcting for the self-interaction<sup>34</sup>. Patra et al. have speculated that the SCAN functional should overbind CO on transition metal surfaces primarily due to density driven errors in the self-consistent SCAN energy $^{84}$ .

The revTPSS functional shows a MAD value with the  $D_2 + Cu(111)$  experiment of figure 3.11 of 6.8 kJ/mol (see figure 3.12). While this presents good agreement for a standard semilocal functional, it does not yet correspond to chemical accuracy. We also note that it is not possible to construct an SRP density functional on the basis of the three standard meta-GGA functionals tested: none of these functionals underestimates the reaction probability. However, it is probably possible to construct an SRP functional on the basis of one of these three meta-GGA functionals (with the best choice probably being the revTPSS functional) and the MS-RPBEl functional, which consistently underestimates the reactivity of  $H_2$  on Cu(111) (see figure 3.7), or the RTTPS

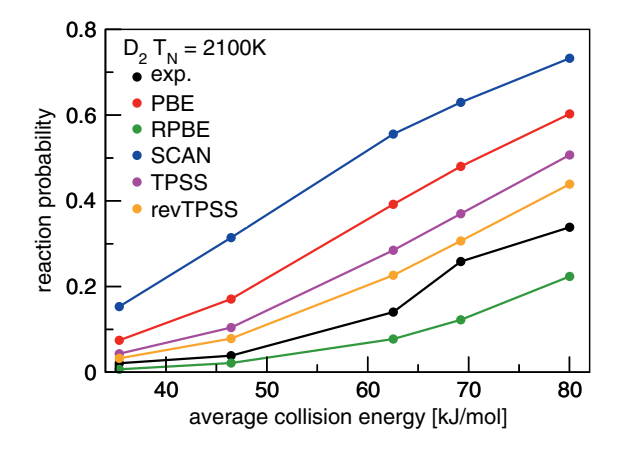


FIGURE 3.11:  $S_0$  values measured in seeded beam experiments on  $D_2 + Cu(111)^{26}$  (black symbols and lines) are shown as a function of  $E_i$ , comparing to the  $S_0$  values computed for these experiments with the PBE<sup>17</sup> (red), RPBE<sup>16</sup> (green), TPSS<sup>32</sup> (purple), rev-TPSS<sup>33</sup> (orange), and SCAN<sup>35</sup> (blue symbols and lines) functionals.

meta-GGA functional, which has a performance on molecular chemisorption on metals that is comparable to that of the RPBE functional<sup>34</sup>.

The  $S_0$  values computed with the MS-PBEl and MS-B86bl functionals are compared to the experimental values for  $D_2 + Ag(111)^{49}$  in figure 3.13. These two functionals perform slightly better than the SRP48 functional, which gave a MAD of 7 kJ/mol<sup>50</sup>, while MAD values of 4.5 and 5.5 kJ/mol were obtained with the MS-PBEl and MS-B86bl functionals, respectively. The improvement of the performance is not as large as one might assume based on barrier heights only (which for MS-B86bl were lower than the SRP48 values by 3.6–10.2 kJ/mol, see above). However, the sticking of  $D_2$  on Ag(111) is dominated by reaction of high vibrational states (the dominant contribution comes from  $\nu = 3)^{50}$ . The barriers are earlier on the MS-B86bl surface than on the SRP48 PES (see table 3.7), and, as summarized by the Polanyi rules<sup>82,83</sup>, the later the barrier is, the more the reaction of vibrationally excited molecules is promoted. Thus, with the B86bl PES, the reaction of the high vibrational states is slightly less promoted, and this to some extent cancels the effect of the lower barriers. However, the main point is that the new MS functionals perform rather well for  $D_2 + Ag(111)$  and in fact slightly better than the SRP48 functional while also yielding a very accurate description of the Ag(111) lattice.

Like the SRP48 functional, the MS-PBEl and MS-B86bl functionals, which

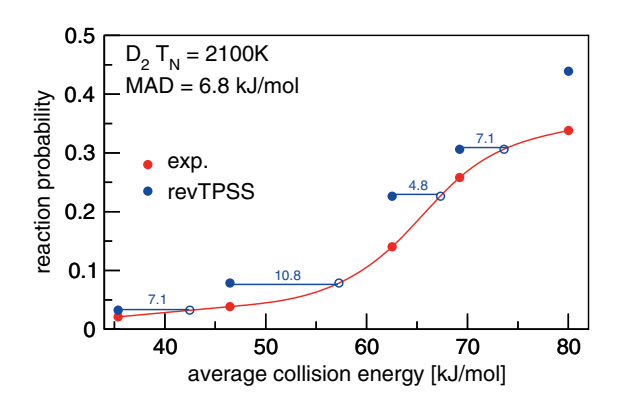


FIGURE 3.12: The  $S_0$  computed with the rev-TPSS functional (blue symbols) are compared to experimental values (red symbols) for  $D_2 + Cu(111)$  measured in Ref.<sup>26</sup>. Horizontal lines indicate the distances along the energy axis between the computed  $S_0$  and the cubic-spline interpolated experimental curve, and the MAD is the mean value of these distances (in kJ/mol).

may in principle be counted as SRP functionals for  $H_2 + Cu(111)$  (i.e., with zero mixing coefficient of the other functional the SRP functional would be based on), are not yet transferable to  $H_2 + Ag(111)$ : they do not give a chemically accurate description of the existing molecular beam experiments for this system (such transferability was observed for the SRP density functional for methane  $+ Ni(111)^{12}$  to methane  $+ Pt(111)^{13}$ ). As the MS-PBEl functional yields the highest reactivity of the three MS functionals tested here for  $H_2 + Ag(111)$ , our results suggest that it should not be possible to base an SRP-DF for this system on a combination of two of these three MS functionals. We attribute this result to the rather limited tunability of the MS functionals tested here. However, our present results for  $H_2 + Ag(111)$  (figure 3.13) and for  $H_2 + Cu(111)$  (figure 3.11) suggest that an SRP-DF for  $H_2 + Ag(111)$  might be constructed on the basis of the MS-PBEl and one of the three meta-GGA functionals (SCAN, TPSS, or revTPSS). For further discussion on the agreement between theory and experiment for sticking of  $D_2$  on Ag(111), the reader is referred to ref.  $^{50}$ 

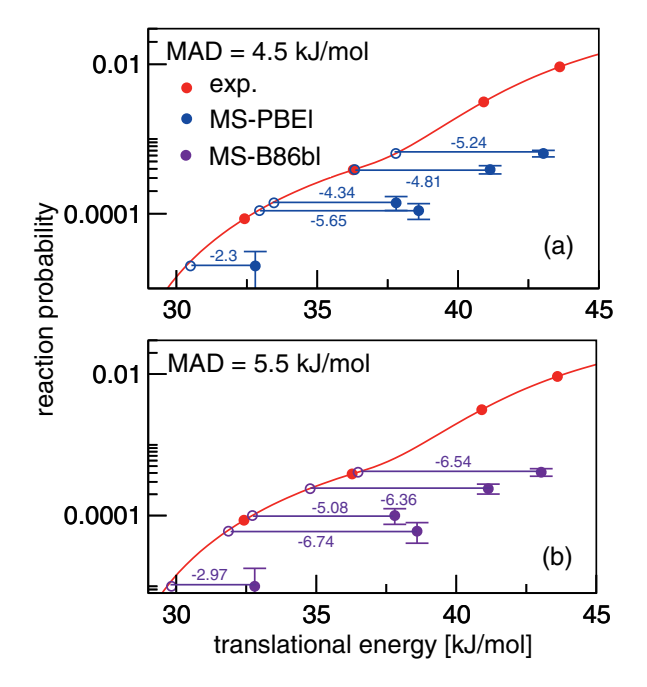


FIGURE 3.13:  $S_0$  values computed with the MS-PBEl (blue symbols, upper panel) and MS-B86bl (purple symbols, lower panel) functionals are shown as a function of  $E_i$ , comparing to the values measured (red symbols) in molecular beam experiments<sup>49</sup>, for  $D_2 + Ag(111)$ . Also indicated are the distances along the energy axis of the computed points to the cubic spline interpolated experimental sticking probability curve. The MAD is the mean value of these distances.

# 3.3.4 Dynamics results: initial-state selected reaction probabilities Ag(111)

Finally, initial-state selected reaction probabilities  $P_{deg}(E_i, \nu, J)$  computed with the MS-PBEl and MS-B86bl functionals are compared with the values extracted from associative desorption experiments<sup>85,86</sup> and computed with the SRP48 functional<sup>50</sup> for  $H_2$  and  $D_2 + Ag(111)$  in figure 3.14. Interestingly, changing to the new MS functionals from the previously used SRP48 functional now seems to lead to more distinct improvement than observed for the sticking (figure 3.13 and discussion above). The reason is that the associative desorption experiments were performed for low vibrational states of  $H_2$  and  $D_2$  ( $\nu = 0$  and 1), so that the effect of the earlier barriers in the MS PESs is less pronounced than for the sticking, which is dominated by the reaction of  $\nu = 3$   $D_2$  as noted before. Note however that the initial-state-selected reaction probabilities from the experiments were extracted from reactive flux measurements in associative desorption, using detailed balance. The measured reaction probabilities are therefore not normalized<sup>85,86</sup>.

# 3.4 Conclusions

The main goal of this study was to determine whether, with a meta-GGA functional constructed within the "made simple" approach, it would be possible to get a chemically accurate description of the dissociative chemisorption of  $H_2$  on Cu(111), while at the same time obtaining a better description of the Cu lattice than possible with previous SRP functionals based on the GGA. A second goal was to determine whether with the meta-GGA "made simple" functionals constructed here it should be possible to also get a more accurate description of the dissociative chemisorption of  $H_2$  on and its associative desorption from Ag(111) than was previously possible with the SRP48 GGA functional for  $H_2$  + Cu(111).

To determine the answer to these questions, we computed bulk lattice constants for Cu, Ag, Au, and Pt, interlayer lattice spacing relaxations for Cu(111) and Ag(111), and PESs for  $H_2 + Cu(111)$  and Ag(111). We did this for three meta-GGA functionals based on the MS concept. In this approach, a function of the kinetic energy density is defined that effectively allows one to vary the exchange functional according to whether the binding in a certain region is metallic or covalent. The exchange parts of the three functionals (MS-PBEl, MS-B86bl, and MS-RPBEl) are based on the expressions for the PBE, B86b, and RPBE exchange functionals, respectively. The three new MS functionals yield metal bulk lattice constants with an accuracy intermediate

3.4. Conclusions 79

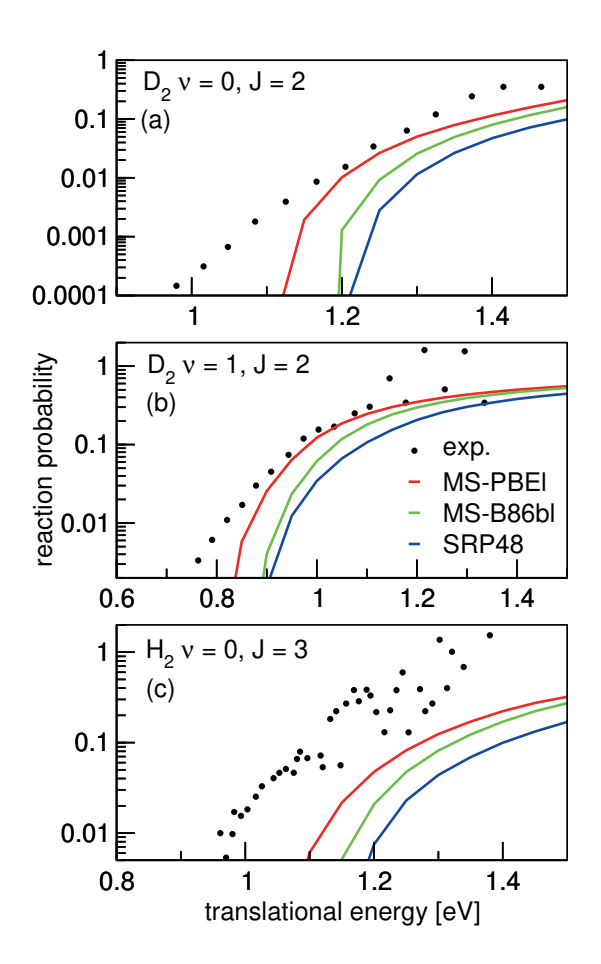


FIGURE 3.14: Initial-state selected reaction probabilities  $P_{deg}(E_i, \nu, J)$  computed with the MS-PBEl and MS-B86bl functionals are shown as a function of  $E_i$ , comparing with values extracted from associative desorption experiments<sup>85,86</sup> and computed with the SRP48 functional<sup>50</sup> for H<sub>2</sub> and D<sub>2</sub> + Ag(111). Results are shown for  $(\nu = 0, J = 2)$  D<sub>2</sub> (a),  $(\nu = 1, J = 2)$  D<sub>2</sub> (b), and  $(\nu = 0, J = 3)$  H<sub>2</sub> (c).

between the all-purpose PBE GGA functional and the PBEsol functional, a GGA functional designed with the specific goal of accurately reproducing observables for the solid state. The interlayer lattice spacing relaxations for the top two layers of Cu(111) and Ag(111) are in good agreement with experimental values.

The barrier heights and geometries obtained for  $H_2 + Cu(111)$  were in good agreement with those obtained earlier with the original SRP functional for  $H_2 + Cu(111)$ . More importantly, the sticking probability curves computed with the three MS functionals and the QCT method agreed with experiments of Rettner and Auerbach and co-workers and of Rendulic and co-workers to within chemical accuracy. The sticking probability curves computed with the MS-PBEl and MS-B86bl functionals for  $D_2 + Ag(111)$  agree slightly better with the molecular beam experiments of Hodgson and co-workers than dynamics calculations based on the SRP48 GGA functional designed for  $H_2 + Cu(111)$ . The initial-state selected reaction probabilities computed for  $H_2$  and  $D_2 + Ag(111)$  also agree quite well with the initial-state selected reaction probabilities extracted from associative desorption experiments of Hodgson and co-workers on these systems.

The main conclusions from this chapter are therefore that, considering the two systems investigated, (i) it is possible to construct non-empirical meta-GGA "made simple" functionals for these two  $\rm H_2$ -metal systems that describe the dissociative chemisorption reaction as accurately as previous semi-empirical functionals based on GGA functionals, while simultaneously giving a more accurate description of the metal lattice, and (ii) on the basis of these MS functionals (in particular, MS-PBEl and MS-RPBEl), an SRP-DF can be constructed for  $\rm H_2 + Cu(111)$ , but not for  $\rm H_2 + Ag(111)$ . This limitation for  $\rm H_2 + Ag(111)$  is due to a potential disadvantage of the SRP approach based on the MS meta-GGA functionals tested: results for  $\rm H_2 + Cu(111)$  suggest that these candidate SRP functionals are less "tunable" than analogous semiempirical GGA functionals for barrier heights. Specifically, for  $\rm H_2 + Cu(111)$ , the minimum barrier height varied by 9 kJ/mol going from MS-PBEl to MS-RPBEl, while it varied by 33 kJ/mol going from PW91 to RPBE.

The behavior of the standard meta-GGA functionals SCAN, TPSS, and revTPPS have been investigated and it has been noted that they all overestimate the sticking probability for  $D_2 + Cu(111)$ , so that they cannot be combined with each other to obtain an SRP functional for this system. However, the revTPSS functional provided a rather good description of the sticking of  $D_2$  on Cu(111), with a MAD of the computed and measured sticking probability curves of only 6.8 kJ/mol. Also, it might be possible to construct an SRP-DF for  $H_2 + Ag(111)$  on the basis of the revTPSS and MS-PBEl functionals, which would probably also give a good description of the Ag lattice. More generally, a good strategy

for constructing an SRP-DF based on meta-GGA functionals might be to start with a weighted average of MS-PBEl and MS-RPBEl, if necessary replacing MS-PBEl with TPSS or revTPSS, or MS-RPBEl by RTPSS<sup>34</sup>, depending on whether a more attractive or more repulsive component functional is required. An alternative strategy for "casting the net wider" might be to relax slightly the condition that either the PBE-like or the RPBE-like MS functional for covalent bonding should exactly correct for the self-interaction correction of the H-atom, by allowing c to vary slightly in equations 3.4-3.6, as done in the RTPSS functional<sup>34</sup>.

The next step would be to apply the MS meta-GGA functionals to the other molecule–metal surface systems for which chemically accurate reaction barrier heights are now available ( $H_2 + Pt(111)$ ) and methane + Ni(111), Pt(111), and Pt(211)). It is anticipated that for these systems it will be necessary to accurately model the van der Waals attractive interaction of the molecule with the metal surface. Results we obtained with the MS functionals investigated here for  $H_2 + Pt(111)$  suggest that these functionals are not accurate for the reaction barrier height for this system (see chapters 5 and 6). This is in line with previous findings that modeling the van der Waals interaction is necessary for an accurate description of weakly activated dissociative chemisorption of  $H_2$  on metal surfaces such as  $Ru(0001)^{64}$  and of dissociative chemisorption of methane on Ni(111).<sup>12,87</sup>

# 3.A Appendix: Details electronic structure calculations and interpolation of the PESs

### 3.A.1 Calculations on bulk metals and on slab relaxation

For each functional, the bulk fcc lattice constant was computed using a four atom unit cell with a  $(28 \times 28 \times 28)$  grid of k-points, a  $0.2\,\mathrm{eV}$  smearing using the Methfessel-Paxton method of order 1, and a plane-wave cut-off energy of  $600\,\mathrm{eV}$ . Slabs were generated by carrying out a relaxation of the interlayer distances of a six-layer slab using a  $(28 \times 28 \times 1)$  grid of k-points and again a plane-wave cut-off energy of  $600\,\mathrm{eV}$  and a  $0.2\,\mathrm{eV}$  smearing using the Methfessel-Paxton method of order 1, for a  $(1 \times 1)$  surface unit cell.

# 3.A.2 Details on the interpolation of the PESs fo $\mathrm{H_2} + \mathrm{Cu}(111)$ and $\mathrm{Ag}(111)$

The configurations  $(U, V, \theta, \phi)$  of the two dimensional cuts used in the interpolation of the six dimensional PES are by design the same high symmetry

two dimensional cuts through the FCC(111) unit cell as reported in ref. <sup>65</sup> We deviate here from previous work in that a denser, non-equidistant grid in r and Z has been used in order to increase the smoothness of the resulting 6D PES. Here we use a  $16 \times 22$  r, Z grid for the 29 two dimensional cuts needed. An added advantage of the denser grids is the better sampling of the electronic structure around the barrier location. We used Z = [0.25, 0.5, 0.75, 1.0, 1.125, 1.25, 1.375, 1.50, 1.75, 2.0, 2.25, 2.50, 2.75, 3.0, 3.25, 3.50, 3.75, 4.0, 4.25, 4.5, 5.0, 5.75] Å, and <math>r = [0.4, 0.5, 0.6, 0.65, 0.7, 0.75, 0.8, 0.85, 0.95, 1.05, 1.15, 1.25, 1.5, 1.75, 2.0, 2.3] Å.

For the interpolation of the three dimensional atomic PES the same ten sites in U and V are used as in ref.<sup>65</sup>, with  $Z_{\rm min}=-1.195 {\rm \AA}$  and  $Z_{\rm max}=7.5 {\rm \AA}$ , with 62 points per site. We deviate here from previous work in that for the reference site at (U=0,V=0) a much denser grid of 162 points was used to reduce noise in the corrugation reducing procedure. The additional points were used to create a denser sampling of the grid between  $Z=-1.195 {\rm \AA}$  and  $Z=+2.0 {\rm \AA}$ .

# References

(1) Smeets, E. W. F.; Voss, J.; Kroes, G.-J. Specific reaction parameter density functional based on the meta-generalized gradient approximation: application to  $H_2 + Cu(111)$  and  $H_2 + Ag(111)$ . J. Phys. Chem. A **2019**, 123, 5395–5406.

- (2) Wolcott, C. A.; Medford, A. J.; Studt, F.; Campbell, C. T. Degree of rate control approach to computational catalyst screening. *J. Catal.* **2015**, *330*, 197–207.
- (3) Sabbe, M. K.; Reyniers, M.-F.; Reuter, K. First-principles kinetic modeling in heterogeneous catalysis: an industrial perspective on best-practice, gaps and needs. *Catal. Sci. Technol.* **2012**, 2, 2010–2024.
- (4) Noyori, R. Synthesizing our future. Nat. Chem. 2009, 1, 5–6.
- (5) Ertl, G. Primary steps in catalytic synthesis of ammonia. J. Vac. Sci. Technol. 1983, 1, 1247–1253.
- (6) Chorkendorff, I.; Niemantsverdriet, J. W., Concepts of modern catalysis and kinetics; John Wiley & Sons, Weinheim: 2017.
- (7) Stegelmann, C.; Andreasen, A.; Campbell, C. T. Degree of rate control: how much the energies of intermediates and transition states control rates. J. Am. Chem. Soc. 2009, 131, 8077–8082.
- (8) Díaz, C.; Pijper, E.; Olsen, R.; Busnengo, H.; Auerbach, D.; Kroes, G. Chemically accurate simulation of a prototypical surface reaction: H<sub>2</sub> dissociation on Cu(111). *Science* **2009**, *326*, 832–834.
- (9) Sementa, L.; Wijzenbroek, M.; Van Kolck, B.; Somers, M.; Al-Halabi, A.; Busnengo, H. F.; Olsen, R.; Kroes, G.-J.; Rutkowski, M.; Thewes, C., et al. Reactive scattering of H<sub>2</sub> from Cu(100): comparison of dynamics calculations based on the specific reaction parameter approach to density functional theory with experiment. J. Chem. Phys. **2013**, 138, 044708.
- (10) Ghassemi, E. N.; Wijzenbroek, M.; Somers, M. F.; Kroes, G.-J. Chemically accurate simulation of dissociative chemisorption of D<sub>2</sub> on Pt(111). *Chem. Phys. Lett.* **2017**, *683*, 329–335.
- (11) Zhu, L.; Zhang, Y.; Zhang, L.; Zhou, X.; Jiang, B. Unified and transferable description of dynamics of H<sub>2</sub> dissociative adsorption on multiple copper surfaces via machine learning. *Phys. Chem. Chem. Phys.* **2020**, 22, 13958–13964.

- (12) Nattino, F.; Migliorini, D.; Kroes, G.-J.; Dombrowski, E.; High, E. A.; Killelea, D. R.; Utz, A. L. Chemically accurate simulation of a polyatomic molecule-metal surface reaction. *J. Phys. Chem. Lett.* **2016**, *7*, 2402–2406.
- (13) Migliorini, D.; Chadwick, H.; Nattino, F.; Gutiérrez-González, A.; Dombrowski, E.; High, E. A.; Guo, H.; Utz, A. L.; Jackson, B.; Beck, R. D., et al. Surface reaction barriometry: methane dissociation on flat and stepped transition-metal surfaces. J. Phys. Chem. Lett. 2017, 8, 4177–4182.
- (14) Nattino, F.; Díaz, C.; Jackson, B.; Kroes, G.-J. Effect of surface motion on the rotational quadrupole alignment parameter of D<sub>2</sub> reacting on Cu(111). *Phys. Rev. Lett.* **2012**, *108*, 236104.
- (15) Perdew, J. P.; Chevary, J. A.; Vosko, S. H.; Jackson, K. A.; Pederson, M. R.; Singh, D. J.; Fiolhais, C. Atoms, molecules, solids, and surfaces: Applications of the generalized gradient approximation for exchange and correlation. *Phys. Rev. B* 1992, 46, 6671–6687.
- (16) Hammer, B. H. L. B.; Hansen, L. B.; Nørskov, J. K. Improved adsorption energetics within density-functional theory using revised Perdew-Burke-Ernzerhof functionals. *Phys. Rev. B* 1999, 59, 7413–7421.
- (17) Perdew, J. P.; Burke, K.; Ernzerhof, M. Generalized gradient approximation made simple. *Phys. Rev. Lett.* **1996**, *77*, 3865–3868.
- (18) Madsen, G. K. Functional form of the generalized gradient approximation for exchange: the PBE $\alpha$  functional. *Phys. Rev. B* **2007**, 75, 195108.
- (19) Dion, M.; Rydberg, H.; Schröder, E.; Langreth, D. C.; Lundqvist, B. I. Van der Waals density functional for general geometries. *Phys. Rev. Lett.* 2004, 92, 246401.
- (20) Lee, K.; Murray, É. D.; Kong, L.; Lundqvist, B. I.; Langreth, D. C. Higher-accuracy van der Waals density functional. Phys. Rev. B 2010, 82, 081101.
- (21) Schimka, L.; Harl, J.; Stroppa, A.; Grüneis, A.; Marsman, M.; Mittendorfer, F.; Kresse, G. Accurate surface and adsorption energies from many-body perturbation theory. *Nature materials* **2010**, *9*, 741–744.
- (22) Haas, P.; Tran, F.; Blaha, P.; Schwarz, K. Construction of an optimal GGA functional for molecules and solids. *Phys. Rev. B* **2011**, *83*, 205117.

(23) Peverati, R.; Truhlar, D. G. Exchange–correlation functional with good accuracy for both structural and energetic properties while depending only on the density and its gradient. *J. Chem. Theory Comput.* **2012**, 8, 2310–2319.

- (24) Klimeš, J. ř.; Bowler, D. R.; Michaelides, A. Van der Waals density functionals applied to solids. *Phys. Rev. B* **2011**, *83*, 195131.
- (25) Rettner, C.; Michelsen, H.; Auerbach, D. Quantum-state-specific dynamics of the dissociative adsorption and associative desorption of H<sub>2</sub> at a Cu(111) surface. J. Chem. Phys. **1995**, 102, 4625–4641.
- (26) Michelsen, H.; Rettner, C.; Auerbach, D.; Zare, R. Effect of rotation on the translational and vibrational energy dependence of the dissociative adsorption of D<sub>2</sub> on Cu(111). *J. Chem. Phys.* **1993**, *98*, 8294–8307.
- (27) Marashdeh, A.; Casolo, S.; Sementa, L.; Zacharias, H.; Kroes, G.-J. Surface temperature effects on dissociative chemisorption of H<sub>2</sub> on Cu(100). *J. Phys. Chem. C* **2013**, *117*, 8851–8863.
- (28) Mondal, A.; Wijzenbroek, M.; Bonfanti, M.; Díaz, C.; Kroes, G.-J. Thermal lattice expansion effect on reactive scattering of  $H_2$  from Cu(111) at  $T_s=925$  K. J. Phys. Chem. A **2013**, 117, 8770–8781.
- (29) Tiwari, A. K.; Nave, S.; Jackson, B. The temperature dependence of methane dissociation on Ni(111) and Pt(111): mixed quantum-classical studies of the lattice response. *J. Chem. Phys.* **2010**, *132*, 134702.
- (30) Tiwari, A. K.; Nave, S.; Jackson, B. Methane dissociation on Ni(111): A new understanding of the lattice effect. *Phys. Rev. Lett.* **2009**, *103*, 253201.
- (31) Sun, J.; Xiao, B.; Fang, Y.; Haunschild, R.; Hao, P.; Ruzsinszky, A.; Csonka, G. I.; Scuseria, G. E.; Perdew, J. P. Density functionals that recognize covalent, metallic, and weak bonds. *Phys. Rev. Lett.* **2013**, 111, 106401.
- (32) Tao, J.; Perdew, J. P.; Staroverov, V. N.; Scuseria, G. E. Climbing the density functional ladder: Nonempirical meta-generalized gradient approximation designed for molecules and solids. *Phys. Rev. Lett.* **2003**, *91*, 146401.
- (33) Perdew, J. P.; Ruzsinszky, A.; Csonka, G. I.; Constantin, L. A.; Sun, J. Workhorse semilocal density functional for condensed matter physics and quantum chemistry. *Phys. Rev. Lett.* **2009**, *103*, 026403.

- (34) Garza, A. J.; Bell, A. T.; Head-Gordon, M. Nonempirical meta-generalized gradient approximations for modeling chemisorption at metal surfaces. J. Chem. Theory Comput. 2018, 14, 3083–3090.
- (35) Sun, J.; Ruzsinszky, A.; Perdew, J. P. Strongly constrained and appropriately normed semilocal density functional. *Phys. Rev. Lett.* **2015**, 115, 036402.
- (36) Wellendorff, J.; Lundgaard, K. T.; Jacobsen, K. W.; Bligaard, T. mBEEF: An accurate semi-local Bayesian error estimation density functional. *J. Chem. Phys.* **2014**, *140*, 144107.
- (37) Sun, J.; Xiao, B.; Ruzsinszky, A. Communication: Effect of the orbital-overlap dependence in the meta generalized gradient approximation. *J. Chem. Phys.* **2012**, *137*, 051101.
- (38) Sun, J.; Haunschild, R.; Xiao, B.; Bulik, I. W.; Scuseria, G. E.; Perdew, J. P. Semilocal and hybrid meta-generalized gradient approximations based on the understanding of the kinetic-energy-density dependence. *J. Chem. Phys.* **2013**, *138*, 044113.
- (39) Sun, J.; Perdew, J. P.; Ruzsinszky, A. Semilocal density functional obeying a strongly tightened bound for exchange. *Proc. Nat. Ac. Sci.* **2015**, *112*, 685–689.
- (40) Lundgaard, K. T.; Wellendorff, J.; Voss, J.; Jacobsen, K. W.; Bligaard, T. mBEEF-vdW: Robust fitting of error estimation density functionals. Phys. Rev. B 2016, 93, 235162.
- (41) Sun, J.; Marsman, M.; Ruzsinszky, A.; Kresse, G.; Perdew, J. P. Improved lattice constants, surface energies, and CO desorption energies from a semilocal density functional. *Phys. Rev. B* **2011**, *83*, 121410.
- (42) Peverati, R.; Truhlar, D. G. An improved and broadly accurate local approximation to the exchange-correlation density functional: The MN12-L functional for electronic structure calculations in chemistry and physics. *Phys. Chem. Chem. Phys.* **2012**, *14*, 13171–13174.
- (43) Luo, S.; Zhao, Y.; Truhlar, D. G. Improved CO Adsorption energies, site preferences, and surface formation energies from a meta-generalized gradient approximation exchange-correlation functional, M06-L. *J. Phys. Chem. Lett.* **2012**, *3*, 2975–2979.
- (44) Becke, A. D. On the large-gradient behavior of the density functional exchange energy. *J. Chem. Phys.* **1986**, *85*, 7184–7187.
- (45) Hou, H.; Gulding, S.; Rettner, C.; Wodtke, A.; Auerbach, D. The stereodynamics of a gas-surface reaction. *Science* **1997**, *277*, 80–82.

(46) Hodgson, A.; Moryl, J.; Traversaro, P.; Zhao, H. Energy transfer and vibrational effects in the dissociation and scattering of D<sub>2</sub> from Cu(111). *Nature* **1992**, *356*, 501–504.

- (47) Kroes, G.-J.; Díaz, C. Quantum and classical dynamics of reactive scattering of H<sub>2</sub> from metal surfaces. *Chem. Soc. Rev.* **2016**, *45*, 3658–3700.
- (48) Burke, K.; Perdew, J. P.; Wang, Y. In *Electronic density functional theory*; Springer: 1998, pp 81–111.
- (49) Cottrell, C.; Carter, R.; Nesbitt, A.; Samson, P.; Hodgson, A. Vibrational state dependence of D<sub>2</sub> dissociation on Ag(111). *J. Chem. Phys.* **1997**, 106, 4714–4722.
- (50) Nour Ghassemi, E.; Somers, M.; Kroes, G.-J. Test of the transferability of the specific reaction parameter functional for  $H_2+$  Cu(111) to  $D_2+$  Ag(111). J. Phys. Chem. C **2018**, 122, 22939–22952.
- (51) Berger, H.; Leisch, M.; Winkler, A.; Rendulic, K. A search for vibrational contributions to the activated adsorption of H<sub>2</sub> on copper. *Chem. Phys. Lett.* **1990**, *175*, 425–428.
- (52) Spiering, P.; Meyer, J. Testing electronic friction models: vibrational de-excitation in scattering of H<sub>2</sub> and D<sub>2</sub> from Cu(111). *J. Phys. Chem. Lett.* **2018**, *9*, 1803–1808.
- (53) Zhang, Y.; Maurer, R. J.; Guo, H.; Jiang, B. Hot-electron effects during reactive scattering of H<sub>2</sub> from Ag(111): the interplay between modespecific electronic friction and the potential energy landscape. *Chem.* Sci. 2019, 10, 1089–1097.
- (54) Perdew, J. P.; Ruzsinszky, A.; Csonka, G. I.; Vydrov, O. A.; Scuseria, G. E.; Constantin, L. A.; Zhou, X.; Burke, K. Restoring the density-gradient expansion for exchange in solids and surfaces. *Phys. Rev. Lett.* **2008**, *100*, 136406.
- (55) Hamada, I. van der Waals density functional made accurate. *Phys. Rev.* B **2014**, 89, 121103.
- (56) Koch, W.; Holthausen, M. C., A chemist's guide to density functional theory; John Wiley & Sons, Weinheim: 2015.
- (57) Kresse, G.; Hafner, J. Ab initio molecular-dynamics simulation of the liquid-metal–amorphous-semiconductor transition in germanium. *Phys. Rev. B* **1994**, *49*, 14251–14269.
- (58) Kresse, G.; Hafner, J. Ab initio molecular dynamics for liquid metals. *Phys. Rev. B* **1993**, *47*, 558–561.

- (59) Kresse, G.; Furthmüller, J. Efficient iterative schemes for ab initio totalenergy calculations using a plane-wave basis set. *Phys. Rev. B* **1996**, 54, 11169–11186.
- (60) Kresse, G.; Furthmüller, J. Efficiency of ab-initio total energy calculations for metals and semiconductors using a plane-wave basis set. *Comput. Mater. Sci.* **1996**, *6*, 15–50.
- (61) Blöchl, P. E. Projector augmented-wave method. Phys. Rev. B 1994, 50, 17953–17979.
- (62) Busnengo, H.; Salin, A.; Dong, W. Representation of the 6D potential energy surface for a diatomic molecule near a solid surface. *J. Chem. Phys.* **2000**, *112*, 7641–7651.
- (63) Olsen, R.; Busnengo, H.; Salin, A.; Somers, M.; Kroes, G.; Baerends, E. Constructing accurate potential energy surfaces for a diatomic molecule interacting with a solid surface: H<sub>2</sub> + Pt(111) and H<sub>2</sub> + Cu(100). *J. Chem. Phys.* **2002**, *116*, 3841–3855.
- (64) Wijzenbroek, M.; Kroes, G. The effect of the exchange-correlation functional on H2 dissociation on Ru(0001). *J. Chem. Phys.* **2014**, *140*, 084702.
- (65) Wijzenbroek, M.; Klein, D. M.; Smits, B.; Somers, M. F.; Kroes, G.-J. Performance of a non-local van der Waals density functional on the dissociation of H<sub>2</sub> on metal surfaces. J. Phys. Chem. A 2015, 119, 12146–12158.
- (66) Raff, L. M.; Karplus, M. Theoretical investigations of reactive collisions in molecular beams: K+CH<sub>3</sub>I and related systems. *J. Chem. Phys.* **1966**, 44, 1212–1229.
- (67) Kroes, G.-J. Six-dimensional quantum dynamics of dissociative chemisorption of H<sub>2</sub> on metal surfaces. *Prog. Surf. Sci.* **1999**, *60*, 1–85.
- (68) Kroes, G.-J.; Somers, M. F. Six-dimensional dynamics of dissociative chemisorption of H<sub>2</sub> on metal surface. *J. Theor. Comput. Chem.* **2005**, 4, 493–581.
- (69) Díaz, C.; Olsen, R. A.; Auerbach, D. J.; Kroes, G.-J. Six-dimensional dynamics study of reactive and non reactive scattering of H<sub>2</sub> from Cu(111) using a chemically accurate potential energy surface. *Phys. Chem. Chem. Phys.* **2010**, *12*, 6499–519.
- (70) Smeets, E. W. F.; Füchsel, G.; Kroes, G.-J. Quantum dynamics of dissociative chemisorption of  $H_2$  on the Stepped Cu(211) Surface. *J. Phys. Chem. C* **2019**, *123*, 23049–23063.

(71) Stoer, J.; Bulirsch, R., *Introduction to numerical analysis*; Springer Science & Business Media, New York: 2013; Vol. 12.

- (72) Michelsen, H. A.; Auerbach, D. J. A critical examination of data on the dissociative adsorption and associative desorption of hydrogen at copper surfaces. *J. Chem. Phys.* **1991**, *94*, 7502–7520.
- (73) Scoles, G.; Bassi, D.; Buck, U.; Laine, D., Atomic and molecular beam methods; Oxford university press, New York: 1988; Vol. 1.
- (74) Haas, P.; Tran, F.; Blaha, P. Calculation of the lattice constant of solids with semilocal functionals. *Phys. Rev. B* **2009**, *79*, 085104.
- (75) Honkala, K.; Hellman, A.; Remediakis, I. N.; Logadottir, A.; Carlsson, A.; Dahl, S.; Christensen, C. H.; Nørskov, J. K. Ammonia synthesis from first-principles calculations. *Science* **2005**, *307*, 555–558.
- (76) Chae, K.; Lu, H.; Gustafsson, T. Medium-energy ion-scattering study of the temperature dependence of the structure of Cu(111). *Phys. Rev. B* **1996**, *54*, 14082.
- (77) Soares, E.; Leatherman, G.; Diehl, R.; Van Hove, M. Low-energy electron diffraction study of the thermal expansion of Ag(111). *Surf. Sci.* **2000**, 468, 129–136.
- (78) Statiris, P.; Lu, H.; Gustafsson, T. Temperature dependent sign reversal of the surface contraction of Ag(111). *Phys. Rev. Lett.* **1994**, *72*, 3574–3577.
- (79) Patra, A.; Bates, J. E.; Sun, J.; Perdew, J. P. Properties of real metallic surfaces: effects of density functional semilocality and Van der Waals nonlocality. *Proc. Natl. Acad. Sci.* 2017, 114, E9188–E9196.
- (80) Wijzenbroek, M.; Helstone, D.; Meyer, J.; Kroes, G.-J. Dynamics of H<sub>2</sub> dissociation on the close-packed (111) surface of the noblest metal: H<sub>2</sub> + Au(111). J. Chem. Phys. 2016, 145, 144701.
- (81) Lindgren, S.; Walldén, L.; Rundgren, J.; Westrin, P. Low-energy electron diffraction from Cu(111): subthreshold effect and energy-dependent inner potential; surface relaxation and metric distances between spectra. *Phys. Rev. B* **1984**, *29*, 576–588.
- (82) Polanyi, J. C. Some concepts in reaction dynamics. *Science* **1987**, *236*, 680–690.
- (83) Polanyi, J. C. Some concepts in reaction dynamics (Nobel lecture). *Angew. Chem.* **1987**, *26*, 952–971.

- (84) Patra, A.; Peng, H.; Sun, J.; Perdew, J. P. Rethinking CO adsorption on transition-metal surfaces: Effect of density-driven self-interaction errors. *Phys. Rev. B* **2019**, *100*, 035442.
- (85) Murphy, M.; Hodgson, A. Translational energy release in the recombinative desorption of H<sub>2</sub> from Ag(111). Surf. Sci. **1997**, 390, 29–34.
- (86) Murphy, M.; Hodgson, A. Role of surface thermal motion in the dissociative chemisorption and recombinative desorption of D<sub>2</sub> on Ag(111). Phys. Rev. Lett. 1997, 78, 4458–4461.
- (87) Nattino, F.; Migliorini, D.; Bonfanti, M.; Kroes, G.-J. Methane dissociation on Pt(111): Searching for a specific reaction parameter density functional. *J. Chem. Phys.* **2016**, *144*, 044702.

# 4 Quantum dynamics of dissociative chemisorption of $H_2$ on the stepped Cu(211) surface

### This Chapter is based on:

Smeets, E. W. F.; Füchsel, G.; Kroes, G.-J. Quantum dynamics of dissociative chemisorption of  $H_2$  on the Stepped Cu(211) Surface. *J. Phys. Chem. C* **2019**, 123, 23049-23063

# Abstract

Reactions on stepped surfaces are relevant to heterogeneous catalysis, in which reaction often takes place at the edges of nanoparticles where the edges resemble steps on single crystal stepped surfaces. Previous results on H<sub>2</sub> + Cu(211) show that in this system steps do not enhance the reactivity, and raised the question of whether this effect could be in anyway related to the neglect of quantum dynamical effects in the theory. To investigate this full quantum dynamical molecular beam simulations of sticking of H<sub>2</sub> on Cu(211) are presented in which all important rovibrational states populated in a molecular beam experiment are taken into account. It is found that the reaction of H<sub>2</sub> with Cu(211) is very well described with quasi-classical dynamics when simulating molecular beam sticking experiments, in which averaging takes place over a large number of rovibrational states and over translational energy distributions. The results show that the stepped Cu(211) surface is distinct from its component Cu(111) terraces and Cu(100) steps and cannot be described as a combination of its component parts with respect to the reaction dynamics when considering the orientational dependence. Specifically, we present evidence that at translational energies close to the reaction threshold vibrationally excited molecules show a negative rotational quadrupole alignment parameter on Cu(211), which is not found on Cu(111) and Cu(100). The effect arises because these molecules react with a site specific reaction mechanism at the step, i.e., inelastic rotational

enhancement, which is only effective for molecules with a small absolute value of the magnetic rotation quantum number. From a comparison to recent associative desorption experiments as well as Born-Oppenheimer molecular dynamics (BOMD) calculations it follows that the effects of surface atom motion and electron hole-pair (ehp) excitation on the reactivity fall within chemical accuracy, i.e., modeling these effect shifts extracted reaction probability curves by less then 1 kcal/mol translational energy. No evidence is found in the fully-state-resolved calculations for the 'slow' reaction channel that was recently reported for associative desorption of H<sub>2</sub> from Cu(111) and Cu(211), but the results for the fast channel are in good agreement with the experiments on H<sub>2</sub> + Cu(211).

### Introduction 4.1

The rate limiting step in a heterogeneously catalysed process is often a dissociative chemisorption reaction<sup>2,3</sup>. Hydrogen (H<sub>2</sub>) dissociation is important to heterogeneously catalyzed production of syngas and ammonia<sup>4</sup> and has recently gained industrial importance with the production of methanol from CO<sub>2</sub> over a Cu/ZnO/Al<sub>2</sub>O<sub>3</sub> catalyst, in which the rate limiting step is considered to be the dissociation of H<sub>2</sub><sup>5-7</sup>. Stepped, kinked or otherwise defective surfaces more closely resemble real catalytic surfaces, as catalyzed reactions tend to proceed at the corners or edges of nanoparticles<sup>8,9</sup>. A better theoretical understanding of the reaction dynamics of H<sub>2</sub> dissociation on stepped surfaces could well be a first step to the design of new catalysts from first principles 10.

H<sub>2</sub> reacting on copper surfaces is a prototypical example of a highly activated late barrier system<sup>11–14</sup>. For the flat Cu(111), Cu(110) and Cu(100) surfaces a plethora of experimental<sup>14–25</sup> and theoretical<sup>13,26–44</sup> results have been reported that are generally in good agreement with each other. This large body of work has allowed for the development of a chemically accurate description of molecular beam experiments using the semi-empirical specific reaction parameter approach to density functional theory (SRP-DFT)<sup>36</sup>. Recently molecular beam adsorption experiments<sup>45</sup> and associative desorption experiments<sup>46</sup> for H<sub>2</sub> reacting on Cu(211) have been reported, allowing for a more stringent comparison between theory and experiment for this system. Theoretical reaction dynamics results of H<sub>2</sub> reacting on stepped or defective surfaces have only been reported sparingly, most notably for D<sub>2</sub> on Cu(211)<sup>47</sup>, H<sub>2</sub> on Pt(211)<sup>48-52</sup> and H<sub>2</sub> on defective  $Pd(111)^{53}$ .

In previous work we and others have shown that the Cu(211) surface is less reactive towards H<sub>2</sub> than the Cu(111) surface<sup>47</sup>, which indicates that predictions based on the d-band model of Nørskov and Hammer<sup>54,55</sup> are not always reliable. 4.1. Introduction 93

In the d-band model increased reactivity at steps, defects, or otherwise less coordinated surface atoms, is ascribed to a reduced width of the d-band  $^{54,56}$  and a shift of the center of the d-band towards the Fermi level at these sites. In the case of Cu(211) the breakdown of the d-band model is due to the geometric effect of the lowest barrier to reaction for  $H_2$  on Cu(111) not being situated at a top site<sup>47</sup>.

Due to the corrugated nature of the molecule surface interaction and the denser distribution of barriers to reaction it is unclear whether quantum effects can have a significant effect on the reaction dynamics of  $H_2$  reacting on Cu(211). Our main goal is to investigate if including quantum effects during the dynamics significantly affects observables such as the macroscopic molecular reaction probability and rotational quadrupole alignment parameters. To this end we will mainly focus on a comparison of fully state-resolved quantum dynamical (QD) and quasi-classical trajectory (QCT) reaction probabilities for H<sub>2</sub> incident on Cu(211), and the effect of Boltzmann averaging over all rovibrational states populated in a molecular beam experiment. Employing the time-dependent wave packet (TDWP) method<sup>57,58</sup>, we have carried out QD calculations mainly for H<sub>2</sub>. Due to the low mass of H<sub>2</sub> quantum effects are presumed to be most prevalent for H<sub>2</sub> and energy transfer to the surface during collision is expected to be small. Performing this large body of calculations for D<sub>2</sub> would have been much more expensive because its larger mass necessitates the use of denser numerical grids and longer propagation times.

Another aim will be to investigate if the reaction dynamics of  $H_2$  dissociation on the stepped Cu(211) differs from the reaction dynamics at low Miller index copper surfaces, for which the reaction dynamics is reasonably similar<sup>31–33,44</sup>. This is relevant because the Cu(211) surface has Cu(111) terraces and Cu(100) steps, and considering this question might thus provide more insight in how a stepped surface can alter reaction mechanisms. Rotational quadrupole alignment parameters for vibrationally excited molecules are similar in behavior for  $Cu(111)^{17,33}$  and  $Cu(100)^{31,32}$ . It will be investigated whether the same holds for  $H_2 + Cu(211)$ .

Recent associative desorption experiments on Cu(111) and  $Cu(211)^{46}$ , which were in good agreement with earlier theoretical and experimental work<sup>17,31,35,36,47,59</sup>, have shown a 'slow' reaction channel to be active for both Cu(111) and Cu(211) which has not been reported before. In this channel reaction could be facilitated by trapping on the surface and distortion of the surface due to thermal motion forming a reactive site<sup>46</sup>. Our calculations on sticking of  $H_2$  are performed using the static surface approximation, which suggests that we might not be able to model this slow channel. We do however make a direct comparison to the experimental effective barrier heights obtained

by applying the principle of detailed balance and direct inversion of time-of-flight measurements reported by Kaufmann et al.<sup>46</sup> for the fast channel.

The highly accurate potential energy surface (PES) used in our calculations and our previous work<sup>47</sup> has been constructed using the corrugation reducing procedure (CRP)<sup>60</sup> together with the SRP48 density functional<sup>33</sup>, which was proven to be chemically accurate for  $H_2$  dissociating on  $Cu(111)^{36}$ . It has also been shown previously that the SRP functional for  $H_2 + Cu(111)$  is transferable to  $H_2 + Cu(100)^{31}$ . All our calculations have been carried out using the BOSS model which works well for activated  $H_2$  dissociation on metals at low surface temperatures<sup>27,34–37,61</sup>.

# 4.2 Computational methods and simulations

In the following, we present details on the different simulations we have performed to describe the dynamics of  $H_2$  ( $D_2$ ) incident on Cu(211). In our six-dimensional QD, QCT and MDEF simulations we used the static surface approximation. They are carried out on a six-dimensional PES that was previously developed by us<sup>47</sup> on the basis of the corrugation reducing procedure<sup>60</sup> and  $\sim 116~000~\rm DFT$  energy points computed with the SRP48 functional<sup>33</sup>. The SRP48 functional contains 48% RPBE<sup>62</sup> and 52% PBE<sup>63</sup> exchange correlation and was fitted to quantitatively reproduce experimental sticking probabilities for the reaction of  $H_2(D_2)$  on a flat Cu(111) surface<sup>33</sup>. The very similar SRP functional<sup>36</sup> performed excellently at describing the  $H_2 + Cu(100)$  reaction<sup>31</sup>.

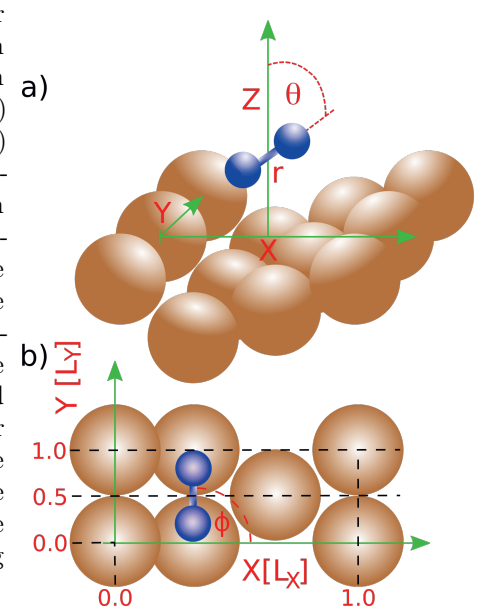
## 4.2.1 Coordinate system

The six-dimensional dynamics calculations account only for the motion along the six molecular degrees of freedom (DOF) of  $H_2$  ( $D_2$ ), while the surface atoms are kept frozen at their ideal 0 K configuration as computed with DFT. The molecular coordinates include the center of mass (COM) position of  $H_2$  given by the coordinates X, Y, Z, where Z is molecule-surface distance and X, Y describe the lateral position measured relative to a Cu reference atom at the step edge. Also included are the H-H bond distance r and the angular orientation of  $H_2$  given by the polar angle  $\theta$  defined with respect to the surface normal and the azimuthal angle  $\phi$ . The coordinate system is drawn in figure 4.1a, and the Cu(211) surface unit cell in figure 4.1b, and additional details about the dimensions of the  $(1\times1)$ Cu(211) unit cell are specified in the corresponding caption.

## 4.2.2 Ab initio molecular dynamics simulations

To describe the reaction of  $D_2$  on Cu(211) at normal incidence with the Born-Oppenheimer molecular dynamics (BOMD) technique, we employ a modified version of the Vienna Ab Initio Simulation Package<sup>64–67</sup> (VASP). Note that in previous publications, we referred to the direct dynamics technique using SRP-DFT as the ab-initio molecular dynamics (AIMD) method. Because this might be taken to imply that the SRP functional is not semi-empirical we abandoned this name and we now refer to it as Born-Oppenheimer molecular dynamics (BOMD). The modifications of the computer package concern the propagation algorithm and were first introduced in work<sup>68,69</sup> on electronically non-adiabatic effects in gas-surface systems using VASP. To be consistent with our previous work on the system<sup>47</sup>, we adopt the same computational setup

FIGURE 4.1: Coordinate system for  $H_2(D_2)$  on Cu(211). H atoms are drawn in blue and Cu atoms in brown. Shown in a) is a side view of a  $(1 \times 2)$ Cu(211)supercell and b) a top view on a  $(1 \times 1)$ unit cell. The six molecular DOF are indicated, i.e., the COM coordinates given by X, Y, Z, where X, Y are the lateral coordinates and Z is the molecule surface distance. Furthermore, the H-H distance is represented by r and the angular orientation by the polar angle  $\theta$  and the azimuthal angle  $\phi$ . The latter is defined with respect to the X axis, the former with respect to the macroscopic surface normal. The computed lengths of the lattice vectors of the  $(1 \times 1)$  unit cell are  $L_X = 6.373 \text{ Å and } L_Y = 2.602 \text{ Å along}$ X and Y.



for the electronic structure calculations specified in the supporting information of ref.<sup>47</sup> Here, we briefly recall only the most important details. The Cu(211) surface is represented using a five layer slab model periodically repeated over a  $(1\times2)$  supercell with a vacuum spacing of 15 Å. Ultrasoft pseudopotentials are used and plane waves corresponding to energies of up to 370 eV. The k-points are sampled using the Monkhorst-Pack grid scheme and an  $8\times8\times1$  mesh centered at the  $\Gamma$  point. Fermi smearing is used with a width of 0.1 eV.

BOMD simulations are performed at different average incidence energies and mimic corresponding molecular beam conditions at which Michelsen et al. <sup>16</sup> originally performed experiments on the dissociation of  $D_2$  on flat Cu(111). The inclusion of beam parameters in the simulations is explained below in section 4.2.5. For each incidence energy point, we perform 500 trajectory calculations. This allows us to achieve an absolute standard error of smaller than 0.02 in the computed initial sticking coefficient. All BOMD trajectories start at a molecule-surface distance of Z = 7 Å and are propagated until dissociation or scattering of  $D_2$  has occurred. Here, we count trajectories to be dissociatively adsorbed if the D-D distance r is larger than 2.45 Å. A non-reactive scattering event is counted when trajectories return to the gas phase and have reached a molecule-surface distance of  $Z \geq 7.1$  Å. We use a time-step discretization  $\Delta t$  of 1 fs in the dynamics propagation and a maximum propagation time  $t_f$  of 2 ps. Geometries between consecutive time steps are updated if the electronic energy is converged to  $10^{-5}$  eV. The setup allows on average for an energy

conservation error of typically  $\sim 10$  meV.

BOMD simulations performed within the static surface approximation employ the same slab model described in our earlier work<sup>47</sup>. Therein, the first four layers of the slab are relaxed through energy minimization (the positions of the fifth layer atoms are fixed during relaxation). The resulting optimized Cu(211) surface conserves the p1m1 space group and remains unchanged during the BOMD simulations. This prevents energy transfer to take place between the molecule and the surface due to excitation of surface atom motion upon scattering. To model a thermalized Cu(211) surface at a temperature  $T_s=120$  K according to experiments, we follow the NVE/NVT procedure explained in Refs.<sup>33,70</sup> and generate 10,000 slab configurations resembling the phase space. The initial condition of an BOMD trajectory at  $T_s=120$  K is set up by randomly mixing thermalized slab models with a random configurations of  $D_2$  generated according to the molecular beam conditions.

#### 4.2.3 Quasi-classical simulations

The MD(EF) simulations presented in this work use the 6D-PES of Ref.<sup>47</sup> and assume quasi-classical conditions<sup>71</sup>, that is, initial conditions of the classical trajectories reflect the quantum mechanical energies of incident H<sub>2</sub>(D<sub>2</sub>) in their initial rovibrational state(s). To do so, we use the method described in ref.<sup>70</sup> The dynamics is studied by integrating a Langevin equation<sup>72</sup> numerically using the stochastic Ermak-Buckholz algorithm<sup>73</sup> and the methodology is outlined in refs.<sup>70,74</sup> Note that in the non-dissipative limit, i.e. the MD case, the Langevin equation obeys Newton's equation of motion for which the propagation algorithm is also suitable. In the MDEF case, energy dissipation between molecule and surface is mediated through electronic friction as computed from the local density friction approximation within the independent atom approximation (LDFA-IAA) model<sup>75</sup>. Specifically, friction coefficients of the hydrogen atoms are represented as a function of the electron density of the ideal bare Cu(211) surface. The latter is extracted from a single DFT calculation, see Ref.<sup>70</sup> for details.

QCT calculations are used here i) to model fictitious molecular beam experiments using realistic beam parameters, and ii) to perform initial state-resolved calculations. In the former case, 100 000 QCT calculations per energy point are computed, whereas state-resolved sticking coefficients are evaluated per energy point from 50 000 trajectories. As with BOMD, all MD(EF) trajectories start at a molecule-surface distance of Z=7 Å. A time step of  $\Delta t=0.5$   $\hbar/E_{\rm h}$  ( $\approx$ 0.012 fs) is used for the propagation resulting in an energy conservation error for the MD simulations of smaller than 1 meV. To determine probabilities

for dissociative adsorption and non-reactive scattering, we impose the same conditions used for the BOMD simulations, see above.

#### 4.2.4 Quantum dynamics simulations

To perform 6D quantum dynamics simulations, we solve the time-dependent Schrödinger equation:

$$i\hbar \frac{d\Psi(\underline{Q};t)}{dt} = \hat{H}(\underline{Q})\Psi(\underline{Q};t), \tag{4.1}$$

using the time-dependent wave packet (TDWP) approach as implemented in our in-house computer package<sup>57,58</sup>. In Eq.4.1,  $\underline{Q} = (X,Y,Z,r,\theta,\phi)^T$  is a six-dimensional position vector,  $\psi(\underline{Q};t)$  is the time-dependent nuclear wave function of the system and  $\hat{H}(\underline{Q})$  is the time-independent Hamiltonian which reads:

$$\hat{H}(\underline{Q}) = -\frac{\hbar^2}{2M}\nabla^2 - \frac{\hbar^2}{2\mu}\frac{\partial^2}{\partial r^2} + \frac{1}{2\mu r^2}\hat{J}^2(\theta, \phi) + V(\underline{Q}). \tag{4.2}$$

Here, M and  $\mu$  are the mass and the reduced mass of  $H_2$ , and  $\nabla$  and  $\hat{J}$  are the Nabla and the angular momentum operators. The 6D PES,  $V(\underline{Q}) = V(X,Y,Z,r,\theta,\phi)$ , is taken from ref<sup>47</sup> and was computed with the SRP48 functional<sup>33</sup>. The initial wave function is represented as a product of a Gaussian wave packet  $u(Z_0, k_0^Z)$  centered around  $Z_0$ , a two-dimensional plane wave function  $\phi(k_0^X, k_0^Y)$  describing motion along X,Y and the rovibrational wave function  $\psi_{\nu,i,m_i}(r,\theta,\phi)$  of incident  $H_2$ :

$$\Psi(\underline{Q}, t = 0) = \psi_{\nu, j, m_j}(r, \theta, \phi)\phi(k_0^X, k_0^Y)u(Z; Z_0, k_0^Z)$$
(4.3)

where the two-dimensional plain wave function and the Gaussian wave packet are defined as

$$\phi(k_0^X, k_0^Y) = e^{i(k_0^X X_0 + k_0^Y Y_0)} \tag{4.4}$$

$$u(Z; Z_0, k_0^Z) = \left(\frac{2\sigma^2}{\pi}\right)^{\frac{1}{4}} \int_0^\infty dk_0^Z e^{-\sigma^2(\underline{k} - k_0^Z)} e^{i(\underline{k} - k_0^Z)Z_0} e^{ik_0^Z Z_0}.$$
(4.5)

Here,  $\sigma$  is the width of the wave packet centered around  $Z_0$  with the average momentum  $\underline{k}$  and  $k_0^{X,Y,Z}$  are the initial momenta of the COM. The width  $\sigma$  is chosen in such a way that 90% of the Gaussian wave packet is placed in a energy range  $E_i \in [E_{min}, E_{max}]$ . Eq.4.1 is solved numerically using the split operator method with a time step  $\Delta t$ . We apply a quadratic form of optical potentials<sup>76</sup> in the scattering (at large values of Z) and adsorption regions (at large values

of r). The scattered fraction of the wave function is analyzed through the scattering matrix formalism<sup>77</sup> and the scattering probability  $P_{sc}$  is computed accordingly. Substracting  $P_{sc}$  from 1 then yields the sticking probability  $S_0$ .

Parameters for the wave packet calculations defining the initial wave packet, the rotational basis set, the grid representation, time step and the optical potentials are compiled in Table 4.1. The final propagation time can vary since we stop simulations if the remaining norm on the grid is below 0.01.

Table 4.1: Input parameters for the 6D quantum simulations on the reactive scattering of  $H_2$  on Cu(211). All wave packets were propagated until the remaining norm was less then one percent.

|   | 0.05 - 0.22 eV |         | 0.2 - 0.6 eV |         | 0.57 - 1.4 eV  |                 |         | $D_2$               |
|---|----------------|---------|--------------|---------|----------------|-----------------|---------|---------------------|
|   | $\nu_0$        | $\nu_1$ | $\nu_0$      | $\nu_1$ | $\nu_0$        | $\nu_0$         | $\nu_1$ | $\nu_1 \tilde{J}_6$ |
|   |                |         |              |         | $J \in [0, 7]$ | $J \in [8, 11]$ |         |                     |
| $Z_{start}$ (Bohr)  | -2.0           | -2.0    | -2.0         | -2.0    | -2.0           | -2.0            | -2.0    | -2.0                |
| $N_{Zspec}$   | 280            | 280     | 280          | 280     | 280            | 280             | 280     | 280                 |
| $N_Z$   | 180            | 180     | 176          | 176     | 176            | 176             | 176     | 176                 |
| $\Delta Z$ (Bohr)   | 0.1            | 0.1     | 0.08         | 0.08    | 0.08           | 0.08            | 0.08    | 0.08                |
| $R_{start}$ (Bohr)  | 0.8            | 0.8     | 0.8          | 0.8     | 0.8            | 0.8             | 0.8     | 0.8                 |
| $N_R$   | 60             | 60      | 56           | 56      | 56             | 56              | 56      | 56                  |
| $\Delta R$ (Bohr)   | 0.15           | 0.15    | 0.15         | 0.15    | 0.15           | 0.15            | 0.15    | 0.15                |
| $N_X$   | 36             | 36      | 36           | 36      | 36             | 36              | 36      | 42                  |
| $N_Y$   | 12             | 12      | 12           | 12      | 12             | 12              | 12      | 16                  |
| $J_{ m max}$  | 26 / 25        | 30 / 29 | 26 / 25      | 32 / 31 | 38 / 37        | 42 / 41         | 36 / 35 | 42                  |
| $mJ_{\max}$   | 26 / 25        | 30 / 29 | 26 / 25      | 32 / 31 | 30 / 29        | 42 / 41         | 28 / 27 | 40                  |
| Complex absorbing pot                                       | entials        |         |              |         |                |                 |         |                     |
| $Z^{CAP}$ start $[a_0]$                                     | 8.9            | 8.9     | 8.88         | 8.88    | 8.88           | 8.88            | 8.88    | 8.88                |
| $Z^{CAP}$ end $[a_0]$                                       | 15.9           | 15.9    | 12.0         | 12.0    | 12.0           | 12.0            | 12.0    | 12.0                |
| $Z^{CAP}$ Optimum [eV]                                      | 0.16           | 0.16    | 0.3          | 0.3     | 0.95           | 0.95            | 0.95    | 0.3                 |
| $Z_{spec}^{CAP}$ start $[a_0]$ $Z_{spec}^{CAP}$ end $[a_0]$ | 18.1           | 18.1    | 16.8         | 16.8    | 18.16          | 18.16           | 18.16   | 16.8                |
| $Z_{spec}^{CAP}$ end $[a_0]$                                | 25.9           | 25.9    | 20.32        | 20.32   | 20.32          | 20.32           | 20.32   | 20.32               |
| $Z^{CAP}$ Optimum [eV]                                      | 0.16           | 0.16    | 0.3          | 0.3     | 1.2            | 1.2             | 1.2     | 0.3                 |
| R <sup>CAP</sup> start [ao]                                 | 4.55           | 4.55    | 4.55         | 4.55    | 4.55           | 4.55            | 4.55    | 4.55                |
| $R^{CAP}$ end $[a_0]$                                       | 9.65           | 9.65    | 9.05         | 9.05    | 9.05           | 9.05            | 9.05    | 9.05                |
| $R^{CAP}$ optimum [eV]                                      | 0.12           | 0.12    | 0.3          | 0.3     | 1.0            | 1.0             | 1.0     | 0.3                 |
| Propagation   |                |         |              |         |                |                 |         |                     |
| $\Delta t \left[ \hbar / E_{\rm h} \right]$                 | 2              | 2       | 2            | 2       | 2              | 2               | 2       | 2                   |
| $t_f [\hbar/E_{ m h}]$                                      | 44000          | 44000   | 14000        | 14000   | 10000          | 10000           | 10000   | 20000               |
| Initial wave packet   |                |         |              |         |                |                 |         |                     |
| $E_{min}$ [eV]  | 0.05           | 0.05    | 0.2          | 0.2     | 0.57           | 0.57            | 0.57    | 0.2                 |
| $E_{max}$ [eV]  | 0.22           | 0.22    | 0.6          | 0.6     | 1.4            | 1.4             | 1.4     | 0.6                 |
| $Z_0 [a_0]$   | 13.50          | 13.5    | 11.44        | 11.44   | 11.44          | 11.44           | 11.44   | 11.44               |

## 4.2.5 Computation of observables

To incorporate the effect of a molecular beam on the computed sticking coefficient we need to take into account the distributions of translational energies and the rovibrational state population due to a nozzle temperature  $T_n$ . The probability to find a molecule with velocity v + dv in a rovibrational state described by the vibrational quantum number  $\nu$  and the angular momentum quantum number J is given by:

$$P(v, \nu, J, T_n)dv = P_{flux}(v; T_n)dv \times P_{int}(\nu, J, T_n)$$
(4.6)

where the flux-weighted velocity distribution  $P_{flux}$  is a parameterized function of  $T_n$  and determined by the width parameter  $\alpha$  and the stream velocity  $v_0$  according to<sup>78</sup>

$$P_{flux}(v; T_n)dv = Cv^3 e^{-(v-v_0)^2/\alpha^2} dv$$
(4.7)

where C is a normalization constant. The ensemble representation of the rovibrational state population distribution reads:

$$P_{int}(\nu, J, T_n) = \frac{w(J)f(\nu, J, T_n)}{\sum_{\nu', J' \equiv J(mod\ 2)} f(\nu', J', T_n)}$$
(4.8)

with

$$f(\nu, J, T_n) = (2J+1) \times e^{(-(E_{\nu,0} - E_{0,0})/k_B T_{vib})} \times e^{(-(E_{\nu,J} - E_{\nu,0})/k_B T_{rot})}.$$
 (4.9)

Here,  $k_B$  is the Boltzmann constant and  $E_{\nu,J}$  is the energy of the quantum state characterized by  $\nu$  and J. In equation 4.9 the first and second Boltzmann factor describe vibrational and rotational state populations, respectively. Note, that the rotational temperature is  $T_{rot} = 0.8 T_n^{19}$  whereas the vibrational temperature  $T_{vib} = T_n$ . This setting is in agreement with the observation that rotational but no vibrational cooling occurs during gas expansion in the nozzle. The factor w(J) in Eq. 4.8 is due to ortho- and para-hydrogen molecules present in the beam. For  $H_2$ , w(J) is 1/4 (3/4) for even (odd) values of J, and for  $D_2$ , w(j) = 2/3 (1/3) for even (odd) values of J.

In the case of classical dynamics calculations (MD, MDEF and BOMD), the probability distribution  $P(v, \nu, J, T_n)$  is randomly sampled as described in ref<sup>70</sup> using the different beam parameters of H<sub>2</sub> and D<sub>2</sub> listed in Table 4.2. The sticking coefficient per energy point is given by the ratio of the number of adsorbed trajectories  $N_{ads}$  and the total number of computed trajectories N, that is,  $S_0 = N_{ads}/N$ . To extract quantum mechanical results on H<sub>2</sub> beam simulations, a direct sampling of  $P(v, \nu, J, T_n)$  is not feasible. Instead, initial state-resolved reaction probabilities  $R_{mono}(E_i, \nu, j)$  are first computed as functions of the monochromatic incidence energy  $E_i$  by degeneracy averaging fully initial state-resolved reaction probabilities  $P_R(E_i, \nu, J, m_j)$  over the magnetic rotational quantum number  $m_J$ , i.e.,

$$R_{mono}(E_i, \nu, J) = \sum_{m_J=0}^{j} (2 - \delta_{m_J,0}) P_R(E_i, \nu, J, m_J) / (2J + 1). \tag{4.10}$$

The initial sticking probability  $S_0(\langle E_i \rangle)$  is then calculated as a function of average incidence energy  $\langle E_i \rangle$  by averaging over the rovibrational  $(\nu, J)$  states populated in the beam (see Eq. 4.8) and the flux-weighted distribution of the incident translational energies of the beam, according to

$$S_0(\langle E_i \rangle) = \sum_{J} \sum_{\nu} \frac{\int_0^{\infty} P'(E_i, \nu, J, T_n) R_{mono}(E_i, \nu, J) dE_i}{\int_0^{\infty} P'(E_i, \nu, J, T_n) dE_i}.$$
 (4.11)

We note that although  $S_0(\langle E_i \rangle)$  is written and plotted in publications as a function of average incidence only, it also implicitly depends on  $T_n$  through the distribution  $P'(E_i, \nu, J, T_n)$  of incidence energies and the rovibrational state populations

$$P'(E_i, \nu, J, T_n)dE_i = P'_{flux}(E_i; T_n)dE_i \times P_{int}(\nu, J, T_n). \tag{4.12}$$

 $P'(E_i, \nu, J, T_n)$  makes the initial sticking also depend implicitly on incident beam conditions other than just  $T_n$ , due to the occurrence of the flux-weighted distribution of incidence energies  $P'_{flux}(E_i; T_n)$ , which depends on a number of factors including the molecular beam geometry, backing pressure, whether or not a seeding gas is used, and can be described by the parameters  $E_0$  and  $\Delta E_0$  according to:

$$P'_{flux}(E_i; T_n) dE_i = C' E_i e^{-4E_0(\sqrt{E_i} - \sqrt{E_0})^2/\Delta E_0^2} dE_i.$$
 (4.13)

Instead of averaging over incidence energies using  $P'_{flux}(E_i; T_n)$  as done in Eq. 4.12 it is also possible to average over the flux-weighted velocity distribution of the molecules in the beam,  $P'_{flux}(v_i; T_n)$ , and the derivation  $P'_{flux}(E_i; T_n)$  from  $P_{flux}(v; T_n)$  is discussed in Ref<sup>78</sup>. For a particle of mass m, the parameters are defined as  $E_0 = mv_0^2/2$  and  $\Delta E_0 = 2E_0\alpha/v_0$ .

To obtain sticking coefficients  $S_0$ , we perform 114 state-resolved calculations (corresponding to 342 wave packet calculations) for an energy range of  $E_i \in [0.05, 1.4]$  eV. The initial states of incident H<sub>2</sub> considered here to evaluate Eq.4.11 are characterized by the quantum numbers  $J \in [0, 11]$  for  $\nu = 0$  and

TABLE 4.2: Molecular beam parameters taken from experiments performed on the  $H_2(D_2) + Cu(111)$  system and the  $D_2 + Pt(111)$  system. The parameters  $v_0$ ,  $\alpha$ ,  $T_n$  represent the stream velocity of the beam, the velocity width of the beam and the nozzle temperature, yielding an average translational incidence energy  $\langle E_i \rangle$ . Parameters were taken from refs<sup>16,35</sup>.

| $T_n$ [K]  | $\langle E_i \rangle  [\mathrm{kJ/mol}]$         | $v_0  [\mathrm{m/s}]$ | $E_0$ [eV] | $\alpha  [\mathrm{m/s}]$ |  |  |  |
|--|--|-----------------------|------------|--------------------------|--|--|--|
| Seeded molecular $H_2$ beams, $T_S = 120K$           |  |                       |            |                          |  |  |  |
| 1740   | 19.9   | 3923                  | 0.160      | 1105                     |  |  |  |
| 1740   | 28.1   | 4892                  | 0.250      | 1105                     |  |  |  |
| 1740   | 38.0   | 5906                  | 0.364      | 945                      |  |  |  |
| 2000   | 18.2   | 3857                  | 0.155      | 995                      |  |  |  |
| 2000   | 25.1   | 4625                  | 0.223      | 1032                     |  |  |  |
| 2000   | 44.1   | 6431                  | 0.432      | 886                      |  |  |  |
| Seeded m   | Seeded molecular $D_2$ beams, $T_S = 120K$       |                       |            |                          |  |  |  |
| 2100   | 62.6   | 5377                  | 0.829      | 649                      |  |  |  |
| 2100   | 69.2   | 5658                  | 0.860      | 717                      |  |  |  |
| 2100   | 80.1   | 6132                  | 0.849      | 830                      |  |  |  |
| Pure mol   | Pure molecular H <sub>2</sub> beam, $T_S = 120K$ |                       |            |                          |  |  |  |
| 1435   | 31.7   | 5417                  | 0.307      | 826                      |  |  |  |
| 1465   | 32.0   | 5446                  | 0.310      | 830                      |  |  |  |
| 1740   | 38.0   | 5906                  | 0.364      | 945                      |  |  |  |
| 1855   | 40.5   | 6139                  | 0.394      | 899                      |  |  |  |
| 2000   | 44.1   | 6431                  | 0.432      | 886                      |  |  |  |
| 2100   | 47.4   | 6674                  | 0.465      | 913                      |  |  |  |
| 2300   | 49.7   | 6590                  | 0.454      | 1351                     |  |  |  |
| Pure molecular H <sub>2</sub> beam, Rendulic and co. |  |                       |            |                          |  |  |  |
| 1118.07  | 25.1   | 3500                  | 0.12794    | 1996                     |  |  |  |
| 1331.89  | 29.9   | 3555                  | 0.13200    | 2342                     |  |  |  |
| 1438.82  | 32.3   | 3380                  | 0.11932    | 2611                     |  |  |  |
| 1501.19  | 35.7   | 3151                  | 0.10371    | 2819                     |  |  |  |
| 1581.35  | 35.5   | 3219                  | 0.10816    | 2903                     |  |  |  |

 $J \in [0,7]$  for  $\nu = 1$ , respectively, and  $m_J \in [0,J]$ .

The rotational quadrupole alignment parameter as a function of  $\nu$  and J is a measure of the extent to which the reaction depends on the orientation of the molecule. The rotational quadrupole alignment parameter is calculated from the fully-state-resolved reaction probability as follows<sup>79</sup>

$$A_0^{(2)}(\nu, J) = \frac{\sum_{m_J=0}^J (2 - \delta_{m_J,0}) P_r(\nu, J, m_J) \left( \frac{3m_J^2}{J(J+1)} - 1 \right)}{\sum_{m_J=0}^J (2 - \delta_{m_J,0}) P_r(\nu, J, m_J)}.$$
 (4.14)

## 4.3 Results and discussion

#### 4.3.1 Fully-state-resolved reaction probabilities

In order to highlight the difference between a QD and QCT treatment of the  $\rm H_2$  +  $\rm Cu(211)$  system we first present initial-state-resolved reaction probabilities in figure 4.2a, 4.2b and 4.2c. QD calculations have been performed for a large number of rovibrational states. All input parameters can be found in table 4.1. The biggest differences between QD and QCT calculations at the fully-state-resolved level are observed for the lowest rovibrational states, as shown in figure 4.2b and 4.2c. The differences get increasingly smaller with increasing J for J>1. From QCT data at higher translational energies that are not shown in this figure it is clear that all states converge towards an asymptotic maximum reaction probability which depends slightly on the rovibrational state with respect to the maximum reaction probability. We note that for very high J, J>10 (not shown here), QD predicts a marginally smaller (less then 2%) asymptotic maximum reaction probability, while figure 4.2c suggest the opposite is true for the vibrational ground state and the first vibrationally excited state.

Figure 4.2b shows the largest discrepancy between the QCT and QD calculations observed. Here  $|m_J| = J$  pertains to a 'helicoptering' H<sub>2</sub> molecule, and  $m_J = 0$  to a 'cartwheeling' H<sub>2</sub> molecule rotating in a plane perpendicular to the surface. The preference for reacting parallel to the surface (i.e.  $m_J = J$  having a higher reaction probability then  $m_J = 0$ ) is bigger for QD calculations than for QCT calculations. This difference is negligible however when looking at degeneracy averaged reaction probabilities, which are shown in figure 4.2a. This also holds for the states not shown here. When looking at degeneracy averaged reaction probabilities, the agreement between the QCT and QD method is excellent.

In the calculations no evidence of the "slow channel" reactivity reported by Kaufmann et al.<sup>46</sup> in their very recent paper is observed, i.e. of reaction at low translational energies. It can now be ruled out that quantum effects during the dynamics are the source of this slow channel reactivity, in which reaction supposedly is inhibited by translational- and promoted by vibrational energy<sup>46</sup>. When looking at the individual rovibrational states that exhibit the biggest difference in reactivity between QD and QCT calculations, no evidence of the slow reaction channel is present in our results. The translational energy range sampled in our calculations should overlap with the translational energy range where the slow channel is reported to be active by Kaufmann et al.<sup>46</sup>. We therefore propose that the observed slow reaction channel must originate

from surface motion at a very high surface temperature (923K), which has not been incorporated into our QD calculations and is challenging to incorporate in QCT calculations<sup>80</sup>.

#### 4.3.2 Rotational quadrupole alignment parameters

As might be suspected from figure 4.2b from the larger preference for a parallel reaction orientation for J=1, calculated rotational quadrupole alignment parameters show a large difference between QCT and QD calculations for the J=1 states shown there. However, here we will now focus on rotational quadrupole alignment parameters for two particular rovibrational states of  $H_2$ :  $(\nu=0,J=7)$  and  $(\nu=1,J=4)$  (figure 4.3a), and  $D_2$ :  $(\nu=0,J=11)$  and  $(\nu=1,J=4)$  (figure 4.3b). These two sets of states were selected because they are very similar in rotational energy to the two rovibrational states for which rotational quadrupole alignment parameters for  $D_2$  desorbing from Cu(111) have been measured experimentally  $^{17}$  and studied theoretically using the BOMD method  $^{33}$ . Results for both states of  $D_2$  reacting on Cu(111) have been included in figure 4.3b. Note that a positive  $A_0^{(2)}(\nu,J)$  indicates a preference for a parallel reaction orientation, a negative value indicates a preference for a perpendicular orientation, and zero means the reaction proceeds independent of orientation.

We observe that the predicted rotational quadrupole alignment parameters eventually tend to zero with increasing translational energy, as all molecules irrespective of orientation will have enough energy to traverse the barrier. It is also clear that for  $H_2$  ( $\nu=0,J=7$ ) the agreement between QCT and QD calculations is excellent. The slight deviations at the lowest translational energies can be attributed to noise in the very low reaction probabilities of the underlying individual states.

The increase of the rotational quadrupole alignment parameter with decreasing translational energy, for the  $H_2$  ( $\nu = 0, J = 7$ ) and  $D_2$  ( $\nu = 0, J = 11$ ) states, is comparable to what is reported in the literature for  $H_2$  and  $D_2$  associatively desorbing from Cu(111) and  $Cu(100)^{17,31-33}$ . This monotonic increase of the rotational quadrupole alignment parameter with decreasing translational energy can be explained by a static effect of orientational hindering, in which slow- or non-rotating molecules will scatter when their initial orientation does not conform to the lowest barrier geometry<sup>32</sup>. Specifically, the molecule must be in favourable orientation to begin with in order to react, especially with the energy available to reaction being close to the threshold energy.

The blue lines in figure 4.3a correspond to the  $(\nu = 1, J = 4)$  rovibrational state of H<sub>2</sub> and in figure 4.3b to the  $(\nu = 1, J = 6)$  rovibrational state of D<sub>2</sub>.

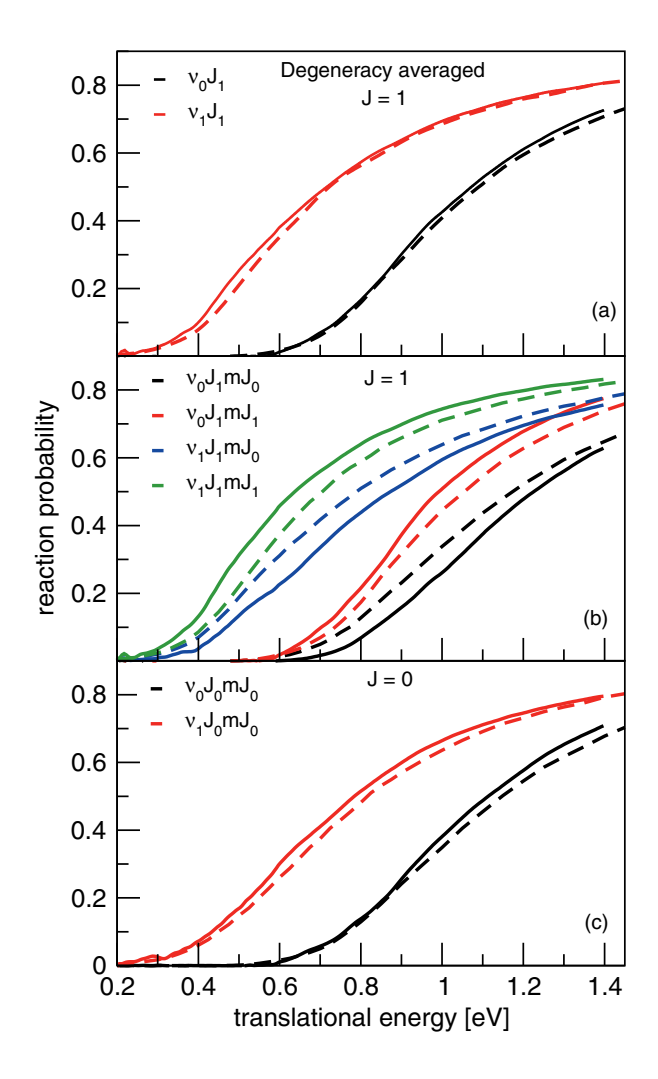


FIGURE 4.2: Reaction probability computed with QD calculations (solid lines) and QCT calculations (dashed lines) for normal incidence. Panel (a) shows degeneracy averaged reaction probabilities for J=1 for both the ground state and the first vibrationally excited state. Panel (b) shows the reaction probability obtained for the  $m_J=0,1$  states belonging to J=1 for both the ground state and the first vibrationally excited state. Panel (c) shows the reaction probability for the J=0 state for both the ground state and the first vibrationally excited state as well.

In contrast to the previously described states ( $\nu=0$ ,high J), the rotational quadrupole alignment parameter now first increases with increasing translational energy until reaching a maximum around 0.43 eV for H<sub>2</sub> and 0.52 eV for D<sub>2</sub> before decreasing towards zero with increasing translational energy. From figure 4.3 it is clear that around the maximum the agreement between the QD and QCT calculations is not as excellent for H<sub>2</sub> than for D<sub>2</sub>, although the agreement is still good.

The downturn of the rotational quadrupole alignment parameter with decreasing translational energy seen here for  $D_2$  and  $H_2$  in their ( $\nu=1$ ) states colliding with Cu(211) was not observed for  $D_2$  desorbing from Cu(111) for which, as can be seen in figure 4.3b, only a monotonous increase with decreasing translational energy has been reported<sup>17,33</sup>. A slight downturn of the rotational quadrupole alignment parameters has been predicted for vibrationally excited  $H_2$  reacting on  $Cu(100)^{31,32}$ , although the downturn was too small to lead to a negative rotational quadrupole alignment parameter. Because the behavior predicted for ( $\nu=1$ ) hydrogen colliding with Cu(211) qualitatively differs from that observed previously for Cu(111) and Cu(100), we will now first attempt an explanation for the dependence of the rotational quadrupole alignment parameter on incidence energy that we predict for  $D_2$  ( $\nu=1, J=6$ ), and then discuss the case  $D_2$  ( $\nu=0, J=11$ ).

From the literature it is known that the behavior of the rotational quadrupole alignment parameter as a function of incidence energy can be related to features of the molecule-surface interaction at the preferred reaction site of the molecule, for the initial rovibrational state considered<sup>32</sup>. For example, vibrationally excited  $H_2$  with a translational energy close to the threshold to reaction was found to prefer to react on a top site of Cu(100) due to features in the PES being more favorable, for instance, the increased lateness of the barrier at this site allowed more efficient conversion of energy from vibration to motion along the reaction path<sup>32,38,39</sup>. Next, the dependence of the rotational quadrupole alignment parameter on incidence energy of vibrationally excited  $H_2$  on Cu(100) could be explained on the basis of the anisotropy of the molecule-surface interaction energy at the top site. In our explanation of the behavior seen for  $H_2$  and  $D_2$  on Cu(211), we will therefore proceed in a similar manner.

Figure 4.4a shows the reaction density of  $D_2$  ( $\nu=1,J=6$ ) extracted from QCT calculations projected onto the Cu(211) unit cell. Here we focus specifically on the  $D_2$  ( $\nu=1,J=6$ ) rovibrational state because it has been experimentally measured on Cu(111)<sup>17</sup>, but the same mechanism appears to be present in our data for  $H_2$  ( $\nu=1,J>2$ ). All reacted trajectories up to a translational energy of 0.35 eV have been included. It is immediately clear that molecules in this particular state prefer to react on the  $t_1$  top site<sup>47</sup>,

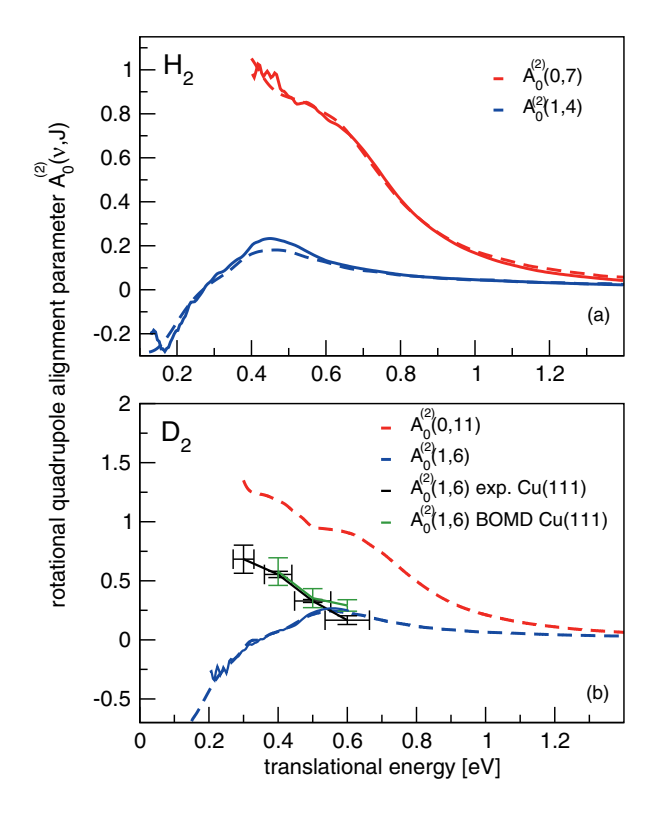


FIGURE 4.3: Panel (a) shows rotational quadrupole alignment parameters,  $A_0^{(2)}(\nu, J)$ , for two rovibrational states of H<sub>2</sub>:  $(\nu = 0, J = 7)$  and  $(\nu = 1, J = 4)$ . Panel (b) shows rotational quadrupole alignment parameters for two rovibrational states of D<sub>2</sub>:  $(\nu = 0, J = 11)$  and  $(\nu = 1, J = 6)$ . Solid lines correspond to QD calculations, dashed lines to QCT calculations. Panel (b) also shows experimental results for D<sub>2</sub> on Cu(111) (black)<sup>17</sup>, as well as BOMD results for D<sub>2</sub>  $(\nu = 1, J = 6)$  on Cu(111) (green)<sup>33</sup>.

which in the case of Cu(211) is at the step, with small outliers in reactivity pointing towards the bottom of the step. The  $t_1$  barrier is an extremely late barrier ( $r_{t_1} = 1.44 \text{ Å}$ ), as can be seen in table 3 of ref<sup>47</sup>. The very late barrier allows for efficient conversion of vibrational energy to motion along the reaction coordinate<sup>11,12,41</sup>.

Figure 4.5 shows a representative reactive trajectory of  $D_2$  ( $\nu = 1, J =$  $6, m_J = 0$ ) with a translational energy of 0.3 eV, and plots the classical angular momentum,  $J_C$ , as a function of the propagation time.  $J_C$  is decreased before reaching the barrier, and a minimum in  $J_C$  is reached at the transition state, where r becomes equal to 1.44 Å corresponding to the  $t_1$  barrier<sup>47</sup>. In the majority of the reacted trajectories the minimum of  $J_C$  is reached when r reaches the value of the  $t_1$  transition state, even when the molecule would make one or more bounces on the surface. This is a clear indication that rotational de-excitation takes place before the molecule reaches the transition state. This suggests that the reaction proceeds through rotational inelastic enhancement<sup>32</sup>, i.e., the reaction is promoted by rotational energy flowing to the reaction coordinate. The bump in  $J_C$  (i.e. its increase) still relatively far away from the surface is a feature that is also present in the majority of reactive trajectories. It is not completely clear to us what the cause is of this increase of  $J_C$  still relatively far away from the surface before proceeding towards the transition state. We speculate that the increasing vicinity to the surface turns on the anisotropy of the molecule-surface interaction, thereby coupling rotational motion and stretching motion, and providing a mechanism for the rotational energy to remain more constant while the bond extends and compresses due to the molecular vibration. This mechanism could consist in the classical angular momentum increasing when the bond extends, to offset the effect of the bond extension on the rotational constant (upon bond extension the rotational constant decreases and if not compensated this would decrease the rotational energy). This could possibly explain the hump observed in  $J_C$ at  $t \approx 4500$  atomic units of time in figure 4.5.

There is also indirect evidence for rotationally enhanced reaction of  $D_2$  ( $\nu=1,J=6,m_J=0$ ) in our QD calculations. Figure 4.6a shows inelastic scattering probabilities for  $D_2$  ( $\nu=1,J=6,m_J=0$ ) and figure 4.6b shows inelastic scattering probabilities for  $D_2$  ( $\nu=1,J=6,m_J=6$ ). From a pairwise comparison of data with the same color between figure 4.6a and figure 4.6b it is clear that  $D_2$  ( $\nu=1,J=6,m_J=0$ ) has a considerably higher probability to rotationally de-excite in the scattering process compared to  $D_2$  ( $\nu=1,J=6,m_J=6$ ). This suggests that the reaction of ( $\nu=1,J=6,m_J=0$ ) is also rotationally enhanced in the quantum dynamics if the de-excitation occurs

before the barrier is reached and the released rotational energy is transferred to motion along the reaction coordinate.

There are four possible mechanisms that affect the reaction probability and may affect the rotational quadrupole alignment parameters, two enhancing mechanisms and two steric hindering mechanisms<sup>32</sup>. Here we have focused on one enhancement mechanism, inelastic rotational enhancement, since the evidence presented in figures 4.5, 4.6a and 4.6b is consistent with this mechanism. Inelastic rotational enhancement requires reaction to take place on a site with a low anisotropy in  $\phi$  and a large anisotropy in  $\theta$  at the barrier<sup>32</sup>. The main reasons for proposing the presence of this mechanism are the sharp downturn of the quadrupole alignment parameters for ( $\nu = 1, J > 2$ ) rovibrational states in figure 4.3a and 4.3b and the rotational de-excitation seen in figures 4.5, 4.6a and 4.6b. We note that inelastic rotational enhancement is the only mechanism that predicts a lowering of the rotational quadrupole alignment parameters<sup>32</sup>. A complete overview of the four mechanisms and what features of the PES they depend on can be found in table 3 of ref.<sup>32</sup>.

A feature of the  $t_1$  site that facilitates the conversion of rotational energy to motion along the reaction coordinate is a low anisotropy of the potential in  $\phi$  combined with a large anisotropy in  $\theta$ . Figure 4.7 shows the anisotropy at the  $t_1$  barrier<sup>47</sup> (r and Z are kept constant here), the top panel shows the anisotropy in  $\phi$  and the bottom panel shows the anisotropy in  $\theta$ . It is clear that the anisotropy in  $\theta$  is substantial, while the anisotropy in  $\phi$  is very small compared to the anisotropy in  $\theta$ . Somers et al.<sup>32</sup> have shown that the high anisotropy in  $\theta$  may facilitate inelastic rotational enhancement. Inelastic rotational enhancement is expected to be most effective for low  $|m_J|$  states with J > 2, and the mechanism would lead to decreased rotational quadrupole alignment parameters<sup>32</sup>. The reason for the decrease in the rotational quadrupole alignment parameters is that  $m_J$  is approximately conserved, so that a decrease in J, which can promote reaction through rotationally inelastic enhancement, is possible only for low  $|m_J|$ .

It is also clear from figure 4.3b that from the point of view of the orientational dependence of reaction Cu(211) cannot be described as a combination of (100) steps and (111) terraces. The monotonic increase of the rotational quadrupole alignment parameter for  $D_2$  reacting on  $Cu(111)^{17,33}$  is very similar to the behavior reported for  $Cu(100)^{31,32}$ . A slight downturn at translational energies close to the threshold to reaction has been reported in the case of Cu(100), indicating that the inelastic rotational enhancement mechanism is taking place. The downturn is however small and does not lead to negative quadrupole alignment parameters as we show here for  $H_2$  and  $D_2$  reacting on Cu(211). This is a clear indication that the reaction dynamics of the Cu(211)

surface is distinct from the reaction dynamics of its component Cu(111) terraces and Cu(100) steps when looked at individually. This is most likely because the energetic corrugation of the Cu(211) surface is much lower compared to Cu(111) and Cu(100), a feature that favors the reaction of vibrationally excited molecules if sites with late barriers are present.

We now turn to an explanation for the monotonic decrease of the rotational quadrupole alignment parameter predicted for the  $(\nu = 0, \text{ high } J)$  states of H<sub>2</sub> and D<sub>2</sub> colliding with Cu(211) in figure 4.3a and 4.3b. No downturn of the rotational quadrupole alignment parameter is observed for the  $(\nu = 0)$ states even though  $D_2$  ( $\nu = 0, J = 11, m_J = 11$ ) reacts at the step as well as  $D_2$  ( $\nu = 1, J = 6$ ), as can be seen in figure 4.4b. The lack of a downturn in the rotational quadrupole alignment parameter arises because the  $D_2$  ( $\nu = 0$ ) states react using a different mechanism. Figure 4.8 shows a representative reactive trajectory of  $D_2$  ( $\nu = 0, J = 11, m_J = 11$ ), and it is clear that the angular momentum only drops after the transition state has been reached. This is a clear combination of elastic rotational enhancement for the helicopter molecules together with orientational hindering for the cartwheeling molecules which causes the increase of the rotational quadrupole alignment parameters of the  $(\nu = 0)$  molecules<sup>32</sup>. We note that D<sub>2</sub>  $(\nu = 0, J = 11)$  reacting on the step at the  $t_1$  site is due to the high initial rotational quantum number. The  $t_1$ barrier is slightly higher in energy than the lowest barrier to reaction but at this site the reaction is less rotationally hindered if the molecule rotates in a plane parallel to the surface, and the barrier is much later than at the lowest  $b_2$ site on the terrace. This allows molecules in the vibrational ground state that are rotating fast in helicopter fashion and have incidence energies close to the threshold to reaction to react there, by converting rotational energy to motion along the reaction path as the bond extends and the rotational constant of the molecule drops, while J remains roughly the same.

Above, we have shown that  $D_2$  in its ( $\nu = 0, J = 11$ ) and ( $\nu = 1, J = 6$ ) states prefers to react near the  $t_1$ -site, i.e., on or near the steps (see figure 4.4a and 4.4b). This might seem to contradict an earlier conclusion, that at low incidence energies  $D_2$  prefers to react on the terrace<sup>47</sup>. However, this conclusion was based on molecular beam experiments and simulations of those experiments, and under the conditions addressed<sup>47</sup> the ( $\nu = 0, J = 11$ ) and ( $\nu = 1, J = 6$ ) states would hardly have population in them. A more appropriate picture of the reaction probability density for molecules under the conditions of ref.<sup>47</sup> is shown in figure 4.4c. There it can be seen that  $D_2$  ( $\nu = 0, J = 2$ ) (this state would be highly populated in the beams used and simulated in Ref.<sup>47</sup>) prefers to react at the terrace  $b_2$  site, which has the lowest barrier to reaction.

The reaction density for  $D_2$  ( $\nu = 0, J = 2$ ) is in line with earlier findings that molecules in the vibrational ground state with low J react at the lowest barrier to reaction<sup>32,38,39</sup>, and with the findings for  $D_2 + Cu(211)$  of ref.<sup>47</sup>.

Kaufmann et al.<sup>46</sup> did not measure rotational quadrupole alignment parameters in their recent study. We believe that the downturn of the rotational quadrupole alignment parameter at low incidence energies, which has not been observed before with this large downward shift for both  $H_2$  and  $D_2$  reacting on copper, may well be experimentally verified for both isotopes on Cu(211). Specifically, the reaction probability of  $H_2$  and  $D_2$  is large enough, and the  $(\nu=1,J=4)$  rovibrational state of  $H_2$  and the  $(\nu=1,J=6)$  of  $D_2$  have large enough Boltzmann weights at reasonable surface temperatures (923K) to make the downturn measurable. Comparing experimental rotational quadrupole alignment parameters to theoretical ones will provide a very stringent, and detailed way of testing the accuracy of the electronic structure calculations used in the construction of the PES.

#### 4.3.3 Comparing to experimental $E_0(\nu, J)$ parameters

Next we will make a direct comparison with the state-specific, or degeneracy averaged, reaction probabilities reported by Kaufmann et al. 46 From their experiments they could derive dissociative adsorption probabilities by applying the principle of detailed balance to the measured time-of-flight distributions. However, comparing the relative saturation value of the reaction probability obtained from associative desorption experiments to the zero coverage absolute saturation values predicted by theory is not straightforward. The authors of the experimental paper pose several ways of scaling the experimental data in order to make a comparison to theoretical work possible. Scaling the experimental data to experimental molecular adsorption results introduces the uncertainties related to the direct molecular adsorption experiment used as a reference in this process. Theory calculates sticking probabilities in the zero coverage limit. When scaling the experimental desorption data to experimental adsorption data the zero coverage limit will only be a lower bound, especially when a molecular beam experiment with a very broad translational energy distribution is chosen as a reference. (Note that in section 5.2.6 of Chapter 5 a more exhaustive disccusion is presented on the different methods to compare theory to experimental  $E_0(\nu, J)$  parameters.)

We opt for the simplest and most direct method to scale to the relative experimental associative desorption data. In order to compare to the experimental  $E_0(\nu, J)$  parameters, where  $E_0(\nu, J)$  is the translational energy for which the

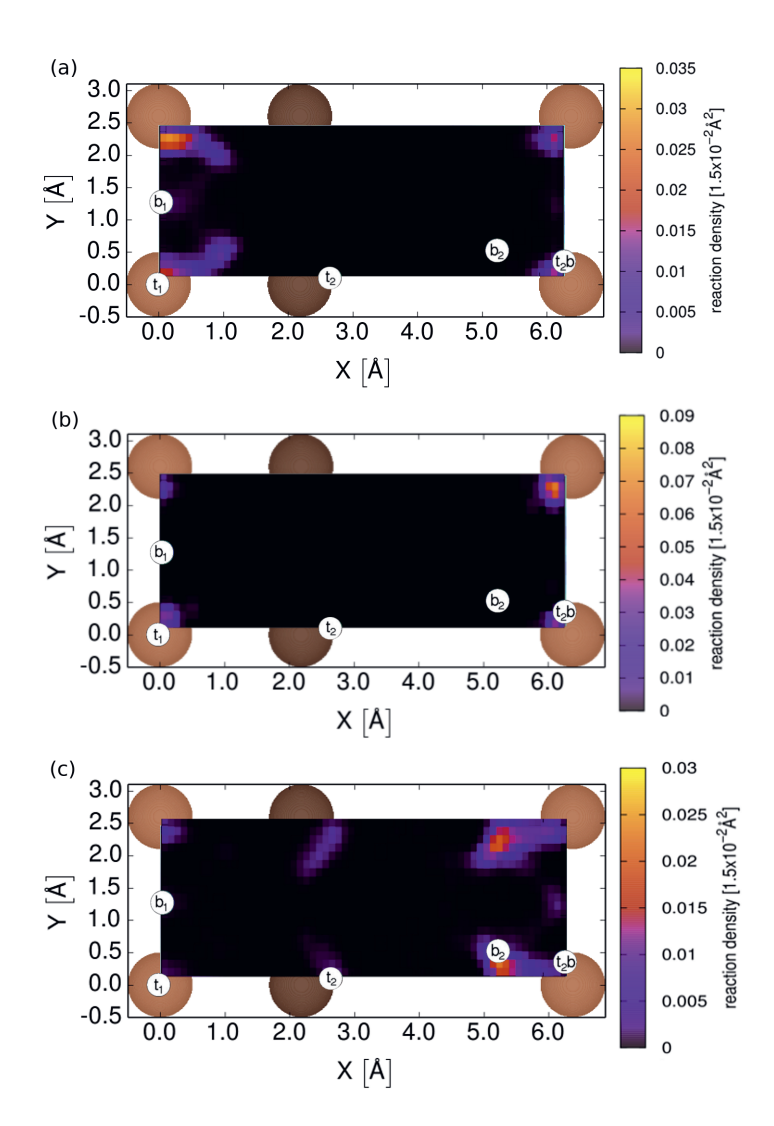


FIGURE 4.4: Three plots of the reaction probability density of  $D_2$  projected onto the Cu(211) unit cell. Panel a shows the reaction density of  $D_2$  ( $\nu=1,J=6$ ); all reacted trajectories up to a translational energy of 0.35 eV are included. Panel b shows the reaction density of  $D_2$  ( $\nu=0,J=11$ ); all reacted trajectories up to a translational energy of 0.35 eV are included. Panel c shows the reaction density of  $D_2$  ( $\nu=0,J=2$ ); all reacted trajectories up to a translational energy of 0.65 eV are included.

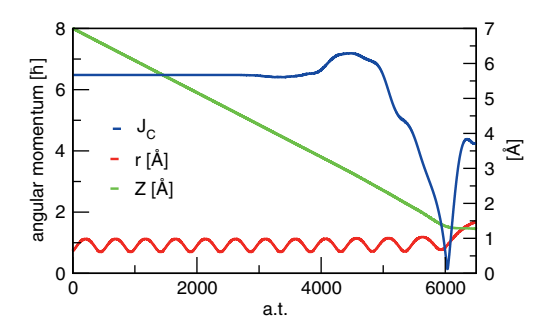


FIGURE 4.5: A single representative reactive trajectory of  $D_2$  ( $\nu = 1, J = 6, m_J = 0$ ) with a translational energy of 0.3 eV. The blue curve shows the angular momentum  $(J_C)$ , the red curve shows the bond length (r), and the green curve shows the center of mass distance to the surface (Z).

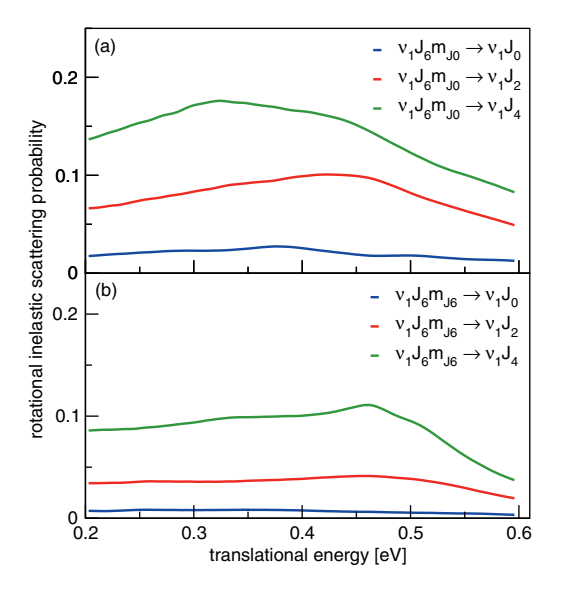


FIGURE 4.6: Rotationally inelastic scattering probabilities for  $D_2$  for two different inital rovibrational states as a function of translational energy. Panel (a) shows rotationally inelastic scattering probabilities for  $D_2$  ( $\nu = 1, J = 6, m_J = 0$ ), panel (b) shows rotationally inelastic scattering probabilities for  $D_2$  ( $\nu = 1, J = 6, m_J = 6$ ). Colors correspond to the final rovibrational state of the molecule, with blue being for ( $\nu' = 1, J' = 0$ ), red being for ( $\nu' = 1, J' = 2$ ), and green being for ( $\nu' = 1, J' = 4$ ).

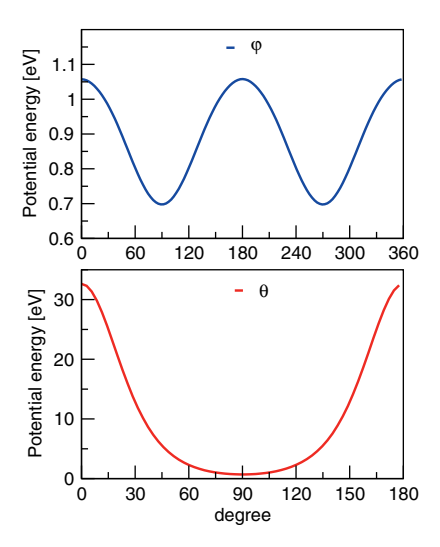


FIGURE 4.7: The anisotropy of the interaction potential at the t1 top site barrier<sup>47</sup> is shown for  $\theta$  (bottom panel) and  $\phi$  (top panel).

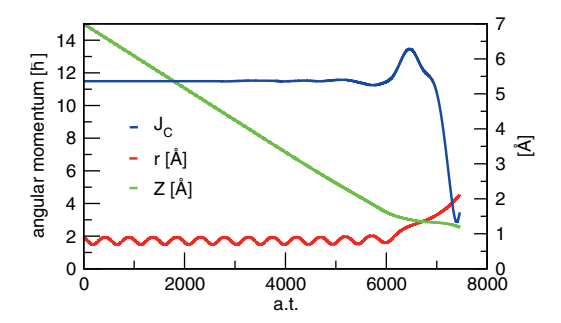


FIGURE 4.8: A single representative reactive trajectory of  $D_2$  ( $\nu=0, J=11, m_J=11$ ) with a translational energy of 0.3 eV. The blue curve shows the angular momentum  $(J_C)$ , the red curve shows the bond length (r), and the green curve shows the center of mass distance to the surface (Z).

reaction probability of the  $(\nu, J)$  state is half of the maximum reaction probability measured for that  $(\nu, J)$  state, we use the reported maximum translational energy sensitivity presented in tables S7 and S9 of ref.<sup>46</sup> Theoretical  $E_0(\nu, J)$  are taken to be the translational energy to which the reaction probability is half that of the reaction probability at the maximum translational energy for which the experiment is sensitive. This method also corresponds to what is showcased in figure 13a of ref.<sup>46</sup> Note that in section 2.4.3 the method described here to make a comparison to experimental effective barrier heights is denoted as method B1.

Figure 4.9 shows  $E_0(\nu, J)$  parameters for H<sub>2</sub> and D<sub>2</sub> reacting on Cu(211). The agreement between theory and experiment is excellent for  $H_2$ . We calculated mean absolute and mean signed deviations between the experimental and theoretical  $E(\nu, J)$  parameters, see table 4.3. It is clear from figure 4.9 and table 4.3 that the agreement between theory and experiment is excellent in the case of  $H_2$ , for which the total mean absolute deviation (MAD)  $(n^{-1}\sum_n |E_{0,exp}-E_0|)$ and mean signed deviation (MSD)  $(n^{-1}\sum_{n}E_{0,exp}-E_{0})$  values for QD and QCT calculations fall within chemical accuracy. We note that for H<sub>2</sub> the agreement is best for vibrationally excited molecules, while the reverse is true with respect to  $D_2$ . For  $D_2$  the agreement is not yet within chemical accuracy, mainly due to the slightly bigger discrepancies between theory and experiment for the first vibrationally excited state. Theory, however, does not reproduce the rotational hindering that can be seen in the experimental data, i.e.  $E_0(\nu, J)$ does not first increase with J until a maximum before falling off with increasing J. Theory shows no such behavior, here the  $E_0(\nu, J)$  parameter falls off with increasing J for all methods investigated here.

Experiments on associative desorption of  $H_2$  from  $Cu(111)^{19,46}$  and of  $D_2$  from  $Cu(111)^{16,33,46}$  likewise found the rotational hindering effect on reaction for low J. As for  $H_2$  and  $D_2$  interacting with Cu(211), we have not been able to reproduce this subtle effect in calculations on  $H_2 + Cu(111)^{35,36}$  and  $D_2 + Cu(111)^{33,35}$  in electronically adiabatic dynamics calculations. Here we find that MDEF calculations on  $H_2$  and  $D_2 + Cu(211)$  do not reproduce the trend either, suggesting that in the previous calculations the neglect of electron-hole pair excitation was not the cause of the discrepancy between theory and experiment. However, it is possible that calculations modeling electron-hole pair excitation with orbital-dependent friction (ODF) will succeed in recovering the subtle trend observed in experiments. For this, it may well be necessary that the ODF coefficients explicitly model the dependence of the tensor friction coefficients on the molecule's orientation angles; earlier MDEF calculations on  $H_2 + Cu(111)$  using ODF coefficients did not yet do this<sup>26</sup>.

According to figure 4.9, the reactivity measured experimentally in the

associative desorption experiments is, for most  $(\nu, J)$  states, larger than that predicted theoretically, with the experimental  $E_0(\nu, J)$  being lower. With the use of the same scaling method to relate theory to experiment, Kaufmann et al.<sup>46</sup> obtained the same result for H<sub>2</sub> and D<sub>2</sub> reacting on Cu(111), and also in their case they compared with theory on the SRP48 functional<sup>33</sup>. To some extent these results are odd, as calculations for H<sub>2</sub> and D<sub>2</sub> + Cu(111) using the original SRP functional showed that the theory overestimated the experimentally measured sticking coefficients<sup>36</sup>. However, also in this work theory generally underestimated the reactivity measured in associative desorption experiments<sup>36</sup>.

The paradox noted above may be explained on the basis of the BOSS model used in the calculations. This model neglects the effect of ehp excitation. Modeling this effect on sticking experiments should lower the theoretical reactivity, with computed sticking curves shifting to higher energies. Modeling the effect on associative desorption experiments should show the opposite effect, if the modeling is done correctly, i.e., starting with molecules being formed at the transition state and then desorbing<sup>36,81</sup>. The effect of ehp excitation in such calculations should lead to translational energy distributions of desorbed molecules being shifted to lower translational energies. The reaction probability curves obtainable from these distributions by assuming detailed balance (which, strictly speaking, is not applicable if ehp excitation is active) should then lead to computed reaction probability curves ( $E_0(\nu, J)$  values) shifted towards lower energies, in better agreement with experiment (see figure 4.9).

The above also explains why our present MDEF calculations led to decreased agreement with experiment: In these calculations we modeled the associative desorption experiment as an initial-state selected dissociative chemisorption experiment, in which ehp excitation should have the opposite effect. If we assume the ehp excitation to have an effect that is similar in magnitude, but opposite in sign with respect to the QCT calculations, the net effect of modeling ehp excitation is to increase the agreement with experiment to the extent that chemical accuracy is obtained for both ( $\nu = 0$ ) and ( $\nu = 1$ ) H<sub>2</sub> on Cu(211). This is illustrated by the MDEF\* mean absolute and mean signed deviations in table 4.3. The MDEF\* values have been calculated by subtracting the difference between the MDEF and QCT values from the QCT values. We finally note that we have assumed that surface temperature does not much affect the measured  $E_0(\nu, J)$  through surface atom vibrational motion, which is in line with experiments<sup>24,25</sup>, as discussed in the supporting information of Díaz et al.<sup>36</sup>.

|       | MAD [eV] H <sub>2</sub> |           |           | $MSD [eV] H_2$ |           |           |  |
|-------|-------------------------|-----------|-----------|----------------|-----------|-----------|--|
|       | total                   | $\nu = 0$ | $\nu = 1$ | total          | $\nu = 0$ | $\nu = 1$ |  |
| QCT   | 0.0362                  | 0.0384    | 0.0289    | 0.0209         | 0.0384    | -0.0044   |  |
| QD    | 0.0362                  | 0.0449    | 0.0235    | 0.0241         | 0.0449    | -0.006    |  |
| MDEF  | 0.0509                  | 0.0531    | 0.0272    | 0.0342         | 0.0532    | 0.0069    |  |
| MDEF* | 0.0239                  | 0.0237    | 0.0306    | 0.0076         | 0.0236    | -0.0157   |  |
|       | MAD [eV] D <sub>2</sub> |           |           | $MSD [eV] D_2$ |           |           |  |
|       | total                   | $\nu = 0$ | $\nu = 1$ | total          | $\nu = 0$ | $\nu = 1$ |  |
| QCT   | 0.0485                  | 0.0354    | 0.0675    | 0.0485         | 0.0354    | 0.0675    |  |

Table 4.3: Mean absolute and mean signed deviations for the theoretical  $E_0(\nu, J)$  parameters are compared to the experimental values shown in figure 4.9.

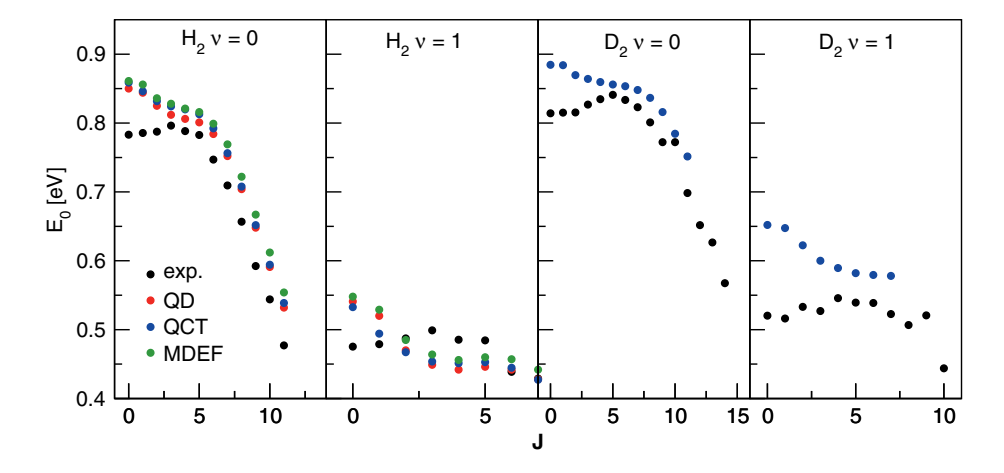


FIGURE 4.9:  $E_0(\nu, J)$  parameters as a function of J for H<sub>2</sub> and D<sub>2</sub> reacting on Cu(211). Blue dots represent QCT results, red dots QD results, green dots MDEF results, and black dots experimental results<sup>46</sup>.

#### 4.3.4 Classical molecular beam simulations

One of the goals of this project was to carry out a molecular beam simulation using the QD method. Since surface atom motion and ehp excitations cannot be incorporated in QD calculations we have also performed molecular beam simulations using the BOMD, QCT and MDEF methods for  $D_2$  impinging on Cu(211) in order to quantify their effects on the reactivity measured in a molecular beam experiment. As discussed together with the comparison between our state resolved reaction probabilities and the associative desorption experiments of Kaufmann et al.<sup>46</sup> there are some effects on the reactivity from surface atom motion and ehp excitations though the effect falls within chemical accuracy. The molecular beam experiments we treat here were carried for a surface temperature of  $120K^{16,35}$ .

In figure 4.10 we compare BOMD calculations performed for a surface temperature of 120K (red) to QCT (black) and MDEF (green) calculations carried out on our six-dimensional PES. As an additional validation of the PES we have also calculated one energy point using the BOMD method with a rigid surface (blue). Each BOMD point is based on five hundred trajectories, each QCT and MDEF point on a hundred thousand trajectories. The molecular beam parameters were taken from refs<sup>16,36</sup> and can be found in table 4.2. From the excellent agreement in figure 4.10 between the black and blue data points at 80.1 kJ/mol it is clear that our PES was accurately fitted, as was previously demonstrated in figure S2 of ref<sup>47</sup>. There we showed that for the dynamically relevant region of the PES ( $V_{MAX} < 2\text{eV}$ ) the PES has a RMSE < 0.035 eV. Therefore results obtained from QD calculations performed on our PES should not be influenced much by any (small) lingering inaccuracies still present in the PES related to the fitting procedure. It can also be observed from figure 4.10 that the effect of surface motion is small, and well within the limits of chemical accuracy with respect to incidence energy. Due to the fact that H<sub>2</sub> has a lower mass, we expect the effect of including surface motion during the dynamics will be even less pronounced for  $H_2$  than for  $D_2$ . We should also note here that when low surface temperature experiments are considered, as with the 120K surface temperature here, it is known from the literature that the BOSS model works well for activated  $H_2$  dissociation on metals<sup>27,34,35,37,61</sup>.

It can also be seen from figure 4.10 that including the effect of ehp's as a classical friction force shifts the reaction probability curve slightly to higher energies, and that the effect is rather small and linear with respect to the average translational energy. From the literature it is also known that including ehp excitations in the dynamics of H<sub>2</sub> reacting on Cu(111) has only a marginal effect on the reaction probability <sup>26,33,37,82</sup>.

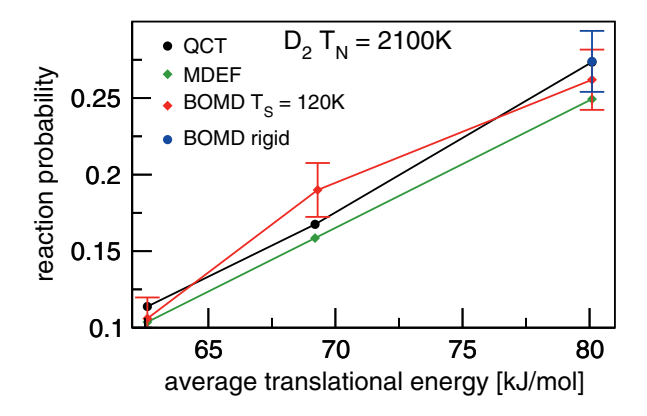


FIGURE 4.10: Reaction probability as function of the average translational energy for  $D_2$  on Cu(211), as computed with the molecular beam parameters of table 4.2. BOMD results for a surface temperature of 120K are shown in red, MDEF results are shown in green, and QCT results are shown in black. The blue point is a BOMD result for  $D_2$  on rigid Cu(211).

Due to the very small contribution of surface atom motion, and non-adiabatic effects incorporated in the MDEF calculations to the overall reaction probability, we pose that  $H_2$  impinging on Cu(211) is an excellent system to fully simulate a molecular beam experiment using quantum dynamics methods since large discrepancies between theory and experiment can reasonably be attributed to quantum effects during the dynamics, as the BOSS model should be quite accurate.

## 4.3.5 Quantum molecular beam simulations

Figure 4.11 shows results of simulations for four sets of molecular beam experiments, with varying molecular beam conditions. The experiment of Rendulic and coworkers<sup>15</sup> has the broadest translational energy distributions. The molecular beam parameters are taken from (the supporting information of) refs.  $^{16,35,36}$  Here, theoretical results obtained for the  $H_2 + Cu(211)$  system are compared to theoretical results for the  $H_2 + Cu(111)$  system, where for all theoretical results the SRP48 density functional was used. We only make a comparison to theoretical work since, to the best of our knowledge, there exists no published experimental molecular beam dissociative adsorption data for  $H_2$  reacting on Cu(211).

In order to make the best possible comparison between the QCT and QD results, both results are calculated from initial-state-resolved reaction

probabilities for the same set of initial states. The molecular beam reaction probabilities predicted by QCT and QD calculations are in excellent agreement (figure 4.11). The excellent agreement holds for the very broad molecular beams of Rendulic and coworkers in figure 4.11a, as well as for the translationally narrow molecular beams of Auerbach and coworkers<sup>16</sup> shown in figures 4.11b-d. However, QCT predicts slightly higher reaction probabilities, especially for the lowest translational energies. The consistently higher QCT reaction probability can be attributed to zero-point energy (ZPE) leakage, which is not possible by design in the QD calculations wherein the ZPE is preserved.

The excellent agreement between the QCT and QD calculations implies that on the scale of a molecular beam experiment, in which a large number of rovibrational states are populated, quantum effects during the dynamics affect the reaction probability only in a very limited manner for reaction probabilities > 0.1%. The similarity between the QCT and QD calculations also holds over a wide range of molecular beam conditions, ranging from high to low incidence energies and from high to low nozzle temperatures.

From figure 4.11 it is also clear that for most incidence energies (> 22 kJ/mol) Cu(211) is predicted to be less reactive then Cu(111), as was reported previously for  $D_2 + Cu(211)^{47}$ . The lower reactivity of Cu(211) compared to Cu(111) cannot be explained by the d-band model<sup>54,55</sup>. In our previous paper we and others showed that the d-band model does make accurate predictions of the reactivity of different facets when similar reaction geometries are considered but that the breakdown of the predictive prowess of the d-band model is caused by the geometric effect of the lowest barrier to reaction for  $H_2$  dissociation on the low index Cu(111) surface not being on a top site.

Based on the results in figure 4.11 we can now say definitively that, on the scale of a molecular beam experiment, neglect of quantum effects during the dynamics cannot be invoked to explain the lower reactivity of Cu(211) than of Cu(111). This corroborates the theoretical results obtained in previous work<sup>45,47</sup>, where QCT calculations were performed for  $D_2$  and  $H_2$ , and  $S_0$  were measured for  $D_2 + Cu(111)$  for  $E_i > 27$  kJ/mol. More generally we can state that molecular beam sticking of  $H_2$  on cold Cu(211) is well described with quasi-classical dynamics, and this very probably also holds for  $H_2$  reacting on Cu(111) and Cu(100).

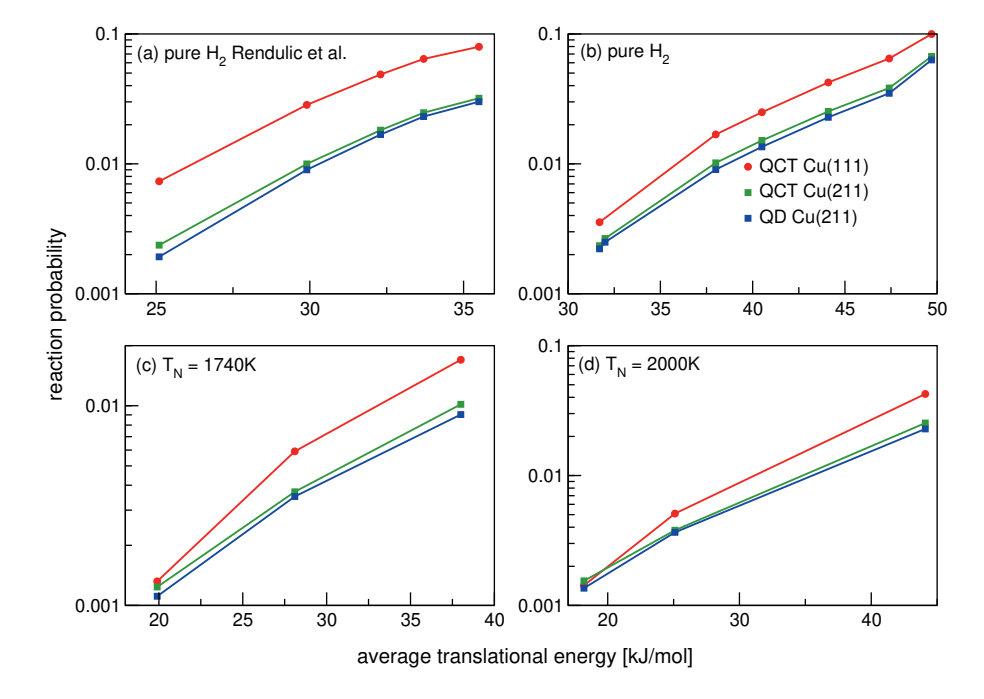


FIGURE 4.11: Comparison between four sets of molecular beam simulations for  $\rm H_2 + Cu(111)$  and  $\rm Cu(211)$ , using the SRP48 functional, and for normal incidence. Reactivity is shown as a function of average translational energy. The red dots correspond to QCT calculations for  $\rm H_2 + Cu(111)$ . The green and blue dots correspond to, respectively, the QCT and QD calculations for  $\rm H_2 + Cu(211)$ .

## 4.4 Conclusions

In this chapter a comprehensive study of the quantum reaction dynamics of  $H_2$  reacting on the Cu(211) surface has been carried out. A large number of TDWP calculations has been performed for all important individual rovibrational states reasonably populated in a molecular beam experiment. The main conclusion is that the reaction of  $H_2$  ( $D_2$ ) with Cu(211) is well described quasi-classically. This is especially true when simulating molecular beam experiments where one averages over a large number of rovibrational states and molecular beam energy distributions.

It is however found that the extent to which the reaction depends on the alignment of H<sub>2</sub> is somewhat dependent on whether QD or the QCT method is used, requiring a careful validation of the dynamical model depending on the type of experiment that is being simulated. The QD method predicts stronger alignment effects on the reactivity than the QCT method for low lying rotational states.

A comparison to recent associative desorption experiments suggests and BOMD calculations appear to show that the effect of surface atom motion and ehp's on the reactivity falls within chemical accuracy, even for the high surface temperature used in the associative desorption experiments. No evidence has been found in the fully-state-resolved data for the recently reported 'slow' reaction channel, even though we carried out calculations over a translational energy range were this reported reactivity should be manifest. It is speculated that the 'slow' reaction channel is related to surface atom motion and that its modelling requires the description of this motion, which is why we did not see it here.

In contrast to the theoretical and experimental results for  $D_2$  reacting on Cu(111) and Cu(100), at low translational energy we observe a sharp downturn of the rotational quadrupole alignment parameters for vibrationally excited molecules. This downturn can be attributed to a site specific reaction mechanism of inelastic rotational enhancement.

## References

(1) Smeets, E. W. F.; Füchsel, G.; Kroes, G.-J. Quantum dynamics of dissociative chemisorption of H<sub>2</sub> on the Stepped Cu(211) Surface. *J. Phys. Chem. C* **2019**, *123*, 23049–23063.

- (2) Wolcott, C. A.; Medford, A. J.; Studt, F.; Campbell, C. T. Degree of rate control approach to computational catalyst screening. *J. Catal.* **2015**, *330*, 197–207.
- (3) Sabbe, M. K.; Reyniers, M.-F.; Reuter, K. First-principles kinetic modeling in heterogeneous catalysis: an industrial perspective on best-practice, gaps and needs. *Catal. Sci. Technol.* **2012**, *2*, 2010–2024.
- (4) Ertl, G. Reactions at surfaces: from atoms to complexity (Nobel lecture). *Angew. Chem. Int. Ed.* **2008**, *47*, 3524–3535.
- (5) Waugh, K. Methanol synthesis. Catal. Today 1992, 15, 51–75.
- (6) Grabow, L.; Mavrikakis, M. Mechanism of methanol synthesis on Cu through CO<sub>2</sub> and CO hydrogenation. *Acs Catalysis* **2011**, *1*, 365–384.
- (7) Behrens, M.; Studt, F.; Kasatkin, I.; Kühl, S.; Hävecker, M.; Abild-Pedersen, F.; Zander, S.; Girgsdies, F.; Kurr, P.; Kniep, B.-L., et al. The active site of methanol synthesis over Cu/ZnO/Al<sub>2</sub>O<sub>3</sub> industrial catalysts. *Science* **2012**, *336*, 893–897.
- (8) Zambelli, T.; Wintterlin, J.; Trost, J.; Ertl, G. Identification of the active sites" of a surface-catalyzed reaction. *Science* **1996**, *273*, 1688–1690.
- (9) Somorjai, G.; Joyner, R.; Lang, B. The reactivity of low index [(111) and (100)] and stepped platinum single crystal surfaces. *Proc. Royal Soc. Lond. A.* **1972**, *331*, 335–346.
- (10) Kroes, G.-J. Toward a database of chemically accurate barrier heights for reactions of molecules with metal surfaces. J. Phys. Chem lett. 2015, 6, 4106–4114.
- (11) Polanyi, J. C. Some concepts in reaction dynamics. *Science* **1987**, *236*, 680–690.
- (12) Polanyi, J. C. Some concepts in reaction dynamics (Nobel lecture). *Angew. Chem.* **1987**, *26*, 952–971.
- (13) Šljivančanin, Ž.; Hammer, B. H<sub>2</sub> dissociation at defected Cu: preference for reaction at vacancy and kink sites. *Phys. Rev. B* **2002**, *65*, 085414.

- (14) Anger, G.; Winkler, A.; Rendulic, K. Adsorption and desorption kinetics in the systems  $H_2/Cu(111)$ ,  $H_2/Cu(110)$  and  $H_2/Cu(100)$ . Surf. Sci. **1989**, 220, 1–17.
- (15) Berger, H.; Leisch, M.; Winkler, A.; Rendulic, K. A search for vibrational contributions to the activated adsorption of H<sub>2</sub> on copper. *Chem. Phys. Lett.* **1990**, *175*, 425–428.
- (16) Michelsen, H.; Rettner, C.; Auerbach, D.; Zare, R. Effect of rotation on the translational and vibrational energy dependence of the dissociative adsorption of D<sub>2</sub> on Cu(111). J. Chem. Phys. 1993, 98, 8294–8307.
- (17) Hou, H.; Gulding, S.; Rettner, C.; Wodtke, A.; Auerbach, D. The stereodynamics of a gas-surface reaction. *Science* **1997**, *277*, 80–82.
- (18) Comsa, G.; David, R. The purely "fast" distribution of H<sub>2</sub> and D<sub>2</sub> molecules desorbing from Cu(100) and Cu(111) surfaces. *Surf. Sci.* **1982**, *117*, 77–84.
- (19) Rettner, C.; Michelsen, H.; Auerbach, D. Quantum-state-specific dynamics of the dissociative adsorption and associative desorption of H<sub>2</sub> at a Cu(111) surface. J. Chem. Phys. **1995**, 102, 4625–4641.
- (20) Rettner, C.; Michelsen, H.; Auerbach, D. Determination of quantum-state-specific gas—surface energy transfer and adsorption probabilities as a function of kinetic energy. *Chem. Phys.* **1993**, *175*, 157–169.
- (21) Gostein, M.; Parhikhteh, H.; Sitz, G. Survival probability of  $H_2$  ( $\nu = 1$ , J=1) scattered from Cu(110). *Phys. Rev. Lett.* **1995**, 75, 342.
- (22) Hodgson, A.; Samson, P.; Wight, A.; Cottrell, C. Rotational excitation and vibrational relaxation of  $H_2$  ( $\nu = 1$ , J = 0) Scattered from Cu(111). *Phys. Rev. Lett.* **1997**, 78, 963–966.
- (23) Watts, E.; Sitz, G. O. State-to-state scattering in a reactive system:  $H_2$  (v= 1, j= 1) from Cu(100). J. Chem. Phys. **2001**, 114, 4171–4179.
- (24) Rettner, C.; Auerbach, D.; Michelsen, H. Dynamical studies of the interaction of D<sub>2</sub> with a Cu(111) surface. J. Vac. Sci. Technol. A 1992, 10, 2282–2286.
- (25) Michelsen, H.; Rettner, C.; Auerbach, D. On the influence of surface temperature on adsorption and desorption in the D<sub>2</sub>/Cu(111) system. Surf. Sci. **1992**, 272, 65–72.
- (26) Spiering, P.; Meyer, J. Testing electronic friction models: vibrational de-excitation in scattering of H<sub>2</sub> and D<sub>2</sub> from Cu(111). *J. Phys. Chem. Lett.* **2018**, *9*, 1803–1808.

(27) Spiering, P.; Wijzenbroek, M.; Somers, M. An improved static corrugation model. *J. Chem. Phys.* **2018**, *149*, 234702.

- (28) Kroes, G.-J.; Wiesenekker, G.; Baerends, E.; Mowrey, R. Competition between vibrational excitation and dissociation in collisions of H<sub>2</sub> with Cu(100). *Phys. Rev. B* **1996**, *53*, 10397.
- (29) Kroes, G.-J.; Juaristi, J.; Alducin, M. Vibrational excitation of H<sub>2</sub> scattering from Cu(111): effects of surface temperature and of allowing energy exchange with the surface. J. Phys. Chem. C 2017, 121, 13617–13633.
- (30) Salin, A. Theoretical study of hydrogen dissociative adsorption on the Cu(110) surface. J. Chem. Phys. **2006**, 124, 104704.
- (31) Sementa, L.; Wijzenbroek, M.; Van Kolck, B.; Somers, M.; Al-Halabi, A.; Busnengo, H. F.; Olsen, R.; Kroes, G.-J.; Rutkowski, M.; Thewes, C., et al. Reactive scattering of H<sub>2</sub> from Cu(100): comparison of dynamics calculations based on the specific reaction parameter approach to density functional theory with experiment. J. Chem. Phys. **2013**, 138, 044708.
- (32) Somers, M.; McCormack, D.; Kroes, G.-J.; Olsen, R.; Baerends, E.; Mowrey, R. Signatures of site-specific reaction of H<sub>2</sub> on Cu(100). *J. Chem. Phys.* **2002**, *117*, 6673–6687.
- (33) Nattino, F.; Díaz, C.; Jackson, B.; Kroes, G.-J. Effect of surface motion on the rotational quadrupole alignment parameter of D<sub>2</sub> reacting on Cu(111). *Phys. Rev. Lett.* **2012**, *108*, 236104.
- (34) Kroes, G.-J.; Díaz, C. Quantum and classical dynamics of reactive scattering of H<sub>2</sub> from metal surfaces. *Chem. Soc. Rev.* **2016**, *45*, 3658–3700.
- (35) Díaz, C.; Olsen, R. A.; Auerbach, D. J.; Kroes, G.-J. Six-dimensional dynamics study of reactive and non reactive scattering of H<sub>2</sub> from Cu(111) using a chemically accurate potential energy surface. *Phys. Chem. Chem. Phys.* 2010, 12, 6499–519.
- (36) Díaz, C.; Pijper, E.; Olsen, R.; Busnengo, H.; Auerbach, D.; Kroes, G. Chemically accurate simulation of a prototypical surface reaction: H<sub>2</sub> dissociation on Cu(111). *Science* **2009**, *326*, 832–834.
- (37) Wijzenbroek, M.; Somers, M. F. Static surface temperature effects on the dissociation of H<sub>2</sub> and D<sub>2</sub> on Cu(111). *J. Chem. Phys.* **2012**, *137*, 054703.

- (38) McCormack, D. A.; Kroes, G.-.-J.; Olsen, R. A.; Groeneveld, J. A.; van Stralen, J. N.; Baerends, E. J.; Mowrey, R. C. Quantum dynamics of the dissociation of H<sub>2</sub> on Cu(100): dependence of the site-reactivity on initial rovibrational state. *Faraday Discuss.* **2000**, *117*, 109–132.
- (39) McCormack, D. A.; Kroes, G.-J.; Olsen, R. A.; Groeneveld, J. A.; van Stralen, J. N.; Baerends, E. J.; Mowrey, R. C. Molecular knife throwing: aiming for dissociation at specific surface sites through state-selection. *Chem. Phys. Lett.* **2000**, *328*, 317–324.
- (40) Chen, J.; Zhou, X.; Jiang, B. Eley Rideal recombination of hydrogen atoms on Cu(111): quantitative role of electronic excitation in cross sections and product distributions. *J. Chem. Phys.* **2019**, *150*, 061101.
- (41) Darling, G.; Holloway, S. Rotational motion and the dissociation of H<sub>2</sub> on Cu(111). J. Chem. Phys. **1994**, 101, 3268–3281.
- (42) Nienhaus, H.; Bergh, H.; Gergen, B.; Majumdar, A.; Weinberg, W.; McFarland, E. Electron-hole pair creation at Ag and Cu surfaces by adsorption of atomic hydrogen and deuterium. *Phys. Rev. Lett.* **1999**, 82, 446.
- (43) Sakong, S.; Groß, A. Dissociative adsorption of hydrogen on strained Cu surfaces. *Surf. Sci.* **2003**, *525*, 107–118.
- (44) Kroes, G.-J.; Pijper, E.; Salin, A. Dissociative chemisorption of H<sub>2</sub> on the Cu(110) surface: A quantum and quasiclassical dynamical study. *J. Chem. Phys.* **2007**, *127*, 164722.
- (45) Cao, K.; Füchsel, G.; Kleyn, A. W.; Juurlink, L. B. Hydrogen adsorption and desorption from Cu(111) and Cu(211). *Phys. Chem. Chem. Phys.* **2018**, *20*, 22477–22488.
- (46) Kaufmann, S.; Shuai, Q.; Auerbach, D. J.; Schwarzer, D.; Wodtke, A. M. Associative desorption of hydrogen isotopologues from copper surfaces: characterization of two reaction mechanisms. J. Chem. Phys. 2018, 148, 194703.
- (47) Füchsel, G.; Cao, K.; Er, S.; Smeets, E. W. F.; Kleyn, A. W.; Juurlink, L. B. F.; Kroes, G.-J. Anomalous dependence of the reactivity on the presence of steps: dissociation of D<sub>2</sub> on Cu(211). *J. Phys. Chem. Lett.* 2018, 9, 170–175.
- (48) Ghassemi, E. N.; Smeets, E. W. F.; Somers, M. F.; Kroes, G.-J.; Groot, I. M.; Juurlink, L. B.; Füchsel, G. Transferability of the specific reaction parameter density functional for H<sub>2</sub> + Pt(111) to H<sub>2</sub> + Pt(211). *J. Phys. Chem. C* **2019**, *123*, 2973–2986.

(49) Olsen, R.; McCormack, D.; Baerends, E. How molecular trapping enhances the reactivity of rough surfaces. *Surf. Sci.* **2004**, *571*, L325–L330.

- (50) McCormack, D. A.; Olsen, R. A.; Baerends, E. J. Mechanisms of H<sub>2</sub> dissociative adsorption on the Pt(211) stepped surface. J. Chem. Phys. 2005, 122, 194708.
- (51) Luppi, M.; McCormack, D. A.; Olsen, R. A.; Baerends, E. J. Rotational effects in the dissociative adsorption of H<sub>2</sub> on the Pt(211) stepped surface. *J. Chem. Phys.* **2005**, *123*, 164702.
- (52) Olsen, R.; McCormack, D.; Luppi, M.; Baerends, E. Six-dimensional quantum dynamics of H 2 dissociative adsorption on the Pt (211) stepped surface. *The Journal of chemical physics* **2008**, *128*, 194715.
- (53) Huang, X.; Yan, X.; Xiao, Y. Effects of vacancy and step on dissociative dynamics of H<sub>2</sub> on Pd(111) surfaces. *Chem. Phys. Lett.* **2012**, *531*, 143–148.
- (54) Hammer, B.; Nørskov, J. Electronic factors determining the reactivity of metal surfaces. *Surf. Sci.* **1995**, *343*, 211–220.
- (55) Hammer, B.; Nørskov, J. Why gold is the noblest of all the metals. *Nature* **1995**, *376*, 238.
- (56) Mavrikakis, M.; Hammer, B.; Nørskov, J. K. Effect of strain on the reactivity of metal surfaces. *Phys. Rev. Lett.* **1998**, *81*, 2819.
- (57) Pijper, E.; Kroes, G.-J.; Olsen, R. A.; Baerends, E. J. Reactive and diffractive scattering of H<sub>2</sub> from Pt(111) studied using a six-dimensional wave packet method. *J. Chem. Phys.* **2002**, *117*, 5885–5898.
- (58) Kroes, G.-J.; Somers, M. F. Six-dimensional dynamics of dissociative chemisorption of H<sub>2</sub> on metal surface. *J. Theor. Comput. Chem.* **2005**, 4, 493–581.
- (59) Wijzenbroek, M.; Klein, D. M.; Smits, B.; Somers, M. F.; Kroes, G.-J. Performance of a non-local van der Waals density functional on the dissociation of H<sub>2</sub> on metal surfaces. J. Phys. Chem. A 2015, 119, 12146–12158.
- (60) Busnengo, H.; Salin, A.; Dong, W. Representation of the 6D potential energy surface for a diatomic molecule near a solid surface. *J. Chem. Phys.* **2000**, *112*, 7641–7651.
- (61) Wei, C. Y.; Lewis, S. P.; Mele, E. J.; Rappe, A. M. Structure and vibrations of the vicinal copper (211) surface. *Phys. Rev. B* **1998**, *57*, 10062–10068.

- (62) Hammer, B. H. L. B.; Hansen, L. B.; Nørskov, J. K. Improved adsorption energetics within density-functional theory using revised Perdew-Burke-Ernzerhof functionals. *Phys. Rev. B* 1999, 59, 7413–7421.
- (63) Perdew, J. P.; Burke, K.; Ernzerhof, M. Generalized gradient approximation made simple. *Phys. Rev. Lett.* **1996**, *77*, 3865–3868.
- (64) Kresse, G.; Hafner, J. Ab initio molecular-dynamics simulation of the liquid-metal–amorphous-semiconductor transition in germanium. *Phys. Rev. B* **1994**, *49*, 14251–14269.
- (65) Kresse, G.; Hafner, J. Ab initio molecular dynamics for liquid metals. *Phys. Rev. B* **1993**, *47*, 558–561.
- (66) Kresse, G.; Furthmüller, J. Efficient iterative schemes for ab initio totalenergy calculations using a plane-wave basis set. *Phys. Rev. B* 1996, 54, 11169–11186.
- (67) Kresse, G.; Furthmüller, J. Efficiency of ab-initio total energy calculations for metals and semiconductors using a plane-wave basis set. *Comput. Mater. Sci.* **1996**, *6*, 15–50.
- (68) Blanco-Rey, M.; Juaristi, J. I.; Díez Muiño, R.; Busnengo, H. F.; Kroes, G.-J.; Alducin, M. Electronic friction dominates hydrogen hot-atom relaxation on Pd(100). *Phys. Rev. Lett.* **2014**, *112*, 103203.
- (69) Novko, D.; Blanco-Rey, M.; Juaristi, J. I.; Alducin, M. Ab initio molecular dynamics with simultaneous electron and phonon excitations: Application to the relaxation of hot atoms and molecules on metal surfaces. *Phys. Rev. B* **2015**, *92*, 201411.
- (70) Füchsel, G.; del Cueto, M.; Díaz, C.; Kroes, G.-J. Enigmatic HCl + Au(111) reaction: a puzzle for theory and experiment. *J. Phys. Chem. C* **2016**, *120*, 25760–25779.
- (71) Raff, L. M.; Karplus, M. Theoretical investigations of reactive collisions in molecular beams: K+CH<sub>3</sub>I and related systems. *J. Chem. Phys.* **1966**, *44*, 1212–1229.
- (72) Lemons, D. S.; Gythiel, A. On the Theory of Brownian Motion. Am. J. Phys. 1997, 65, 1079–1081.
- (73) Ermak, D. L.; Buckholz, H. Numerical integration of the Langevin equation: Monte Carlo simulation. *J. Comput. Phys.* **1980**, *35*, 169–182.
- (74) Füchsel, G.; Klamroth, T.; Monturet, S.; Saalfrank, P. Dissipative dynamics within the electronic friction approach: the femtosecond laser desorption of H<sub>2</sub>/D<sub>2</sub> from Ru(0001). Phys. Chem. Chem. Phys. 2011, 13, 8659–8670.

(75) Juaristi, J.; Alducin, M.; Muiño, R. D.; Busnengo, H. F.; Salin, A. Role of electron-hole pair excitations in the dissociative adsorption of diatomic molecules on metal surfaces. *Phys. Rev. Lett.* **2008**, *100*, 116102.

- (76) Vibók, Á.; Balint-Kurti, G. G. Parametrization of complex absorbing potentials for time-dependent quantum dynamics. *J. Phys. Chem.* **1992**, 96, 8712–8719.
- (77) Balint-Kurti, G. G.; Dixon, R. N.; Marston, C. C. Grid methods for solving the Schrödinger equation and time dependent quantum dynamics of molecular photofragmentation and reactive scattering processes. *Int. Rev. Phys. Chem.* 1992, 11, 317–344.
- (78) Michelsen, H. A.; Auerbach, D. J. A critical examination of data on the dissociative adsorption and associative desorption of hydrogen at copper surfaces. *J. Chem. Phys.* **1991**, *94*, 7502–7520.
- (79) Zare, R. N.; Harter, W. G. Angular momentum: understanding spatial aspects in chemistry and physics. *Phys. Today* **1989**, *42*, 68–72.
- (80) Shakouri, K.; Behler, J.; Meyer, J.; Kroes, G.-J. Accurate neural network description of surface phonons in reactive gas-surface dynamics: N<sub>2</sub>+ Ru(0001). *J. Phys. Chem. Lett.* **2017**, *8*, 2131–2136.
- (81) Díaz, C.; Perrier, A.; Kroes, G. Associative desorption of N<sub>2</sub> from Ru(0001): a computational study. *Chem. Phys. Lett.* **2007**, 434, 231–236.
- (82) Muzas, A. S.; Juaristi, J. I.; Alducin, M.; Díez Muiño, R.; Kroes, G.-J.; Díaz, C. Vibrational deexcitation and rotational excitation of H<sub>2</sub> and D<sub>2</sub> scattered from Cu(111): adiabatic versus non-adiabatic dynamics. J. Chem. Phys. 2012, 137, 064707.

5 Designing new SRP density functionals including non-local vdW-DF2 correlation for  $H_2 + Cu(111)$  and their transferability to  $H_2 + Ag(111)$ , Au(111) and Pt(111)

#### This Chapter is based on:

Smeets, E. W. F.; Kroes, G.-J. Designing new SRP density functionals including non-local vdW-DF2 correlation for  $H_2 + Cu(111)$  and their transferability to  $H_2 + Ag(111)$ , Au(111) and Pt(111). Phys. Chem. Chem. Phys. **2021**, 23, 7875–7901

# Abstract

Specific reaction parameter density functionals (SRP-DFs) that can describe molecular beam sticking experiments of hydrogen (H<sub>2</sub>) on cold transition metal surfaces with chemical accuracy have so far been shown to be only transferable among different facets of the same metal, but not among different metals. We design new SRP-DFs that include non-local vdW-DF2 correlation for the H<sub>2</sub> + Cu(111) system, and evaluate their transferability to the highly activated H<sub>2</sub> + Ag(111) and H<sub>2</sub> + Au(111) systems and the non-activated H<sub>2</sub> + Pt(111) system. We design our functionals for the H<sub>2</sub> + Cu(111) system since it is the best studied system both theoretically and experimentally. Here we demonstrate that a SRP-DF fitted to reproduce molecular beam sticking experiments for H<sub>2</sub> + Cu(111) with chemical accuracy can also describe such experiments for H<sub>2</sub> + Pt(111) with chemical accuracy, and vice versa. Chemically accurate

functionals have been obtained that perform very well with respect to reported Van der Waals well geometries, and which improve the description of the metal over current generalized gradient approximation (GGA) based SRP-DFs. From a systematic comparison of our new SRP-DFs that include non-local correlation with previously developed SRP-DFs, for both activated and non-activated systems, we identify non-local correlation as a key ingredient in the construction of transferable SRP-DFs for  $H_2$  interacting with transition metals. Our results are in excellent agreement with experiment when accurately measured observables are available. It is however clear from our analysis that, except for the  $H_2 + Cu(111)$  system, there is a need for more, more varied, and more accurately described experiments in order to further improve the design of SRP-DFs. Additionally, we confirm that, when including non-local correlation, the sticking of  $H_2$  on Cu(111) is still well described quasi-classically.

### 5.1 Introduction

Hydrogen ( $H_2$ ) dissociation on various noble transition metal surfaces is an example of an intensely studied activated elementary surface reaction within surface science. Chemically accurate computation of rate-controlling states is essential in order to accurately describe the complex overall processes that take place during heterogeneous catalysis under real world conditions<sup>2–6</sup>. Industrially  $H_2$  dissociation is an important step in the production of methanol from  $CO_2$  over a  $Cu/ZnO/Al_2O_3$  catalyst<sup>7–9</sup>. Additionally  $H_2$  dissociation is an important process in the production of syngas and ammonia<sup>5</sup>. Increasing the predictive power of theoretical models of heterogeneous catalysis potentially has an important financial impact on the chemical industry<sup>10</sup>.

An important step to increasing the predictive power of theoretical models is to create density functionals (DFs) that are chemically accurate for specific systems  $^{2,11-14}$ , i.e. DFs that can describe reaction barrier heights to within 1 kcal/mol<sup>6</sup>. A next step is to investigate what ingredients of a DF that is chemically accurate for one system might make it transferable to another system without loss of accuracy. Presently, specific reaction parameter (SRP) density functional theory (DFT) is the only method that can describe the interaction of  $H_2$  with metal surfaces with demonstrated chemical accuracy, while simultaneously being computationally cheap enough to make large comparative studies feasible. Therefore the design of accurate DFs is highly important to the field. The availability of transferable specific reaction parameter density functionals (SRP-DFs) has the potential to greatly speed up theoretical heterogeneous catalysis research. It does so by avoiding the need to design a new DF for each system of interest. The availability of transferable SRP-DFs would

5.1. Introduction 133

greatly improve the predictive power of theory for systems for which only sparse experimental results have been published.

The fitting of SRP-DFs is meticulous work and presently<sup>15</sup> requires experimental data as reference data<sup>2,11–14,16</sup>. Transferability of a DF among systems in which one specific molecule interacts with surfaces of different metals has so far only been reported for the DF designed for CH<sub>4</sub> dissociation on Ni(111)<sup>14</sup>, which could also describe the dissociation of CH<sub>4</sub> on Pt(111) with chemical accuracy<sup>17</sup>, where Ni and Pt belong to the same group. So far, for SRP-DFs fitted to reproduce molecular beam adsorption experiments for H<sub>2</sub> interacting with transition metals transferability was shown among systems in which H<sub>2</sub> interacts with different faces of the same metal<sup>18,19</sup>, but not among systems where the interaction is with surfaces of different metals<sup>13,16,20,21</sup>.

The transferability of the SRP-DF that was fitted for the  $CH_4 + Ni(111)$  system to the  $CH_4 + Pt(111)$  system suggests that non-local correlation is an important ingredient for a transferable DF, as this SRP-DF contains non-local correlation. For this reason here we investigate the design of new SRP-DFs that include non-local correlation for  $H_2 + \text{transition}$  metal systems. In this work we present two new SRP-DFs featuring GGA exchange but using non-local correlation. These DFs were fitted to experiments on the  $H_2 + Cu(111)$  system, since theoretically  $^{11,13,22-45}$  and experimentally  $^{46-62}$  this is the best studied system. For this system we can have the most confidence that discrepancies between theory and experiment can be attributed to either shortcomings in DF design or the limitations of using the Born-Oppenheimer static surface (BOSS) model. It is well known that the BOSS model works well for activated  $H_2$  dissociation on cold metals  $^{24,28-30,63}$ . Additionally we evaluate the performance of a SRP-DF that was fitted to the  $H_2 + Pt(111)$  system.

In undertaking this study we have two aims. The first is to identify features of the newly constructed SRP-DFs that increase their transferability to other systems. Since we use the BOSS model, a direct assessment of the quality of a given DF is really only possible for molecular beam sticking experiments on reasonably cold metal surfaces. Apart from the  $H_2 + Cu(111)$  system we will consider such experiments for the the  $H_2 + Pt(111)$  system<sup>64,65</sup> and the  $H_2 + Ag(111)$  system<sup>55</sup>. For the latter two systems there exists some uncertainty about the validity of the molecular beam parameters describing the experiments<sup>20,66</sup>. We however feel that, although there are some uncertainties in the parameters describing the experiments, nevertheless valuable insights on transferability can be derived by analysing the predicted reactivity of the SRP-DFs considered here.

Our second aim is to analyse the limits of our dynamical model to the extent

that this is possible. We hope that a detailed analysis of the  $H_2 + Cu(111)$  system's large body of experimental work<sup>46–62</sup> will indicate how to proceed with improving the theoretical description of this system. To this end we will analyse both associative desorption experiments<sup>48,52</sup> and dissociative chemisorption experiments<sup>46,47</sup>. Naturally, our primary motive is to achieve chemical accuracy. We have also carried out a full quantum mechanical molecular beam simulation by carrying out a large number of fully initial-state resolved quantum dynamical  $(QD)^{67,68}$  calculations for the  $H_2 + Cu(111)$  system. This is important because the inclusion of a Van der Waals well in the PES might lead to discrepancies between quasi-classical trajectory  $(QCT)^{69}$  and QD results compared to the good agreement that was obtained for these two methods for the  $H_2 + Cu(211)$  system<sup>37</sup> using the SRP48 DF<sup>11,63</sup>, which does not employ non-local correlation.

For the  $H_2 + Cu(111)$  system it is known that the effect of surface motion cannot readily be ignored for specific observables at high surface temperature<sup>63</sup>  $(T_s)$ . Analysing associative desorption and dissociative chemisorption experiments as linked through detailed balance<sup>70</sup>, might allow us to disentangle the effects of surface motion and the non-adiabatic contributions of electron-hole pair (ehp) excitations, a methodology that was suggested by results of Shuai et al. 71 for the  $H_2 + Au(111)$  system. If detailed balance is applicable then an analysis of both associative desorption and dissociative chemisorption experiments should yield the same result. A detailed analysis might therefore allow us to identify which dynamical effects not included in the BOSS model may have to be included in future work. Here we will make a direct comparison to experimental effective barrier  $(E_0(\nu, J))$  parameters<sup>48</sup>. Even though a complementary molecular beam sticking experiment is not available with the associative desorption experiment of Shuai et al.  $^{71}$  on  $H_2 + Au(111)$ , we extend our analysis also to this system. We note that it is also possible to simulate associative desorption directly by running trajectories starting around the transition state using Metropolis sampling of the initial conditions<sup>72–76</sup>, and that this has also been done for H<sub>2</sub> and D<sub>2</sub> desorbing from Cu(111). However, the calculations published so far do have limitations. The early work<sup>73,74</sup> used a PES that is an approximate fit<sup>40</sup> to unconverged DFT calculations<sup>41</sup> using the PW91 DF<sup>77</sup>, and the statistical accuracy of the results of the later work<sup>76</sup> was limited by the number of ab initio molecular dynamics (AIMD) trajectories that could be run. However, an interesting aspect of the later work<sup>76</sup> is that the effects of surface atom motion and electron-hole pair excitation could also be investigated.

Furthermore we will treat vibrationally and rotationally inelastic scattering for the  $H_2 + Cu(111)$  system, since the opinion has been voiced that these properties might be extra sensitive to the Van der Waals well<sup>25</sup>, which is present

5.1. Introduction 135

in potential energy surfaces (PESs) computed here with the use of non-local correlation.

For the  $H_2 + Ag(111)$  system the only molecular beam dissociative chemisorption experiments we are aware of are those of Hodgson and coworkers<sup>55</sup>. We will also make a comparison to initial-state resolved associative desorption experiments for this system<sup>78,79</sup>, as was recently done by Jiang et al.<sup>80</sup> using quantum dynamics calculations on a permutation invariant polynomial (PIP) neural network potential<sup>81</sup> and in work done in our group<sup>13,20</sup>. Earlier experimental work on the  $H_2 + Ag(111)$  system suggested that  $H_2$  prefers to physisorb on silver surfaces<sup>82–84</sup>, and that the dissociation of H<sub>2</sub> on silver is endothermic<sup>85</sup>, exhibiting a relatively low barrier for associative desorption of H<sub>2</sub><sup>85–87</sup>. For this reason some earlier experimental studies have focused on scattering at low translational energies of  $H_2$  from  $Ag(111)^{88-91}$  and  $Ag(110)^{92}$ . Recent theoretical studies that addressed the effects of electron-hole pair excitation have shown very interesting effects at low translational energies with respect to inelastic scattering and dynamical steering <sup>93–95</sup>. The non-adiabatic energy loss during the dynamics was however shown to be small<sup>95</sup>. This is in agreement with work on  $H_2 + Cu(111)$ , which also showed little effect of electron-hole pair excitation on sticking<sup>23,96</sup>. Therefore we presume the BOSS model to be accurate enough for our first aim, which is to identify the features of SRP functionals that contribute to their transferability.

Our DFT calculations using van der Waals correlation functionals<sup>97,98</sup> also yield results regarding the geometry and the depth of the van der Waals wells for the systems investigated, and we will compare these results to the experimental results for the systems investigated here. In many cases the experimental results come from an analysis of experiments on selective adsorption 60,62,90,91,99–105. In these experiments, an increase or a dip is observed in a peak for a diffractive (corrugation mediated selective adsorption, CMSA<sup>106,107</sup>) or a rotational (rotationally mediated selective adsorption, RMSA<sup>99</sup>) transition if the translational energy goes through a value that coincides with the energy between two parallel translational or hindered rotational metastable states, respectively. In the transient state, the H<sub>2</sub> molecule is trapped in the Van der Waals well close to the surface 101,104. Information about the resonance energies that are present can be used to reconstruct the shape of the potential, and thus the Van der Waals well geometries and well depths. The H<sub>2</sub> -(111) metal-surface systems investigated here exhibit little corrugation. For this reason experiments using RMSA of HD, in which rotational excitation is used to probe the bound levels of the gas-surface potential, have been particularly important for gathering information concerning van der Waals interactions in these systems. The off-center position of the center of mass of HD results in very pronounced resonances when

using the RMSA technique  $^{62,99-102}$ . Experimentalists have also been able to carry out RMSA measurements using  $H_2$  or  $D_2$  instead of  $HD^{90,91,103}$ . Van der Waals well depths can also be obtained from the temperature dependence of the Debye-Waller attenuation of peaks for (rotationally) inelastic diffraction  $^{108,109}$ , from potential inversion using calculations on (rotationally inelastic) diffractive scattering using the eikonal approximation  $^{108}$ , and from potential inversion using measurements on phonon-assisted RMSA (also called rotationally mediated focused inelastic resonances, RMFIR  $^{110}$ ). For all systems investigated here, studies using experiments to analyze the Van der Waals interaction have been performed, i.e., for  $H_2 + Cu(111)^{60,62}$ ,  $H_2 + Ag(111)^{90,91,102}$ ,  $H_2 + Au(111)^{62}$ , and  $H_2 + Pt(111)^{99-101,111}$ .

# 5.2 Methodology

#### 5.2.1 Coordinate system

All calculations in this work are carried out using the BOSS model<sup>11</sup>. This means that the atoms of the metal slab are fixed to their ideal positions, and that we only take into account the six molecular degrees of freedom (DOF) of the impinging  $H_2$  ( $D_2$ ) molecule (see figure 5.1a). Three of the DOFs taken into account are the centre of mass (COM) coordinates X, Y and Z, where (X, Y) describes the lateral position of the molecule and Z describes the molecule-surface distance. The other DOFs are the  $H_2$  bond length r, the polar orientation angle with respect to the surface normal  $\theta$  and the azimuthal angle  $\phi$ . The geometry of the (111) face of an fcc metal together with its high symmetry sites is shown in relation to the coordinate system used in figure 5.1b.

#### 5.2.2 SRP DFT

We use periodic DFT calculations to construct PESs, testing DFs at the GGA, the meta-GGA (mGGA), and GGA + non-local correlation level, where in this Chapter non-local correlation refers to either vdW-DF1 non-local correlation<sup>97</sup> or vdW-DF2 non-local correlation<sup>98</sup> (see the types of DF defined in table 5.1). In many cases we test a DF that is a SRP-DF for at least one of the four systems considered. In the present context a SRP-DF is constructed by taking a weighted average of a DF that overestimates the sticking probability, and one DF that underestimates the sticking probability for the system of interest<sup>11</sup>. More specifically, the mixing often occurs for the exchange part of the DF, as was done for many of the previously developed SRP-DFs<sup>12,14,17,27</sup>.

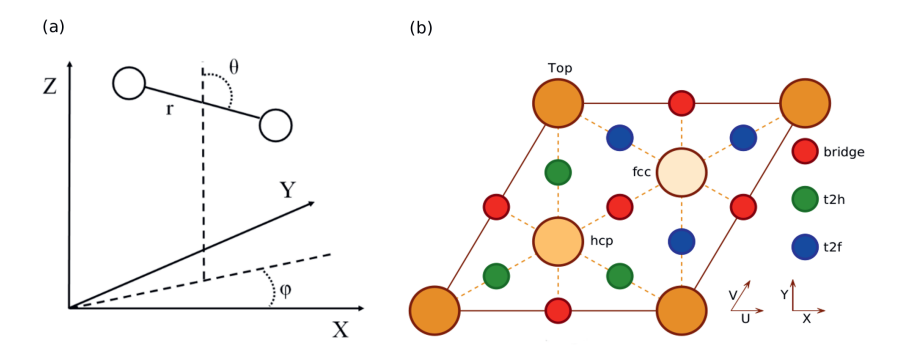


FIGURE 5.1: The COM coordinate system used for the description of the  $H_2$  ( $D_2$ ) molecule (a). The unit cell of a (111) face of a fcc metal together with the high symmetry sites as well as the relationship with the coordinate system chosen for  $H_2$  ( $D_2$ ) relative to the (111) surface (b). The origin of the COM coordinate system (X,Y,Z)=(0,0,0) is at an atom in the top surface layer (a top site). We define the polar angle and azimuth such that  $(\theta=90^\circ,\phi=0^\circ)$  corresponds to molecules parallel to the surface pointing along the X (or equivalent U) direction. The hcp and fcc hollow sites correspond to metal atoms in the second and third layer, respectively.

The SRP-DFs developed in this work are all DFs in which the exchange part is taken at the GGA level, and the exchange correlation functional takes the following form:

$$E_{XC}^{SRP}(\rho, \nabla \rho) = \underbrace{\alpha E_X^1(\rho, \nabla \rho) + (1 - \alpha) E_X^2(\rho, \nabla \rho)}_{\text{mixed exchange}} + \underbrace{E_C^{local}(\rho)}_{\text{LDA correlation}} + \underbrace{E_C^{non-local}(\rho)}_{\text{Van der Waals}}$$
(5.1)

Here  $\alpha$  is the SRP mixing parameter,  $\rho$  is the three dimensional electron density and  $\nabla \rho$  is the gradient of the electron density.  $E_X^1(\rho, \nabla \rho)$  and  $E_X^2(\rho, \nabla \rho)$  are the two DFs that are to be mixed into the exchange part of the SRP-DF. The non-local correlation part here can correspond to the non-local correlation used in the vdW-DF1 or vdW-DF2 DFs<sup>97,98</sup>. The DFs used in this work (i.e., the B86SRP68-DF2 and SRPsol63-DF2 DFs, and the other DFs considered in this work) are shown in table 5.1. Table 5.1 also shows the type of each DF and the exchange and correlation components contained in each function (see Eq. 5.1).

| Name                   | $_{ m type}$ | exchange  | correlation     |
|------------------------|--------------|---|-----------------|
| B86SRP68-DF2           | vdW-DF       | $0.68~\mathrm{B86r^{112}} + 0.32~\mathrm{RPBE^{113}}$ | $vdW-DF2^{98}$  |
| $MS-B86bl^{13}$        | mGGA         | $MS-B86bl^{13}$                                       | $revTPSS^{114}$ |
| $MS-PBEl^{13}$         | mGGA         | MS-PBEl <sup>13</sup>                                 | $revTPSS^{114}$ |
| $optPBE-DF1^{115}$     | vdW-DF       | $ m optPBE^{115}$                                     | $vdW-DF1^{97}$  |
| $PBE^{116}$            | GGA          | $PBE^{116}$   | $PBE^{116}$     |
| $PBE\alpha57-DF2^{12}$ | vdW-DF       | $PBE\alpha = 0.57^{117}$                              | $vdW-DF2^{98}$  |
| $PBEsol^{118}$         | GGA          | $PBEsol^{118}$  | $PBE^{116}$     |
| $RPBE^{113}$           | GGA          | $RPBE^{113}$  | $PBE^{116}$     |
| $SRP48^{63}$           | GGA          | $0.52~\mathrm{PBE^{116}} + 0.48~\mathrm{RPBE^{113}}$  | $PBE^{118}$     |
| SRPsol63-DF2           | vdW-DF       | $0.63~{ m PBE}{ m sol}^{118}+0.37~{ m RPBE}^{113}$    | $vdW-DF2^{98}$  |
| $vdW-DF1^{97}$         | vdW-DF       | $revPBE^{119}$  | $vdW-DF1^{97}$  |
| $vdW-DF2^{98}$         | vdW-DF       | $rPW86^{120}$   | $vdW-DF2^{98}$  |

TABLE 5.1: The exchange-correlation DFs used in this work are presented in alphabetical order. Also shown is the type of each functional as well as the constituent exchange and correlation parts. By the type "vdW-DF" we mean that GGA exchange is combined with vdW-DF1<sup>97</sup> of vdW-DF2<sup>98</sup> correlation.

#### 5.2.3 Construction of the PESs

A continuous representation of the PESs is obtained by the interpolation of DFT results calculated on a grid using the corrugation reducing procedure (CRP)<sup>121</sup> (see also section 2.2 of Chapter 2). The method we use is analogous to that used by Wijzenbroek et al.<sup>42</sup>, but we used denser grids to represent the full six dimensional molecule-surface interaction potential and the three dimensional atom-surface interaction potential to further increase the accuracy of the resulting CRP<sup>121</sup> PESs with respect to the underlying DFT calculations. Details are presented in appendix 5.A.

# 5.2.4 Quasi-classical dynamics

The QCT calculations presented in this work are carried out on six dimensional PESs and assume quasi-classical initial conditions<sup>69</sup>. This means that we take into account the quantum mechanical energies of the impinging  $H_2$  and  $D_2$  molecules in their initial rovibrational states. The method used is described more fully in ref.<sup>122</sup> and section 2.3.1 of Chapter 2. The equations of motion are integrated using the method of Stoer et al.<sup>123</sup>.

When simulating a molecular beam experiment 200,000 trajectories are propagated per energy point, and when calculating initial-state resolved reaction probabilities 50,000 trajectories are propagated per energy point. All trajectories start in the gas phase, at  $Z_{\rm gas}=8$  Å. For all QCT calculations we use a minimum time step of dt=0.001 fs. Trajectories are assumed to result in reaction if r becomes bigger then some critical value  $r_c$  (2.2Å) and in scattering if Z becomes bigger then  $Z_{\rm gas}$  which is also the starting point of all trajectories.

#### 5.2.5 Quantum dynamics

Six dimensional quantum dynamics (QD) calculations are performed by solving the time-dependent Schrödinger equation,

$$i\hbar \frac{d\Psi(\vec{Q};t)}{dt} = \hat{H}\Psi(\vec{Q};t), \tag{5.2}$$

using the time-dependent wave packet (TDWP) method<sup>124,125</sup> with our in-house computer package<sup>67,68</sup>. Here,  $\Psi(\vec{Q};t)$  denotes the nuclear wave function of H<sub>2</sub> at time t with  $\vec{Q}$  being the position vector. Furthermore we employ the following Hamiltonian in order to take into account the six degrees of freedom of H<sub>2</sub>:

$$\hat{H} = -\frac{\hbar^2}{2M} \nabla^2 - \frac{\hbar^2}{2\mu} \frac{\partial^2}{\partial r^2} + \frac{1}{2\mu r^2} \hat{J}^2(\theta, \phi) + V(\vec{Q}).$$
 (5.3)

Here, M and  $\mu$  are the mass and reduced mass of  $H_2$ ,  $\hat{J}^2(\theta,\phi)$  is the angular momentum operator and  $V(\vec{Q})$  is the six dimensional PES. The scattered wave packet is analysed using the scattering matrix formalism<sup>126</sup>, yielding fully initial-state resolved S-matrix elements for vibrationally, rotationally, and diffractionally inelastic scattering. From the S-matrix elements the corresponding state-to-state probabilities  $P_{\nu Jm_J \to \nu' J'm'_J nm}(E)$  for scattering at the incident energy E can be obtained<sup>67,68</sup>. Subsequently the sticking probability can be computed<sup>67,68</sup> by subtracting the sum of the scattering probabilities from one.

Further information on how we construct the initial wave packet can be found in section 2.3.2 of Chapter 2. Table 5.2 presents parameters describing all the initial wave packets used, and table 5.3 shows the rovibrational states taken into account in the molecular beam simulations of sticking with the QCT and QD methods.

### 5.2.6 Computation of observables

### Simulating molecular beam sticking.

In order to compute molecular beam sticking probabilities the translational energy and rovibrational state distributions need to be taken into account according to the nozzle temperature,  $T_n$ . The sticking probability  $S_0$  is computed using

$$S_0(\langle E \rangle) = \sum_{\nu,J} \int P(\nu,\nu,J,T_n) P_{\text{deg}}(E,\nu,J) dE.$$
 (5.4)

Table 5.2: Input parameters for the 6D quantum simulations on the reactive scattering of  $H_2$  on Cu(111). All wave packets were propagated until the remaining norm was less then one percent.

|   |             |                    |   | H <sub>2</sub> + Cu(111 | )                  |                    |                    |
|---|-------------|--------------------|---|-------------------------|--------------------|--------------------|--------------------|
|   | $(\nu = 1,$ | 0.                 | .15 eV - 0.55 e   |                         |                    | 0.5 eV - 1.4 eV    | 7                  |
|   | J=0,        | $\nu = 0$          | $\nu = 0$   | $\nu = 1$               | $\nu = 0$          | $\nu = 0$          | $\nu = 1$          |
|   | $m_J = 0)$  | $J \in [0, 7]$     | $J \in [8, 11]$   | $J \in [0, 7]$          | $J \in [0, 7]$     | $J \in [8, 11]$    | $J \in [0, 7]$     |
| $Z_{start}$ (Bohr)  | -1.0        | -1.0               | -1.0  | -1.0                    | -1.0               | -1.0               | -1.0               |
| $N_{Z_{spec}}$  | 280         | 252                | 252   | 252                     | 224                | 224                | 224                |
| $N_Z$   | 240         | 198                | 198   | 198                     | 192                | 192                | 192                |
| $\Delta Z$ (Bohr)   | 0.1         | 0.1                | 0.1   | 0.1                     | 0.1                | 0.1                | 0.1                |
| $R_{start}$ (Bohr)  | 0.8         | 0.8                | 0.8   | 0.8                     | 0.8                | 0.8                | 0.8                |
| $N_R$   | 64          | 56                 | 56  | 56                      | 48                 | 48                 | 48                 |
| $\Delta R$ (Bohr)   | 0.15        | 0.15               | 0.15  | 0.15                    | 0.15               | 0.15               | 0.15               |
| $N_X$   | 20          | 20                 | 20  | 20                      | 20                 | 20                 | 20                 |
| $N_Y$   | 20          | 20                 | 20  | 20                      | 20                 | 20                 | 20                 |
| $J_{\max}$  | 36<br>28    | 26 / 25<br>26 / 25 | $\begin{array}{c c} 32 & / & 31 \\ 32 & / & 31 \end{array}$ | 36 / 35<br>28 / 27      | 36 / 35<br>28 / 27 | 42 / 41<br>40 / 39 | 40 / 39<br>32 / 31 |
| $\frac{m_{J_{\text{max}}}}{\text{Complex absorbing pot}}$                                 |             | 20 / 25            | 32 / 31   | 20 / 21                 | 20 / 21            | 40 / 39            | 32 / 31            |
| $Z^{CAP}$ start $[a_0]$   | 15.2        | 15.2               | 15.2  | 15.2                    | 15.2               | 15.2               | 15.2               |
| [[]   |             |                    |   |                         | -                  |                    |                    |
| $Z^{CAP}$ end $[a_0]$   | 22.90       | 18.7               | 18.7  | 18.7                    | 18.1               | 18.1               | 18.1               |
| Z <sup>CAP</sup> Optimum [eV]   | 0.03        | 0.1                | 0.1   | 0.1                     | 0.3                | 0.3                | 0.3                |
| $Z_{spec_{-}}^{CAP}$ start $[a_{0}]$  | 19.8        | 19.8               | 19.8  | 19.8                    | 18.8               | 18.8               | 18.8               |
| $Z_{spec}^{CAP}$ end $[a_0]$  | 26.90       | 24.1               | 24.1  | 24.1                    | 21.3               | 21.3               | 21.3               |
| $Z_{spec}^{CAP}$ start $[a_0]$ $Z_{spec}^{CAP}$ end $[a_0]$ $Z_{spec}^{CAP}$ Optimum [eV] | 0.05        | 0.08               | 0.08  | 0.08                    | 0.25               | 0.25               | 0.25               |
| RCAP start [go]   | 4.55        | 4.55               | 4.55  | 4.55                    | 4.55               | 4.55               | 4.55               |
| $R^{CAP}$ end $[a_0]$   | 10.25       | 9.05               | 9.05  | 9.05                    | 7.85               | 7.85               | 7.85               |
| $R^{CAP}$ optimum [eV]  | 0.1         | 0.1                | 0.1   | 0.1                     | 0.25               | 0.25               | 0.25               |
| Propagation   |             |                    |   |                         |                    |                    |                    |
| $\Delta t \left[ \hbar / E_{\rm h} \right]$   | 2           | 2                  | 2   | 2                       | 2                  | 2                  | 2                  |
| $t_f \left[ \hbar / E_{ m h} \right]$   | 45000       | 20000              | 20000   | 20000                   | 13000              | 13000              | 13000              |
| Initial wave packet   |             |                    |   | •                       |                    | •                  |                    |
| $E_{min}$ [eV]  | 0.055       | 0.15               | 0.15  | 0.15                    | 0.5                | 0.5                | 0.5                |
| $E_{max}$ [eV]  | 0.45        | 0.55               | 0.55  | 0.55                    | 1.4                | 1.4                | 1.4                |
| $Z_0 [a_0]$   | 17.50       | 17.40              | 17.40   | 17.40                   | 16.8               | 16.8               | 16.8               |

|     | $(\nu = 0)J_{\rm max}$ | $(\nu = 1)J_{\max}$ | $(\nu = 2)J_{\text{max}}$ | $(\nu = 3)J_{\text{max}}$ | $(\nu = 4)J_{\text{max}}$ |
|-----|------------------------|---------------------|---------------------------|---------------------------|---------------------------|
| QCT | 30                     | 30                  | 30                        | 30                        | 30                        |
| QD  | 11                     | 7                   | -                         | -                         | -                         |

Table 5.3: Rovibrational states taken into account, according to their Boltzmann weight, in molecular beam simulations for the QCT and QD methods for all  $H_2$  ( $D_2$ , only QCT) + metal systems.

Here,  $\langle E \rangle$  is the average translational energy. The probability for a molecule present in the beam to be in a rovibrational state described by the vibrational quantum number  $\nu$  and the angular momentum quantum number J and to have a velocity between v and v+dv is denoted by:

$$P(v, \nu, J, T_n)dv = P_{flux}(v; T_n)dv \times P_{int}(\nu, J, T_n).$$
 (5.5)

The flux-weighted velocity distribution  $P_{flux}$  is a function of  $T_n$  and is determined by the width parameter  $\alpha$  and the stream velocity  $v_0$  according to<sup>45</sup>

$$P_{flux}(v; T_n)dv = Cv^3 e^{-(v-v_0)^2/\alpha^2} dv$$
 (5.6)

with C being a normalization constant. Through Eq. 5.4 and 5.5 the reactivity of each rovibrational state is weighted according to its Boltzmann weight as follows:

$$P_{int}(\nu, J, T_n) = \frac{g_N f(\nu, J, T_n)}{\sum_{\nu', J' \equiv J(mod\ 2)} f(\nu', J', T_n)},$$
(5.7)

with

$$f(\nu, J, T_n) = (2J+1) \times e^{(-(E_{\nu,0} - E_{0,0})/k_B T_{vib})} \times e^{(-(E_{\nu,J} - E_{\nu,0})/k_B T_{rot})}.$$
 (5.8)

Here,  $k_B$  is the Boltzmann constant and  $E_{\nu,J}$  is the energy of the quantum state characterized by  $\nu$  and J. The first and second Boltzmann factor describe vibrational and rotational state populations, respectively. Here we take into account the effect of rotational cooling during the supersonic expansion by taking the rotational temperature to be  $T_{rot} = 0.8 * T_n^{52}$ , while the vibrational temperature,  $T_{vib}$ , is taken to be equal to  $T_n$ . The factor  $g_N$  in Eq. 5.7 reflects the ortho/para ratio of hydrogen in the beam. For  $H_2$ ,  $g_N$  is 1/4 (3/4) for even (odd) values of J, and for  $D_2$ ,  $g_N = 2/3$  (1/3) for even (odd) values of J.

In the QCT calculations presented in this work the probability distribution  $P(v, \nu, J, T_n)$  is randomly sampled as described in ref<sup>122</sup>. All parameters describing molecular beam experiments used for the calculations presented here can be found in table 5.4. The reaction probability is then computed by dividing the number of adsorbed trajectories,  $N_{ads}$ , by the total number of calculated trajectories, N, i.e.  $P_r = N_{ads}/N$ .

We compute initial-state selected but degeneracy averaged reaction probabilities,  $P_{\text{deg}}(E, \nu, J)$ , as:

$$P_{\text{deg}}(E,\nu,J) = \sum_{m_J=0}^{J} (2 - \delta_{m_J 0}) \frac{P_r(E,\nu,J,m_J)}{2J+1},$$
 (5.9)

where  $P_r(E, \nu, J, m_J)$  is the fully initial-state resolved reaction probability,  $m_J$  is the magnetic rotational quantum number, and E is the translational energy. For the QD calculations it is not possible to directly sample  $P(v, \nu, J, T_n)$ . Molecular beam reaction probabilities for the QD method are instead calculated from initial-state resolved reaction probabilities in the same manner as discussed in our Chapter 4.

### Comparing to experimental $E_0(\nu, J)$ parameters.

Experimentally, for H<sub>2</sub>-metal surface reactions the initial state-selected reaction probabilities are usually obtained<sup>46,48,52,71</sup> from associative desorption measurements using the principle of detailed balance<sup>70</sup>. Experiments on H<sub>2</sub> associatively desorbing from metals typically measure the (unnormalized) state-resolved translational energy distributions of molecules from the surface using resonance-enhanced multi-photon ionization (REMPI)<sup>19,46,52</sup>. These distributions,  $P_{\text{des}}(E,\nu,J)$ , may be related to the degeneracy averaged initial-state resolved reaction probability, using:

$$P_{\text{des}}(E,\nu,J) \propto Ee^{-\frac{E}{k_b T_s}} P_{\text{deg}}(E,\nu,J). \tag{5.10}$$

The extracted reaction probabilities are usually fitted to a sigmoid function, e.g. the function involving the error function:

$$P_{\text{deg}}(E,\nu,J) = \frac{A_{\nu,J}}{2} \left[ 1 + erf\left(\frac{E - E_0(\nu,J)}{W_{\nu,J}}\right) \right].$$
 (5.11)

Here, the  $A_{\nu,J}$  values are the saturation values of the extracted degeneracy averaged reaction probabilities, and the effective barrier height  $(E_0(\nu,J))$  is the incidence energy at which  $P_{\text{deg}}(E,\nu,J)$  first becomes equal to  $\frac{1}{2}A_{\nu,J}$ . Using Eq. 5.11,  $E_0(\nu,J)$  also is the inflexion point of the reaction probability curve if the saturation value  $A_{\nu,J}$  corresponds to the absolute saturation value.  $W_{\nu,J}$  is a measure of the width of the reaction probability curve.

If the proportionality factor implicit in Eq. 5.10 would also be measured in the experiment (for instance, because the exact state-selective flux would have been measured), it should be possible to directly extract absolute values of the initial-state selected reaction probabilities from the experiment by assuming detailed balance. In this case, the directly extracted  $A_{\nu,J}$  value would be the true saturation value of the reaction probability. These values could then be directly compared to computed degeneracy averaged initial-state resolved reaction probabilities (Eq. 5.9).

Table 5.4: Molecular beam parameters taken from experiments performed on the  $H_2$  ( $D_2$ ) + Cu(111) system and the  $D_2$  + Pt(111) system. The parameters  $v_0$ ,  $\alpha$ ,  $T_n$  represent the stream velocity of the beam, the width of the beam and the nozzle temperature at an average translational incidence energy  $\langle E_i \rangle$ . Parameters were taken from (the supporting information of) Refs<sup>11,29,46,47,64,66,127,128</sup>.

| $T_n$ [K]           | $\langle E_i \rangle$ [kJ/mol] | $v_0$ [m/s]      | $E_0$ [eV]         | $\alpha$ [m/s]    |
|---------------------|--------------------------------|------------------|--------------------|-------------------|
|                     | olecular H <sub>2</sub> beam   |                  | and cowork         | ers <sup>46</sup> |
| 1740                | 19.9                           | 3923             | 0.160              | 1105              |
| 1740                | 28.1                           | 4892             | 0.250              | 1105              |
| 1740                | 38.0                           | 5906             | 0.364              | 945               |
| 2000                | 18.2                           | 3857             | 0.155              | 995               |
| 2000                | 25.1                           | 4625             | 0.223              | 1032              |
| 2000                | 44.1                           | 6431             | 0.432              | 886               |
|                     | olecular $D_2$ beam            |                  | and cowork         |                   |
| 2100                | 35.4                           | 3925             | 0.322              | 816               |
| 2100                | 46.4                           | 4595             | 0.441              | 782               |
| 2100                | 62.6                           | 5377             | 0.829              | 649               |
| $\frac{2100}{2100}$ | 69.2<br>80.1                   | 5658<br>6132     | 0.860<br>0.849     | 717<br>830        |
|                     | ecular $H_2$ beams,            | Abb              | 0.849              |                   |
| Pure mon            | 31.7                           | 5417             | 0.307              | S .               |
| 1435 $1465$         | 32.0                           | 5417             | 0.307              | 826<br>830        |
| 1740                | 38.0                           | 5906             | 0.364              | 945               |
| 1855                | 40.5                           | 6139             | 0.394              | 899               |
| 2000                | 44.1                           | 6431             | 0.432              | 886               |
| 2100                | 47.4                           | 6674             | 0.465              | 913               |
| 2300                | 49.7                           | 6590             | 0.454              | 1351              |
| Pure mol            | ecular $D_2$ beams,            | Auerbach ar      | nd coworker        | $s^{46}$          |
| 1435                | 32.8                           | 4014             | 0.336              | 299               |
| 1790                | 37.8                           | 4196             | 0.368              | 614               |
| 1670                | 38.6                           | 4337             | 0.393              | 371               |
| 1905                | 41.4                           | 4374             | 0.399              | 685               |
| 1975                | 43.0                           | 4461             | 0.415              | 687               |
|                     | ecular $H_2$ beams,            |                  |                    |                   |
| 1118.07             | 25.1                           | 3500             | 0.12794            | 1996              |
| 1331.89             | 29.9                           | 3555             | 0.13200            | 2342              |
| 1438.82             | 32.3                           | 3380             | 0.11932            | 2611              |
| 1501.19<br>1581.35  | 35.7<br>35.5                   | 3151<br>3219     | 0.10371<br>0.10816 | 2819<br>2903      |
|                     | olecular D $_2$ beam           |                  |                    |                   |
| 473                 | 10.0                           | 2004.6           | 0.083              | 528.7             |
| 673                 | 9.7                            | 2127.9           | 0.085              | 297.9             |
| 673                 | 13.9                           | 2256.8           | 0.106              | 741.8             |
| 973                 | 17.6                           | 2484.9           | 0.129              | 881.7             |
| 673                 | 24.6                           | 3204.7           | 0.214              | 766.3             |
| 873                 | 27.5                           | 3302.7           | 0.228              | 906.7             |
| 873                 | 30.1                           | 3449.1           | 0.248              | 955.3             |
| 873                 | 30.6                           | 3521.1           | 0.259              | 909.4             |
| 1223                | 41.9                           | 4015.0           | 0.337              | 1181.0            |
| 1223                | 42.8                           | 4096.5           | 0.350              | 1151.1            |
| 1503                | 52.8                           | 4039.3           | 0.340              | 1744.7            |
|                     | olecular D <sub>2</sub> beam   |                  | coworkers          | 100.0             |
| 300                 | 7.5                            | 1932.3           | 0.078              | 193.6             |
| 500                 | 12.0                           | 2372.5           | 0.117              | 295.1             |
| 900                 | 21.1                           | 3090.8           | 0.199              | 527.4             |
| 1300<br>1700        | 30.5<br>35.0                   | 3625.4<br>3818.9 | 0.274 $0.304$      | 765.6<br>908.9    |
| 1700                | 43.9                           | 4051.2           | 0.304              | 1261.8            |
| 1700                | 45.0                           | 4268.9           | 0.342              | 1097.1            |
|                     | 40.0                           | 4200.0           | 0.000              | 1001.1            |

In practice, even if the prefactor in Eq. 5.10 is not measured in associative desorption, it is still possible to extract normalized values from a wholly experimental procedure, if measured sticking probabilities are also available. This has been done for  $H_2 + Cu(111)^{48,52}$  and  $D_2 + Cu(111)^{46,48,63}$ . In this method, which we call method A1, essentially the sticking probability is described in terms of the initial-state selected probabilities extracted from the associative desorption experiments, thereby obtaining the saturation values describing the latter. Method A1 is described more fully in appendix 5.B.

If no sticking experiments are available, as for the  $H_2 + Au(111)$  system also studied here, the experimentalists may chose not to normalize the extracted reaction probabilities in an absolute sense. However, the extracted reaction probabilities may still be normalized relative to one another. This was done in recent experiments on  $H_2$  and  $D_2 + Au(111)$ , in which  $A_{\nu,J}$  was set to one for  $(\nu = 0, J = 6)$   $H_2$  and for  $(\nu = 0, J = 0)$   $D_2$ , and the  $A_{\nu,J}$  values for different  $(\nu, J)$  states of  $H_2$  and  $D_2$ , respectively, reflected the values of the reaction probabilities relative to these reference states<sup>71</sup>. We will call this method A2, where the A in A2 emphasizes that this method is also wholly experimental.

If no measured sticking probabilities are available for the system of interest, one may still choose to normalize reaction probabilities extracted from associative desorption experiments, but now with reference to theory<sup>48,71</sup>. We label such methods with "B" to emphasize that the normalization is done with reference to theory. In the methods we are aware of, the experimentalists define a translational energy  $E_{\rm max}(\nu, J)$ , which is the maximum translational energy for which the not yet normalized value can still be accurately extracted using Eq. 5.10<sup>48,71</sup>. At higher E this becomes difficult because the desorption flux becomes small due to the exponential factor in Eq. 5.10, leading to too much noise in the determined  $P_{\text{deg}}(E,\nu,J)$ . Parameters can then be described in two ways (methods B1 and B2). Briefly, in method B1 the saturation parameters are determined by setting them equal to the theoretical reaction probability computed for  $E = E_{\text{max}}(\nu, J)$ . The  $E_{1/2}(\nu, J)$  parameters is then determined as the energy at which the computed reaction probability equals half this computed reaction probability. Method B2 aims to improve upon this. Method B1 was previously followed in experimental papers to enable comparison with theory for  $H_2$ ,  $D_2$  and HD desorbing from Cu surfaces<sup>48</sup>, and for  $H_2$  and  $D_2$ desorbing from Au(111)<sup>71</sup>. Further details of methods B1 and B2 are presented in appendix 5.B.

#### Rotational quadrupole alignment parameters.

The rotational quadrupole alignment parameter,  $A_0^{(2)}(E,\nu,J)$ , is computed from initial-state resolved reaction probabilities as follows:<sup>129</sup>

$$A_0^{(2)}(E,\nu,J) = \frac{\sum_{m_J=0}^J (2 - \delta_{m_J,0}) P_r(E,\nu,J,m_J) \left(\frac{3m_J^2}{J(J+1)} - 1\right)}{\sum_{m_J=0}^J (2 - \delta_{m_J,0}) P_r(E,\nu,J,m_J)}.$$
 (5.12)

The rotational quadrupole alignment parameter is a measure of the dependence of the reaction on the alignment of H<sub>2</sub> relative to the surface.

#### Rovibrational state populations of $H_2$ and $D_2$ desorbing from Au(111).

State distributions of desorbing molecules are calculated in the following manner:  $^{71}$ 

$$N(\nu, J) = \int_0^{E_{\max(\nu, J)}} P_{int}(\nu, J, T_S) \sqrt{E} \, e^{\left(-\frac{E}{k_B T_S}\right)} P_{\text{deg}}(E, \nu, J) dE.$$
 (5.13)

Here  $T_S$  is the surface temperature, and  $E_{\rm max}(\nu,J)$  is the maximum kinetic energy sensitivity of the experiment<sup>71</sup>, which is plotted as a function of J in figure 5.B.2. To make a comparison between theory and experiment possible, the experimental  $P_{\rm deg}(E,\nu,J)$  are replaced by the error function expressions of ref.<sup>71</sup>. In order to make this comparison valid, we only integrate Eq. 5.13 up to  $E_{\rm max}(\nu,J)$ . The error function fits derived in ref.<sup>71</sup> are only valid below  $E_{\rm max}(\nu,J)$  and can yield sticking probabilities substantially bigger than one for higher energies. Integration of Eq. 5.13 is done by taking a right Riemann sum with a dE of 0.2 meV. The  $N(\nu,J)$  populations are normalized to the total  $\nu=0$  population according to:.

$$N(\nu, J) = \frac{N(\nu, J)}{\sum_{J} N(\nu = 0, J)}$$
 (5.14)

The ratio  $\nu = 1 : \nu = 0$  can then calculated as:

$$\nu = 1: \nu = 0 = \frac{\sum_{J} N(\nu = 1, J)}{\sum_{J} N(\nu = 0, J)}$$
 (5.15)

The upper limits to J used in Eqs 5.14 and 5.15 are discussed below.

#### 5.2.7 Computational details

All the electronic structure calculations were carried out by performing plane wave periodic DFT calculations using a user modified version of the Vienna Ab Initio Simulation Package<sup>130–133</sup> (VASP). The modification of the computer package concerns an interface to VASP with the LibXC density functional library<sup>134</sup>. The standard VASP projector augmented wave (PAW) potentials<sup>135</sup> and vdW-DF correlation<sup>97,98</sup> as implemented in VASP<sup>136,137</sup> were used for all calculations at the GGA level except for the SRP48 calculations on Pt(111), for which the standard VASP ultrasoft pseudopotentials<sup>138</sup> and PBE correlation<sup>116</sup> were used. Calculations done using a mGGA use mGGA correlation (see table 5.1).

All calculations at the GGA level presented in this work have been carried out using a plane wave cutoff energy of 450 eV together with smearing of 0.2 eV using the Methfessel-Paxton method of order 1. The input parameters for calculations with a mGGA DF can be found in ref. Lattice constants have been calculated using a four atom bulk unit cell and a  $28 \times 28 \times 28$  Monckhorst-Pack k-point grid. All metal slabs consist of six layers of which the bottom two layers were fixed at the ideal bulk interlayer distance. Slab relaxation has been carried out using a  $1 \times 1$  supercell, a  $32 \times 32 \times 1$   $\Gamma$ -centered k-point grid and a vacuum distance of 16 Å. PES calculations have been carried out using a  $3 \times 3$  supercell, a  $11 \times 11 \times 1$   $\Gamma$ -centered k-point grid and a vacuum distance of 16 Å.

# 5.3 Results

#### 5.3.1 Electronic structure

#### Description of the metal.

Table 5.5 shows calculated lattice constants for different DFs, comparing with zero-point energy corrected experimental results<sup>139</sup>. Table 5.6 shows the percentage change of the distance between the top two layers of the metal slab relative to the calculated bulk interlayer distance, also comparing to experimental results<sup>57–59,140–144</sup>.

#### $H_2$ + metal surface PESs

Barrier heights and geometries for  $H_2 + Cu(111)$  for high symmetry geometries are shown in table 5.7. The energetic corrugation  $\xi$ , which is the difference

|    | SAPE |       | 2.48          | 3.31                       | 4.97                 | 1.65         | 1.75         | 2.27                      | 2.47                     | 90.0            | 1.57          | -0.17          |
|----|------|-------|---------------|----------------------------|----------------------|--------------|--------------|---------------------------|--------------------------|-----------------|---------------|----------------|
| _  | UAPE |       | 2.48          | 3.31                       | 4.97                 | 1.65         | 1.75         | 2.27                      | 2.47                     | 0.51            | 1.57          | 0.54           |
|    | %    |       | 2.17          | 3.04                       | 4.98                 | 1.68         | 1.78         | 2.63                      | 2.24                     | -0.13           | 1.84          | 0.48           |
| Pt | Ā    | 3.913 | 3.998         | 4.032                      | 4.108                | 3.979        | 3.983        | $4.016^{12}$              | 4.001                    | 3.908           | $3.985^{139}$ | $3.932^{139}$  |
|    | %    |       | 2.81          | 3.40                       | 5.18                 | 1.75         | 1.88         | 2.42                      | 2.47                     | 0.49            | 1.85          | 0.15           |
| Pd | Ā    | 3.876 | 3.985         | 4.008                      | 4.077                | 3.944        | 3.949        | 3.970                     | 3.972                    | 3.895           | $3.948^{139}$ | $3.882^{139}$  |
|    | %    |       | 0.65          | 1.76                       | 2.82                 | 0.57         | 0.48         | 0.74                      |                          | -0.86           | 0.28          | -1.29          |
| Z  | Ā    | 3.508 | 3.531         | 3.570                      | 3.607                | $3.528^{21}$ | 3.525        | $3.534^{21}$              |                          | 3.478           | $3.518^{139}$ | $3.463^{139}$  |
|    | %    |       | 3.44          | 4.50                       | 6.74                 | 2.56         | 2.68         | 3.34                      | 3.32                     | 0.61            | 2.26          | 0.46           |
| Au | ¥    | 4.062 | $4.202^{145}$ | 4.245                      | 4.336                | 4.166        | 4.171        | 4.198                     | 4.197                    | 4.087           | $4.154^{139}$ | $4.081^{139}$  |
|    | %    |       | 3.56          | 4.38                       | 6.05                 | 2.16         | 2.33         | 2.80                      | 2.88                     | 0.61            | 2.21          | -0.10          |
| Ag | ¥    | 4.062 | $4.207^{20}$  | 4.240                      | 4.308                | 4.150        | 4.157        | 4.176                     | 4.179                    | 4.087           | $4.152^{139}$ | $4.058^{139}$  |
|    | %    |       | 2.30          | 2.80                       | 4.06                 | 1.19         | 1.33         | 1.66                      | 1.47                     | -0.37           | 1.00          | -0.73          |
| Cu | Ā    | 3.596 | 3.679         | 3.697                      |                      |              |              |                           |                          |                 |               | $3.570^{139}$  |
|    |      | exp.  | $SRP48^{63}$  | $^{\mathrm{vdW-DF1}^{97}}$ | $^{ m vdW-DF2}^{98}$ | B86SRP68-DF2 | SRPsol63-DF2 | $PBE_{\alpha}57-DF2^{12}$ | $^{ m optPBE-DF1}^{115}$ | $MS-B86b1^{13}$ | $PBE^{116}$   | $PBEsol^{118}$ |

Table 5.5: Zero-point energy corrected experimental lattice constants  $^{139}$  in Å and percentage deviations of computed values from the experimental value. The UAPE and the SAPE are the unsigned and signed average percentage differences with the experimental value, respectively.

to the bulk interlayer distance in %.

| $0.8\%^{146}$ | $0.6\%^{146}$  |                | $0.8\%^{146}$ | $-0.1\%^{146}$         | $-0.4\%^{146}$           | PBEsol <sup>118</sup>  |
|---------------|----------------|----------------|---------------|------------------------|--------------------------|------------------------|
|               | $-0.5\%^{146}$ |                | $1.0\%^{146}$ | $-0.2\%^{146}$         | $-0.3\%^{146}$           | $PBE^{116}$            |
|               | 0.3%           |                | 1.0%          | -0.5%                  | -1.0%                    | MS-B86bl <sup>13</sup> |
| 0.8%          | 0.2%           |                | 1.0%          | -0.2%                  | $-0.8\%^{42}$            | optPBE-DF1115          |
|               | 0.6%           | $-0.8\%^{21}$  | 1.5%          | 0.0%                   | -0.4%                    | $PBE\alpha57-DF2^{12}$ |
|               | 0.6%           | -1.1%          | 1.4%          | -0.2%                  | -0.4%                    | SRPsol63-DF2           |
|               | 0.7%           | $-1.1\%^{21}$  | 1.3%          | -0.1%                  | -0.4%                    | B86SRP68-DF2           |
|               | 0.8%           | -1.1%          | 2.1%          | 0.5%                   | 0.0%                     | $vdW-DF2^{98}$         |
|               | 0.7%           | -1.1%          |               | 0.1%                   | -0.2%                    | vdW-DF197              |
| 1.0%          | 0.0%           | $-1.0\%^{21}$  | $0.6\%^{145}$ | $-0.6\%^{20}$          | $-1.3\%^{11}$            | $SRP48^{11}$           |
| $1.1\%^{144}$ | $1.3\%^{143}$  | $-0.07\%^{57}$ |               | $-2.5\%,^{140},^{141}$ | -1.0%, 57, 59 $-0.7%$ 58 | exp.                   |
| 1.            | Fu             | INI            | Au            | Ag                     | Cu                       |                        |

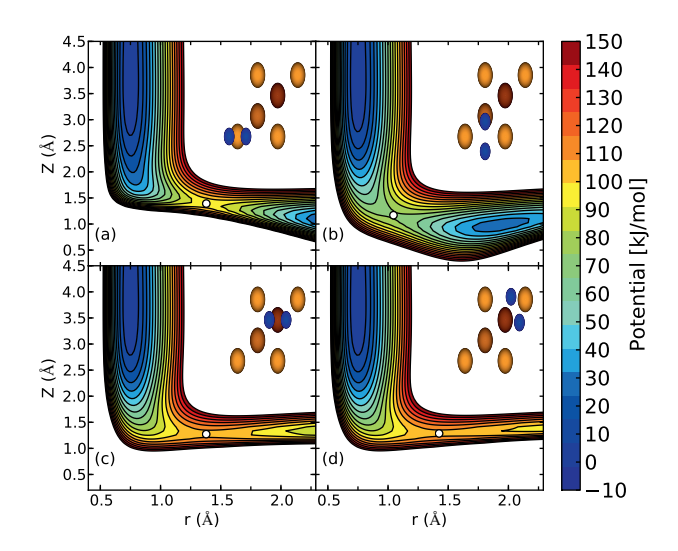


FIGURE 5.2: Elbow plots, i.e. V(Z,r) resulting from the  $H_2 + Cu(111)$  PES computed using the B86SRP68-DF2 DF and interpolated using the CRP method for four high symmetry geometries in which the molecular axis is parallel to the surface ( $\theta = 90^{\circ}$ ) as depicted by the insets for (a) the top site and  $\phi = 0^{\circ}$ , (b) the bridge site and  $\phi = 90^{\circ}$ , (c) the fcc site and  $\phi = 0^{\circ}$ , and (d) the t2f site and  $\phi = 120^{\circ}$ . Barrier positions are indicated with white circles.

between the highest and the lowest barrier height, is shown as well. Elbow plots for four geometries are shown in figure 5.2 for the B86SRP68-DF2 SRP-DF.

Barrier heights and positions for  $H_2 + Ag(111)$ , Au(111) and Pt(111) are shown in tables 5.8, 5.9 and 5.10 respectively. With respect to the  $H_2 + Pt(111)$  system the most striking result is that only the  $PBE\alpha57-DF2^{12}$  and  $MS-PBE1^{13}$  DFs exhibit a double barrier structure for the top-to-bridge (t2b) geometry whereas the other DFs tested do not. The  $PBE\alpha57-DF2^{12}$  SRP-DF is the only DF that predicts a negative early barrier to reaction for this reaction.

We have checked the fit accuracy of our CRP<sup>121</sup> PES for the B86SRP68-DF2 DF for  $H_2 + Cu(111)$  using ~4900 randomly sampled geometries. Based on all the randomly sampled points taken together our CRP<sup>121</sup> fit has a root mean square (rms) error of 31 meV. When only looking at the 3538 geometries that have an interaction energy of  $H_2$  with the surface lower then 4 eV the rms error is reduced to 8 meV (~0.2 kcal/mol). Our CRP<sup>121</sup> PES is thus highly accurate with respect to the underlying electronic structure calculations. Since the other PESs calculated for this paper have been constructed in the same manner, we presume their accuracy with respect to the electronic structure calculations to be similar, and high enough for our purposes.

| refers to the COM of the molecule being placed on a top site, with the H-atoms | $\theta = 90^{\circ}$ . The high symmetry locations are shown in figure 5.1b, the t2b geometry | For the bridge site $\phi = 90^{\circ}$ and $\theta = 90^{\circ}$ , for the t2b and hcp geometries $\phi = 0^{\circ}$ and | Table 5.7: Barrier heights for $H_2$ reacting on $Cu(111)$ for high symmetry geometries | MS-B86bl <sup>13</sup> | optPBE-DF1 <sup>42</sup> | $\mathrm{PBE}_{lpha}$ 57- $\mathrm{DF}2$ | SRPsol63-DF2 | B86SRP68-DF2 | ${ m SRP48^{11,42}}$ |                  |          |
|--|--|---|---|------------------------|--------------------------|--|--------------|--------------|----------------------|------------------|----------|
| COM  | e high s   | ge site $\phi$  | Barrier l   | 0.683                  | 0.712                    | 0.720                                    | 0.712        | 0.725        | 0.636                | $\mathrm{E}_{b}$ |          |
| of the r   | symmeti  | $=90^{\circ}$   | heights i   | 0.997                  | 1.053                    | 1.063                                    | 1.045        | 1.045        | 1.030                | $\mathbf{r}_b$   | bridge   |
| nolecule   | ry locat   | and $\theta =$  | for $ m H_2$ r  | 1.205                  | 1.165                    | 1.142                                    | 1.167        | 1.169        | 1.172                | $\mathbf{Z}_b$   |          |
| e being  | ions are   | : 90°, fo   | eacting   | 0.895                  | 0.915                    | 0.934                                    | 0.925        | 0.936        | 0.887                | $\mathrm{E}_{b}$ |          |
| placed   | shown  | r the t2  | on Cu(1   | 1.351                  | 1.382                    | 1.385                                    | 1.379        | 1.380        | 1.396                | $\mathbf{r}_b$   | t2b      |
| on a to  | in figu  | b and h   | .11) for  | 1.391                  | 1.396                    | 1.390                                    | 1.392        | 1.392        | 1.394                | $Z_b$            |          |
| p site,  | re 5.1b,   | ıcp geor  | high syı  | 1.079                  | 1.070                    | 1.035                                    | 1.038        | 1.056        | 1.047                | $\mathrm{E}_{b}$ |          |
| with th  | the t2l  | netries   | $\operatorname{mmetry}$   | 1.369                  | 1.427                    | 1.373                                    | 1.373        | 1.379        | 1.539                | $\mathbf{r}_b$   | hcp      |
| ie H-ato   | b geome  | $\phi = 0^{\circ}$  | geomet  | 1.266                  | 1.271                    | 1.268                                    | 1.270        | 1.273        | 1.269                | $\mathbf{Z}_b$   |          |
| $_{ m ms}$   | $\operatorname{try}$   | and   | ries.   | 0.396                  | 0.358                    | 0.315                                    | 0.326        | 0.331        | 0.411                |                  | <b>√</b> |
|  |  |   |   |                        |                          |  |              |              |                      |                  |          |

pointing to the nearest bridge sites. Barrier heights are in eV, and the barrier positions in Å. Additionally the energetic corrugation,  $\xi$ , is also shown in eV.

|  |            | $_{ m bridge}$ |                 |               | t2b             |                     |                  | $_{\rm fcc}$  |                  |
|--|------------|----------------|-----------------|---------------|-----------------|---------------------|------------------|---|------------------|
|  | Ē          | $\Gamma_b$     | $Z_b$           | $E_b$         | $\Gamma b$      | $  Z_b   E_b   r_b$ | $\mathbf{E}_{b}$ | r <sub>b</sub>  | $\mathbf{Z}_{b}$ |
| $\mathrm{SRP48}^{20}$  | 1.38       | 1.27           | 1.10            | 1.69 1.57     | 1.57            | 1.51                | 1.51 1.70        | 1.67  | 1.34             |
| B86SRP68-DF2   1.379   1.286   1.125   1.614   1.549   1.510   1.608   1.591   1.354   | 1.379      | 1.286          | 1.125           | 1.614         | 1.549           | 1.510               | 1.608            | 1.591   | 1.354            |
| $\mathrm{PBE}_{lpha}$ 57- $\mathrm{DF}$ 2  | 1.409      | 1.292          | 1.114           | 1.640         | 1.555           | 1.511               | 1.613            | $1.409 \mid 1.292 \mid 1.114 \mid 1.640 \mid 1.555 \mid 1.511 \mid 1.613 \mid 1.586 \mid 1.348$ | 1.348            |
| MS-PBEI  | 1.288      | 1.230          | 1.116           | 1.534         | 1.508           | 1.493               | 1.601            | 1.288   1.230   1.116   1.534   1.508   1.493   1.601   1.566                                   | 1.314            |
|  |            |                |                 |               |                 |                     |                  |   |                  |
| Table 5.8: Barrier heights for H <sub>2</sub> reacting on Ag(111). For the bridge site $\phi = 90^{\circ}$                   | rier heig  | shts for       | ${ m H}_2$ reac | ting on       | Ag(1111         | ). For t            | he bridg         | ge site $\phi$  | = 60             |
| and $\theta = 90^{\circ}$ , while for the t2b and fcc sites $\phi = 0^{\circ}$ and $\theta = 90^{\circ}$ . The high symmetry | ile for tl | ne t2b a       | nd fee s        | ites $\phi =$ | $0^{\circ}$ and | $\theta = 60$       | . The l          | nigh syn  | nmetry           |
| locations are shown in figure 1b, the t2b geometry refers to the COM of the molecule   | wn in fi   | gure 1b,       | the t2b         | geome         | ry refer        | s to the            | COM              | of the m  | olecule          |
| being placed on a top site, with the molecular bond pointing to a bridge site. Barrier                                       | a top sit  | e. with        | the mol         | ecular b      | od puo          | inting to           | a brids          | ze site.  | 3arrier          |

a top site, with the molecular bond pointing to a Di heights are in eV, and the barrier positions in Å.

| pointing to a bridge site. Barrier heights are in eV, and the barrier positions in A. | to the COM of the molecule being placed on a top site, with the molecular bond | $\theta = 30^{\circ}$ . The high symmetry locations are shown in figure 1b, the t2b geometry refers | and $\theta = 90^{\circ}$ , for the t2b site $\phi = 0^{\circ}$ and $\theta = 90^{\circ}$ , and for the t2h site $\phi = 0^{\circ}$ and | Table 5.9: Barrier heights for H <sub>2</sub> reacting on Au(111). For the bridge site $\phi = 90^{\circ}$ | MS-B86bl <sup>13</sup>                                       | MS-PBEl <sup>13</sup> | B86SRP68-DF2 | $\mathrm{PBE}_{lpha}$ 57- $\mathrm{DF}2$ | $SRP48^{145}$ | PBE   |                  |                               |
|---|--|---|---|--|--|-----------------------|--------------|--|---------------|-------|------------------|-------------------------------|
| a bridge  | of the   | high sy   | , for the   | Barrier  | 1.481  | 1.432                 | 1.470        | 1.496                                    | 1.407         | 1.245 | $\mathbf{E}_{b}$ |                               |
| site. B   | molecu   | $_{ m mmetry}$  | e t2b sit   | $_{ m heights}$  | 1.142  | 1.144                 | 1.218        | 1.232                                    | 1.180         | 1.187 | $\mathbf{r}_b$   | bridge                        |
| arrier k  | le being   | locatio   | $e \phi = 0$  | for $H_2$  | 1.130  | 1.127                 | 1.091        | 1.071                                    | 1.089         | 1.096 | $Z_b$            |                               |
| eights a  | placed   | ns are s  | )° and $\bar{\ell}$   | reacting   | 1.355  | 1.301                 | 1.333        | 1.340                                    | 1.382         | 1.237 | $\mathbf{E}_{b}$ |                               |
| are in e  | on a to  | hown in   | $\theta = 90^{\circ}$   | on Au  | 1.438  | 1.433                 | 1.480        | 1.492                                    | 1.493         | 1.504 | $\mathbf{r}_b$   | t2b                           |
| V, and $t$  | op site,   | figure 1  | and fo  | (111). F   | 1.467  | 1.466                 | 1.470        | 1.469                                    | 1.470         | 1.468 | $Z_b$            |                               |
| the barr  | with th  | b, the t  | r the t2  | or the b   | 1.753  | 1.701                 | 1.704        | 1.707                                    | 1.783         | 1.637 | $\mathbf{E}_{b}$ | t2                            |
| ier posi  | ie mole  | 2b geon   | h site q  | oridge si  | 1.583  | 1.578                 | 1.659        | 1.664                                    | 1.689         | 1.685 | $\mathbf{r}_b$   | $\mathrm{t2h}\;\phi=30^\circ$ |
| tions in  | cular bo   | netry ref   | $\delta = 0^{\circ} a$  | te $\phi = 9$  | 1.130   1.355   1.438   1.467   1.753   1.583   1.539   0.2° | 1.538                 | 1.556        | 1.558                                    | 1.552         | 1.549 | $Z_b$            | 0°                            |
| A   | $\inf_{\circ}$   | ers   | $\operatorname{pn}_{\parallel}$   | °00  | 0.2  | 0.26                  | 0.23         | 0.2                                      | 0.37          | 0.39  |                  | Λ-                            |

0.392 0.376 0.211 0.234 0.269 0.272

Additionally the energetic corrugation,  $\xi$ , is shown in eV as well.

|                             | t                | 2b early      |                  |                  | t2b late |                  |                | bridge   |                  | t2             | $^{\mathrm{t}}2\mathrm{h}~\phi=30^{\circ}$ | 5     |
|-----------------------------|------------------|---------------|------------------|------------------|----------|------------------|----------------|----------|------------------|----------------|--|-------|
|                             | $\mathbb{E}_{b}$ | $^{\Gamma_b}$ | $\mathbf{Z}_{b}$ | $\mathbb{E}_{b}$ | $r_b$    | $\mathbf{Z}_{b}$ | $\mathbb{E}_b$ | $^{r_b}$ | $\mathbf{Z}_{b}$ | $\mathbb{E}_b$ | $\mathbf{r}_{b}$                           | $Z_b$ |
| Ĺ                           | 960.0            | 0.769         | 2.256            |                  |          |                  | 0.473          | 0.831    | 1.628            | 0.252          | 0.802                                      | 1.860 |
| _                           | 0.050            | 0.776         | 2.157            |                  |          |                  | 0.505          | 0.853    | 1.547            | 0.246          | 0.816                                      | 1.778 |
| $PBE_{\alpha}57-DF2^{12}$ - | -0.008           | 0.769         | 2.202            | -0.055           | 1.096    | 1.549            | 0.275          | 0.837    | 1.777            | 0.200          | 0.837                                      | 1.679 |
| _                           | 0.145            | 992.0         | 2.205            | -0.035           | 1.096    | 1.529            | 0.616          | 0.838    | 1.599            | 0.339          | 0.800                                      | 1.840 |

Table 5.10: Barrier heights for H<sub>2</sub> reacting on Pt(111). For the bridge site  $\phi = 90^{\circ}$ and  $\theta=90^\circ$ , for the t2b site  $\phi=0^\circ$  and  $\theta=90^\circ$ , and for the t2h site  $\phi=0^\circ$  and  $\theta=30^\circ$ . The high symmetry locations are shown in figure 1b, the t2b geometry refers to the COM of the molecule being placed on a top site, with the molecular bond pointing to a bridge site. Barrier heights are in eV, and the barrier positions in Å.

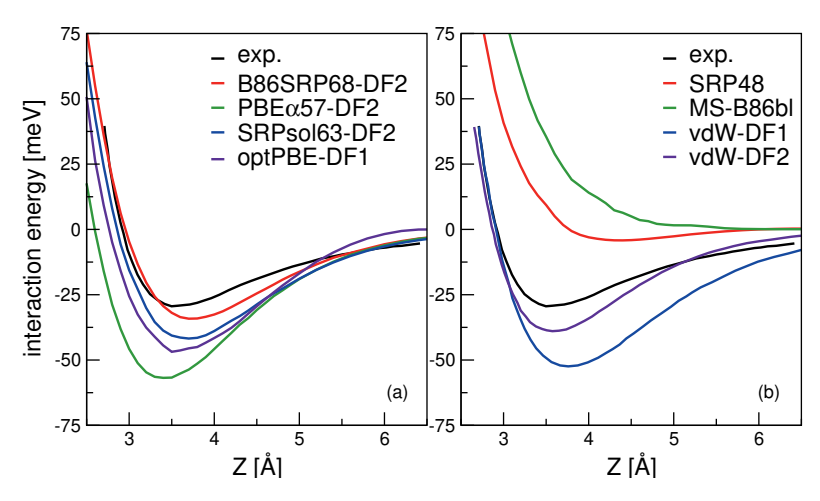


FIGURE 5.3: The computed interaction energy of  $H_2$  parallel to the Cu(111) surface above a top site ( $\phi = 0^{\circ}, \theta = 90^{\circ}$ ) is compared with experimental results<sup>60</sup> (black). Panel (a) shows the calculated Van der Waals well for the B86SRP68-DF2 (red), PBE $\alpha$ 57-DF2 (green), SRPsol63-DF2 (blue) and optPBE-DF1<sup>42</sup> (purple) DFs, and panel (b) for the SRP48<sup>11</sup> (red), MS-B86bl<sup>13</sup> (green), vdW-DF1<sup>97</sup> (blue) and vdW-DF2<sup>98</sup> (purple) DFs.

#### Van der Waals wells

Figures 5.3a and b show Van der Waals potential curves for  $H_2$  in a parallel orientation ( $\phi = 0^{\circ}, \theta = 90^{\circ}$ ) above a top atom of Cu(111) for different DFs, comparing with experimental results<sup>60</sup>. Panel a shows calculated Van der Waals wells obtained with the non-standard DFs with non-local Van der Waals correlation investigated in this work. Panel b shows Van der Waals potential curves for SRP-DFs developed previously in our group<sup>11,13</sup>, as well as for the two standard vdW-DF1<sup>97</sup> and vdW-DF2<sup>98</sup> DFs. Agreement with experiment is best for the B86SRP68-DF2 DF.

All Van der Waals well depths and geometries for the systems and DFs investigated in this work are tabulated in table 5.11. With respect to the Van der Waals well depths for  $H_2 + Ag(111)$ ,  $H_2 + Au(111)$ , and  $H_2 + Pt(111)$  we find depths that are in good agreement with experimental work<sup>62,91,100,111</sup> for the B86SRP68-DF2 DF.

| Cu(111)            | Z [Å]                  | $E_{vdW}$ [meV]        |
|--------------------|------------------------|------------------------|
| exp.               | $3.51^{60}, 2.71^{62}$ | $29.5^{60}, 22.2^{62}$ |
| $SRP48^{11}$       | 4.38                   | 3.73                   |
| vdW-DF1            | 3.77                   | 52.4                   |
| vdW-DF2            | 3.58                   | 39.0                   |
| B86SRP68-DF2       | 3.74                   | 34.3                   |
| $PBE\alpha57-DF2$  | 3.34                   | 56.7                   |
| SRPsol63-DF2       | 3.71                   | 41.8                   |
| $optPBE-DF2^{42}$  | 3.52                   | 46.9                   |
| Ag(111)            |                        |                        |
| exp. <sup>91</sup> | 1.98                   | 32.5                   |
| $SRP48^{20}$       | 4.42                   | 2.3                    |
| B86SRP68-DF2       | 3.75                   | 33.3                   |
| $PBE\alpha57-DF2$  | 3.39                   | 56.1                   |
| Au(111)            |                        | •                      |
| exp. <sup>62</sup> | 2.2                    | 40.0                   |
| $SRP48^{145}$      | 4.26                   | 3.0                    |
| B86SRP68-DF2       | 3.62                   | 41.4                   |
| $PBE\alpha57-DF2$  | 3.30                   | 68.7                   |
| Pt(111)            |                        |                        |
| exp.               |                        | $55^{100}, 76^{111}$   |
| SRP48              | 4.14                   | 5.5                    |
| B86SRP68-DF2       | 3.48                   | 48.0                   |
| $PBE\alpha57-DF2$  | 3.24                   | 72.4                   |

TABLE 5.11: Van der Waals well depths and positions for Cu(111), Ag(111), Au(111) and Pt(111).

## 5.3.2 Molecular beam sticking probabilities

Molecular beam sticking probabilities computed with five DFs for  $H_2$  and  $D_2$  reacting on Cu(111) are shown in figure 5.4, comparing to experimental results of Auerbach and coworkers<sup>46,52</sup> and Rendulic and coworkers<sup>47</sup>. Figure 5.5 shows the comparison with an additional experiment for the five DFs discussed here, namely for the pure  $D_2$  molecular beams of Auerbach and coworkers<sup>46</sup>. The difference between theory and experiment is assessed by determining how far the theoretical result needs to be shifted along the incidence energy axis to be superimposed on a spline interpolated curve going through the experimental results. Values of the mean absolute deviation (MAD) are calculated as the mean of the absolute number of these shifts for a particular set of molecular beam experiments From the MAD values it can be seen that all five DFs considered describe the experiments on  $H_2 + Cu(111)$  shown in figure 5.4 with chemical accuracy. Figure 5.6 shows comparisons to two additional sets of molecular beam experiments of Auerbach and coworkers<sup>46,52</sup> for  $H_2$  reacting on Cu(111) for a more limited set of DFs.

For the B86SRP68-DF2 DF QD results are also shown for the experiments concerning  $H_2$  in figures 5.4e,f and in figure 5.6. Note that in these figures the

QCT results are based on more rovibrational states than those included in the QD calculations (see table 5.3). In figure 5.7 we also explicitly compare QCT and QD results obtained while averaging over the same rovibrational states, and compare those to the QCT results shown in figures 5.4e,f and in figure 5.6. Table 5.12 displays the computed MADs for all experiments considered.

Figure 5.8 shows molecular beam sticking experiments for D<sub>2</sub> reacting on Ag(111). Experimental results of Hodgson and coworkers<sup>147</sup> are also shown. The calculated results are obtained using the pure D<sub>2</sub> molecular beam parameters of Auerbach and coworkers<sup>46</sup> obtained from experiments on Cu(111). The DFs treated in this work, as well as the MS-PBEl mGGA<sup>13</sup>, reproduce the experiment to almost within chemical accuracy. The SRP48 DF<sup>20,63</sup> yields the worst and the MS-PBEl<sup>13</sup> the best performance.

In figure 5.9 molecular beam sticking probabilities for D<sub>2</sub> reacting on Pt(111) for three DFs are shown, comparing to the molecular beam experiments of Luntz et al.<sup>65</sup>. A comparison to the experimental results of Cao et al.<sup>61</sup> is shown in figure 5.10. For the comparison to the experiment of Luntz et al.<sup>65</sup> the molecular beam parameters of Groot et al.<sup>128</sup> are used, while Cao et al.<sup>61</sup> have actually reported their molecular beam parameters. Figure 5.9a shows that the B86SRP68-DF2 DF describes the experiment<sup>65</sup> with overall chemical accuracy, albeit that the energy shifts are larger than 4.2 kJ/mol at the lowest energies. However, figure 5.10a shows that the experiments of Cao et al.<sup>61</sup> are not described to within chemical accuracy using the B86SRP68-DF2 DF. The SRP48 and MS-PBEl DFss are not able to describe either experiment to within chemical accuracy.

The parameters describing the beams used in the experiment can be found in table 5.4.

### 5.3.3 Initial-state resolved reaction probabilities

Initial-state resolved reaction probabilities will be presented for  $H_2$  reacting on both Cu(111) and Ag(111). Figure 5.11 shows fully initial-state resolved reaction probabilities for  $H_2$  reacting on Cu(111), as obtained with the QD and QCT methods. At the level of degeneracy averaged reaction probabilities the agreement is very good (figures 5.11a,c), but the QD method predicts a slightly larger orientational dependence of the reaction probability (figure 5.11b). Figure 5.12 shows a comparison of degeneracy averaged reaction probabilities obtained using the QD and QCT method for the 20 rovibrational states included in the QD calculations. The agreement between the QD and QCT method is very good for all states, though there are some differences for the J < 3 rovibrational states.

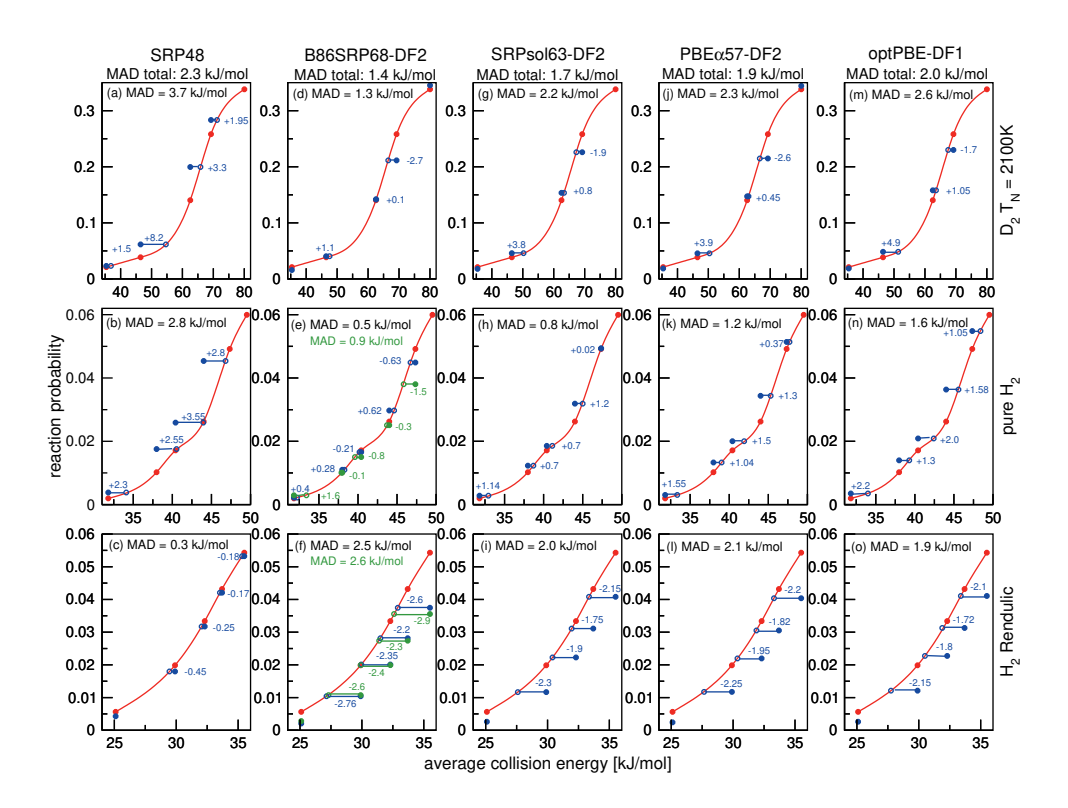


FIGURE 5.4: Molecular beam sticking probabilities for H<sub>2</sub> and D<sub>2</sub> reacting on Cu(111) for three sets of molecular beam experiments, as computed with five SRP-DFs. Experimental results are shown in red<sup>46,47,52</sup>, QCT results are shown in blue, and QD results are shown in green in two panels (panels e and f). The values next to each data point denote the shift along the translational energy axis from the computed reaction probability to the interpolated experimental reaction probability curve in kJ/mol. The MAD values are the mean value of the absolute energy differences for each experiment.

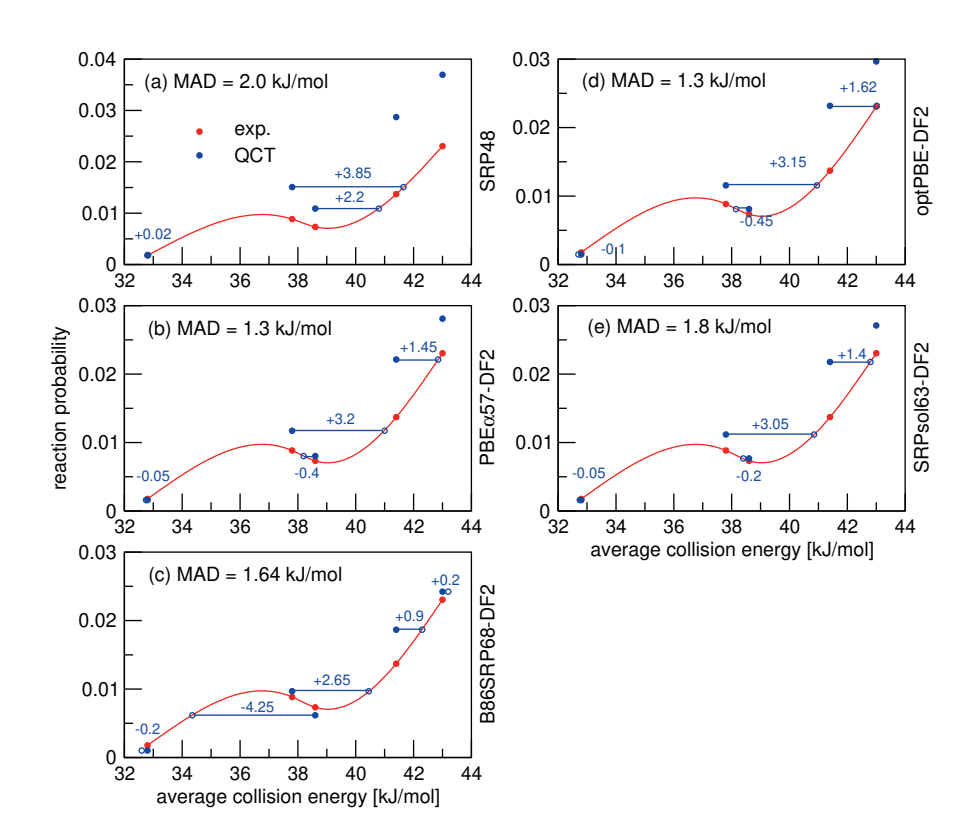


FIGURE 5.5: Molecular beam sticking probabilities for  $D_2$  reacting on Cu(111). Experimental values are shown in red<sup>46</sup>. QCT results are shown in blue. The values next to each data point denote the shift along the translational energy axis from the computed reaction probability to the interpolated experimental reaction probability curve in kJ/mol.

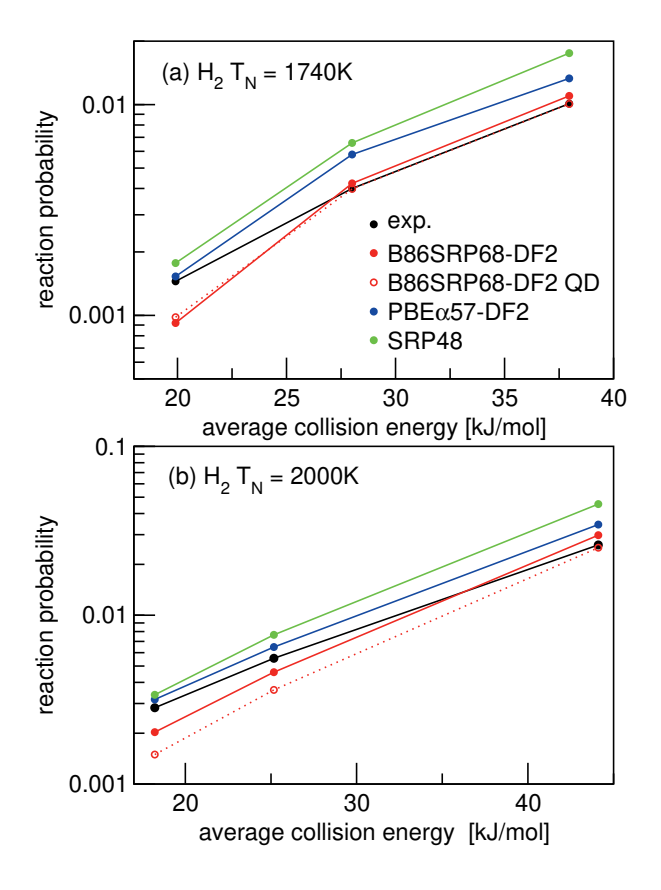


FIGURE 5.6: Molecular beam sticking probabilities for  $H_2$  reacting on Cu(111). Experimental values are shown in black<sup>52</sup>, computed reaction probabilities are shown for the B86SRP68-DF2 (red), PBE $\alpha$ 57-DF2 (blue), and the SRP48 (green) DFs. The solid lines correspond to QCT calculations, the dashed lines to QD calculations.

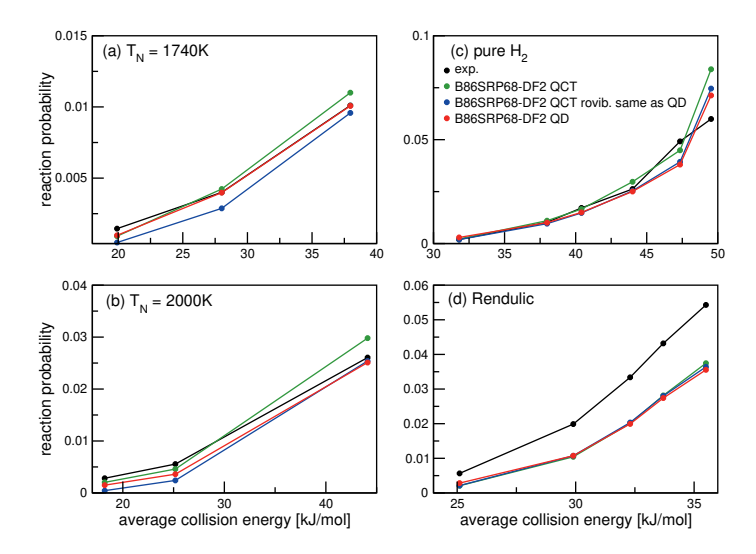


FIGURE 5.7: Molecular beam sticking probabilities for H<sub>2</sub> reacting on Cu(111). Experimental values are shown in black<sup>52</sup>, B86SRP68-DF2 QCT results are shown in green, B86SRP68-DF2 QCT results based on the same rovibrational states as taken into account in the QD calculations in blue, and B86SRP68-DF2 QD results in red.

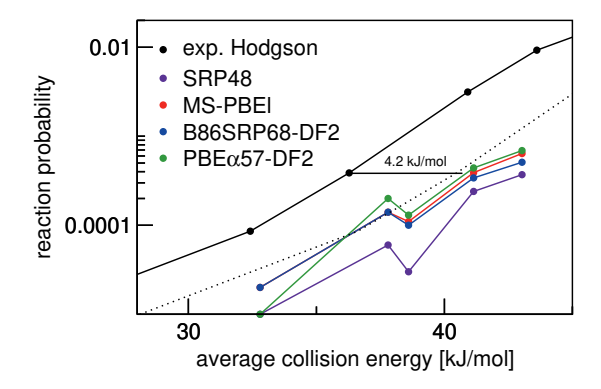


FIGURE 5.8: Molecular beam sticking probability as a function of the average incidence energy for  $D_2$  reacting on Ag(111). Experiment is shown in black<sup>147</sup>. QCT results are shown for the following DFs: SRP48 (purple)<sup>20</sup>, MS-PBEl (red)<sup>13</sup>, B86SRP68-DF2 (blue), and PBE $\alpha$ 57-DF2 (green). The dotted line represents the experimental curve shifted by 4.2 kJ/mol, denoting the limit to chemical accuracy.

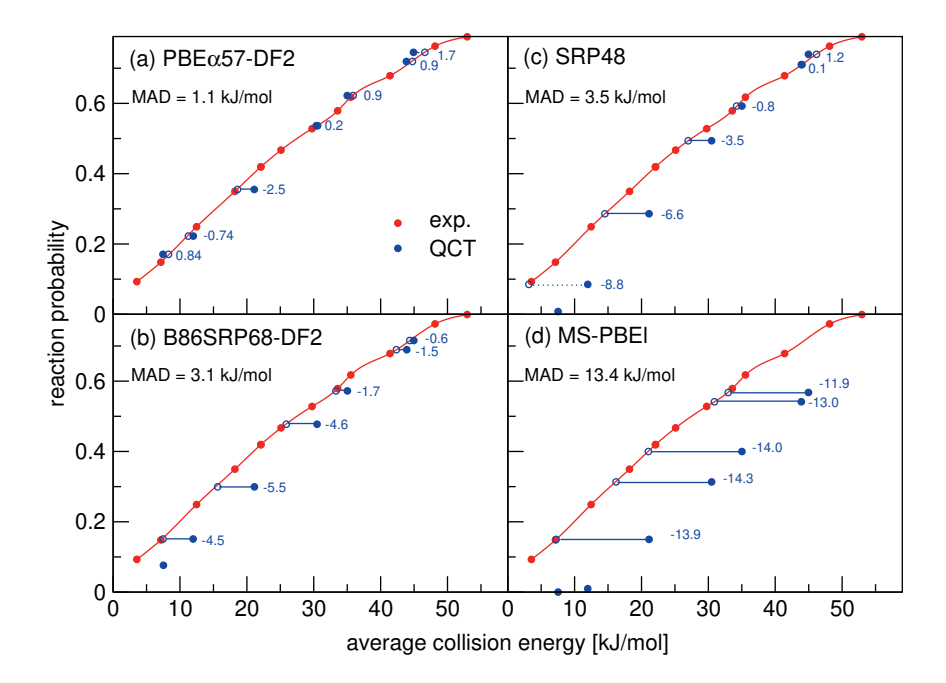


FIGURE 5.9: Molecular beam sticking probabilities for  $D_2$  reacting on Pt(111) for (a) the PBE $\alpha$ 57-DF2, (b) B86SRP68-DF2, (c) SRP48 and (d) MS-PBEl DFs. Experimental results are shown in red<sup>65</sup>, QCT results in blue. The values next to each data point denote the shift along the translational energy axis from the computed reaction probability to the interpolated experimental reaction probability curve.

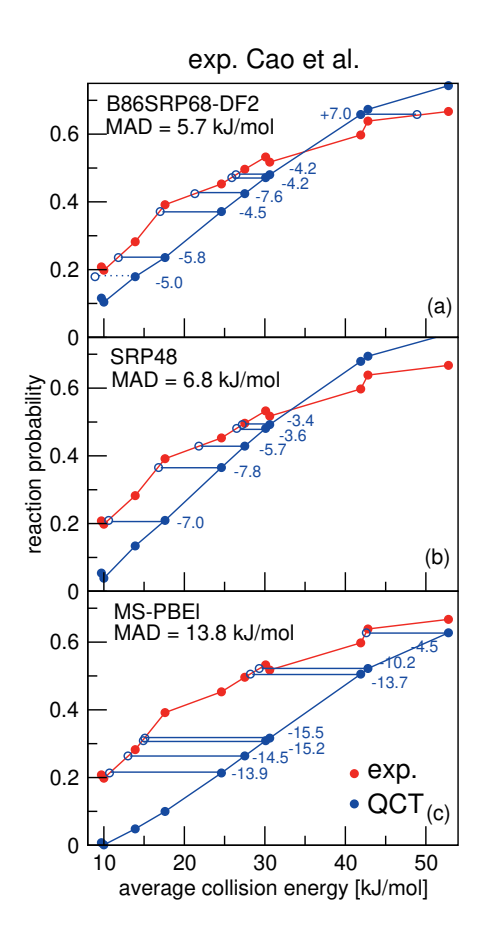


FIGURE 5.10: Molecular beam sticking probabilities for  $D_2$  reacting on Pt(111) for the B86SRP68-DF2, SRP48 and MS-PBEl functionals. Experimental values are shown in red<sup>61</sup>. QCT results are shown in blue. The values next to each data point denote the shift along the translational energy axis from the computed reaction probability to the interpolated experimental reaction probability curve.

| $K = H_2 \; T_N =$     | O MAD MSD          | 2.6   | 0.4 0.4      | 0.9 0.5      | 1.7 1.7                   | 1.4 1.4    | _ |
|------------------------|--------------------|-------|--------------|--------------|---------------------------|------------|---|
| = 2000                 | MSD                | 1.6   | -1.9         | 0.2          | 8.0                       | 9.0        |   |
| $H_2 T_N$              | MAD                | 1.6   | 1.9          | 0.2          | 8.0                       | 9.0        |   |
| dulic47                | MSD                | -0.3  | -2.5         | -2.0         | -2.1                      | -1.9       |   |
| H <sub>2</sub> Renduli | MAD                | 0.3   | 2.5          | 2.0          | 2.1                       | 1.9        |   |
| pure H <sub>2</sub>    | MSD                | 2.8   | 0.3          | 8.0          | 1.2                       | 1.6        |   |
| pure                   | MAD                | 2.8   | 0.5          | 8.0          | 1.2                       | 1.6        |   |
| $D_2$                  | MSD                | 2.0   | -0.1         | 1.1          | 1.1                       | 1.1        |   |
| pure D <sub>2</sub>    | MAD                | 2.0   | 1.6          | 1.2          | 1.3                       | 1.3        |   |
| $= 2100 \mathrm{K}$    | MSD                | 3.7   | -0.5         | 6.0          | 9.0                       | 1.4        |   |
| $D_2 T_N$              | MAD                | 3.7   | 1.3          | 2.2          | 2.3                       | 2.6        |   |
| $H_2 / D_2 + Cu(111)$  | exp. <sup>46</sup> | SRP48 | B86SRP68-DF2 | SRPsol63-DF2 | $PBE_{\alpha}57-DF2^{12}$ | optPBE-DF2 |   |

exp. Cao<sup>61</sup>
MAD | MSD
1.9 -1.1
6.8 -6.8
5.7 -3.5
13.8 -13.8

exp. Luntz<sup>65</sup>

MAD MSD

1.1 0.19

3.5 -3.1

3.1 -3.1

13.4 -13.4

 $PBE_{lpha}57\text{-}DF2 \ SRP48 \ B86SRP68\text{-}DF2 \ MS-PBE<math>^{13}$ 

 $D_2 + Pt(111)$ 

| exp. Hodgson <sup>55</sup> | MSD | -8.4         | -4.6         | -4.3                              | 7.5            |
|----------------------------|-----|--------------|--------------|-----------------------------------|----------------|
|                            | MAD | 8.4          | 4.6          | 4.3                               | 4.5            |
| $D_2 + Ag(111)$            |     | $SRP48^{20}$ | B86SRP68-DF2 | ${ m PBE}_{lpha 57}$ -DF $2^{12}$ | $MS-PBEl^{13}$ |

Table 5.12: Mean absolute and mean signed deviations (MADs and MSDs, in kJ/mol) of the sticking probabilities computed with different DFs for the experimental reaction probability curves.

Figure 5.13 shows degeneracy averaged initial-state resolved reaction probabilities for  $H_2$  and  $D_2$  reacting on Ag(111). A comparison is made to reaction probabilities extracted from associative desorption experiments assuming detailed balance<sup>78,79</sup>. The agreement with experiment seems best for  $D_2$  and when using the MS-PBEl mGGA<sup>13</sup>. Note, however, that the  $P_{\text{deg}}(E, \nu, J)$  extracted from experiments were not normalized, but simply assumed to saturate at unity, making it hard to perform an accurate comparison with experiment.

### **5.3.4** $\mathbf{E}_{1/2}(\nu, J)$ parameters

 $E_{1/2}(\nu,J)$  parameters calculated for  $H_2$  ( $D_2$ ) + Cu(111) using method A1 and method B1 are shown in figure 5.14 and figure 5.15, respectively, also comparing with experiment<sup>48</sup>. Using method B1, the DFs that include non-local correlation qualitatively reproduce the rotational hindering observed experimentally for  $(\nu=0)$ , i.e. the increase of  $E_{1/2}(\nu,J)$  parameters with increasing J for low J before decreasing with increasing J. A third degree polynomial has been fitted to the calculated  $E_{1/2}(\nu,J)$  parameters, which describes the dependence of the  $E_{1/2}(\nu,J)$  parameters on J. The polynomials are shown, without the energy axis offset resulting from the fit to a third degree polynomial, in figure 5.16.

 $E_{1/2}(\nu, J)$  parameters calculated for  $H_2$  ( $D_2$ ) + Au(111) using method B2 are shown in figure 5.17, also comparing to experiment<sup>71</sup>.

Accompanying MAD and mean signed deviations (MSD) values of the computed  $E_{1/2}(\nu, J)$  parameters from the experimental values are presented in table 5.13 for both  $H_2$  (D<sub>2</sub>) + Cu(111) and  $H_2$  (D<sub>2</sub>) + Au(111).

# 5.3.5 Rotational quadrupole alignment parameters Cu(111)

In figure 5.18 we compare calculated rotational quadrupole alignment parameters using the QCT method to experimental ones for  $D_2$  desorbing from  $Cu(111)^{50}$ . Note that a positive  $A_0^{(2)}(\nu, J)$  indicates a preference for parallel reaction, a negative value a preference for perpendicular reaction, and zero means the reaction proceeds independent of  $D_2$  orientation. We observe only a monotonous increase of the rotational quadrupole alignment parameters with decreasing translational energy, indicating that at translational energies close to the reaction threshold molecules prefer to react in a parallel orientation.

# 5.3.6 Inelastic scattering of $H_2$ from Cu(111)

Vibrationally inelastic scattering probabilities,  $P(\nu = 0, J \rightarrow \nu = 1, J = 3)$  for  $H_2$  scattering from Cu(111) are shown in figure 5.19 for scattering from the initial J = 1, 3 and 5 states. Results were obtained using the QD method. The

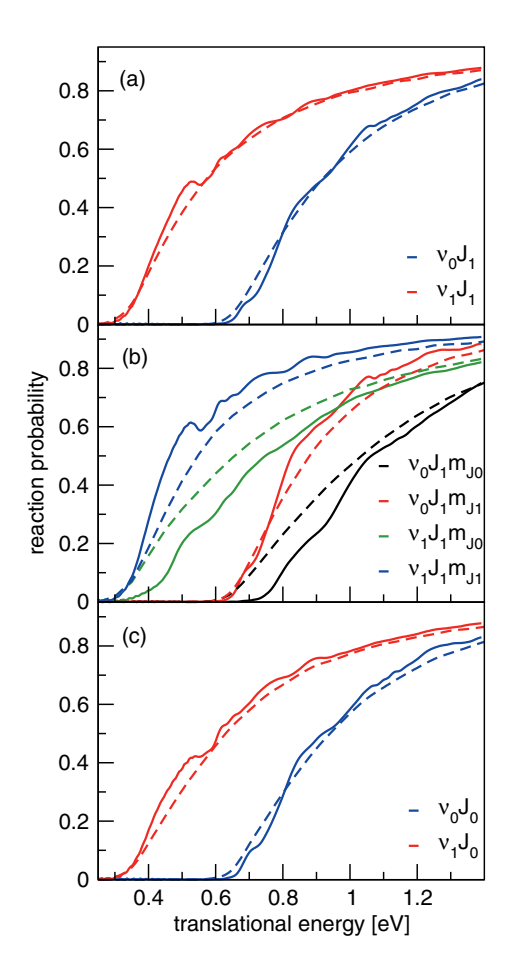


FIGURE 5.11: Reaction probabilities computed for  $H_2 + Cu(111)$  with QD calculations (solid lines) and QCT calculations (dashed lines) for normal incidence using the B86SRP68-DF2 DF. Degeneracy averaged reaction probabilities computed for J=1 for both the ground state and the first vibrationally excited state (a). Fully initial-state resolved reaction probabilities are shown for the  $m_J=0$  and 1 states belonging to J=1 for both the ground vibrational and the first excited vibrationally state (b). Reaction probabilities computed for the J=0 state for both the ground vibrational and the first excited vibrational state (c).

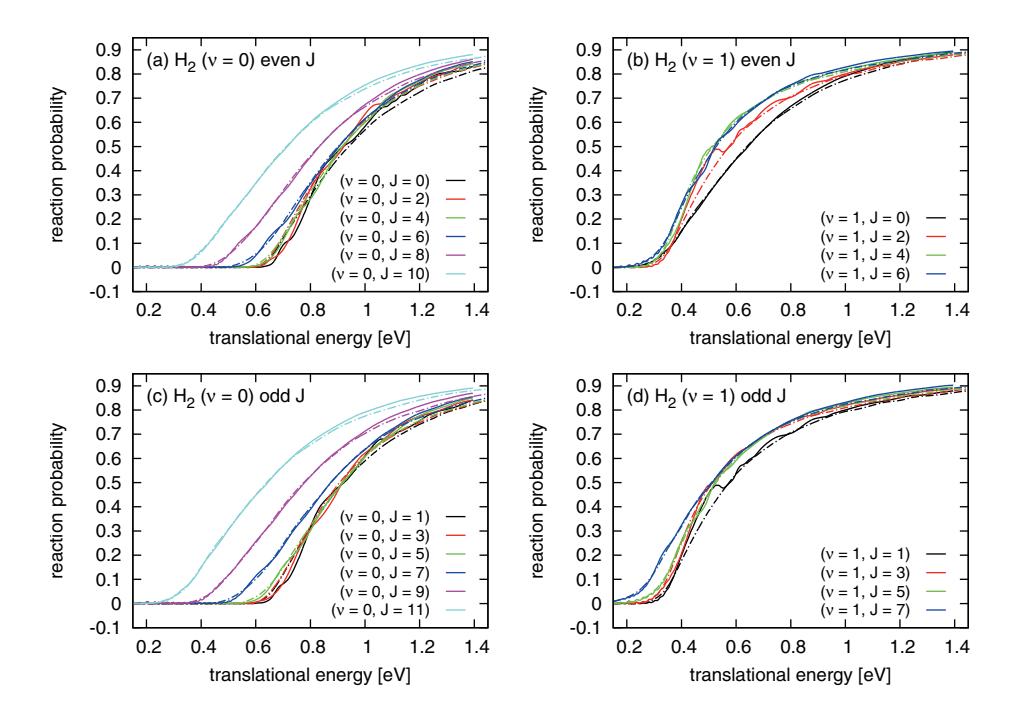


FIGURE 5.12: Degeneracy averaged reaction probabilities for  $H_2$  reacting on Cu(111), obtained using the B86SRP68-DF2 functional. Solid lined correspond to QD results, dot-dashed lines correspond to QCT results.

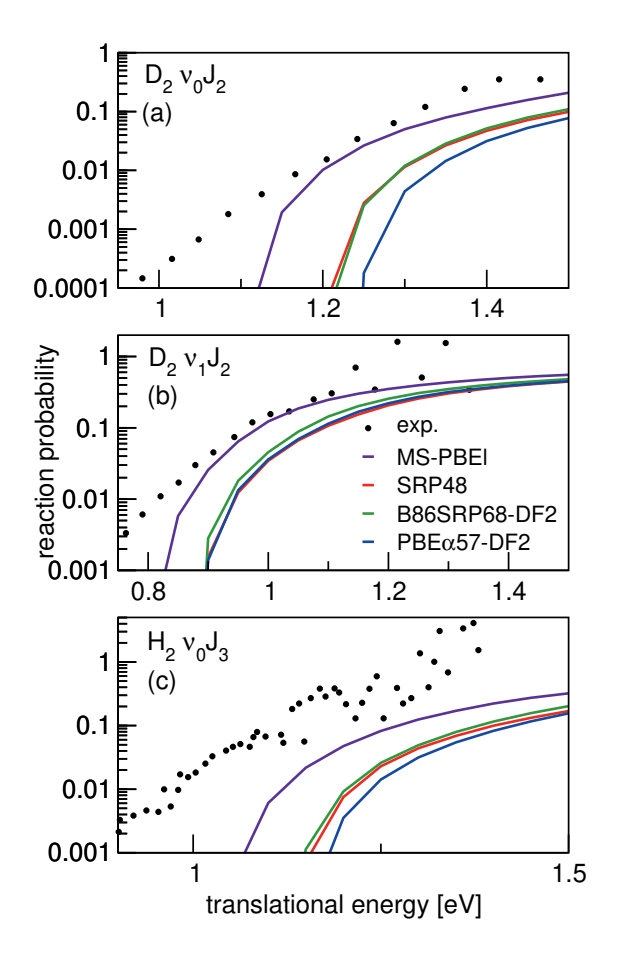


FIGURE 5.13: Initial-state selected reaction probabilities  $P_{deg}(E,\nu,J)$  computed for  $H_2$  ( $D_2$ ) + Ag(111) using the MS-PBEl (purple), SRP48<sup>20</sup> (red), B86SRP68-DF2 (green) and the PBE $\alpha$ 57-DF2 (blue) DFs are shown as a function of translational energy, comparing with values extracted from associative desorption experiments<sup>78,79</sup>. Results are shown for  $D_2$  ( $\nu=0,J=2$ ) (a),  $D_2$  ( $\nu=1,J=2$ ) (b), and  $H_2$  ( $\nu=0,J=3$ ) (c).

| optPBE-DF1*** 0.0959 MS-PBEl <sup>13</sup> 0.1057 |         | )F2     | $SRP48^{145}$   0.0891 | PBE 0.0464 | total     | Au(111) Method B2       |         | optPBE-DF1 <sup>145</sup>   0.0260 |         | PBE $\alpha$ 57-DF2   0.0189 | SRP48 <sup>145</sup> 0.0309 | PBE 0.1025 | total     | Au(111) Method B1           | optPBE-DF1 <sup>42</sup> 0.0688 | _       | PBE $\alpha$ 57-DF2   0.0676 | Dai et al. 38 QD | B86SRP68-DF2 QD   0.0846 | B86SRP68-DF2   0.0843 | MS-B86bl <sup>13</sup> 0.0826 | $SRP48^{11}$ 0.0409 | total     | Cu(111) Method B1       | optPBE-DF1 <sup>42</sup>   0.0146 |         | PBE $\alpha$ 57-DF2 0.0140 | Dai et al. 38 QD | ව<br>ව<br>ව | )F2     | l13     | $SRP48^{11}$ 0.0434 | Cu(111) Method A1 total  |
|---|---------|---------|------------------------|------------|-----------|-------------------------|---------|------------------------------------|---------|------------------------------|-----------------------------|------------|-----------|-----------------------------|---------------------------------|---------|------------------------------|------------------|--------------------------|-----------------------|-------------------------------|---------------------|-----------|-------------------------|-----------------------------------|---------|----------------------------|------------------|-------------|---------|---------|---------------------|--|
| 0.0860  | 0.0797  | 0.1143  | 0.0774                 | 0.0471     | $\nu = 0$ | MAD (eV) I              | 0.0393  | 0.0225                             | 0.0457  | 0.0241                       | 0.0468                      | 0.1333     |           | MAD (eV) I                  | 0.0635                          | 0.0660  | 0.0647                       | 0.0703           | 0.0812                   | 0.0756                | 0.0664                        | 0.0317              |           | MAD (eV)                | 0.0147                            | 0.0136  | 0.0117                     | 0.0091           | 0.0183      | 0.0142  | 0.0165  | 0.0522              | $\begin{array}{c c} \text{MAD (eV) } H_2 \\ \hline & \nu = 0 \end{array}$        |
| 0.1058  | 0.0911  | 0.0958  | 0.1008                 | 0.0457     | $\nu = 1$ | ) H <sub>2</sub>        | 0.0264  | 0.0259                             | 0.0083  | 0.0136                       | 0.0151                      | 0.0718     | $\nu = 1$ | $H_2$                       | 0.0768                          | 0.0855  | 0.0718                       |                  | 0.0897                   | 0.0974                | 0.1067                        | 0.0549              | $\nu = 1$ | $H_2$                   | 0.0143                            | 0.0177  | 0.0174                     |                  | 0.0303      | 0.0308  | 0.0438  | 0.0301              | $\nu = 1$  |
| -0.0959<br>-0.1057                                | -0.0854 | -0.1050 | -0.0891                | -0.0463    | total     | N                       | 0.0028  | -0.0044                            | 0.0217  | 0.0026                       | 0.0158                      | 0.1025     | total     | W                           | -0.0688                         | -0.0738 | -0.0676                      |                  | -0.0845                  | -0.0843               | -0.0826                       | -0.0409             | total     | ×                       | 0.0054                            | -0.0025 | 0.0040                     |                  | -0.0222     | -0.0176 | -0.0149 | 0.0373              | total  |
| -0.0860<br>-0.1043                                | -0.0797 | -0.1143 | -0.0774                | -0.0470    | $\nu = 0$ | MSD (eV) H <sub>2</sub> | 0.0320  | 0.0206                             | 0.0457  | 0.0177                       | 0.0468                      | 0.1333     | $\nu = 0$ | $MSD (eV) H_2$              | -0.0635                         | -0.0660 | -0.0648                      | -0.0703          | -0.0813                  | -0.0756               | -0.0664                       | -0.0317             | $\nu = 0$ | MSD (eV) H <sub>2</sub> | 0.0111                            | 0.0064  | 0.0054                     | 0.0017           | -0.0169     | -0.0089 | 0.0044  | 0.0522              | $\begin{array}{c c} \text{MSD (eV) } \text{H}_2 \\ \hline & \nu = 0 \end{array}$ |
| -0.1058<br>-0.1072                                | -0.0911 | -0.0958 | -0.1008                | -0.0457    | $\nu = 1$ | 2                       | -0.0264 | -0.0296                            | -0.0022 | -0.0125                      | -0.0151                     | 0.0718     | $\nu = 1$ | 2                           | -0.0767                         | -0.0855 | -0.0718                      |                  | -0.0897                  | -0.0974               | -0.1068                       | -0.0549             | $\nu = 1$ | 2                       | -0.0032                           | -0.0158 | 0.0018                     |                  | -0.0303     | -0.0308 | -0.0438 | 0.0151              | $\nu = 1$  |
| 0.1037  | 0.0955  | 0.0957  | 0.0948                 | 0.0579     | total     | M                       | 0.0270  | 0.0212                             | 0.0190  | 0.0187                       | 0.0229                      | 0.0955     | total     | M                           | 0.0642                          | 0.0682  | 0.0674                       |                  |                          | 0.0785                | 0.0712                        | 0.0336              | total     | M                       | 0.0480                            | 0.0510  | 0.0573                     |                  |             | 0.0663  | 0.0551  | 0.0254              | total M  |
| 0.0952  | 0.0888  | 0.0905  | 0.0856                 | 0.0551     | $\nu = 0$ | MAD (eV) D <sub>2</sub> | 0.0116  | 0.0116                             | 0.0275  | 0.0246                       | 0.0325                      | 0.1178     | $\nu = 0$ | MAD ( $eV$ ) D <sub>2</sub> | 0.0583                          | 0.0613  | 0.0642                       |                  |                          | 0.0709                | 0.0567                        | 0.0252              | $\nu = 0$ | MAD (eV) D              | 0.0481                            | 0.0487  | 0.0615                     |                  |             | 0.0640  | 0.0440  | 0.0243              | $\begin{array}{c c} \text{MAD (eV) } D_2 \\ \hline & \nu = 0 \end{array}$        |
| 0.1123  | 0.1015  | 0.1009  | 0.1041                 | 0.0607     | $\nu = 1$ | )2                      | 0.0105  | 0.0309                             | 0.0105  | 0.0127                       | 0.0133                      | 0.0734     | $\nu = 1$ | )2                          | 0.0729                          | 0.0785  | 0.0723                       |                  |                          | 0.0898                | 0.0929                        | 0.0336              | $\nu = 1$ | $D_2$                   | 0.0478                            | 0.0545  | 0.0509                     |                  |             | 0.0698  | 0.0717  | 0.0272              | $\nu = 1$  |
| -0.1037<br>-0.0835                                | -0.0951 | -0.0957 | -0.0948                | -0.0579    | total     | N                       | 0.0212  | -0.0143                            | 0.0113  | 0.0125                       | 0.0094                      | 0.0955     | total     | V                           | -0.0642                         | -0.0682 | -0.0674                      |                  |                          | -0.0785               | -0.0712                       | -0.0332             | total     | N                       | -0.0480                           | -0.0511 | -0.0573                    |                  |             | -0.0663 | -0.0551 | -0.0066             | total N  |
| -0.0952<br>-0.0551                                | -0.0888 | -0.0905 | -0.0856                | -0.0551    | $\nu = 0$ | $MSD (eV) D_2$          | 0.0435  | 0.0023                             | 0.0275  | 0.0246                       | 0.0321                      | 0.1176     |           | $MSD (eV) D_2$              | -0.0583                         | -0.0613 | -0.0642                      | _                | _                        | -0.0709               | -0.0567                       | -0.0246             |           | $MSD (eV) D_2$          | -0.0615                           | -0.0487 | -0.0616                    | _                | _           | -0.0640 | -0.0440 | -0.0008             | $MSD (eV) D_2$ $\mid \nu = 0 \mid$   |
| -0.1123<br>-0.1120                                | -0.1015 | -0.1009 | -0.1041                | -0.0607    | $\nu = 1$ | 2                       | -0.0009 | -0.0307                            | -0.0050 | 0.0005                       | -0.0131                     | 0.0733     | $\nu = 1$ | 12                          | -0.0729                         | -0.0785 | -0.0723                      |                  |                          | -0.0897               | -0.0929                       | -0.0460             | $\nu = 1$ | 12                      | -0.0478                           | -0.0545 | -0.0509                    |                  |             | -0.0698 | -0.0717 | -0.0152             | $\nu = 1$  |

Table 5.13: Mean absolute and mean signed deviations of the theoretical  $E_{1/2}(\nu,J)$  parameters from the experimental  $E_0(\nu,J)$  values for  $H_2$  (D<sub>2</sub>) + Cu(111)<sup>48</sup> and  $H_2$  (D<sub>2</sub>) + Au(111)<sup>71</sup>.

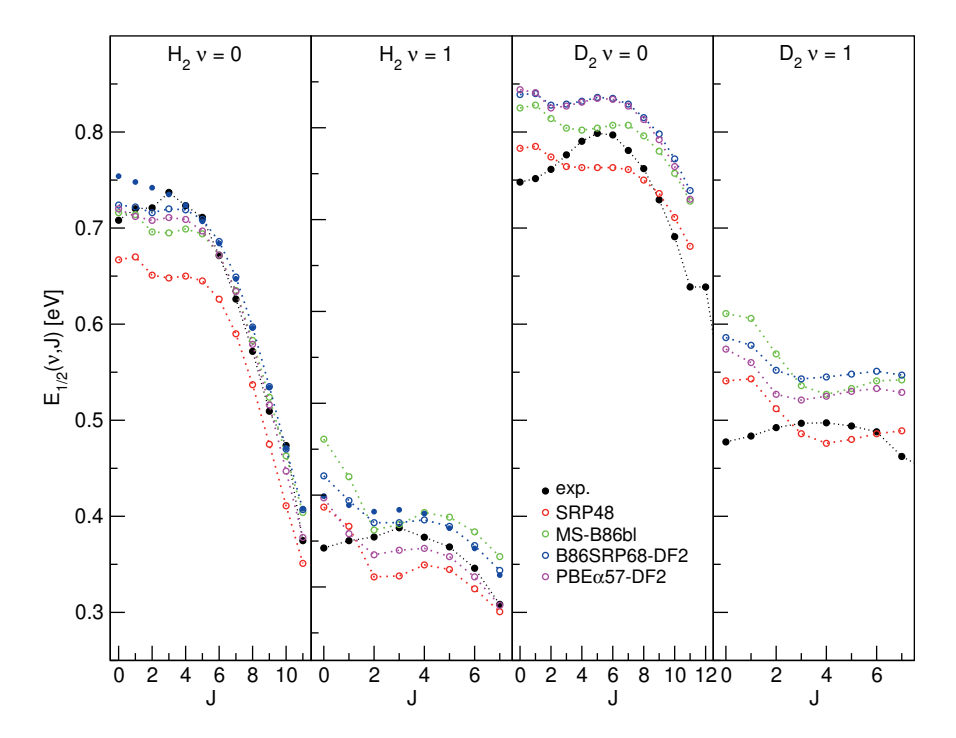


FIGURE 5.14:  $E_{1/2}(\nu,J)$  parameters as a function of J obtained using method A1 for H<sub>2</sub> and D<sub>2</sub> reacting on Cu(111). Red circles represent the SRP48 values<sup>63</sup>, green circles the MS-B86bl values<sup>13</sup>, blue circles represent the B86SRP68-DF2 values with the solid blue circles corresponding to QD calculations, magenta circles represent the PBE $\alpha$ 57-DF2 values, and solid black circles represent experimental results<sup>48</sup>.

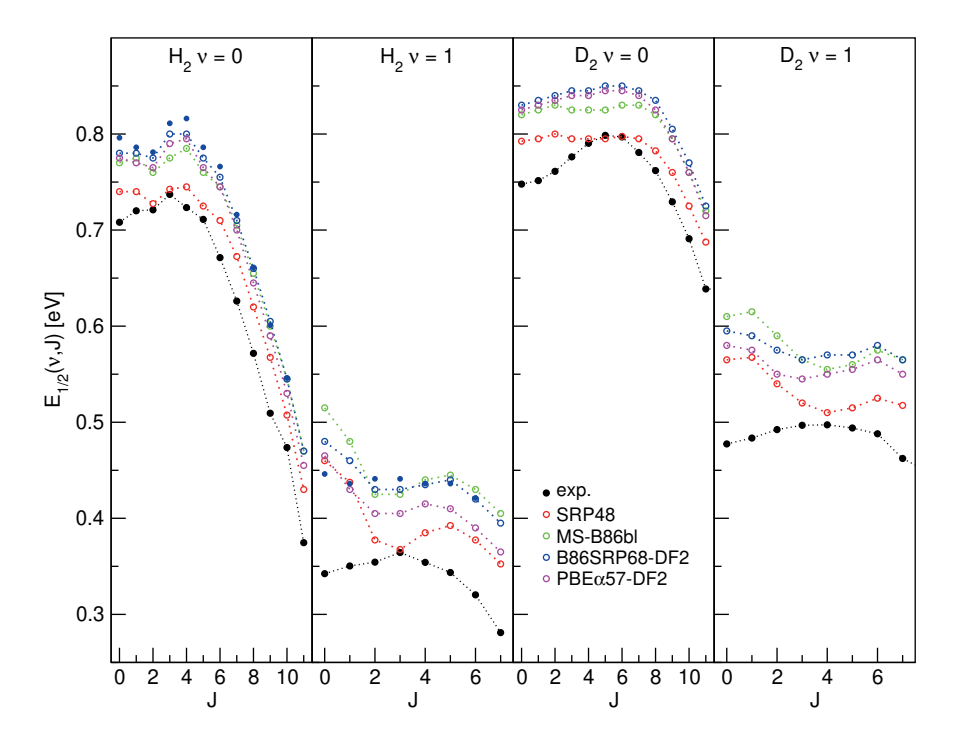


FIGURE 5.15:  $E_{1/2}(\nu,J)$  parameters as a function of J obtained using method B1 for  ${\rm H_2}$  and  ${\rm D_2}$  reacting on Cu(111). Red circles represent the SRP48 values<sup>63</sup>, green circles the MS-B86bl values<sup>13</sup>, blue circles the B86SRP68-DF2 values with the solid blue circles corresponding to QD calculations, magenta circles represent the PBE $\alpha$ 57-DF2 values, and solid black circles represent experimental results<sup>48</sup>.

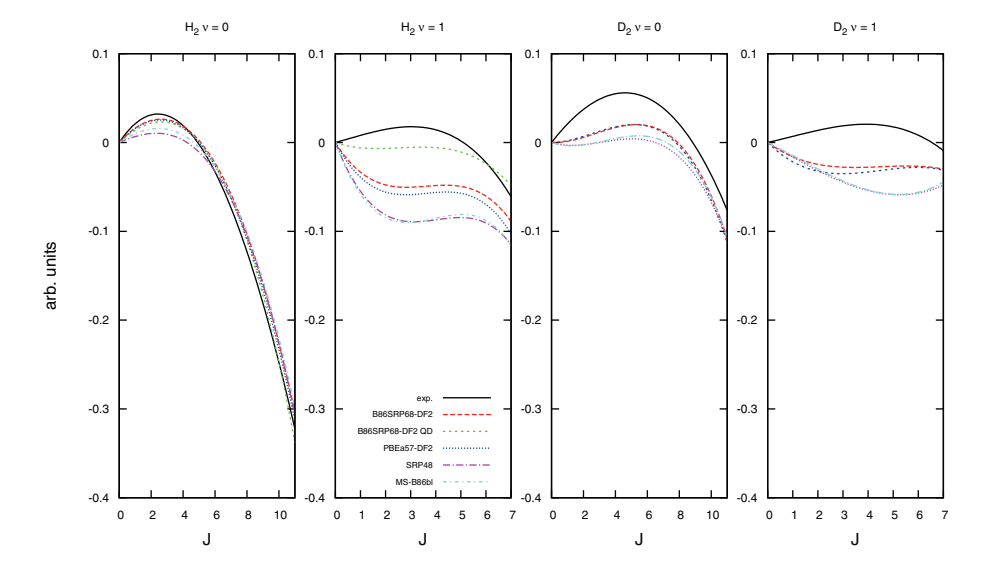


FIGURE 5.16: The trend in the J-dependence of the  $E_{1/2}(\nu, J)$  parameters calculated using procedure B1 as a function of J for the  $H_2$  ( $D_2$ ) + Cu(111) system. Here the trend is represented by third degree polynomial fits of the calculated and experimental<sup>48</sup> results, plotted here without the y-axis offset for easy comparison.

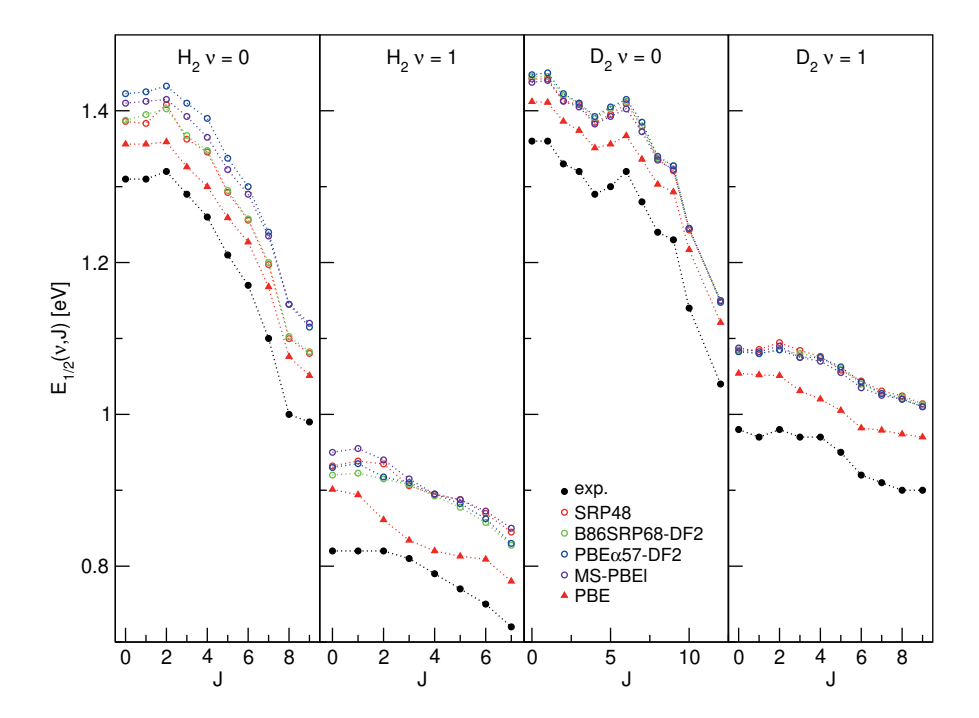


FIGURE 5.17:  $E_{1/2}(\nu,J)$  parameters as a function of J obtained using method B2 for  ${\rm H_2}$  and  ${\rm D_2}$  reacting on Au(111), experimental values are shown in black<sup>71</sup>. Red circles represent the SRP48 values<sup>145</sup>, green circles the B86SRP68-DF2 values, blue circles the PBE $\alpha$ 57-DF2<sup>12</sup> values, purple circles the MS-PBEl<sup>13</sup> values and red triangles the PBE values<sup>145</sup>.

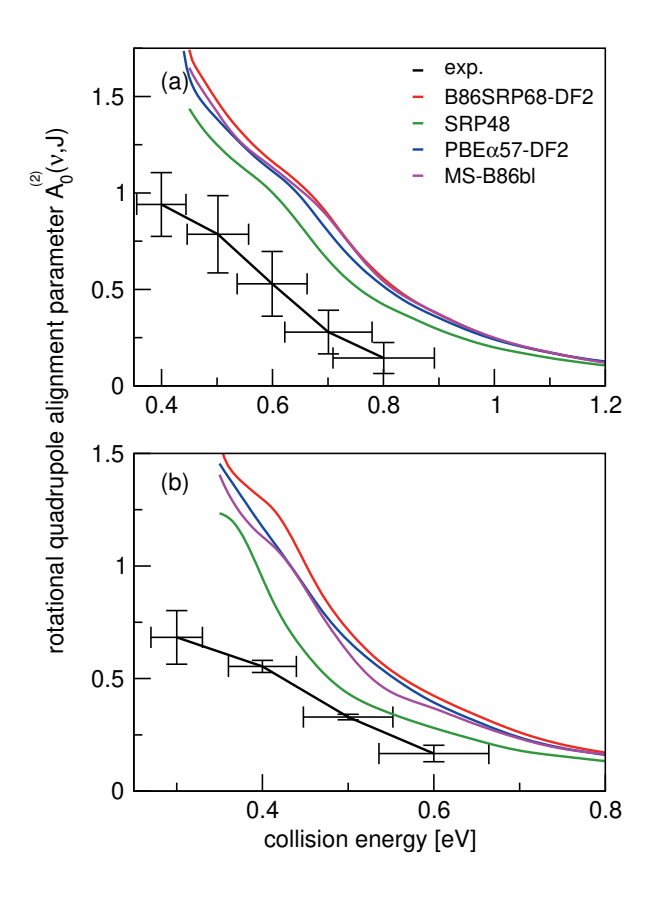


FIGURE 5.18: Panel (a) shows rotational quadrupole alignment parameter,  $A_0^{(2)}(\nu=0,J=11)$ , and panel (b) shows the rotational quadrupole alignment parameter  $A_0^{(2)}(\nu=1,J=6)$  for D<sub>2</sub> reacting with Cu(111). Experimental results are shown in black<sup>50</sup>. Theoretical results obtained using the QCT method are shown for the B86SRP68-DF2 (red), SRP48<sup>11</sup> (green), PBE $\alpha$ 57-DF2<sup>12</sup> (blue), and the MS-B86bl<sup>13</sup> (magenta) DFs.

|              | $H_2$ | $D_2$ |
|--------------|-------|-------|
| $\exp^{.71}$ | 0.552 | 0.424 |
| SRP48        | 0.250 | 0.473 |
| B86SRP68-DF2 | 0.249 | 0.522 |

TABLE 5.14: The ratio of  $\nu = 1$ :  $\nu = 0$  molecules desorbing from Au(111) as measured in experiments<sup>71</sup> and computed with the SRP48 and B86SRP68-DF2 DFs.

onset of the vibrational inelastic scattering probabilities is correlated with the onset of reactivity for each particular state. The DFs yield similar results for the initial ( $\nu=0,J=5$ ) rovibrational state, except that the SRP48 DF yields smaller vibrational excitation probabilities for  $E>0.8\mathrm{eV}$  (panel c). For the ( $\nu=0,J=1$ ) and ( $\nu=0,J=3$ ) initial rovibrational states the differences are larger (panels a and b).

Figure 5.20 shows the ratio of rotationally elastic and inelastic scattering probabilities  $P(\nu=1,J=0\to\nu=1,J=2)/P(\nu=1,J=0\to\nu=1,J=0)$  computed with two DFs and comparing with experiment<sup>55</sup>. Note that both curves need to be shifted by 40 meV in order to overlap with the onset of the experimental curves measured for a surface temperature of 300 K<sup>55</sup>.

# 5.3.7 Rovibrational state populations of $H_2$ and $D_2$ desorbing from Au(111)

Figure 5.21 shows rovibrational state populations of  $H_2$  and  $D_2$  desorbing from Au(111). Here we plot  $ln[N/g_N(2J+1)]$  versus the rotational energy, with N being the total population for each  $(\nu, J)$  state (see Eq. 5.13) and  $g_N(2J+1)$  being the statistical weight for rotational level  $J^{71}$ . For  $D_2$ ,  $g_N=2$  for even J and 1 for odd J; for  $H_2$ ,  $g_N=1$  for even J and 3 for odd J. In such a plot a Boltzmann distribution will appear as a straight line<sup>71</sup>. Here we integrate Eq. 5.13 up to  $E_{\text{max}}(\nu, J)$ .

Figure 5.22 shows the rovibrational state populations of  $H_2$  desorbing from Au(111) as reported in by Shuai et al.<sup>71</sup> together with the values we calculate using Eq. 5.13 with an upper integration limit of 5 eV to be in line with the procedure used by Shuai et al.<sup>71</sup> as outlined in a private communication<sup>148</sup>.

Table 5.14 shows the ratio of the fluxes of molecules desorbing in the first excited and in the vibrational ground state for both  $H_2$  and  $D_2$  desorbing from Au(111). The ratios are calculated using Eq. 5.15 and are solely based on the rovibrational states for which results are shown in figure 5.21. Again, here we integrate Eq. 5.13 up to  $E_{\text{max}}(\nu, J)$ .

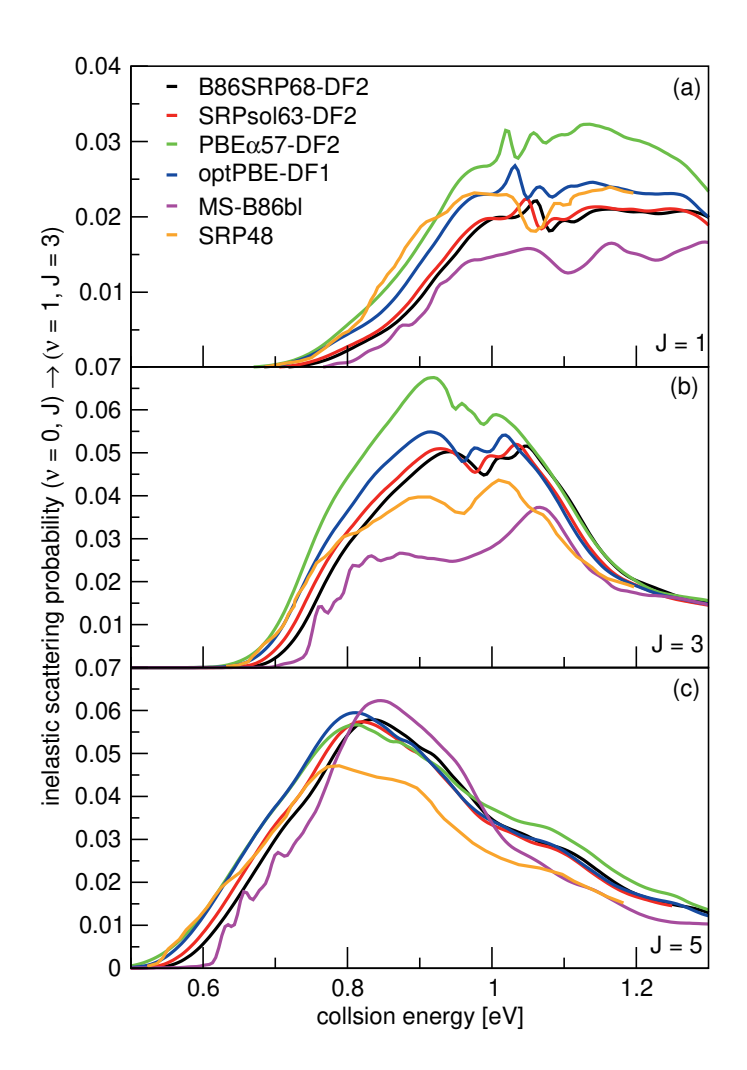


FIGURE 5.19: Vibrationally inelastic scattering probabilities for  $P(\nu = 0, J \rightarrow \nu = 1, J = 3)$ . Shown are results for J = 1 (a), J = 3 (b), and J = 5 (c). QD results for the following DFs are shown: B86SRP68-DF2 (black), SRPsol63-DF2 (red), PBE $\alpha$ 57-DF2 (green), optPBE-DF1 (blue), MS-B86bl (magenta), and SRP48<sup>25</sup> (orange).

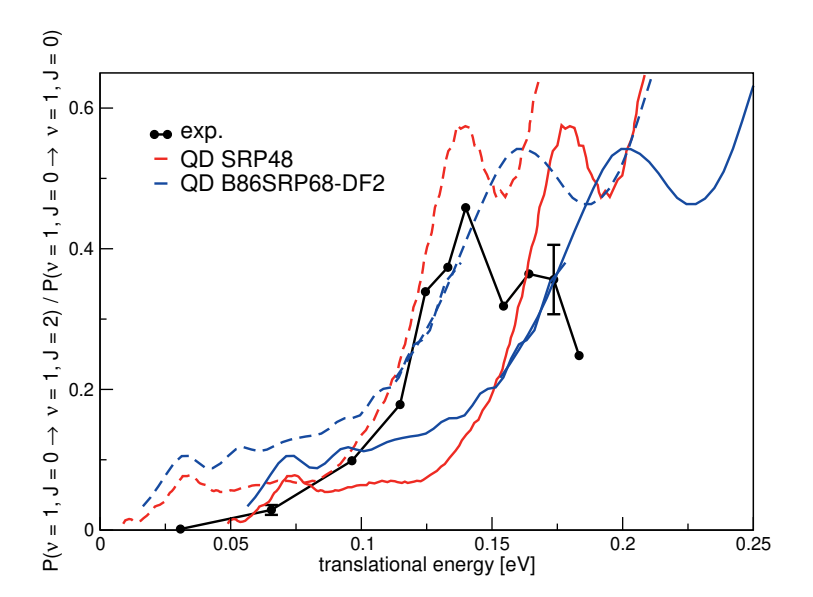


FIGURE 5.20: A comparison of the ratios of theoretical and experimental rotationally inelastic scattering probabilities  $P(\nu=1,J=0\to\nu=1,J=2)/P(\nu=1,J=0\to\nu=1,J=0)$  for H<sub>2</sub> impinging on Cu(111). Experimental results are shown in black<sup>55</sup> with the error bars representing maximum deviations in repeated measurements constituting estimated standard deviations. QD results for the SRP48 DF are shown in red<sup>11</sup> and QD results for the B86SRP68-DF2 DF are shown in blue. Dashed lines constitute the calculated ratio's of rotationally inelastic scattering shifted by 40 meV.

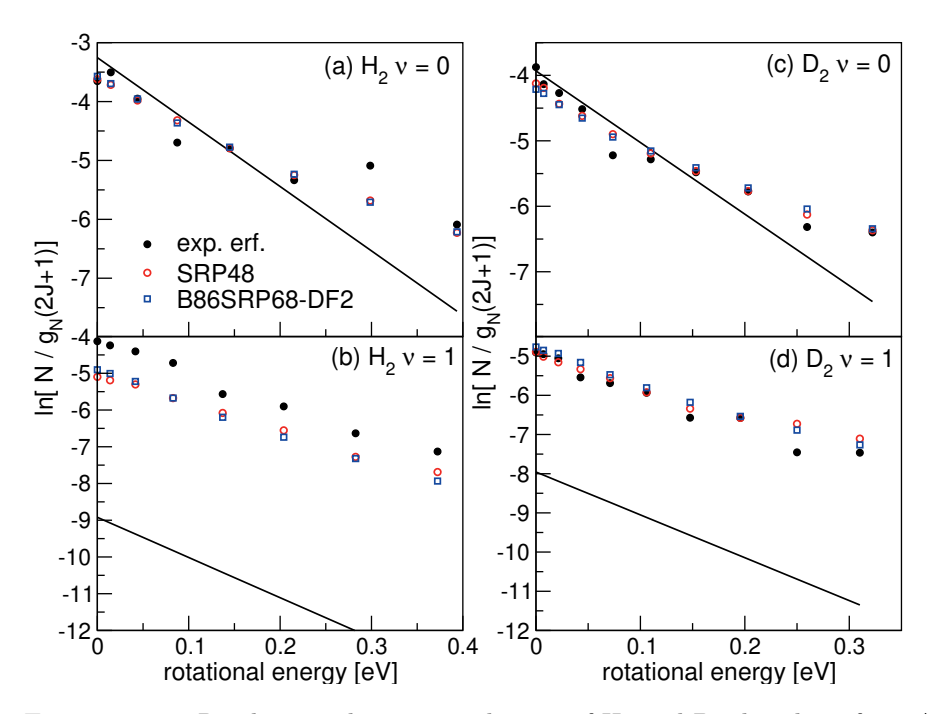


FIGURE 5.21: Rovibrational state populations of  $H_2$  and  $D_2$  desorbing from Au(111) are shown versus the rotational energy. Experimental results are shown in black<sup>71</sup>, theoretical results are shown in red for the SRP48 DF<sup>145</sup> and in blue for the B86SRP68-DF2 DF. The straight lines represent Boltzmann distributions for the surface temperature of the experiment.

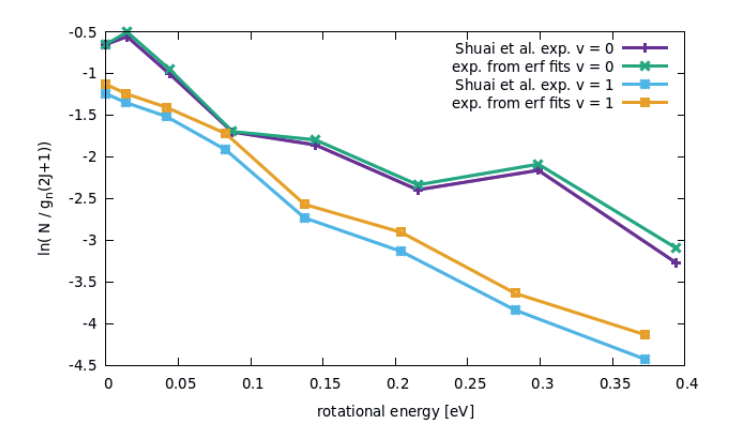


FIGURE 5.22: Rovibrational state populations of  $H_2$  desorbing from Au(111) are plotted against the data for  $H_2$  shown in figure 2 of ref.<sup>71</sup>. Here the calculated normalized experimental results based on the error function fits have been obtained by performing the integration in Eq. 18 until 5 eV to be consistent with the procedure used in ref.<sup>71</sup>. Additionally, the calculated curves have been shifted such that the calculated value for  $(\nu = 0, J = 0)$  matches with the  $(\nu = 0, J = 0)$  result reported in ref.<sup>71</sup>, and the calculated results for  $(\nu = 1)$  have been shifted by the same amount (+3.0).

Our aim has been to develop new SRP-DFs that include non-local correlation for the  $H_2 + Cu(111)$  system, and afterwards assess the transferability of these DFs to other systems. The reason for taking this approach, instead of fitting the DF to best reproduce experiments on all systems shown in the results section, is that numerous experimental results are available for the reaction of  $H_2$  and  $D_2$  on  $Cu(111)^{46-56}$ . For the non-copper systems discussed in this work experimental results are sparse<sup>18,71</sup>, and there is discussion about the validity of the available parameters describing the molecular beams used in the experiments on  $H_2$  ( $D_2$ ) + Ag(111) and  $Pt(111)^{20,61,65,66}$ .

The good agreement between different molecular beam dissociative chemisorption experiments  $^{46,47,52}$  on the reaction of  $H_2$  ( $D_2$ ) + Cu(111), and their resultant constraints for a to be developed SRP-DF, provides an opportunity to design the best performing SRP-DF for this system yet reported. The DF that best describes sticking probabilities obtained from dissociative chemisorption molecular beam experiments for  $H_2$  ( $D_2$ ) + Cu(111), will be considered the best performing DF. We choose this definition since our calculations are carried out using the BOSS model. From the literature it is known that the BOSS model

works rather well for activated  $H_2$  dissociation on cold metals<sup>24,28–30,63,149</sup>.

Comparisons to experimental results obtained from associative desorption experiments will not be included in the assessment of the quality of the newly constructed SRP-DFs for two reasons. The first reason is that associative desorption experiments are carried out at high surface temperatures. Since we have carried out calculations using the BOSS model we neglect surface temperature effects. The second reason is that in obtaining state-specific information from associative desorption experiments requires the assumption of detailed balance, which is strictly speaking not applicable if an electronically non-adiabatic process is involved and energy exchange with the surface is allowed. Since neither process can be ruled out we feel it safer to base our judgement on the sticking experiments. We still discuss the valuable experimental results on associative desorption since they do provide insight into the reaction dynamics. However, as we will discuss, it is fraught with difficulty to make a direct quantitative comparison between calculations on dissociative chemisorption and associative desorption experiments without improving our dynamical model by incorporating phonons and ehp excitations, which is challenging to do<sup>150–152</sup>. Recently, this has been done for  $H_2 + Cu(111)^{76}$  using ab initio molecular dynamics with electronic friction (AIMDEF) calculations employing the PBE<sup>116</sup> DF. It is hard to draw firm conclusions from this work on the effect of electronhole pair excitation as the statistical accuracy of the AIMDEF calculations is limited through the small number of AIMDEF trajectories. Other recent work employed the orbital dependent friction model  $(ODF)^{23}$ . However the effects of incorporating ODF in the reaction dynamics of H<sub>2</sub> are small and require additional experiments for theoretical predictions to be verified $^{23}$  and for proving that ODF should be better.

# 5.4.1 Metal properties

Using a GGA DF for a theoretical description of gas surface dynamics is in most cases a compromise between a good description of the metal slab and a good description of the interaction of a molecule with the metal slab  $^{153}$ . Table 5.5 shows the calculated lattice constants for all DFs investigated in this work. Highly accurate results are only achieved using PBEsol  $^{118}$  and our previously developed mGGA MS-B86bl  $^{13}$ . All our candidate SRP-DFs yield improved results over the vdW-DF1 $^{97}$ , vdW-DF2 $^{98}$ , and SRP48 $^{11}$  DFs. We generally see a large improvement in the calculated lattice constant if a DF has at least one component with a  $\mu$  value closer to the second gradient expansion  $\mu = \frac{10}{81}$ , as used in the PBEsol  $^{118}$ , MS-B86bl  $^{13}$ , SRPsol63-DF2 and the B86SRP68-DF2 DFs.

When looking at the relaxations of the interlayer distance of the two top most layers relative to the bulk interlayer distance (table 5.6) no clear trend can be discerned. The best performing DF is again MS-B86bl<sup>13</sup>. We do note that the SRP48 DF appears to produce top interlayer distances that on the whole are closer to the experimental values than DFs obtained combining GGA exchange DFs with vdW-DF2 non-local correlation. The reason for this is unclear.

### 5.4.2 Static PES properties

The experimental Van der Waals well depth that has been measured for  $\rm H_2 + Cu(111)^{60}$  can provide us with a constraint when fitting a new SRP-DF. The new SRP-DFs we present here are B86SRP68-DF2 and SRPsol63-DF2 (table 5.1). The two original Van der Waals DFs, namely vdW-DF1<sup>97</sup> and vdW-DF2<sup>98</sup>, yield wells that are too deep, especially for vdW-DF1<sup>97</sup>, as also found in earlier work<sup>154</sup> (figure 5.3b, see also table 5.11). The two previous SRP-DFs for this system produce a very tiny (SRP48<sup>11</sup>) or no (MS-B86bl<sup>13</sup>) Van der Waals well at all (figure 5.3b). Of the four DFs considered in figure 5.3b, the vdW-DF2<sup>98</sup> DF produces the best results. Other exploratory calculations carried out by us showed that using vdW-DF1<sup>97</sup> correlation yields Van der Waals wells that are much to deep and too close to the surface, although they are not shown here. The better performance of vdW-DF2 correlation is most likely due to the large-N asymptote correction used in this DF<sup>98</sup>.

Figure 5.3a shows the same Van der Waals well depth for the SRP-DFs that include vdW-DF2 correlation, and one SRP-DF that includes vdW-DF1 correlation. These four DFs are all chemically accurate with respect to the reactivity of H<sub>2</sub> on Cu(111), as can be seen from the MAD values in figure 5.4. The PBE $\alpha$ 57-DF2 DF has originally been fitted to reproduce experiments for  $H_2(D_2) + Pt(111)^{12}$ , and the optPBE-DF1<sup>115</sup> DF has previously been shown to be chemically accurate  $H_2$  ( $D_2$ ) +  $Cu(111)^{42}$ . The exchange part of the optPBE-DF1 DF was optimized to reduce intermediate range effects to avoid double counting when combining it with non-local vdW-DF1 correlation<sup>115</sup>. It is clear that the choice of exchange functional greatly impacts the depth and position of the Van der Waals well. The difference between the depths of the deepest and the shallowest Van der Waals well obtained with the non-standard DFs using vdW-DF2 non-local correlation<sup>98</sup> (figure 5.3a, 23.4 meV) is greater than the difference between the depths of the vdW-DF1 and vdW-DF2 wells (figure 5.3b, 13.4 meV, see also table 5.11). It can also be seen that going from  $PBE\alpha57-DF2$  to SRPsol63-DF2 the calculated Van der Waals well more closely

resembles experiment  $^{60}$ . The closest agreement with experiment is achieved using the B86SRP68-DF2 DF.

All Van der Waals wells computed by us are tabulated in table 5.11, also comparing with experimental Van der Waals wells that have been reported for  $H_2 + Cu(111)^{60,62}$ ,  $H_2 + Ag(111)^{91}$ ,  $H_2 + Au(111)^{62}$  and  $H_2 + Pt(111)^{100,111}$ . With respect to the Cu(111) well depth the experimental results are in reasonable agreement with each other. However, the position reported by Harten et al.<sup>62</sup> is somewhat closer to the surface. This difference in the Z dependence of the Van der Waals well can be attributed to ambiguities in the bound state level assignments from the Feshbach resonances in the earlier experiment 105, and it has been remarked that the results obtained later<sup>60</sup> are in fact also consistent with the earlier measurements<sup>105</sup>. Additionally we suspect that the reported Van der Waals wells for  $H_2 + Ag(111)^{91}$  and  $H_2 + Au(111)^{62}$  might possibly be too close to the surface 105 for the same reason. This drawback of using the RMSA technique<sup>99</sup> might be alleviated by redoing the potential inversion on the basis of the original data on Feshbach resonances with more advanced theoretical models<sup>155</sup>, e.g., using an analysis in which the molecule-surface potential is not laterally averaged. In yet a different approach, instead of using the RMSA approach<sup>99</sup> Poelsema et al.<sup>111</sup> presented a combined thermal energy atom scattering/thermal desorption spectroscopy (TEAS/TDS) study of the H<sub>2</sub> + Pt(111) system, obtaining Van der Waals well geometries that were subsequently accurately reproduced by theory<sup>12</sup>. For the H<sub>2</sub> + metal(111) systems studied here it would certainly be advantageous if additional experimental data were to become available addressing the Van der Waals interaction, using either a sophisticated analysis of results for RMSA studies or through combined TEAS/TDS studies. New experiments would allow for a better comparison between theory and experiment with respect to the predictions obtained by the inclusion of non-local correlation in DFT calculations on the systems addressed here.

# 5.4.3 Molecular beam sticking

# Molecular beam sticking of $H_2$ ( $D_2$ ) + Cu(111): QCT results

The fitting of the candidate SRP-DFs was done by reproducing six different sets of molecular beam experiments  $^{46,47,52}$  for which the molecular beam parameters were taken from (the supporting information of) Refs<sup>11,29</sup>. Figure 5.4 compares results of three sets of molecular beam sticking probabilities,  $S_0$ , with results computed with the SRP48<sup>11</sup>, B86SRP68-DF2, SRPsol63-DF2, PBE $\alpha$ 57-DF2<sup>12</sup> and optPBE-DF1<sup>42,118</sup> DFs using the QCT method. We focus on these three sets of molecular beam experiments because for these enough experimental

data points are available to perform a cubic spline interpolation. The quality of the DFs is assessed by computing MAD values, i.e. the mean distance along the incidence energy axis from the computed  $S_0$  data point to the interpolated experimental data point with the same  $S_0$  value.

It is clear from the total MAD values that all DFs evaluated in figure 5.4 are chemically accurate with respect to the three sets of molecular beam experiments for  $H_2$  ( $D_2$ ) + Cu(111) shown in figure 5.4, and that the agreement between theory and experiment is good for all molecular beam conditions. The theoretical results shown here were obtained using the BOSS model. The experiments of Michelsen et al. 46 and Rettner et al. 54 considered here employed a low surface temperature of 120K, the experiment of Berger et al. 47 was reportedly done on a 'cold' surface, and from the literature it is known that the BOSS model works well for activated  $H_2$  dissociation on cold metals  $^{24,27-30}$ . Another advantage of fitting a SRP-DF to these sets of molecular beam experiments is that they cover both  $H_2$  and  $D_2$  for very different experimental conditions with respect to the nozzle temperature, the average collision energy, and the width of the velocity distributions  $^{11}$ .

The B86SRP68-DF2 DF exhibits a MAD of  $1.4 \,\mathrm{kJ/mol}$  for the experiments shown in figure 5.4, which is the lowest value obtained with the five DFs discussed. Of the DFs that include non-local correlation the B86SRP68-DF2 DF also performs best with respect to the calculated lattice constants, as can be seen in table 5.5. In addition it performs best with respect to the shape and depth of the Van der Waals well. We therefore select the B86SRP68-DF2 DF as the new, and most accurate, SRP-DF for the  $\mathrm{H_2} + \mathrm{Cu}(111)$  system. From this point onward we will mainly focus on the results obtained with the newly selected B86SRP68-DF2 DF and the PBE $\alpha$ 57-DF2<sup>12</sup> DF, and on how the performance of these two DFs compares to that of the original SRP48<sup>11</sup> DF and of our previously developed mGGA DFs<sup>13</sup>.

One additional comparison to experiment is made in figure 5.5, concerning pure  $D_2$  molecular beams<sup>46</sup>. This comparison highlights a limitation of assessing the quality of a candidate SRP-DF by computing the mean distance along the incidence energy axis from the computed  $S_0$  value to interpolated experimental values. In this experiment the average translational energy does not monotonically increase with increasing nozzle temperature. Due to the high sensitivity of the sticking probability to the width of the velocity distribution of the molecular beam, the sticking probability also does not monotonically increase with the average translational energy. In figure 5.5 the application of our quality assessment strategy leads, in some cases, to large deviations with respect to the interpolated experimental results (note, however, that only for one data point and for one DF chemical accuracy was not achieved, see figure

5.5c). Our quality assessment strategy works best if the reactivity increases monotonically with increasing average translational energy.

## Molecular beam sticking in $H_2 + Cu(111)$ : QD results

Due to the computational expense of calculating molecular beam sticking probabilities using the QD method we only carried out QD molecular beam simulations for  $H_2 + Cu(111)$  for the B86SRP68-DF2 DF (figures 5.4e,f and 5.6). We have used the same methodology to carry out QD molecular beam simulations as in Chapter 4. Overall, for the four experiments considered with both methods, the MAD value obtained with the B86SRP68-DF2 DF increases from a QCT value of 1.3 kJ/mol to 1.6 kJ/mol for QD. In the QCT calculations more rovibrational states are taken into account compared to the QD calculations (see table 5.3). In figure 5.7 we explicitly compare QD and QCT results calculated from the same set of rovibrational states, and compare those results to the QCT results shown in figures 5.4e,f and 5.6. Overall the agreement between QD and QCT sticking probabilities is very good when both are calculated from the same set of initial rovibrational states. There are however small differences when looking at narrow low average translational energy molecular beams (see e.g. figure 5.7a).

Figures 5.7a,b show that for narrow low average translational energy molecular beams<sup>52</sup> the QD method predicts slightly larger sticking probabilities than the QCT sticking probabilities calculated from the same set of rovibrational states. This small gap between QD and QCT sticking probabilities based on the same set of initial rovibrational states is slightly bigger then what was obtained for  $H_2 + Cu(211)$  when using the SRP48 DF<sup>37</sup>. This suggests that quantum effects might play a role in the dynamics. It is possible that the slightly higher sticking probability predicted by QD is due to the underlying reaction probability curves for specific included rovibrational states showing more structure than for  $H_2 + Cu(211)^{37}$ . Since the molecular beam sticking probabilities are very small in figures 5.7a,b, they could also be very sensitive to noise in the underlying reaction probability curves. We shall further discuss the differences between fully initial-state resolved QD and QCT reaction probabilities in section 5.4.6.

Figures 5.7c,d show very good agreement between QD and QCT results, also for the QCT results that were based on more initial rovibrational states. Only for the highest nozzle temperature points in figure 5.7c (see table 5.4) taking into account more initial rovibrational states in the QD than those listed in table 5.3 might be advisable. This is also the reason that QD now predicts a somewhat lower sticking probability than QCT in figure 5.4e. The

QD and QCT results based on the same set of initial rovibrational states in figure 5.7c,d are however in good agreement at these high nozzle temperature points, indicating that for all but the lowest average translational energies  $H_2 + Cu(111)$  is well described quasi-classically.

Note that for a nozzle temperature of 2000 K we take into account all rovibrational states that have a Boltzmann weight > 0.001. Highly excited rovibrational states, either with high  $\nu$ , high J, or both, yield high reaction probabilities at low translational energies, therefor the effect of not taking into account these rovibrational states might be larger than expected from their Boltzmann weight. It is however computationally very expensive to take into account all initial rovibrational states that have a Boltzmann weight > 0.001 at a nozzle temperature of 2300K in the QD calculations, i.e. the nozzle temperature for the point in figures 5.7c where the QCT results and the QCT results based on the same, smaller, set of initial rovibrational states as the QD calculations diverge most. Doing this would nearly double the amount of wave packet calculations, and these additional calculations would also require larger basis sets.

## Molecular beam sticking in $D_2 + Pt(111)$

Figure 5.9 shows a comparison of calculations on  $D_2 + Pt(111)$  to the molecular beam experiments of Luntz et al.<sup>65</sup>. The PBE $\alpha$ 57-DF2 DF was originally fitted<sup>12</sup> in order to reproduce these experiments. In figure 5.9b we see that the B86SRP68-DF2 DF can also describe these experiments with overall chemical accuracy (MAD = 3.1 kJ/mol), although the agreement with experiment at low incidence energies is just shy of being chemically accurate, which would adversely affect the extraction of the minimum barrier height for this system. The SRP48 DF also describes the experiments with overall chemical accuracy, but at low E the agreement with experiment is really poor (figure 5.9c). The MS-PBEl DF does not agree with experiments to within overall chemical accuracy (figure 5.9d).

The discrepancy between theory and experiment at low incidence energies for the SRP48 and B86SRP68-DF2 DFs most likely arises because these DFs exhibit a too high early barrier to reaction at the top site minimum barrier geometry (see table 5.10). These two DFs also do not possess the double barrier structure for the t2b site that the PBE $\alpha$ 57-DF2 DF predicts. The MS-PBEl functional does predict a double barrier structure for the t2b site. The early t2b barrier predicted by the MS-PBEl DF is however very high when compared to results obtained with the other DFs, which is most likely the root cause of its poor performance for this system.

The molecular beam experiments of Cao et al.<sup>61</sup> are not as well described by the B86SRP68-DF2 DF, as can be seen in figure 5.10. However we note that the increase of the MAD value in going from figure 5.9a to figure 5.10a is similar in size to what was reported for the PBE $\alpha$ 57-DF2 DF<sup>66</sup> (see table 5.12). Earlier work from our group has shown that the experimental results of Luntz et al.<sup>65</sup> and Cao et al.<sup>64</sup> are in good agreement with each other for the lower incidence energies but somewhat diverge for the higher incidence energies<sup>66</sup>. The possible origins of the discrepancy between these two sets of experimental data are discussed in ref.<sup>66</sup>. There it was surmised that at high average incidence energies the reaction probabilities of Cao et al.<sup>64</sup> are most likely somewhat underestimated compared to the results of Luntz et al.<sup>65</sup> because the average incidence energies themselves are somewhat underestimated in the experiment of Cao et al.<sup>61</sup>.

# Molecular beam sticking in $D_2 + Ag(111)$

We now make a comparison to molecular beam experiments on  $D_2 + Ag(111)^{147}$ . Even though silver is only one row below copper in the periodic table, the SRP48 DF that was fitted to reproduce experiments on Cu(111) was not able to describe experiments on Ag(111) with chemical accuracy<sup>20</sup>. Figure 5.8 shows the computed  $S_0$  for  $D_2 + Ag(111)$ . Hodgson and coworkers have reported translational energy distributions that were symmetric in the energy domain. In our view, and as discussed in previous work from our group<sup>20</sup>, the symmetric translational energy distributions are somewhat unphysical. Therefore we opted to use the molecular beam parameters of pure D<sub>2</sub> reacting on Cu(111) reported by Auerbach and coworkers<sup>46</sup>, which likewise describe beams that are narrow in translational energy. Here we see that the PBE $\alpha$ 57-DF2 and B86SRP68-DF2 DF are similar in accuracy to our previously developed MS-PBEl mGGA DF<sup>13</sup>, and that these three DFs predict a reactivity just shy of chemical accuracy when compared to the molecular beam experiment of Hodgson and coworkers (see table 5.12). Note that the PBE $\alpha$ 57-DF2 DF seems to perform worse than the other three DFs at the lowest translational energy. All three SRP-DFs yield an overall performance that is better than that of SRP48.

Although we are not yet able to describe the molecular beam experiment with chemical accuracy, the improvement of the DFs that include non-local correlation over the SRP48 DF again suggests that non-local correlation is an important ingredient for constructing SRP-DFs describing  $\rm H_2$  + metal systems that incorporate GGA exchange. The MS-PBEl mGGA<sup>13</sup> does not include non-local correlation but performs similarly well as the GGA based SRP-DFs

that do include non-local correlation. As will be shown in Chapter 6, further improvement is possible by adding non-local correlation to the MS-PBEl DF.

### 5.4.4 Associative desorption

#### Comparing to experimental $E_0(\nu, J)$ parameters

When comparing to experimental  $E_0(\nu, J)$  parameters by calculating  $E_{1/2}(\nu, J)$  parameters from calculated degeneracy averaged reaction probabilities we effectively try to model an associative desorption experiment as an initial-state resolved dissociative chemisorption experiment. Additionally our QCT results are obtained using the BOSS model, while the associative desorption experiments necessitate high surface temperatures. The J dependence of the calculated  $E_{1/2}(\nu, J)$  parameters is a measure of how accurate the reactivity of the individual rovibrational states is described relative to each other. The trend is here to be understood as the dependence of the  $E_0(\nu, J)$  parameters on J, which we can visualize using a third degree polynomial fit to the calculated results (see e.g. figure 5.16).

In this work we have not included MDEF calculations in which the effect of ehp excitations is modeled as a classical friction force. In our previous work<sup>37</sup> the MDEF method shifted the  $E_{1/2}(\nu, J)$  parameters to slightly higher values since, again, we model an associative desorption experiment using a dissociative chemisorption calculations. Including the effect of ehp excitations in the dynamics here then has a similar effect in both cases, and shifts the  $E_{1/2}(\nu, J)$  parameters to slightly higher energies. However, as mentioned in our previous work<sup>37</sup>, if ehp excitations are important then assuming detailed balance to extract degeneracy averaged reaction probability curves is, strictly speaking, not correct. More specifically, we would expect that if we applied electronic friction to the simulation of an associative desorption experiment in the manner discussed here, the predicted translational energy distributions would shift to higher energies as opposed to lower energies as expected in a direct simulation of associative desorption. In other words: extracting  $E_{1/2}(\nu, J)$  parameters from dissociative chemisorption calculations applying electronic friction would shift our  $E_{1/2}(\nu, J)$  parameters to higher energies instead of the expected lower energies, because the effective barrier for dissociative chemisorption would go up. However, we note that the MDEF calculations in our previous  $work^{37}$  only shifted the trend in  $E_{1/2}(\nu, J)$  parameters to slightly higher values on the energy axis and did not influence the observed trend in their J-dependence. This is in accordance with very recent direct simulations of associative desorption of H<sub>2</sub> from Cu(111)<sup>76</sup> using AIMD and AIMDEF calculations and the PBE DF,

which find little effect of ehp excitations modeled at the local density friction approximation  $(LDFA)^{156}$  level.

In section 5.4.9 we will further discuss how a combined analysis of dissociative chemisorption and associative desorption experiments might be used in the future to determine a possible fingerprint of non-adiabatic effects.

 $\mathbf{E}_{1/2}(\nu,J)$  parameters  $\mathbf{Cu(111)}$  The comparison of the measured  $E_0(\nu,J)$  parameter values with the  $E_{1/2}(\nu,J)$  parameters computed using method B1 is shown in figure 5.15. The  $E_{\max}(\nu,J)$  parameters needed in this method (see Eq. 5.16) were taken from Tables S4 and S6 of Ref. <sup>48</sup>. The comparison of the experimental  $E_0(\nu,J)$  parameters with theoretical  $E_{1/2}(\nu,J)$  parameters extracted using method A1 is presented in figure 5.14. In this method we used A=0.325 for  $H_2$  and A=0.513 for  $D_2$ , as obtained in Ref<sup>48</sup>.

Table 5.13 presents MAD and MSD values obtained with both methods. The following conclusions can be drawn: for almost all DFs method A1 (based fully on experiments) yields the lowest MAD and MSD values. The only exception occurs for  $\rm H_2 + Cu(111)$  when using the SRP48 DF, for which method B1 gives a lower MAD value (41 meV), although the difference with method A1 (43 meV) is quite small. From this point of view, method A1 works better.

The use of method A1 for H<sub>2</sub> would seem to yield conclusions that are more consistent with the conclusions from the comparisons of the sticking probabilities. Specifically, the mGGA DF and the DFs containing non-local van der Waals correlation all perform better than SRP48 DF for H<sub>2</sub>. Nonetheless, SRP48 performs best for D<sub>2</sub>, regardless of whether method A1 or B1 is used. We also note that the better behavior of the other DFs in procedure A1 is to some extent suspect due to the rather low A value employed for  $H_2$  (0.325). This A value is much lower than the A value extracted for D<sub>2</sub> in method A1 (0.513). This may well be a simple artifact resulting from the method followed: the A value determined for D<sub>2</sub> is likely to be more accurate because the sticking experiments were done for a kinetic energy up to  $0.83~\mathrm{eV^{46}}$ , whereas the sticking experiments for  $H_2$  only went up to about  $0.5 \text{ eV}^{52}$ . This suggest that the A-value for D<sub>2</sub> (figure 5.B.1c) is much more accurate than for H<sub>2</sub> (figure 5.B.1a), and it is not clear why the A value for H<sub>2</sub> should differ much from it. Furthermore, the A value established for H<sub>2</sub> in method A1 is much lower than the A-values established for H<sub>2</sub> in method B1 (see also figure 5.B.1a and 5.B.1c), while for D<sub>2</sub> the A values extracted with the two methods resemble each other, and the A values extracted with method B1 for H<sub>2</sub>, much more (see figure 5.B.1b, 5.B.1c and 5.B.1d).

Finally, we note at this stage that the  $E_{1/2}(\nu, J)$  parameters computed using method A1 do, in general, not reproduce the subtle trend found experimentally

that the  $E_0(\nu, J)$  parameters first increase somewhat with J (see figure 5.14) (attributed to rotational hindering  $^{46,48,52}$ ).

The  $E_{1/2}(\nu,J)$  parameters calculated using method B1 (especially the ones calculated with DFs incorporating non-local Van der Waals correlation) better reproduce this subtle rotational hindering effect (figure 5.15). The reasonable performance of method B1 is also clear from figure 5.16, which presents a third degree polynomial fit to the  $E_{1/2}(\nu,J)$  parameters as a function of J obtained using the B1 method. The polynomial fits are shown without the energy axis offset. DFs that include non-local correlation reproduce the subtle rotational hindering effect, DFs that do not include non-local correlation do not or hardly show rotational hindering. Additionally, for  $H_2$ , the agreement with the experimental dependence of the  $E_0(\nu,J)$  parameters on J improves when using the QD method for vibrationally exited molecules.

That DFs including non-local correlation better reproduce the subtle rotational hindering effect with the use of method B1 is wholly due to the rovibrational state dependence of the  $E_{\rm max}(\nu,J)$  parameters. The extracted degeneracy averaged reaction probabilities in fact monotonically increase with increasing J (figure 5.12), and this is true for all DFs used in this work. Reproducing rotational hindering based on these degeracy averaged reaction probability curves is therefore not possible when selecting the same A value for all rovibrational states, as done with method A1.

The  $E_{1/2}(\nu, J)$  parameters calculated using both method A1 and B1 do reproduce the clear trend (figures 5.14 and 5.15) that at high J the  $E_0(\nu, J)$  parameters decrease with J (attributed to energy transfer from rotation to the reaction coordinate as the rotational constant decreases when the molecule stretches to reach the dissociation barrier<sup>26,37,129</sup>).

We are aware of one single PES that does reproduce the rotational hindering effect as observed in the experiment, namely the LEPS PES<sup>40</sup> used by Dai et al.<sup>38</sup> for six-dimensional QD calculations. As discussed in appendix 5.C, we have investigated whether the rotational hindering observed by Dai et al.<sup>38</sup> could be due to their QD calculations being unconverged. We find that this is not the case, but that the observed difference with our calculations using the best SRP-DF (B86SRP68-DF2) only arises for J < 3, suggesting that the rotational hindering effect is very subtle (see figure 5.C.1). Further research is needed to check whether the difference between the calculations could be due to the LEPS fit<sup>40</sup> being inaccurate, the underlying electronic structure calculations being unconverged<sup>40,41</sup>, or both. See appendix 5.C for further details.

Reported density functional molecular dynamics (DFMD) calculations that include surface motion have shown that at low translational energies surface temperature effects somewhat increase the reactivity of  $D_2$  reacting on

 $Cu(111)^{24,63}$ . Increased reactivity at low translational energies might lower calculated  $E_{1/2}(\nu, J)$  parameters for both methods A1 and B1. We have extracted  $E_{1/2}(\nu, J)$  parameters using both methods A1 and B1 from Nattino et al.<sup>63</sup>. The results are shown in figure 5.23. The reported data was obtained using the SRP48 DF<sup>63</sup>. There were only three rovibrational states for which a data point was available at a translational energy higher than the maximum kinetic energy sensitivity of the experiment<sup>48</sup>. To validate the obtained  $E_{1/2}(\nu, J)$  parameters we have also extracted  $E_{1/2}(\nu, J)$  parameters using the same methodology for the reported logistics function fits to BOSS direct dynamics data<sup>63</sup>. The good agreement for both methods A1 and B1 between our SRP48  $E_{1/2}(\nu, J)$ parameters and those obtained from logistics function fits to BOSS direct dynamics data validates this comparison. For both the A1 and B1 method the single point for  $(\nu = 0, J = 11)$  suggests that a small decrease can be expected from allowing the surface to move, for the  $(\nu = 1, J = 6)$  point this is not so clear. There is however a dramatic decrease of the  $E_{1/2}(\nu, J)$  parameter for  $(\nu = 1, J = 4)$ . This is a clear indication that, at least for low J, taking into account surface motion leads to lower  $E_{1/2}(\nu, J)$  parameters, and this might thus be partly responsible for the observed rotational hindering. The decrease of the  $E_{1/2}(\nu=1,J=4)$  value with the introduction of surface motion is less pronounced when using the A1 method.

Note however that the  $E_0(\nu, J)$  parameters are extremely sensitive to the quality of the logistics function fits. The agreement between our SRP48  $E_{1/2}(\nu, J)$  parameters and those obtained from logistics function fits to BOSS direct dynamics for which no data point existed at a translational energy higher then the maximum kinetic energy sensitivity to which the experiment was sensitive was not so good.

The above observations warrant the following tentative conclusions: within the BOSS approximation, the mGGA DF and the DFs containing non-local correlation perform best for sticking. However, assuming method B1 to be best, the SRP48 performs best for associative desorption. For associative desorption and again within the BOSS approximation, the two different methods (A1 and B1) for extracting the  $E_{1/2}(\nu,J)$  parameters describing the reaction probabilities extracted from associative desorption experiments yield rather different results. It follows that, at this stage, the associative desorption experiments are not as useful as the sticking experiments for assessing the accuracy of theory. Hopefully this can be changed in future by taking into account surface atom motion and ehp excitation in the theory, and by computing associative desorption fluxes directly from theory, as was recently done using the PBE DF by Galparsoro et al.  $^{76}$ .

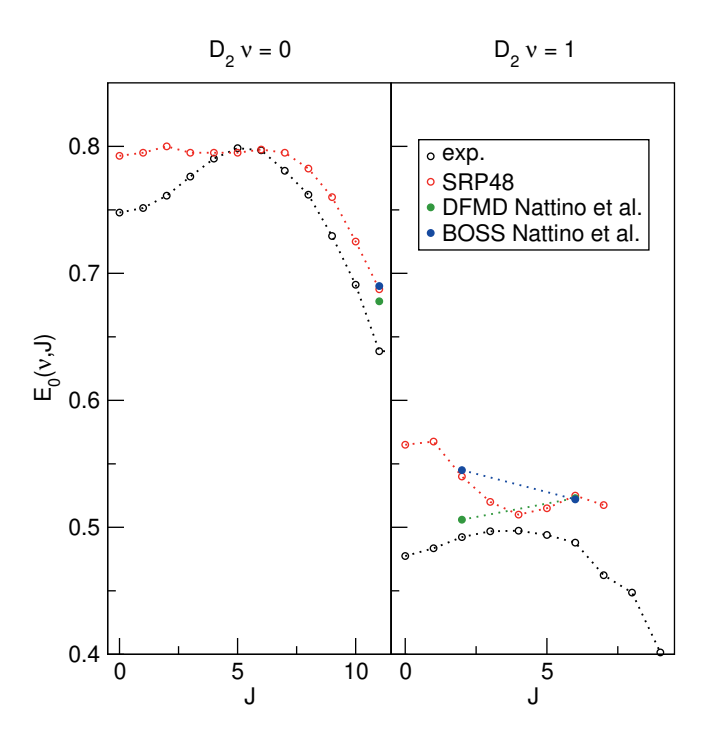


FIGURE 5.23:  $E_{1/2}(\nu, J)$  parameters as a function of J for  $D_2$  reacting on Cu(111). Closed symbols pertain to  $E_{1/2}(\nu, J)$  parameters calculated using the A1 method, open symbols refer to the B1 method. Experimental results are shown in black<sup>48</sup>, SRP48 results calculated in this work are shown in red. DFMD (green) and BOSS (blue) results obtained using the SRP48 DF have been extracted from ref.<sup>63</sup>

 $\mathbf{E}_{1/2}(\nu,J)$  parameters  $\mathbf{Au(111)}$  The comparison of the measured  $\mathbf{E}_0(\nu,J)$  values with the  $E_{1/2}(\nu,J)$  parameters computed using method B2 is shown in figure 5.17. The  $E_{\max}(\nu,J)$  parameters needed in this method (see Eq. 5.16) have been obtained from a private communication<sup>148</sup>, and have been plotted in figure 5.B.2 against the  $\mathbf{E}_0(\nu,J)$  parameters extracted from the measurements<sup>71</sup>. We note that the  $E_{\max}(\nu,J)$  parameters typically equal  $E_0(\nu,J)+\frac{1}{3}W$  for the  $\nu=0$  states and  $E_0(\nu,J)+\frac{2}{3}W$  for the  $\nu=1$  states, where W=0.31 eV for  $\nu=0$  and 0.29 eV for  $\nu=1^{71}$  (see figure 5.B.2). This means that method B1 will yield unreliable values for the  $E_{1/2}(\nu,J)$  parameters. It also means that method B2 relies heavily on extrapolation in the method to determine the A values by anchoring the measured reaction probabilities to the reaction probabilities computed at  $E_{\max}(\nu,J)$ . One should therefore exercise extreme caution when comparing the theory to experiment.

Table 5.13 shows the MAD end MSD values obtained with method B2 for  $H_2 + Au(111)$ . The following tentative conclusions can be drawn: the  $E_{1/2}(\nu, J)$  parameters computed with the mGGA DF tested here and with all DFs employing Van der Waals correlation substantially overestimate the measured  $E_0(\nu, J)$  parameters, with MAD values of approximately 0.1 eV for  $H_2$ . The PBE DF would appear to perform best, with a MAD value of 46 meV for  $H_2$ . This conclusions agrees with the observation that PBE reaction probabilities allowed better fits of the measured time-of-flight spectra of  $H_2$  and  $D_2$  desorbing from  $Au(111)^{71}$  than the SRP48 reaction probabilities.

A caveat here is that the experiment was performed with a surface temperature of 1063K, while all calculations were performed using the BOSS model. Allowing surface motion during the dynamics would lead to broadening of the sticking probability curves  $^{24,30,157,158}$ . A higher sticking probability at lower translational energies could potentially lower the theoretical  $E_{1/2}(\nu, J)$  parameters. Additionally, we have performed our calculations on an unreconstructed Au(111) surface because the surface unit cell of reconstructed Au(111) is at present too big to map out a full PES using DFT calculations. Earlier work in our group indicated that the barriers to H<sub>2</sub> dissociation are somewhat higher on the reconstructed Au(111) surface and that using an unreconstructed surface might lead to the underestimation of dynamical barrier heights by about 50 meV ( $\sim$ 1 kcal/mol)<sup>145</sup>, which would lead to slightly higher  $E_{1/2}(\nu, J)$  parameters and therefore to increased disagreement with the measured values.

We are not able to resolve the contradiction posed by Shuai et al.<sup>71</sup> that the vibrational efficacies computed with the SRP48 DF are in good agreement with experiment (as may be derived from figure 5.17) but that the ratio of desorbed molecules in the vibrational ground state versus the vibrationally excited state is not (see table 5.14). The good reproduction of the J dependence of the

 $E_0(\nu, J)$  parameters by theory (figure 5.17) suggests that the reactivity of the individual rovibrational states relative to each other is accurately described by theory as long as states are considered with the same vibrational level. Previously reported experiments implied that the recombination of H<sub>2</sub> on Au(111) is coupled to the electronic degrees of freedom of the metal 159–162. In line with Shuai et al. 71 we think that non-adiabatic effects together with surface motion effects and surface reconstruction represent the most likely causes for the lower translational energy distributions of the desorbing  $H_2$  ( $\nu = 0$ ) molecules compared to theory. If molecular beam dissociative chemisorption experiments on a reasonably cold surface would become available for this system (like for  $H_2 + Ag(111)$ ) this would allow for a more direct comparison to experiment of QCT and MDEF calculations. Molecular beam adsorption experiments would also allow us to check if the absolute reactivity predicted by the DFs shown here is in agreement with experiment. Therefore, at present, we cannot corroborate or refute the conclusion reached by Shuai et al. 71, namely that the experimentally observed lower translational energy distributions compared to theoretical predictions (see figure 1 of Shuai et al.<sup>71</sup>) is most likely due to ehp excitations in the desorption dynamics.

### Rovibrational state populations of $H_2$ and $D_2$ desorbing from Au(111).

Figure 5.21 shows the rovibrational state populations of  $H_2$  and  $D_2$  desorbing from Au(111). Note that we have consistently applied the normalization procedure outlined by Eq. 5.14 to the objects shown in figure 5.21. In the case of  $(\nu=0)$  the populations deviate from the slope set by the Boltzmann distributions at the surface temperature of 1063 K indicating that rotationally excited molecules are more likely to adsorb<sup>71</sup>. The populations of vibrationally excited molecules also lie on gentler slope than implied by the Boltzmann distribution and are consistenly higher than would be obtained with the Boltzmann distribution indicating that vibrationally excited molecules are more likely to adsorb. Both these observations are in line with the Polanyi rules for a late barrier system like  $H_2 + \mathrm{Au}(111)^{163,164}$ .

Figure 5.22 shows the state distributions of molecules desorbing from Au(111) as reported by Shuai et al.<sup>71</sup> in their figure 2 together with experimental results calculated by us using Eq. 5.13, an upper integration limit of 5 eV, and our normalization procedure, which were the boundary conditions and integration parameters suggested to us by Shuai et al.<sup>71,148</sup> As can be seen from figure 5.22 our "experimental results" calculated using Eq. 5.13 and the error function fits reported in Ref.<sup>71</sup> are in good agreement with the experimental results reported by Shuai et al.<sup>71</sup>, i.e. the calculated curves have the correct shape and

can be mostly superimposed on one another, provided that they are shifted by a constant value as explained in the caption of figure 5.22. However, we are not able to reproduce the results of Shuai et al.<sup>71</sup> with the normalization strategy they employed<sup>71</sup>. Also when we shift the SRP48 ( $\nu = 0$ ) and ( $\nu = 1$ ) curves by the same value we cannot exactly superimpose our results on their computed SRP48 results for both vibrational states simultaneously. It is not clear to us how this discrepancy arises.

The relative populations for the  $(\nu = 0)$  and  $(\nu = 1)$  rovibrational states is not affected by this discrepancy. The difference between our work and Shuai et al. The with respect to the  $\nu = 1$ :  $\nu = 0$  ratios arises because we use  $E_{\rm max}(\nu, J)$ as the upper integration limit in Eq. 5.13. Shuai et al.<sup>71</sup> have used 5 eV as the upper integration limit <sup>148</sup>. The only reason we choose  $E_{\text{max}}(\nu, J)$  as the upper integration boundary is because the reported error function fits are only reliable below  $E_{\text{max}}(\nu, J)$ , for some rovibrational states the error function fits can yield sticking probabilities much larger than unity for high kinetic energies. The ratios we calculate are shown in table 5.14. We note that when we use the upper integration limit of 5 eV, we reproduce the  $\nu = 1 : \nu = 0$  ratios reported by Shuai et al.<sup>71</sup>. In our view only integrating up to  $E_{\text{max}}(\nu, J)$  is a more fair way of calculating the  $N(\nu, J)$  populations, though on the scale of figure 5.21 the difference between integrating to  $E_{\text{max}}(\nu, J)$  or 5 eV would not be visible. Note that the overwhelming majority of the area under the Gaussian fits to the time-of-flight curves, as reported in tables S1-4 of Ref. 71, lies well below  $E_{\rm max}(\nu,J)$ . Note also that we calculate the  $\nu=1:\nu=0$  ratios only using the rovibrational states shown in figure 5.21, which is the same set of rovibrational states used by Shuai et al.<sup>71</sup>.

In figure 5.21 the difference between the desorbing populations computed with the SRP48 and B86SRP68-DF2 DFs is minimal. The agreement between theory and experiment is best for  $D_2$ , although the qualitative agreement between theory and experiment is reasonable for both  $H_2$  and  $D_2$ . It can be seen in table 5.14 that there is only a reasonable agreement for  $D_2$  with respect to the  $\nu = 1 : \nu = 0$  population ratios. The theoretical  $\nu = 1 : \nu = 0$  population ratio for  $H_2$  is however too low, a result similar to what was reported by Shuai et al.<sup>71</sup>. The difference between theory and experiment can perhaps be explained by the experimental time-of-flight distributions being much broader than the theoretical ones, see figure 1 of Ref.<sup>71</sup> Taking into account surface motion in the theoretical calculations might well improve the agreement with experiment with respect to both the rovibrational state distributions of desorbing molecules as well as the  $\nu = 1 : \nu = 0$  population ratio.

## Initial-state resolved reaction probabilities for $D_2 + Ag(111)$ .

In the case of molecular beam sticking results for  $D_2 + Ag(111)$  the MS-PBEl functional performed similarly well as the GGA-exchange based SRP-DFs that include non-local correlation even though the barriers obtained with the DFs including vdW-DF2 correlation are higher (see table 5.8). This is most likely due to the slightly earlier barriers to reaction predicted by the MS-PBEl DF, leading to less promotion of reaction by vibrationally excited  $H_2^{13}$  as obtained with the DFs including vdW-DF2 correlation, as expected from the Polanyi rules  $^{163,164}$ . From this argument it follows that although the molecular beam sticking probabilities are similar the reactivity of individual rovibrational states should be different.

In figure 5.13 we see that, especially for  $D_2$ , the MS-PBEl mGGA DF has the best agreement with the initial-state selected reaction probabilities extracted from the associative desorption experiments. The good performance of the MS-PBEl DF for  $\nu = 0$  and  $\nu = 1$  can be explained by the slightly lower and earlier barriers, as discussed in our previous work<sup>13</sup>. The DFs that include non-local correlation do not show such a large improvement over the SRP48 DF, while they do for sticking.

Without new experimental work for this system, especially molecular beam experiments covering a wide range of translational energies and nozzle temperatures, it will be difficult to further improve the theoretical description of this system. Additional experiments (e.g. a molecular beam sticking experiment on  $D_2$  seeded in  $H_2$  and going up to a translational energy of 0.8 eV as done for  $H_2 + \mathrm{Cu}(111)^{46}$ ) would also allow us to assess more accurately if the dynamics predicted by the MS-PBEl mGGA or the dynamics predicted by the GGA based SRP-DFs that do and do not include non-local correlation are more in line with experimental observations.

# Rotational quadrupole alignment parameters: $H_2 + Cu(111)$ .

In figure 5.18 we compare calculated rotational quadrupole alignment parameters for  $D_2$  to experimental ones measured for  $D_2$  desorbing from  $Cu(111)^{50}$ . We observe only a monotonic increase of the rotational quadrupole alignment parameters with decreasing translational energy, indicating that at translational energies close to the reaction threshold molecules prefer to react in a parallel orientation. This is in line with what has been reported in the literature for  $H_2$  and  $D_2$  associatively desorbing from  $Cu(111)^{27,50}$  and  $Cu(100)^{19,26}$ , and can be explained by invoking a static effect of orientational hindering in which rotating molecules scatter when their initial orientation does not conform to

the lowest barrier geometry<sup>26</sup>. With increasing translational energy the rotational quadrupole alignment parameter approaches zero since all molecules, irrespective of their orientation, will have enough energy to react<sup>50</sup>. The experimental trend is reproduced by all DFs shown in figure 5.18a and b, though the calculated values are higher than the experimental values. The theoretical results presented here have been obtained within the BOSS approximation. Nattino et al.<sup>27</sup> have shown that incorporating surface motion in the dynamics using the DFMD technique leads to better agreement with experiment, for  $D_2 + Cu(111)$ .

Note that the B86SRP68-DF2, PBE $\alpha$ 57-DF2<sup>12</sup> and MS-B86bl<sup>13</sup> DFs are in good agreement with each other for both the ( $\nu=0,J=11$ ) state (figure 5.18a) and the ( $\nu=1,J=6$ ) state (figure 5.18b), but that these three DFs predict slightly higher rotational quadrupole alignment parameters than the SRP48 DF<sup>27</sup>. Given that the SRP48 rotational quadrupole alignment parameters were decreased, but still somewhat too large when surface atom motion was introduced<sup>27</sup>, the present results suggest that the SRP48 DF yields the best description of this observable.

## 5.4.5 Inelastic scattering of $H_2$ from Cu(111)

In this section we will discuss inelastic scattering results for H<sub>2</sub>, obtained with QD. We start with the vibrationally inelastic scattering results for H<sub>2</sub> shown in figure 5.19. We specifically show QD results since the previously voiced expectation that vibrationally inelastic scattering should be well described using the QCT method for translational energies above the lowest barrier to reaction<sup>165</sup> has been shown not to hold<sup>25</sup>. Here we discuss the inelastic scattering probability  $P(\nu = 0, J \rightarrow \nu = 1, J = 3)$  for three different initial J states. Panels a and b suggest that for (J=1) and (J=3) and for the DFs that use non-local correlation the vibrationally inelastic scattering probability is correlated with the depth of the Van der Waals well (see table 5.11). A deeper Van der Waals well is correlated with higher vibrationally inelastic scattering probabilities. Figure 5.19c shows that for (J=5) all DFs yield vibrational excitation probabilities in reasonable agreement with each other. Bringing TOF spectra for vibrational excitation from  $(\nu = 0, J)$  to  $(\nu = 1, J = 3)$  in better agreement with experimental results would require a substantial increase of the vibrational excitation probabilities computed with the SRP48 DF (by a factor of 2-3)<sup>25,165</sup>, which is obtained with non of the DFs tested. We conclude that better agreement with experiment probably requires a different dynamical model, as suggested also by earlier work $^{25,165}$ .

From the computed ratio of rotationally inelastic scattering probabilities  $P(\nu = 1, J = 0 \rightarrow \nu = 1, J = 2)/P(\nu = 1, J = 0 \rightarrow \nu = 1, J = 0)$  shown in figure 5.20 it is clear that the B86SRP68-DF2 DF performs not as well as the SRP48 DF<sup>11</sup>. The shifted SRP48 curve follows the experiment more closely. Both curves need to be shifted by 40 meV in order to better overlap with the experiment performed using a surface temperature of  $300 \text{ K}^{55}$ . The overlap with experiment of the shifted curves only holds until 0.14 eV, but the experimentalists noted that at higher energies the measurements became more difficult<sup>55</sup>. It is rather surprising that both computed ratios need to be shifted by roughly the same amount in order to overlap with experiment, since the SRP48 DF overestimates the initial sticking probability in molecular beam experiment while the B86SRP68-DF2 DF does not. From the literature it is also known that including surface motion during the dynamics might lead to broadening, and an earlier onset, of inelastic scattering probabilities<sup>24,30</sup>. We speculate that allowing surface motion and ehp excitation during the dynamics might obviate the need for the shift in order to superimpose the calculated curves with experiment.

# 5.4.6 QD vs. QCT for $H_2 + Cu(111)$

In figure 5.11 initial state-resolved reaction probabilities are shown calculated using the B86SRP68-DF2 DF. Here the (J=0) and (J=1) state for both the vibrational ground state and the first vibrationally excited state are shown because the differences between the QD and QCT method are most prevalent for the low lying rotational states. The QD reaction probability curves show more structure than was shown for  $H_2 + Cu(211)^{37}$  in Chapter 4, but the agreement between the QD and QCT method for degeneracy averaged reaction probabilities (figure 5.11a and c) is still very good. From the comparison between QD and QCT degeneracy averaged reaction probabilities shown in figure 5.12 it can be seen that the differences between the QD and QCT method get smaller with increasing J for J > 3, though small differences remain even for high J states.

The biggest difference between the QD and QCT method are observed in figure 5.11b. Here we show fully initial-state resolved reaction probabilities, thereby distinguishing between 'cartwheeling' molecules rotating in a plane parallel to the surface normal  $(m_J=0)$  and 'helicoptering' molecules rotating in a plane perpendicular to the surface normal. In line with our previous work presented in Chapter 4, we observe that QD predicts a slightly larger preference for molecules reacting parallel to the surface. The rovibrational states shown in figure 5.11 are the same rovibrational states shown in figure 4.2 of Chapter

4, in which the agreement for degeneracy averaged reaction probabilities was nearly perfect.

In recent experimental work Kaufmann et al. 48 have reported a previously unobserved "slow reaction channel" for H<sub>2</sub> associatively desorbing from Cu(111) and Cu(211). In this channel, the reaction could be facilitated by trapping on the surface and distortion of the surface due to thermal motion forming a reactive site<sup>48</sup>. Even though our PES now contains a Van der Waals well that might facilitate trapping during the reaction dynamics, we do not yet see evidence of the recently reported slow reaction channel for  $H_2 + Cu(111)^{48}$ . The translational energy range used in our calculations overlaps with the translational energies at which the slow channel reactivity was observed<sup>48</sup>. We can therefore rule out quantum effects (like tunneling, see Chapter 4) during the dynamics as the origin of this slow reaction channel for  $H_2 + Cu(111)$ , as we did before for  $H_2 + Cu(211)^{37}$ . We therefore propose, as done earlier for  $H_2 + Cu(211)^{37}$ , that the slow reaction channel reported by Kaufmann et al. 48 originates from the very high surface temperature of 923K used in the associative desorption experiments. Presently it is not possible to take surface motion explicitly into account in QD calculations, and it is challenging to do so in QCT calculations<sup>150–152</sup>. Galparsoro et al.<sup>76</sup> likewise did not yet find evidence for the slow reaction channel in their AIMD calculations.

# 5.4.7 Overall description of systems

When looking at the  $H_2 + Ag(111)$  and  $H_2 + Au(111)$  systems considered in this work together, one stark realization is that further development of chemically accurate DFs for H<sub>2</sub> reacting on transition metal surfaces is still heavily stymied by a lack of experimental data. This is bad news as presently semi-empirical DFT seems to be the only path to extracting chemically accurate information on barriers to reaction. Relying on non-empirical constraints on DF design is not yet feasible, as illustrated by the poor performance of the SCAN<sup>166</sup> DF for  $H_2 + Cu(111)^{13}$  (see figure 3.11 of Chapter 3). Additionally, taking another step upwards on Jacob's ladder from a GGA or mGGA towards hybrid DFs is computationally very expensive, if not prohibitively so 167. Furthermore, recent quantum Monte-Carlo (QMC) calculations on  $H_2 + Cu(111)^{15}$  underestimate the barrier height for this system by more than 1 kcal/mol while dynamics results on O<sub>2</sub> + Al(111) based on a PES obtained with density functional embedded correlated wave function theory showed promising chemically accurate results with respect to the obtained sticking probability<sup>168</sup>. Furthermore, it would be expensive to extend this electronic structure method to sticking of molecules on transition metal surfaces.

For both the activated and non-activated reactions of  $H_2$  on transitions metals there is now only a single well studied system, namely  $H_2 + \text{Cu}(111)$  (and maybe  $H_2 + \text{Pt}(111)^{66}$ ). What we mean by well studied is that there should be different kinds of well described experiments. For example, a combination of an associative desorption experiment and a dissociative chemisorption experiment should be available, or sticking probabilities for normal and off-normal incidence. It is also critical that the experimental conditions are described accurately.  $^{16,20,21,65,66,145}$ 

Without new and detailed experiments on, at least, the related  $H_2 + Pd(111)$  and  $H_2 + Ag(111)$  or  $H_2 + Au(111)$  systems it is not possible to grasp the overarching trends in reactivity imposed by the position of these metals in the periodic table. In many aspects we are dancing in the dark with respect to DF design. The consequence of this is that, presently, theory can only provide models with limited predictive power.

#### $H_2 (D_2) + Cu(111)$

The  $H_2 + Cu(111)$  system is the best described system of the ones treated here. Low surface temperature molecular beam sticking experiments are very accurately described using the BOSS model. The associative desorption experiments are however less well described by the new SRP-DFs that have been designed to reproduce low surface temperature molecular beam experiments with calculations using the BOSS model.  $E_{1/2}(\nu, J)$  parameters obtained from reported DFMD data<sup>63</sup> suggest that, at least for this system, better agreement with experiment can be attained by including the surface degrees of freedom in the dynamics. It also appears that the agreement with  $E_0(\nu, J)$  parameters measured in an associative desorption experiment is also increased for vibrationally excited molecules when using the QD method.

The large amount of published experimental studies  $^{46-62,169,170}$  and theoretical work  $^{11,13,19,22-45,157,171,172}$  have allowed us to get the best description of this system so far. We can however not yet point to one DF that is clearly the best DF for this system. Currently two DFs compete for being the best DF for this system, namely B86SRP68-DF2 and MS-B86bl  $^{13}$ . The latter has a beter description of the metal and might therefor be better when looking at diffraction probabilities. The MS-B86bl DF however misses any description of Van der Waals forces. In all our simulations for the  $H_2 + Cu(111)$  system the B86SRP68-DF2 and MS-B86bl DFs perform similarly well. With the information available now one might argue that the MS-B86bl DF is the best DF for this system since its description of the metal is much better than provided by the B86SRP68-DF2 DF, and because the effect of including non-local correlation

is only apparent when calculating  $E_{1/2}(\nu,J)$  parameters for this system. The MS-B86bl DF is however not transferable to weakly activated systems like H<sub>2</sub> + Pt(111). In our view, the DFs that are more generally applicable, i.e. the B86SRP68-DF2 and PBE $\alpha$ 57-DF2 DFs, are currently the best DFs. A good next step could be to use non-local correlation together with the MS-B86bl DF, as discussed in Chapter 6.

## $D_2 + Ag(111)$

For the  $D_2 + Ag(111)$  system it is more difficult to assess the quality of our theoretical description due to the lack of well defined molecular beam parameters<sup>20</sup>. DFs that use GGA-exchange and non-local correlation, and the MS-PBEl DF predict roughly similar molecular beam sticking probabilities. The comparison to the initial-state resolved reaction probabilities suggests that the MS-PBEl DF performs best due to its slightly lower and earlier barriers<sup>13</sup>. Since the MS-PBEl DF has a better description of the metal, a better description of the initial-state resolved reaction probabilities, and performs similar to the other candidate SRP-DFs concerning molecular beam sticking, one might argue that the MS-PBEl DF is currently the best DF for this system. As said before, the best DF should also exhibit transferability. Therefore we suggest, with some hesitation, that the B86SRP68-DF2 DF is the best DF at the moment for the  $H_2 + Ag(111)$  system. However, as will become clear in Chapter 6, the sticking in  $D_2 + Ag(111)$  can be described with chemical accuracy using the MS-PBEl-rVV10 DF. More and better defined experiments will allow us to refine our description of this system.

# $H_2 (D_2) + Au(111)$

With respect to the  $H_2 + Au(111)$  system we cannot with certainty assess the quality of any of the DFs tested here. Based on the good reproduction of the experimental trend in  $E_{1/2}(\nu, J)$  parameters and the reasonable agreement between theory and experiment with respect to the state distributions of desorbing molecules, we can infer that the reactivity of the rovibrational states relative to each other is described reasonably well. We cannot say anything about the accuracy of the barriers without additional experiments or improvements in our dynamical model that will allow us to disentangle the effects of surface temperature, surface reconstruction and ehp excitations (see section 5.4.9).

Shuai et al.<sup>71</sup> suggested that the PBE DF is better then the SRP48 DF because calculated time-of-flight distributions correlated slightly less worse with experimental observations for the PBE DF. This assertion implicitly assumes the validity of detailed balance for this system. The main conclusion of the

experimentalists was however that the bad agreement between theory and experiment points toward strong non-adiabatic effects, which, if true, would invalidate the assumption of detailed balance<sup>71</sup>.

#### $D_2 + Pt(111)$

Ghassemi et al.<sup>12</sup> have previously designed a SRP-DF for the  $D_2 + Pt(111)$  system. Although the B86SRP68-DF2 DF could describe the experiments of Luntz et al.<sup>65</sup> to within chemical accuracy, the description of the experiments of Cao et al.<sup>61</sup> was not as good. As was the case for the  $H_2 + Ag(111)$  system there is some discussion about molecular beam parameters describing different experiments, but the experiments are in reasonably good agreement with each other<sup>66</sup>. Overall this system is best described by the PBE $\alpha$ 57-DF2 DF that was specifically designed for this system<sup>12</sup>.

### 5.4.8 Transferability

So far SRP-DFs fitted to reproduce molecular beam sticking experiments on  $H_2$  and  $D_2$  dissociating on noble metal surfaces where shown to be transferable among systems in which  $H_2$  interacts with different crystal faces of the same metal<sup>18,19</sup>, but not among systems in which  $H_2$  interacts with surfaces of different metals<sup>20,21</sup>. Here we show examples in which a SRP-DF that was fitted to reproduce molecular beam sticking experiments on the activated late barrier system of  $H_2$  reacting on Cu(111) can also describe the non-activated early barrier system of  $D_2$  reacting on Pt(111) with chemical accuracy, and vice versa. Transferability to a different substrate of a SRP-DF fitted to reproduce gas-surface experiments has so far only been reported for  $CH_4$  dissociation on  $Ni(111)^{14}$  to  $CH_4$  dissociation on  $Pt(111)^{17}$ .

The SRP48 DF for  $H_2 + Cu(111)$  is not transferable to the  $H_2 + Ag(111)$  system<sup>20</sup> or to the  $H_2 + Pt(111)$  system. We have previously shown that a SRP-DF based on the mGGA that does not include non-local correlation (MS-PBEl<sup>13</sup>) greatly improves the transferability from  $H_2 + Cu(111)$  to  $H_2 + Ag(111)^{13}$ , but figure 5.9 shows that this DF is not transferable to the weakly activated  $H_2 + Pt(111)$  system.

The only group of DFs that might be considered transferable between both highly activated and weakly activated systems are DFs that include non-local correlation. We demonstrated that a SRP-DF fitted to  $H_2 + Pt(111)$ , PBE $\alpha$ 57-DF2<sup>12</sup>, can describe  $H_2 + Cu(111)$  with overall chemical accuracy and that a new SRP-DF fitted to  $H_2 + Cu(111)$ , B86SRP68-DF2, can describe the  $D_2 + Pt(111)$  experiments of Luntz et al.<sup>65</sup> with chemical accuracy. We speculate that the transferability between the Cu(111) and Pt(111) systems might be

improved by taking into account relativistic corrections in our DFT calculations beyond those already included in the PAW potentials<sup>135</sup>, which at this accuracy level might be important<sup>173,174</sup>.

Both the B86SRP68-DF2 and PBE $\alpha$ 57-DF2 DFs more or less predict the same reactivity for the H<sub>2</sub> + Ag(111) system. It is not possible however to call the DFs transferable to this system, yet. The lack of well described dissociative chemisorption experiments for this system does not yet allow us to make a broad statement about the accuracy of the theoretical description of this system. At present our description appears to be just shy of chemical accuracy.

# 5.4.9 Adiabatic description of $S_0$ and $E_{1/2}(\nu, J)$ , a possible fingerprint for ehp excitations

The assumption of detailed balance entails that associative desorption is the inverse of dissociative chemisorption. In an adiabatic picture there is just one reason for a possible divergence of the obtained reaction probabilities. This is based on surface temperature, which is usually much higher in the associative desorption experiments than in the sticking experiments. This might lead to a breakdown of the detailed balance assumption that is usually involved when modeling associative desorption experiments with calculations on dissociative chemisorption. We note that it might be possible to model the associative desorption experiment directly<sup>76,175–177</sup>, thereby negating the need to invoke the principle of detailed balance and investigate if associative desorption is indeed the inverse of dissociative chemisorption.

Including ehp excitations in dissociative chemisorption calculations would lower the reactivity thereby increasing the effective barrier<sup>23</sup>. Including ehp excitations in hypothetical associative desorption calculations, where molecules would start at the transition state and then desorb, would probably shift the translational energy distributions of desorbing molecules to lower energies and lead to lower effective barriers. When accounting for the effect of surface temperature, the difference in predicted reactivity as embodied by the  $E_{1/2}(\nu, J)$  parameters obtained by including ehp excitations in associative desorption and dissociative chemisorption calculations, and their differences with results from adiabatic calculations, might then be taken to be a fingerprints for the effect of ehp excitation.

For the  $H_2$  + Cu(111) system we know from DFMD calculations<sup>63</sup> and other approaches<sup>24,30,157,158</sup> that the effect of surface motion on the reactivity in dissociative chemisorption is small, even for high surface temperatures. Figure 5.23 shows some evidence that the broadening of reaction probability curves might affect the calculated  $E_{1/2}(\nu, J)$  parameters for low J. However, in an

adiabatic picture, assuming detailed balance there should be no difference between calculations on dissociative adsorption and associative desorption.

We believe that this suggests a reason for only the SRP48 DF being chemically accurate for  $H_2 + Cu(111)$  for both dissociative chemisorption and associative desorption, since it overestimates the former and underestimates the latter predicted reactivity. The new SRP-DFs that are very accurate for dissociative chemisorption on cold surfaces, for which the BOSS model is valid<sup>24,28–30,63,149</sup>, must underestimate the reactivity obtained from associative desorption by at least the extent to which surface temperature would increase the reactivity in dissociative chemisorption. Any remaining discrepancy can be safely attributed to the effect of ehp excitations.

The analysis of the  $H_2 + Au(111)$  system is more complicated due to the lack of dissociative chemisorption experiments and the current inability to take into account surface reconstruction (and thereby surface motion). Without at least either a dissociative chemisorption experiment or calculations using a reconstructed surface using the BOSS model, it is not yet possible to disentangle the contributions of the surface temperature, surface reconstruction and ehp excitations to the reactivity. Additionally, more detailed associative desorption and dissociative chemisorption experiments for the  $H_2 + Ag(111)$  system would allow for a systematic investigation into the effect of ehp excitations on reactivity for highly activated late barrier reactions.

# 5.5 Conclusions

We have constructed new SRP-DFs that include non-local correlation for the  $H_2$  ( $D_2$ ) + Cu(111) system and assessed the transferability of these DFs to the  $H_2$  ( $D_2$ ) + Ag(111),  $H_2$  ( $D_2$ ) + Au(111) and  $H_2$  ( $D_2$ ) + Pt(111) systems. All newly tested and developed DFs are based on GGA-exchange and use non-local correlation to describe dissociative chemisorption of  $H_2$  ( $D_2$ ) on Cu(111) within chemical accuracy, and, to the extent that it can be assessed, improve the transferability to the other systems discussed in this work over the previously reported SRP48 and MS-B86bl SRP-DFs.

The new SRP-DFs improve the description of the metal over the previously available SRP-DFs based on mixing GGA exchange while using semi-local correlation, especially concerning calculated lattice constants. In general, the new SRP-DFs with non-local correlation exhibit higher and later barriers to reaction in combination with a slightly lower energetic corrugation. We also find that vdW-DF2 non-local correlation performs better than vdW-DF1 correlation for all tested combinations with different exchange functionals, except when the exchange part of a functional was specifically optimized for use with vdW-DF1

5.5. Conclusions 203

correlation. The B86SRP68-DF2 functional best reproduces the measured Van der Waals well depths for  $H_2 + Cu(111)$ ,  $H_2 + Ag(111)$  and  $H_2 + Au(111)$ .

SRP-DFs that include non-local correlation, namely B86SRP68-DF2 and PBE $\alpha$ 57-DF2, are transferable from the highly activated late barrier H<sub>2</sub> + Cu(111) system to the weakly activated earlier barrier H<sub>2</sub> + Pt(111) system and vice versa. This feat could not be demonstrated with GGA and mGGA SRP-DFs that do not include non-local correlation. Assessing the transferability of the tested and developed SRP-DFs to H<sub>2</sub> + Ag(111) and H<sub>2</sub> + Au(111) is difficult due to the lack of well characterized molecular beam experiments. The SRP-DFs for H<sub>2</sub> + Cu(111) that include non-local correlation predict similar results for molecular beam sticking of D<sub>2</sub> + Ag(111), which are just shy of chemical accuracy. However it should be noted that there is some discussion about the validity of the beam parameters describing this particular molecular beam experiment.

A detailed analysis of associative desorption experiments on Cu(111) suggest that accurate calculation of  $E_{1/2}(\nu, J)$  parameters requires an improvement of our dynamical model. Describing the surface degrees of freedom might close the gap between the excellent description of dissociative chemisorption and the good description of associative desorption, for molecules in the vibrational ground state. Any discrepancy in predicted reactivity between simulated associative desorption and dissociative chemisorption remaining after taking into account the effect of surface atom motion can then most likely be attributed to the neglect of ehp excitation. Lack of additional experiments for the  $H_2 + Au(111)$  system, specifically a well described dissociative chemisorption experiment, presently keeps us from disentangling the effects of surface reconstruction, surface temperature and ehp excitation for this system.

We have carried out a full molecular beam simulation for the  $\rm H_2 + Cu(111)$  system using the QD method and the B86SRP68-DF2 DF for sticking in this system, which is the best performing DF for this system, and which includes non-local correlation. Overall  $\rm H_2 + Cu(111)$  is very well described quasiclassically when looking at molecular beam sticking probabilities or degeneracy averaged initial state-selected reaction probabilities. At the level of molecular beam sticking, and degeneracy averaged reaction probabilities, the differences between the QD and QCT method are very small. The QD method predicts slightly higher reaction probabilities for molecular beam sticking for very narrow low average translational energy molecular beams when comparing to QCT results based on the same set of initial rovibrational states. When looking at initial-state resolved reaction probabilities the QD method predicts a somewhat larger orientational dependence of the reaction, in favor of molecules reacting in a parallel orientation. With respect to vibrationally and rotationally inelastic

scattering of H<sub>2</sub> from Cu(111) the B86SRP68-DF2 DF performs almost as well as the previous best SRP-DF for this system, namely the SRP48 DF.

#### 5.A Appendix: CRP interpolation of PESs

In principle we use the following grids:  $r \in \{0.4, 0.5, 0.6, 0.65, 0.7, 0.75, 0.8, 0.85, 1.0, 1.25, 1.5, 1.75, 2.0, 2.3\}$  Å and  $Z \in \{0.25, 0.5, 0.75, 1.0, 1.25, 1.5, 1.75, 2.0, 2.25, 2.5, 2.75, 3.0, 3.25, 3.5, 3.75, 4.0, 4.25, 4.5, 4.75, 5.0, 5.5, 6.0, 7.0\}$  Å for the 29 two dimensional cuts of the six dimensional molecular PES are used. For the atomic PES a grid denoted by  $Z \in [-1.2:9]$  Å with dZ = 0.075 Å for  $Z \le 2$  Å and dZ = 0.15 Å for Z > 2 Å for all but the reference site was used. For the atomic reference site a dZ of 0.025 Å was used for Z < 2 Å. Note that in the case of the atomic PES hard to converge geometries can be discarded and additional points can be added at random Z to improve the quality of the resulting CRP PES.

# 5.B Appendix: Methods for determining parameters describing initial-state selected reaction probabilities from associative desorption experiments

#### 5.B.1 Method A1

In method A1, it is assumed that the effective barrier heights  $(E_0(\nu, J))$  can be kept the same in the description of the sticking and the associative desorption experiments, even though these are done at quite different temperatures  $^{46,52}$ . The surface temperature dependence of  $P_{\text{deg}}(E, \nu, J)$  is taken into account by choosing the  $W_{\nu,J}$  parameters larger in the description of the associative desorption experiments (done at high  $T_s$ , typically > 900 K) than in the sticking experiments (done at low  $T_s$ , usually lower than room temperature), on the basis of experiments<sup>53,56</sup>. Next, the  $A_{\nu,J}$  parameters are determined assuming that they do not depend on  $T_s$ , by requiring that the measured sticking probabilities can be computed according to Eqs. 5.4-5.9. In this procedure, the A parameters are typically taken either independent of the initial rovibrational state, or dependent only on  $\nu$  to obtain a fitting procedure with a properly constrained number of degrees of freedom. In the latter case, one might use information regarding the relative values of the  $A_{\nu,J}$  parameters extracted from the experiments. Procedure A1 was followed to extract initialstate resolved reaction probabilities in experiments on H<sub>2</sub> and D<sub>2</sub> desorbing from  $Cu(111)^{46,48,52}$ .

A comparison between theory and experiment can then be made in terms of  $E_{1/2}(\nu, J)$  parameter values extracted from theory, which represent the incidence energy at which the computed reaction probability becomes equal to half the experimental saturation value  $A_{\nu,J}^{11}$ , and the experimental values of  $E_0(\nu, J)$ . Procedure A1 is illustrated in figure 5.B.1a for  $H_2 + Cu(111)$  and in figure 5.B.1c for  $D_2 + Cu(111)$ . To be specific, here  $E_{1/2}(\nu, J)$  would be taken as the incidence energy E for which the computed reaction probability  $P_{\text{deg}}(E,\nu,J)$  would first become equal to  $\frac{0.325}{2}$  for H<sub>2</sub>. A disadvantage of procedure A1 is that assuming that  $E_{1/2}(\nu,J)$  parameters can be compared with  $E_0(\nu, J)$  parameters presumes, in a way, that the saturation value of the computed sticking probability curve is the same as that of the measured one, which needs not be the case. This is one of the reasons that, in comparisons between theory and experiment, the procedure followed usually does not involve simply fitting computed reaction probabilities to Eq. 5.11 and then comparing the computed parameters of Eq. 5.11 directly to the experimental values. Using Eq. 5.11 to fit experimental reaction probabilities is at best a procedure to represent these probabilities over the range of energies from which they can be extracted with reasonable accuracy using Eq. 5.10. The error function fit form is not the most accurate expression to fit reaction probability curves for  $D_2 + Cu(111)^{63}$ , and comparison to theory suggests that using this expression does not yield an accurate extrapolation procedure to energies that exceed the energy range that can be used for the experimental extraction procedure (Eq. 5.10). We also note that the characteristic energies  $E_{1/2}(\nu, J)$  will not usually be inflexion points of the theoretical reaction probability curves.

#### 5.B.2 Method B1

In method B1, the experimental sticking probability curve is normalized by equating the reaction probability at  $E_{\text{max}}(\nu, J)$  to the computed value:<sup>48,71</sup>

$$A_{\nu,J}^{\rm B1} = P_{\rm deg}^{\rm exp}(E_{\rm max}(\nu,J)) \equiv P_{\rm deg}^{\rm th}(E_{\rm max}(\nu,J)) \tag{5.16}$$

In procedure B1, the thus extracted reaction probability is simply set equal to  $A_{\nu,J}$ . Theory is then compared with experiment by extracting the theoretical characteristic energy  $E_{1/2}(\nu,J)$  using:

$$P_{\text{deg}}^{\text{th}}(E_{1/2}(\nu, J)) = \frac{1}{2} A_{\nu, J}^{\text{B1}}$$
 (5.17)

Method B1 is illustrated in figure 5.B.1b for  $H_2 + Cu(111)$ , and in figure 5.B.1d for  $D_2 + Cu(111)$ . Even though  $E_{\text{max}}(\nu, J)$  will usually not be big

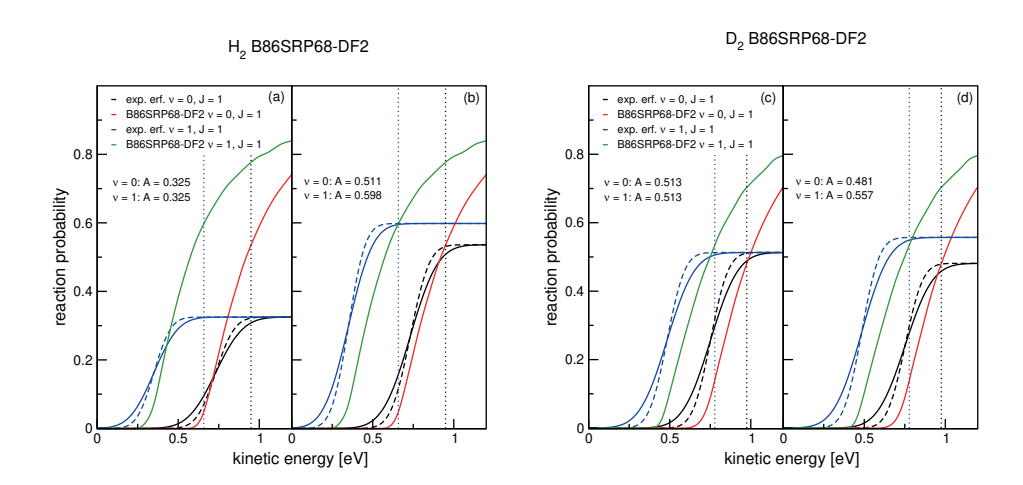


FIGURE 5.B.1: Reaction probability curves as a function of kinetic energy for H<sub>2</sub> + Cu(111) (a,b) and D<sub>2</sub> + Cu(111) (c,d). Experimental results <sup>48</sup> and QCT results obtained using the B86SRP68-DF2 SRP-DF are shown. Results for the ( $\nu=0,J=1$ ) rovibrational state are shown with experimental results in black and theoretical results in red, and for the ( $\nu=1,J=1$ ) rovibrational state are shown with experimental results in blue and theoretical results in green. Vertical dashed lines in the same color as the experimental results show  $E_{\rm max}(\nu,J)$  for the corresponding state. Panels a and c illustrate method A1 to obtain  $E_{1/2}(\nu,J)$  parameters and panels b and d method B1 (see text of appendix 5.B) . The solid experimental lines use the measured  $W(\nu,J)$  parameters as detailed in the supporting information of Ref.<sup>48</sup>

enough for  $P_{\text{deg}}(E_{\text{max}}(\nu,J),\nu,J)$  to essentially equal the absolute A value at high translational energy, the approximate  $E_{1/2}(\nu,J)$  extracted in this way will be rather accurate as long as  $P_{\text{deg}}(E_{\text{max}}(\nu,J),\nu,J) \geq 0.9$ A, in which case  $E_{1/2}(\nu,J)$  will be underestimated by no more than 0.09  $W_{\nu,J}$ , with  $W_{\nu,J}$  typically being 0.2 eV for  $H_2 + \text{Cu}(111)^{48}$  and 0.3 eV for  $H_2 + \text{Au}(111)^{71}$ . This condition is met if  $E_{\text{max}}(\nu,J) > E_0(\nu,J) + 0.9 W_{\nu,J}$ . Figure 5.B.2 shows that this is not the case for  $H_2$  (D<sub>2</sub>) + Au(111).

#### 5.B.3 Method B2

As already mentioned for  $H_2 + Au(111)$ , we found that  $E_{max}(\nu, J)$  was typically not large enough to extract  $E_{1/2}(\nu, J)$  parameters accurately using method B1. For  $H_2 + Au(111)$  we therefore use what we call method B2, which, to our knowledge, has not been used before. In this case we determine  $P_{deg}^{exp}(E_{max}(\nu, J))$  from theory, but we then also use the measured  $E_0(\nu, J)$  and  $W_{\nu, J}$  value to

determine the  $A_{\nu,J}$  value at which the experimental reaction probability curve extracted in this way should saturate according to the fit (Eq. 11). Then the characteristic theoretical  $E_{1/2}(\nu,J)$  value is obtained by requiring that  $P_{\text{deg}}(E_{1/2}(\nu,J),\nu,J)=0.5A_{\nu,J}^{\text{B2}}$ . This effectively means that we take the  $A_{\nu,J}$  resulting from method B1  $(A_{\nu,J}^{\text{B1}})$  and scale it accordingly:

$$A_{\nu,J}^{B2} = \frac{A_{\nu,J}^{B1}}{0.5 + 0.5erf\left(\frac{E_{\text{max}}(\nu,J) - E_0(\nu,J)}{W_{\nu,J}}\right)}$$
(5.18)

Saturation values extracted using method B1 and B2 are compared to the experimental saturation values<sup>71</sup> for  $H_2 + Au(111)$  in figure 5.B.3a and for  $D_2 + Au(111)$  in figure 5.B.3b. Here, we should remember that the experimental saturation values are not on an absolute scale (they were determined using method A2). As shown in figure 5.B.3, the  $A(\nu, J)$  parameters determined using method B1 and B2 do not vary much with  $\nu$  and J, as expected from theory. In this, the  $A(\nu, J)$  parameters obtained with methods B1 and B2 show a far less eratic dependence on J than the experimental values as obtained with method A2 (see figure 5.B.3). Also, as expected, they tend not to exceed unity.

## 5.C Appendix: The rotational hindering effect as obtained with the Dai-Zhang LEPS PES

We are aware of one single PES that does reproduce the rotational hindering effect as observed in the experiment, namely the LEPS PES<sup>40</sup> used by Dai et al.<sup>38</sup> for six-dimensional QD calculations. Dai et al.<sup>38</sup> reported a rotational hindering effect that is much stronger than we observe in all our data sets. We suspected that strong rotational hindering might be due to (i) the use of an unconverged basis set or a too large time step used in the original QD calculations<sup>38</sup>, or to (ii) an inaccurate LEPS PES fit, or a combination of the two. We have recalculated the results reported by Dai et al.<sup>38</sup> which they present in their figure 1a<sup>38</sup> using the same LEPS potential<sup>40</sup> but with the QD input parameters of table 5.2 that are known to yield converged results. Our results are shown in figure 5.C.1b. Our converged TDWP calculations yield reaction probabilities that are somewhat lower than those reported by Dai et al.<sup>38</sup>, but our results for the ground state do however agree very well with those published by Somers et al.<sup>178</sup> who used the same potential.

 $E_{1/2}(\nu,J)$  parameters calculated using method A1 and B1 and using the QD method for the B86SRP68-DF2 functional and the LEPS PES used by Dai et al.<sup>38</sup> are shown in comparison to experimental results for  $(\nu=0)$  in

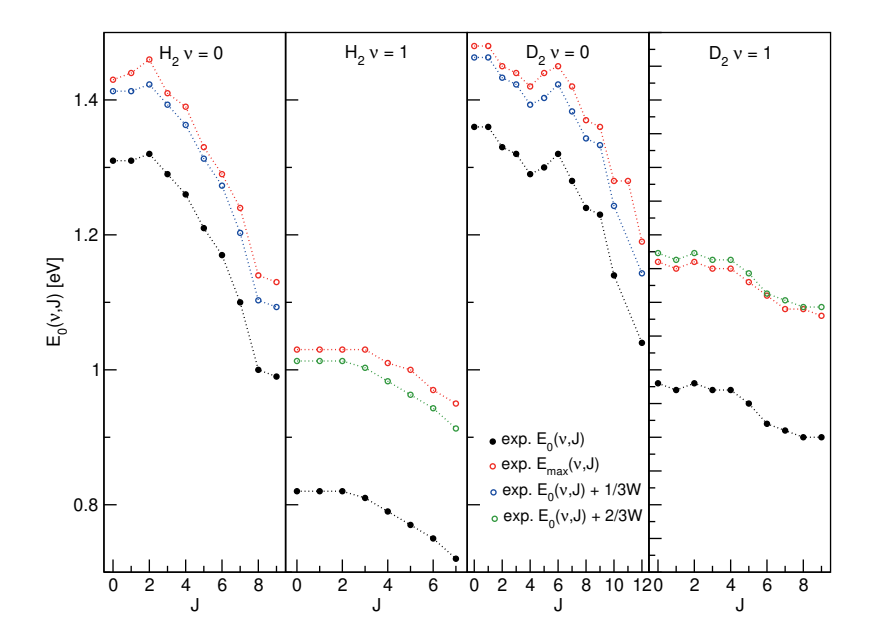


FIGURE 5.B.2: Measured  $^{71}$   $E_0(\nu,J)$  parameters (black) and  $E_{\rm max}(\nu,J)$  parameters (red) for H<sub>2</sub> (D<sub>2</sub>) + Au(111) as a function of J.  $E_0(\nu,J)$  parameters +  $\frac{1}{3}$  W for  $(\nu=0)$  (blue) and  $E_0(\nu,J)$  parameters +  $\frac{2}{3}$  W for  $(\nu=1)$  (green) are shown as well.

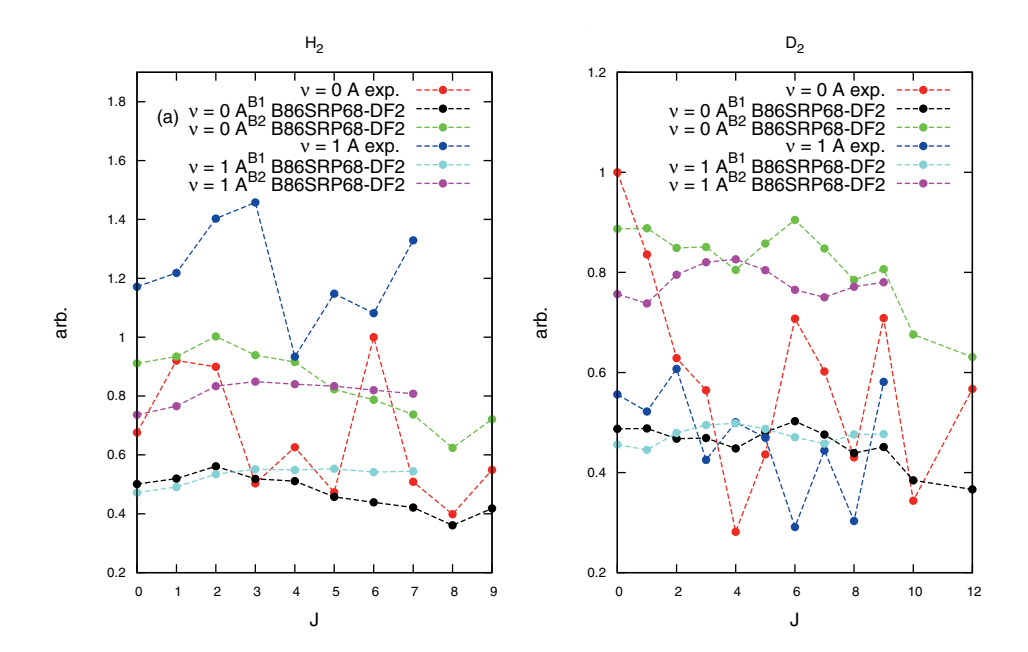


FIGURE 5.B.3: Comparison between the tabulated experimental  $^{71}$   $A(\nu, J)$  values, red for  $(\nu=0)$  and blue for  $(\nu=1)$ , the calculated  $A^{\rm B1}(\nu, J)$  values computed using the B86SRP68-DF2 functional, black for  $(\nu=0)$  and cyan for  $(\nu=1)$ , and the calculated  $A^{\rm B2}(\nu, J)$  values computed using the B86SRP68-DF2 functional, green for  $(\nu=0)$  and magenta for  $(\nu=1)$ , for  $\rm H_2$  (a) and  $\rm D_2$  (b) + Au(111) as a function of J. The experimentally measured values were obtained using method A2.

figure 5.C.1c. The calculated  $E_{1/2}(\nu, J)$  parameters for the B86SRP68-DF2 functional and the LEPS PES are in remarkably good agreement for  $J \geq 3$  for both method A1 and B1. It is clear that the B86SRP68-DF2 functional somewhat underestimates the subtle rotational hindering effect when using procedure B1. Our converged QD calculations reproduce the original finding<sup>38</sup> that using the LEPS PES yields the rotational hindering trend. However, the results obtained for the LEPS PES used by Dai et al.<sup>38</sup> somewhat overestimate the observed rotational hindering effect when using either procedure A1 or B1. This leaves the accuracy of the PES as a possible culprit of the discrepancies observed between the results of our PESs and the results for the LEPS PES. We are unable to check the fit accuracy of the LEPS PES compared to the underlying electronic structure calculations<sup>41</sup>, which however are known to be unconverged<sup>40,41</sup>. We have however checked the fit accuracy of our CRP<sup>121</sup> PES for the B86SRP68-DF2 functional and found that our CRP<sup>121</sup> PES is highly accurate with respect to the underlying electronic structure calculations.

Since we do not observe the strong rotational hindering reported by Dai et al.<sup>38</sup> in any of the calculations we attempted for the reaction of  $H_2$  with Cu(111) with our DFs, we believe that the large rotational hindering effect yielded by this particular LEPS PES must originate from inaccuracies still present in the LEPS fit or the underlying electronic structure calculations being unconverged. The good agreement between the results obtained using the LEPS PES<sup>40</sup> and our best SRP-DF for this system for  $J \geq 3$  suggests that the observed rotational hindering is a very subtle effect.

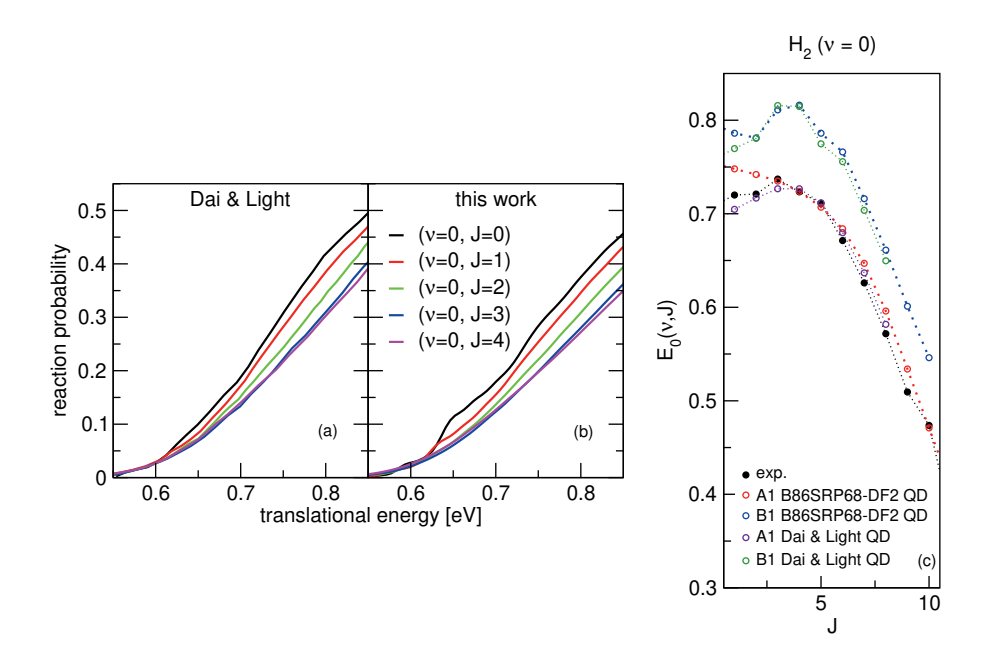


FIGURE 5.C.1: Panel a and b show degeneracy averaged reaction probabilities for  $(\nu=0,J\in[0,4])$  for  $H_2+Cu(111)$ . The results in panel a are the original results of Dai et al.<sup>38</sup>, panel b shows our results obtained using the same potential.  $E_{1/2}(\nu,J)$  parameters calculated using the QD method are shown in panel c, with experimental results shown in black<sup>48</sup>, and B86SRP68-DF2 results in red and blue. The  $E_{1/2}(\nu,J)$  parameters for the LEPS PES used by Dai et al.<sup>38</sup> (purple, green) have been obtained from our QD calculations using the same LEPS PES<sup>40</sup>.

- (1) Smeets, E. W. F.; Kroes, G.-J. Designing new SRP density functionals including non-local vdW-DF2 correlation for  $H_2 + Cu(111)$  and their transferability to  $H_2 + Ag(111)$ , Au(111) and Pt(111). Phys. Chem. Chem. Phys. **2021**, 23, 7875–7901.
- (2) Kroes, G.-J. Toward a database of chemically accurate barrier heights for reactions of molecules with metal surfaces. *J. Phys. Chem lett.* **2015**, 6, 4106–4114.
- (3) Wolcott, C. A.; Medford, A. J.; Studt, F.; Campbell, C. T. Degree of rate control approach to computational catalyst screening. *J. Catal.* **2015**, *330*, 197–207.
- (4) Sabbe, M. K.; Reyniers, M.-F.; Reuter, K. First-principles kinetic modeling in heterogeneous catalysis: an industrial perspective on best-practice, gaps and needs. *Catal. Sci. Technol.* **2012**, *2*, 2010–2024.
- (5) Ertl, G. Reactions at surfaces: from atoms to complexity (Nobel lecture). Angew. Chem. Int. Ed. 2008, 47, 3524–3535.
- (6) Kroes, G.-J. Frontiers in surface scattering simulations. *Science* **2008**, 321, 794–797.
- (7) Waugh, K. Methanol synthesis. Catal. Today 1992, 15, 51–75.
- (8) Grabow, L.; Mavrikakis, M. Mechanism of methanol synthesis on Cu through CO<sub>2</sub> and CO hydrogenation. *Acs Catalysis* **2011**, *1*, 365–384.
- (9) Behrens, M.; Studt, F.; Kasatkin, I.; Kühl, S.; Hävecker, M.; Abild-Pedersen, F.; Zander, S.; Girgsdies, F.; Kurr, P.; Kniep, B.-L., et al. The active site of methanol synthesis over Cu/ZnO/Al<sub>2</sub>O<sub>3</sub> industrial catalysts. *Science* **2012**, *336*, 893–897.
- (10) Park, G. B.; Kitsopoulos, T. N.; Borodin, D.; Golibrzuch, K.; Neugebohren, J.; Auerbach, D. J.; Campbell, C. T.; Wodtke, A. M. The kinetics of elementary thermal reactions in heterogeneous catalysis. *Nature Rev. Chem.* 2019, 3, 723–732.
- (11) Díaz, C.; Pijper, E.; Olsen, R.; Busnengo, H.; Auerbach, D.; Kroes, G. Chemically accurate simulation of a prototypical surface reaction: H<sub>2</sub> dissociation on Cu(111). *Science* **2009**, *326*, 832–834.
- (12) Ghassemi, E. N.; Wijzenbroek, M.; Somers, M. F.; Kroes, G.-J. Chemically accurate simulation of dissociative chemisorption of D<sub>2</sub> on Pt(111). *Chem. Phys. Lett.* **2017**, *683*, 329–335.

(13) Smeets, E. W. F.; Voss, J.; Kroes, G.-J. Specific reaction parameter density functional based on the meta-generalized gradient approximation: application to  $H_2 + Cu(111)$  and  $H_2 + Ag(111)$ . J. Phys. Chem. A **2019**, 123, 5395–5406.

- (14) Nattino, F.; Migliorini, D.; Kroes, G.-J.; Dombrowski, E.; High, E. A.; Killelea, D. R.; Utz, A. L. Chemically accurate simulation of a polyatomic molecule-metal surface reaction. J. Phys. Chem. Lett. 2016, 7, 2402–2406.
- (15) Doblhoff-Dier, K.; Meyer, J.; Hoggan, P. E.; Kroes, G.-J. Quantum Monte Carlo calculations on a benchmark molecule-metal surface reaction: H<sub>2</sub> + Cu(111). J. Chem. Theory Comput. 2017, 13, 3208–3219.
- (16) Boereboom, J.; Wijzenbroek, M.; Somers, M.; Kroes, G. Towards a specific reaction parameter density functional for reactive scattering of H<sub>2</sub> from Pd(111). J. Chem. Phys. 2013, 139, 244707.
- (17) Migliorini, D.; Chadwick, H.; Nattino, F.; Gutiérrez-González, A.; Dombrowski, E.; High, E. A.; Guo, H.; Utz, A. L.; Jackson, B.; Beck, R. D., et al. Surface reaction barriometry: methane dissociation on flat and stepped transition-metal surfaces. J. Phys. Chem. Lett. 2017, 8, 4177–4182.
- (18) Ghassemi, E. N.; Smeets, E. W. F.; Somers, M. F.; Kroes, G.-J.; Groot, I. M.; Juurlink, L. B.; Füchsel, G. Transferability of the specific reaction parameter density functional for H<sub>2</sub> + Pt(111) to H<sub>2</sub> + Pt(211). J. Phys. Chem. C 2019, 123, 2973–2986.
- (19) Sementa, L.; Wijzenbroek, M.; Van Kolck, B.; Somers, M.; Al-Halabi, A.; Busnengo, H. F.; Olsen, R.; Kroes, G.-J.; Rutkowski, M.; Thewes, C., et al. Reactive scattering of H<sub>2</sub> from Cu(100): comparison of dynamics calculations based on the specific reaction parameter approach to density functional theory with experiment. J. Chem. Phys. 2013, 138, 044708.
- (20) Nour Ghassemi, E.; Somers, M.; Kroes, G.-J. Test of the transferability of the specific reaction parameter functional for H<sub>2</sub>+ Cu(111) to D<sub>2</sub> + Ag(111). J. Phys. Chem. C **2018**, 122, 22939–22952.
- (21) Tchakoua, T.; Smeets, E. W. F.; Somers, M.; Kroes, G.-J. Toward a specific reaction parameter density functional for H<sub>2</sub> + Ni(111): comparison of theory with molecular beam sticking experiments. *J. Phys. Chem. C* **2019**, *123*, 20420–20433.
- (22) Šljivančanin, Ž.; Hammer, B. H<sub>2</sub> dissociation at defected Cu: preference for reaction at vacancy and kink sites. *Phys. Rev. B* **2002**, *65*, 085414.

- (23) Spiering, P.; Meyer, J. Testing electronic friction models: vibrational de-excitation in scattering of H<sub>2</sub> and D<sub>2</sub> from Cu(111). *J. Phys. Chem. Lett.* **2018**, *9*, 1803–1808.
- (24) Spiering, P.; Wijzenbroek, M.; Somers, M. An improved static corrugation model. *J. Chem. Phys.* **2018**, *149*, 234702.
- (25) Kroes, G.-J.; Juaristi, J.; Alducin, M. Vibrational excitation of H<sub>2</sub> scattering from Cu(111): effects of surface temperature and of allowing energy exchange with the surface. J. Phys. Chem. C 2017, 121, 13617–13633.
- (26) Somers, M.; McCormack, D.; Kroes, G.-J.; Olsen, R.; Baerends, E.; Mowrey, R. Signatures of site-specific reaction of H<sub>2</sub> on Cu(100). J. Chem. Phys. 2002, 117, 6673–6687.
- (27) Nattino, F.; Díaz, C.; Jackson, B.; Kroes, G.-J. Effect of surface motion on the rotational quadrupole alignment parameter of D<sub>2</sub> reacting on Cu(111). *Phys. Rev. Lett.* **2012**, *108*, 236104.
- (28) Kroes, G.-J.; Díaz, C. Quantum and classical dynamics of reactive scattering of H<sub>2</sub> from metal surfaces. *Chem. Soc. Rev.* **2016**, *45*, 3658–3700.
- (29) Díaz, C.; Olsen, R. A.; Auerbach, D. J.; Kroes, G.-J. Six-dimensional dynamics study of reactive and non reactive scattering of H<sub>2</sub> from Cu(111) using a chemically accurate potential energy surface. *Phys. Chem. Chem. Phys.* 2010, 12, 6499–519.
- (30) Wijzenbroek, M.; Somers, M. F. Static surface temperature effects on the dissociation of H<sub>2</sub> and D<sub>2</sub> on Cu(111). *J. Chem. Phys.* **2012**, *137*, 054703.
- (31) McCormack, D. A.; Kroes, G.-.-J.; Olsen, R. A.; Groeneveld, J. A.; van Stralen, J. N.; Baerends, E. J.; Mowrey, R. C. Quantum dynamics of the dissociation of H<sub>2</sub> on Cu(100): dependence of the site-reactivity on initial rovibrational state. *Faraday Discuss.* **2000**, *117*, 109–132.
- (32) McCormack, D. A.; Kroes, G.-J.; Olsen, R. A.; Groeneveld, J. A.; van Stralen, J. N.; Baerends, E. J.; Mowrey, R. C. Molecular knife throwing: aiming for dissociation at specific surface sites through state-selection. *Chem. Phys. Lett.* **2000**, *328*, 317–324.
- (33) Chen, J.; Zhou, X.; Jiang, B. Eley Rideal recombination of hydrogen atoms on Cu(111): quantitative role of electronic excitation in cross sections and product distributions. *J. Chem. Phys.* **2019**, *150*, 061101.

(34) Darling, G.; Holloway, S. Rotational motion and the dissociation of H<sub>2</sub> on Cu(111). J. Chem. Phys. **1994**, 101, 3268–3281.

- (35) Sakong, S.; Groß, A. Dissociative adsorption of hydrogen on strained Cu surfaces. Surf. Sci. 2003, 525, 107–118.
- (36) Kroes, G.-J.; Pijper, E.; Salin, A. Dissociative chemisorption of H<sub>2</sub> on the Cu(110) surface: A quantum and quasiclassical dynamical study. *J. Chem. Phys.* **2007**, *127*, 164722.
- (37) Smeets, E. W. F.; Füchsel, G.; Kroes, G.-J. Quantum dynamics of dissociative chemisorption of H<sub>2</sub> on the Stepped Cu(211) Surface. *J. Phys. Chem. C* **2019**, *123*, 23049–23063.
- (38) Dai, J.; Light, J. C. The steric effect in a full dimensional quantum dynamics simulation for the dissociative adsorption of H<sub>2</sub> on Cu(111). J. Chem. Phys. **1998**, 108, 7816–7820.
- (39) Dai, J.; Light, J. C. Six dimensional quantum dynamics study for dissociative adsorption of H<sub>2</sub> on Cu(111) surface. *J. Chem. Phys.* **1997**, 107, 1676–1679.
- (40) Dai, J.; Zhang, J. Z. Quantum adsorption dynamics of a diatomic molecule on surface: four-dimensional fixed-site model for H<sub>2</sub> on Cu(111). J. Chem. Phys. 1995, 102, 6280–6289.
- (41) Hammer, B.; Scheffler, M.; Jacobsen, K. W.; Nørskov, J. K. Multidimensional potential energy surface for H<sub>2</sub> dissociation over Cu(111). *Phys. Rev. Lett.* 1994, 73, 1400–1403.
- (42) Wijzenbroek, M.; Klein, D. M.; Smits, B.; Somers, M. F.; Kroes, G.-J. Performance of a non-local van der Waals density functional on the dissociation of H<sub>2</sub> on metal surfaces. J. Phys. Chem. A 2015, 119, 12146–12158.
- (43) Füchsel, G.; Cao, K.; Er, S.; Smeets, E. W. F.; Kleyn, A. W.; Juurlink, L. B. F.; Kroes, G.-J. Anomalous dependence of the reactivity on the presence of steps: dissociation of D<sub>2</sub> on Cu(211). J. Phys. Chem. Lett. 2018, 9, 170–175.
- (44) Kroes, G.-J.; Pavanello, M.; Blanco-Rey, M.; Alducin, M.; Auerbach, D. J. Ab initio molecular dynamics calculations on scattering of hyperthermal H atoms from Cu(111) and Au(111). J. Chem. Phys. 2014, 141, 054705.
- (45) Michelsen, H. A.; Auerbach, D. J. A critical examination of data on the dissociative adsorption and associative desorption of hydrogen at copper surfaces. *J. Chem. Phys.* **1991**, *94*, 7502–7520.

- (46) Michelsen, H.; Rettner, C.; Auerbach, D.; Zare, R. Effect of rotation on the translational and vibrational energy dependence of the dissociative adsorption of D<sub>2</sub> on Cu(111). J. Chem. Phys. 1993, 98, 8294–8307.
- (47) Berger, H.; Leisch, M.; Winkler, A.; Rendulic, K. A search for vibrational contributions to the activated adsorption of H<sub>2</sub> on copper. *Chem. Phys. Lett.* **1990**, *175*, 425–428.
- (48) Kaufmann, S.; Shuai, Q.; Auerbach, D. J.; Schwarzer, D.; Wodtke, A. M. Associative desorption of hydrogen isotopologues from copper surfaces: characterization of two reaction mechanisms. J. Chem. Phys. 2018, 148, 194703.
- (49) Anger, G.; Winkler, A.; Rendulic, K. Adsorption and desorption kinetics in the systems  $H_2/Cu(111)$ ,  $H_2/Cu(110)$  and  $H_2/Cu(100)$ . Surf. Sci. **1989**, 220, 1–17.
- (50) Hou, H.; Gulding, S.; Rettner, C.; Wodtke, A.; Auerbach, D. The stereodynamics of a gas-surface reaction. *Science* **1997**, *277*, 80–82.
- (51) Comsa, G.; David, R. The purely "fast" distribution of H<sub>2</sub> and D<sub>2</sub> molecules desorbing from Cu(100) and Cu(111) surfaces. *Surf. Sci.* **1982**, *117*, 77–84.
- (52) Rettner, C.; Michelsen, H.; Auerbach, D. Quantum-state-specific dynamics of the dissociative adsorption and associative desorption of H<sub>2</sub> at a Cu(111) surface. *J. Chem. Phys.* **1995**, 102, 4625–4641.
- (53) Rettner, C.; Auerbach, D.; Michelsen, H. Dynamical studies of the interaction of D<sub>2</sub> with a Cu(111) surface. J. Vac. Sci. Technol. A **1992**, 10, 2282–2286.
- (54) Rettner, C.; Michelsen, H.; Auerbach, D. Determination of quantum-state-specific gas—surface energy transfer and adsorption probabilities as a function of kinetic energy. *Chem. Phys.* **1993**, *175*, 157–169.
- (55) Hodgson, A.; Samson, P.; Wight, A.; Cottrell, C. Rotational excitation and vibrational relaxation of  $H_2$  ( $\nu = 1$ , J = 0) Scattered from Cu(111). *Phys. Rev. Lett.* **1997**, 78, 963–966.
- (56) Michelsen, H.; Rettner, C.; Auerbach, D. On the influence of surface temperature on adsorption and desorption in the D<sub>2</sub>/Cu(111) system. Surf. Sci. 1992, 272, 65–72.
- (57) Okazawa, T.; Takeuchi, F.; Kido, Y. Enhanced and correlated thermal vibrations of Cu(111) and Ni(111) surfaces. *Physical Review B* **2005**, 72, 075408.

(58) Lindgren, S.; Walldén, L.; Rundgren, J.; Westrin, P. Low-energy electron diffraction from Cu(111): subthreshold effect and energy-dependent inner potential; surface relaxation and metric distances between spectra. *Phys. Rev. B* **1984**, *29*, 576–588.

- (59) Chae, K.; Lu, H.; Gustafsson, T. Medium-energy ion-scattering study of the temperature dependence of the structure of Cu(111). *Phys. Rev. B* **1996**, *54*, 14082.
- (60) Andersson, S.; Persson, M. Sticking in the physisorption well: influence of surface structure. *Phys. Rev. Lett.* **1993**, *70*, 202.
- (61) Cao, K.; Füchsel, G.; Kleyn, A. W.; Juurlink, L. B. Hydrogen adsorption and desorption from Cu(111) and Cu(211). *Phys. Chem. Chem. Phys.* **2018**, *20*, 22477–22488.
- (62) Harten, U.; Toennies, J. P.; Wöll, C. Molecular beam translational spectroscopy of physisorption bound states of molecules on metal surfaces.
  I. HD on Cu(111) and Au(111) single crystal surfaces. J. Chem. Phys. 1986, 85, 2249–2258.
- (63) Nattino, F.; Genova, A.; Guijt, M.; Muzas, A. S.; Díaz, C.; Auerbach, D. J.; Kroes, G.-J. Dissociation and recombination of D<sub>2</sub> on Cu(111): Ab initio molecular dynamics calculations and improved analysis of desorption experiments. J. Chem. Phys. 2014, 141, 124705.
- (64) Cao, K.; van Lent, R.; Kleyn, A.; Juurlink, L. A molecular beam study of D<sub>2</sub> dissociation on Pt(111): testing SRP-DFT calculations. *Chem. Phys. Lett.* **2018**, 706, 680–683.
- (65) Luntz, A.; Brown, J.; Williams, M. Molecular beam studies of H<sub>2</sub> and D<sub>2</sub> dissociative chemisorption on Pt(111). *J. Chem. Phys.* **1990**, *93*, 5240–5246.
- (66) Ghassemi, E. N.; Somers, M. F.; Kroes, G.-J. Assessment of two problems of specific reaction parameter density functional theory: sticking and diffraction of H<sub>2</sub> on Pt(111). J. Phys. Chem. C 2019, 123, 10406–10418.
- (67) Pijper, E.; Kroes, G.-J.; Olsen, R. A.; Baerends, E. J. Reactive and diffractive scattering of H<sub>2</sub> from Pt(111) studied using a six-dimensional wave packet method. *J. Chem. Phys.* **2002**, *117*, 5885–5898.
- (68) Kroes, G.-J.; Somers, M. F. Six-dimensional dynamics of dissociative chemisorption of H<sub>2</sub> on metal surface. *J. Theor. Comput. Chem.* **2005**, 4, 493–581.

- (69) Raff, L. M.; Karplus, M. Theoretical investigations of reactive collisions in molecular beams: K+CH<sub>3</sub>I and related systems. *J. Chem. Phys.* **1966**, 44, 1212–1229.
- (70) Cardillo, M.; Balooch, M.; Stickney, R. Detailed balancing and quasi-equilibrium in the adsorption of hydrogen on copper. *Surf. Sci.* **1975**, 50, 263–278.
- (71) Shuai, Q.; Kaufmann, S.; Auerbach, D. J.; Schwarzer, D.; Wodtke, A. M. Evidence for electron-hole pair excitation in the associative desorption of H<sub>2</sub> and D<sub>2</sub> from Au(111). *J. Phys. Chem. Lett.* **2017**, *8*, 1657–1663.
- (72) Perrier, A.; Bonnet, L.; Liotard, D.; Rayez, J.-C. On the dynamics of H<sub>2</sub> desorbing from a Pt(111) surface. Surf. Sci. **2005**, 581, 189–198.
- (73) Perrier, A.; Bonnet, L.; Rayez, J.-C. Dynamical study of H<sub>2</sub> and D<sub>2</sub> desorbing from a Cu(111) surface. J. Phys. Chem. A **2006**, 110, 1608–1617.
- (74) Perrier, A.; Bonnet, L.; Rayez, J.-C. Statisticodynamical approach of final state distributions in associative desorptions. *J. Chem. Phys.* **2006**, 124, 194701.
- (75) Díaz, C.; Perrier, A.; Kroes, G. Associative desorption of N<sub>2</sub> from Ru(0001): a computational study. *Chem. Phys. Lett.* **2007**, 434, 231–236.
- (76) Galparsoro, O.; Kaufmann, S.; Auerbach, D. J.; Kandratsenka, A.; Wodtke, A. M. First principles rates for surface chemistry employing exact transition state theory: application to recombinative desorption of hydrogen from Cu(111). Phys. Chem. Chem. Phys. 2020, 22, 17532–17539.
- (77) Perdew, J. P.; Chevary, J. A.; Vosko, S. H.; Jackson, K. A.; Pederson, M. R.; Singh, D. J.; Fiolhais, C. Atoms, molecules, solids, and surfaces: Applications of the generalized gradient approximation for exchange and correlation. *Phys. Rev. B* 1992, 46, 6671–6687.
- (78) Murphy, M.; Hodgson, A. Translational energy release in the recombinative desorption of H<sub>2</sub> from Ag(111). Surf. Sci. **1997**, 390, 29–34.
- (79) Murphy, M.; Hodgson, A. Role of surface thermal motion in the dissociative chemisorption and recombinative desorption of D<sub>2</sub> on Ag(111). *Phys. Rev. Lett.* **1997**, *78*, 4458–4461.

(80) Jiang, B.; Guo, H. Six-dimensional quantum dynamics for dissociative chemisorption of H 2 and D 2 on Ag (111) on a permutation invariant potential energy surface. *Physical Chemistry Chemical Physics* **2014**, 16, 24704–24715.

- (81) Jiang, B.; Guo, H. Permutation invariant polynomial neural network approach to fitting potential energy surfaces. III. Molecule-surface interactions. *J. Chem. Phys.* **2014**, *141*, 034109.
- (82) Lee, G.; Plummer, E. Interaction of hydrogen with the Ag(111) surface. *Phys. Rev. B* **1995**, *51*, 7250.
- (83) Sprunger, P.; Plummer, E. Interaction of hydrogen with the Ag(110) surface. *Phys. Rev. B* **1993**, *48*, 14436.
- (84) Avouris, P.; Schmeisser, D.; Demuth, J. Observation of rotational excitations of H<sub>2</sub> adsorbed on Ag surfaces. *Phys. Rev. Lett.* **1982**, 48, 199.
- (85) Healey, F.; Carter, R.; Worthy, G.; Hodgson, A. Endothermic dissociative chemisorption of molecular D2 on Ag (111). *Chemical physics letters* **1995**, 243, 133–139.
- (86) Parker, D. H.; Jones, M. E.; Koel, B. E. Determination of the reaction order and activation energy for desorption kinetics using TPD spectra: Application to D<sub>2</sub> desorption from Ag(111). Surf. Sci. **1990**, 233, 65–73.
- (87) Lee, G.; Sprunger, P.; Okada, M.; Poker, D.; Zehner, D.; Plummer, E. Chemisorption of hydrogen on the Ag(111) surface. *J. Vac. Sci. Technol.* A 1994, 12, 2119–2123.
- (88) Asada, H. Specular reflection of helium and hydrogen molecular beams from the (111) plane of silver. Surface Science 1979, 81, 386–408.
- (89) Horne, J. M.; Yerkes, S. C.; Miller, D. R. An experimental investigation of the elastic scattering of He and H2 from Ag (111). *Surface Science* **1980**, *93*, 47–63.
- (90) Yu, C.-f.; Whaley, K. B.; Hogg, C. S.; Sibener, S. J. Selective Adsorption Resonances in the Scattering of n-H<sub>2</sub> p-H<sub>2</sub> n-D<sub>2</sub> and o-D<sub>2</sub> from Ag(111). *Phys. Rev. Lett.* **1983**, *51*, 2210.
- (91) Yu, C.-f.; Whaley, K. B.; Hogg, C. S.; Sibener, S. J. Investigation of the spatially isotropic component of the laterally averaged molecular hydrogen/Ag(111) physisorption potential. *J. Chem. Phys.* **1985**, *83*, 4217–4234.
- (92) Mattera, L.; Musenich, R.; Salvo, C.; Terreni, S. Hydrogen diffraction from the (110) surface of silver. *Faraday Discuss.* **1985**, *80*, 115–126.

- (93) Maurer, R. J.; Zhang, Y.; Guo, H.; Jiang, B. Hot electron effects during reactive scattering of H<sub>2</sub> from Ag(111): assessing the sensitivity to initial conditions, coupling magnitude, and electronic temperature. *Faraday Discuss.* **2019**, 214, 105–121.
- (94) Zhang, Y.; Maurer, R. J.; Guo, H.; Jiang, B. Hot-electron effects during reactive scattering of H<sub>2</sub> from Ag(111): the interplay between modespecific electronic friction and the potential energy landscape. *Chem.* Sci. 2019, 10, 1089–1097.
- (95) Maurer, R. J.; Jiang, B.; Guo, H.; Tully, J. C. Mode specific electronic friction in dissociative chemisorption on metal surfaces: H 2 on Ag (111). *Physical review letters* **2017**, *118*, 256001.
- (96) Muzas, A. S.; Juaristi, J. I.; Alducin, M.; Díez Muiño, R.; Kroes, G.-J.; Díaz, C. Vibrational deexcitation and rotational excitation of H<sub>2</sub> and D<sub>2</sub> scattered from Cu(111): adiabatic versus non-adiabatic dynamics. J. Chem. Phys. 2012, 137, 064707.
- (97) Dion, M.; Rydberg, H.; Schröder, E.; Langreth, D. C.; Lundqvist, B. I. Van der Waals density functional for general geometries. *Phys. Rev. Lett.* **2004**, *92*, 246401.
- (98) Lee, K.; Murray, É. D.; Kong, L.; Lundqvist, B. I.; Langreth, D. C. Higher-accuracy van der Waals density functional. *Phys. Rev. B* **2010**, 82, 081101.
- (99) Cowin, J. P.; Yu, C.-F.; Sibener, S. J.; Hurst, J. E. Bound level resonances in rotationally inelastic HD/Pt (111) surface scattering. *The Journal of Chemical Physics* **1981**, *75*, 1033–1034.
- (100) Cowin, J. P.; Yu, C.-F.; Sibener, S. J.; Wharton, L. HD scattering from Pt(111): rotational excitation probabilities. *J. Chem. Phys.* **1983**, *79*, 3537–3549.
- (101) Cowin, J. P.; Yu, C.-F.; Wharton, L. HD scattering from Pt(111): Rotationally mediated selective adsorption. Surf. Sci. **1985**, 161, 221–233.
- (102) Yu, C.-F.; Hogg, C. S.; Cowin, J. P.; Whaley, K. B.; Light, J. C.; Sibener, S. J. Rotationally mediated selective adsorption as a probe of isotropic and anisotropic molecule—surface interaction potentials: HD (J)/Ag(111). Israel J. Chem. 1982, 22, 305–314.
- (103) Perreau, J.; Lapujoulade, J. Selective adsorption of He, H<sub>2</sub> on copper surfaces. Surf. Sci. **1982**, 122, 341–354.

(104) Kaufhold, A.; Toennies, J. P. An optical potential for rotationally mediated selective adsorption (Feshbach) resonances in scattering of molecules from smooth crystal surfaces. Surf. Sci. 1986, 173, 320–336.

- (105) Andersson, S.; Wilzén, L.; Persson, M. Physisorption interaction of H<sub>2</sub> with noble-metal surfaces: A new H<sub>2</sub>-Cu potential. *Phys. Rev. B* **1988**, 38, 2967.
- (106) Lennard-Jones, J. E.; Devonshire, A. F. Diffraction and selective adsorption of atoms at crystal surfaces. *Nature* **1936**, *137*, 1069–1070.
- (107) Hoinkes, H.; Wilsch, H. In *Helium Atom Scattering from Surfaces*; Springer: 1992, pp 113–172.
- (108) Bertino, M. F.; Hofmann, F.; Toennies, J. P. The effect of dissociative chemisorption on the diffraction of D<sub>2</sub> from Ni(110). *J. Chem. Phys.* **1997**, 106, 4327–4338.
- (109) Nieto, P.; Pijper, E.; Barredo, D.; Laurent, G.; Olsen, R. A.; Baerends, E.-J.; Kroes, G.-J.; Farías, D. Reactive and nonreactive scattering of H<sub>2</sub> from a metal surface is electronically adiabatic. *Science* 2006, 312, 86–89.
- (110) Bertino, M.; Miret-Artés, S.; Toennies, J.; Benedek, G. Observation of rotationally mediated focused inelastic resonances in D<sub>2</sub> scattering from Cu(001). *Phys. Rev. B* **1997**, *56*, 9964.
- (111) Poelsema, B.; Lenz, K.; Comsa, G. The dissociative adsorption of hydrogen on defect-free Pt(111). *J. Phys. Condens. Matter* **2010**, *22*, 304006.
- (112) Hamada, I. van der Waals density functional made accurate. *Phys. Rev.* B **2014**, 89, 121103.
- (113) Hammer, B. H. L. B.; Hansen, L. B.; Nørskov, J. K. Improved adsorption energetics within density-functional theory using revised Perdew-Burke-Ernzerhof functionals. *Phys. Rev. B* **1999**, *59*, 7413–7421.
- (114) Perdew, J. P.; Ruzsinszky, A.; Csonka, G. I.; Constantin, L. A.; Sun, J. Workhorse semilocal density functional for condensed matter physics and quantum chemistry. *Phys. Rev. Lett.* **2009**, *103*, 026403.
- (115) Klimeš, J.; Bowler, D. R.; Michaelides, A. Chemical accuracy for the van der Waals density functional. J. Phys. Condens. Matter 2009, 22, 022201.
- (116) Perdew, J. P.; Burke, K.; Ernzerhof, M. Generalized gradient approximation made simple. *Phys. Rev. Lett.* **1996**, *77*, 3865–3868.

- (117) Madsen, G. K. Functional form of the generalized gradient approximation for exchange: the PBE $\alpha$  functional. *Phys. Rev. B* **2007**, 75, 195108.
- (118) Perdew, J. P.; Ruzsinszky, A.; Csonka, G. I.; Vydrov, O. A.; Scuseria, G. E.; Constantin, L. A.; Zhou, X.; Burke, K. Restoring the density-gradient expansion for exchange in solids and surfaces. *Phys. Rev. Lett.* **2008**, *100*, 136406.
- (119) Zhang, Y.; Yang, W. Comment on "Generalized gradient approximation made simple". *Phys. Rev. Lett.* **1998**, *80*, 890.
- (120) Perdew, J. P.; Yue, W. Accurate and simple density functional for the electronic exchange energy: generalized gradient approximation. *Phys. Rev. B* **1986**, *33*, 8800.
- (121) Busnengo, H.; Salin, A.; Dong, W. Representation of the 6D potential energy surface for a diatomic molecule near a solid surface. *J. Chem. Phys.* **2000**, *112*, 7641–7651.
- (122) Füchsel, G.; del Cueto, M.; Díaz, C.; Kroes, G.-J. Enigmatic HCl + Au(111) reaction: a puzzle for theory and experiment. *J. Phys. Chem.* C 2016, 120, 25760–25779.
- (123) Stoer, J.; Bulirsch, R., Introduction to numerical analysis; Springer Science & Business Media, New York: 2013; Vol. 12.
- (124) Kosloff, R. Time-dependent quantum-mechanical methods for molecular dynamics. J. Phys. Chem. C 1988, 92, 2087–2100.
- (125) Kosloff, R. In *Time-Dependent Quantum Molecular Dynamics*; Springer: 1992, pp 97–116.
- (126) Balint-Kurti, G. G.; Dixon, R. N.; Marston, C. C. Grid methods for solving the Schrödinger equation and time dependent quantum dynamics of molecular photofragmentation and reactive scattering processes. *Int. Rev. Phys. Chem.* **1992**, *11*, 317–344.
- (127) Wijzenbroek, M.; Kroes, G. The effect of the exchange-correlation functional on H2 dissociation on Ru(0001). *J. Chem. Phys.* **2014**, *140*, 084702.
- (128) Groot, I.; Ueta, H.; Van der Niet, M.; Kleyn, A.; Juurlink, L. Supersonic molecular beam studies of dissociative adsorption of H<sub>2</sub> on Ru(0001). J. Chem. Phys. 2007, 127, 244701.
- (129) Zare, R. N.; Harter, W. G. Angular momentum: understanding spatial aspects in chemistry and physics. *Phys. Today* **1989**, *42*, 68–72.

(130) Kresse, G.; Hafner, J. Ab initio molecular-dynamics simulation of the liquid-metal–amorphous-semiconductor transition in germanium. *Phys. Rev. B* **1994**, *49*, 14251–14269.

- (131) Kresse, G.; Hafner, J. Ab initio molecular dynamics for liquid metals. *Phys. Rev. B* **1993**, *47*, 558–561.
- (132) Kresse, G.; Furthmüller, J. Efficient iterative schemes for ab initio totalenergy calculations using a plane-wave basis set. *Phys. Rev. B* **1996**, 54, 11169–11186.
- (133) Kresse, G.; Furthmüller, J. Efficiency of ab-initio total energy calculations for metals and semiconductors using a plane-wave basis set. *Comput. Mater. Sci.* **1996**, *6*, 15–50.
- (134) Lehtola, S.; Steigemann, C.; Oliveira, M. J.; Marques, M. A. Recent developments in libxc A comprehensive library of functionals for density functional theory. *SoftwareX* **2018**, *7*, 1–5.
- (135) Blöchl, P. E. Projector augmented-wave method. *Phys. Rev. B* **1994**, 50, 17953–17979.
- (136) Klimeš, J. ř.; Bowler, D. R.; Michaelides, A. Van der Waals density functionals applied to solids. *Phys. Rev. B* **2011**, *83*, 195131.
- (137) Román-Pérez, G.; Soler, J. M. Efficient implementation of a Van der Waals density functional: application to double-wall carbon nanotubes. *Phys. Rev. Lett.* **2009**, *103*, 096102.
- (138) Vanderbilt, D. Soft self-consistent pseudopotentials in a generalized eigenvalue formalism. *Phys. Rev. B* **1990**, *41*, 7892–7895.
- (139) Haas, P.; Tran, F.; Blaha, P. Calculation of the lattice constant of solids with semilocal functionals. *Phys. Rev. B* **2009**, *79*, 085104.
- (140) Statiris, P.; Lu, H.; Gustafsson, T. Temperature dependent sign reversal of the surface contraction of Ag(111). *Phys. Rev. Lett.* **1994**, *72*, 3574–3577.
- (141) Soares, E.; Leatherman, G.; Diehl, R.; Van Hove, M. Low-energy electron diffraction study of the thermal expansion of Ag(111). *Surf. Sci.* **2000**, 468, 129–136.
- (142) Nichols, R.; Nouar, T.; Lucas, C.; Haiss, W.; Hofer, W. Surface relaxation and surface stress of Au(111). Surf. Sci. 2002, 513, 263–271.
- (143) Ohtani, H.; Van Hove, M.; Somorjai, G. LEED intensity analysis of the surface structures of Pd(111) and of co adsorbed on Pd (111) in a  $(\sqrt{3} \times \sqrt{3})$  R30 arrangement. Surf. Sci. 1987, 187, 372–386.

- (144) Adams, D. L.; Nielsen, H.; Van Hove, M. A. Quantitative analysis of low-energy-electron diffraction: application to Pt(111). *Phys. Rev. B* **1979**, *20*, 4789.
- (145) Wijzenbroek, M.; Helstone, D.; Meyer, J.; Kroes, G.-J. Dynamics of H<sub>2</sub> dissociation on the close-packed (111) surface of the noblest metal: H<sub>2</sub> + Au(111). J. Chem. Phys. 2016, 145, 144701.
- (146) Patra, A.; Bates, J. E.; Sun, J.; Perdew, J. P. Properties of real metallic surfaces: effects of density functional semilocality and Van der Waals nonlocality. *Proc. Natl. Acad. Sci.* 2017, 114, E9188–E9196.
- (147) Cottrell, C.; Carter, R.; Nesbitt, A.; Samson, P.; Hodgson, A. Vibrational state dependence of D<sub>2</sub> dissociation on Ag(111). *J. Chem. Phys.* **1997**, 106, 4714–4722.
- (148) Kaufmann, S. personal communication.
- (149) Wei, C. Y.; Lewis, S. P.; Mele, E. J.; Rappe, A. M. Structure and vibrations of the vicinal copper (211) surface. *Phys. Rev. B* **1998**, *57*, 10062–10068.
- (150) Shakouri, K.; Behler, J.; Meyer, J.; Kroes, G.-J. Accurate neural network description of surface phonons in reactive gas-surface dynamics: N<sub>2</sub>+Ru(0001). J. Phys. Chem. Lett. **2017**, 8, 2131–2136.
- (151) Gerrits, N.; Chadwick, H.; Kroes, G.-J. Dynamical study of the dissociative chemisorption of CHD<sub>3</sub> on Pd(111). *J. Phys. Chem. C* **2019**, 123, 24013–24023.
- (152) Gerrits, N.; Shakouri, K.; Behler, J.; Kroes, G.-J. Accurate probabilities for highly activated reaction of polyatomic molecules on surfaces using a high-dimensional neural network potential: CHD<sub>3</sub> + Cu(111). *J. Phys. Chem. Lett.* **2019**, *10*, 1763–1768.
- (153) Schimka, L.; Harl, J.; Stroppa, A.; Grüneis, A.; Marsman, M.; Mittendorfer, F.; Kresse, G. Accurate surface and adsorption energies from many-body perturbation theory. *Nature materials* **2010**, *9*, 741–744.
- (154) Lee, K.; Berland, K.; Yoon, M.; Andersson, S.; Schröder, E.; Hyldgaard, P.; Lundqvist, B. I. Benchmarking van der Waals density functionals with experimental data: potential-energy curves for H<sub>2</sub> molecules on Cu(111),(100) and (110) surfaces. J. Phys. Condens. Matter **2012**, 24, 424213.
- (155) Darling, G.; Holloway, S. Resonance-mediated dissociative adsorption of hydrogen. J. Chem. Phys. 1990, 93, 9145–9156.

(156) Juaristi, J.; Alducin, M.; Muiño, R. D.; Busnengo, H. F.; Salin, A. Role of electron-hole pair excitations in the dissociative adsorption of diatomic molecules on metal surfaces. *Phys. Rev. Lett.* **2008**, *100*, 116102.

- (157) Mondal, A.; Wijzenbroek, M.; Bonfanti, M.; Díaz, C.; Kroes, G.-J. Thermal lattice expansion effect on reactive scattering of  $H_2$  from Cu(111) at  $T_s = 925$  K. J. Phys. Chem. A **2013**, 117, 8770–8781.
- (158) Bonfanti, M.; Somers, M. F.; Díaz, C.; Busnengo, H. F.; Kroes, G.-J. 7D quantum dynamics of H<sub>2</sub> scattering from Cu(111): the accuracy of the phonon sudden approximation. Z. Phys. Chem. **2013**, 227, 1397–1420.
- (159) Mukherjee, S.; Libisch, F.; Large, N.; Neumann, O.; Brown, L. V.; Cheng, J.; Lassiter, J. B.; Carter, E. A.; Nordlander, P.; Halas, N. J. Hot electrons do the impossible: plasmon-induced dissociation of H<sub>2</sub> on Au. Nano lett. 2012, 13, 240–247.
- (160) Hasselbrink, E. Non-adiabaticity in surface chemical reactions. *Surf. Sci.* **2009**, *603*, 1564–1570.
- (161) Schindler, B.; Diesing, D.; Hasselbrink, E. Electronic excitations induced by hydrogen surface chemical reactions on gold. *J. Chem. Phys.* **2011**, 134, 034705.
- (162) Schindler, B.; Diesing, D.; Hasselbrink, E. Electronically nonadiabatic processes in the interaction of H with a Au surface revealed using MIM junctions: the temperature dependence. J. Phys. Chem. C 2013, 117, 6337–6345.
- (163) Polanyi, J. C. Some concepts in reaction dynamics. *Science* **1987**, *236*, 680–690.
- (164) Polanyi, J. C. Some concepts in reaction dynamics (Nobel lecture). *Angew. Chem.* **1987**, *26*, 952–971.
- (165) Kroes, G.-J.; Díaz, C.; Pijper, E.; Olsen, R. A.; Auerbach, D. J. Apparent failure of the Born-Oppenheimer static surface model for vibrational excitation of molecular hydrogen on copper. *Proc. Natl. Acad. Sci.* 2010, 107, 20881–20886.
- (166) Sun, J.; Ruzsinszky, A.; Perdew, J. P. Strongly constrained and appropriately normed semilocal density functional. *Phys. Rev. Lett.* **2015**, 115, 036402.

- (167) Gerrits, N.; Smeets, E. W. F.; Vuckovic, S.; Powell, A. D.; Doblhoff-Dier, K.; Kroes, G.-J. Density functional theory for molecule–metal surface reactions: When does the generalized gradient approximation get it right, and what to do if it does not. J. Phys. Chem. Lett, 2020, 11, 10552–10560.
- (168) Yin, R.; Zhang, Y.; Libisch, F.; Carter, E. A.; Guo, H.; Jiang, B. Dissociative chemisorption of O<sub>2</sub> on Al(111): dynamics on a correlated wave-function-based potential energy surface. J. Phys. Chem. Lett. 2018, 9, 3271–3277.
- (169) Gostein, M.; Parhikhteh, H.; Sitz, G. Survival probability of  $H_2$  ( $\nu = 1$ , J=1) scattered from Cu(110). Phys. Rev. Lett. **1995**, 75, 342.
- (170) Watts, E.; Sitz, G. O. State-to-state scattering in a reactive system:  $H_2$  (v= 1, j= 1) from Cu(100). J. Chem. Phys. **2001**, 114, 4171–4179.
- (171) Kroes, G.-J.; Wiesenekker, G.; Baerends, E.; Mowrey, R. Competition between vibrational excitation and dissociation in collisions of H<sub>2</sub> with Cu(100). *Phys. Rev. B* **1996**, *53*, 10397.
- (172) Salin, A. Theoretical study of hydrogen dissociative adsorption on the Cu(110) surface. J. Chem. Phys. **2006**, 124, 104704.
- (173) Olsen, R.; Kroes, G.; Baerends, E. Atomic and molecular hydrogen interacting with Pt(111). J. Chem. Phys. 1999, 111, 11155–11163.
- (174) Olsen, R.; Philipsen, P.; Baerends, E. CO on Pt(111): A puzzle revisited. J. Chem. Phys. 2003, 119, 4522–4528.
- (175) Mills, G.; Schenter, G.; Makarov, D. E.; Jónsson, H. Generalized path integral based quantum transition state theory. Chem. Phys. Lett. 1997, 278, 91–96.
- (176) Mills, G.; Jónsson, H.; Schenter, G. K. Reversible work transition state theory: application to dissociative adsorption of hydrogen. *Surf. Sci.* **1995**, 324, 305–337.
- (177) Mills, G.; Jónsson, H. Quantum and thermal effects in H<sub>2</sub> dissociative adsorption: evaluation of free energy barriers in multidimensional quantum systems. *Phys. Rev. Lett.* **1994**, *72*, 1124.
- (178) Somers, M.; Kingma, S.; Pijper, E.; Kroes, G.; Lemoine, D. Six-dimensional quantum dynamics of scattering of ( $\nu = 0$ , j = 0) H<sub>2</sub> and D<sub>2</sub> from Cu(111): test of two LEPS potential energy surfaces. *Chem. Phys. Lett.* **2002**, 360, 390–399.

# 6 Performance of made-simple meta-GGA functionals with rVV10 non-local correlation for $H_2 + Cu(111)$ , $D_2 + Ag(111)$ , $H_2 + Au(111)$ and $D_2 + Pt(111)$

#### This Chapter is based on:

Smeets, E. W. F.; Kroes, G.-J. Performance of made-simple meta-GGA functionals with rVV10 non-local correlation for  $H_2$  + Cu(111),  $D_2$  + Ag(111),  $H_2$  + Au(111) and  $D_2$  + Pt(111). *J. Phys. Chem. C* **2021**, DOI: 10.1021/acs.jpcc 0c11034

#### Abstract

Accurately modeling heterogeneous catalysis requires accurate descriptions of rate controlling elementary reactions of molecules on metal surfaces, but standard density functionals (DFs) are not accurate enough for this. The problem can be solved with the specific reaction parameter approach to density functional theory (SRP-DFT), but the transferability of SRP-DFs among chemically related systems is limited. We combine the MS-PBEl, MS-B86bl and MS-RPBEl semi-local made simple (MS) meta-GGA (mGGA) DFs with rVV10 non-local correlation, and we evaluate their performance for the hydrogen (H<sub>2</sub>) + Cu(111), deuterium (D<sub>2</sub>) + Ag(111), H<sub>2</sub> + Au(111) and D<sub>2</sub> + Pt(111) gas-surface systems. The three MS mGGA DFs that have been combined with rVV10 non-local correlation were not fitted to reproduce particular experiments, nor has the b parameter present in rVV10 been re-optimized. Of the three DFs obtained the MS-PBEl-rVV10 DF yields an excellent description of van der Waals well geometries. The three original MS mGGA DFs gave a highly accurate description of the metals, which was comparable in quality to that

 $H_2 + Cu(111), D_2 + Ag(111), H_2 + Au(111) \text{ and } D_2 + Pt(111)$ 

obtained with the PBEsol DF. Here we find that combining the three original MS mGGA DFs with rVV10 non-local correlation comes at the cost of a slightly less accurate description of the metal. However the description of the metal obtained in this way is still better than the descriptions obtained with SRP-DFs specifically optimized for individual systems. Using the Born-Oppenheimer static surface (BOSS) model simulations of molecular beam dissociative chemisorption experiments yields chemical accuracy for the  $D_2$  + Ag(111) and  $D_2$  + Pt(111) systems. A comparison between calculated and measured  $E_{1/2}(\nu,J)$  parameters describing associative desorption suggest chemical accuracy for the associative desorption of  $H_2$  from Au(111) as well. Our results suggest that ascending Jacob's ladder to the mGGA rung yields increasingly more accurate results for gas-surface reactions of  $H_2$  ( $D_2$ ) interacting with late transition metals.

#### 6.1 Introduction

In heterogeneous catalysis the rate-limiting step is often the dissociative chemisorption of a molecule on a surface<sup>2,3</sup>. The dissociation of the simple hydrogen ( $\rm H_2$ ) and nitrogen ( $\rm N_2$ ) molecules are important steps in the production of ammonia and syngas<sup>4–6</sup>. The dissociation of  $\rm H_2$  is also relevant to the industrial synthesis of methanol from  $\rm CO_2$  over a  $\rm Cu/ZnO/Al_2O_3$  catalyst, for which the dissociation of  $\rm H_2$  is considered to be a rate-limiting step<sup>7–9</sup>. Calculating chemically accurate barrier heights<sup>10</sup> for rate-controlling reactions to obtain accurate rates of the overall reaction network<sup>11</sup> potentially has a large financial impact on the chemical industry since it allows theoretical screening for more efficient catalysts<sup>12</sup>.

Currently density functional theory (DFT) is the only method that is computationally cheap enough to map out full potential energy surfaces (PESs) for gas-surface reactions. Development of density functionals (DFs) that can accurately describe dissociative chemisorption reactions on surfaces is important to increasing the predictive power of DFT. DFs constructed using the generalized gradient approximation (GGA) that provide chemically accurate results for specific gas-surface reactions and that in some cases show transferability to chemically related systems are based on the semi-empirical specific reaction parameter (SRP) approach to DFT (SRP-DFT)<sup>13-16</sup>. However, DFs at the GGA level are always a compromise between a good description of the molecule and of the metal<sup>17</sup>, despite efforts to construct GGA based DFs<sup>18</sup> or non-separable gradient approximation DFs<sup>19</sup> that perform equally well for both solids and molecules. A good description of the metal is crucial to calculating accurate barrier heights since the barrier height might depend on the interlayer distance

6.1. Introduction 229

of the two top most metal layers<sup>20-22</sup> and the amplitude of thermal motion of the metal atoms in the top layer<sup>23,24</sup>.

In Chapter 3 we developed the semi-local MS-PBEl, MS-B86bl and MS-RPBEl meta-GGA (mGGA) DFs<sup>25</sup> based on the made simple (MS) formalism<sup>26,27</sup>. which yield a description of the metal that is similar in accuracy to that obtained with the PBEsol<sup>28</sup> DF. Additionally the DFs provide a chemically accurate description of molecular beam experiments on dissociative chemisorption of H<sub>2</sub>  $(D_2)$  on  $Cu(111)^{25,29-31}$  and a near chemically accurate description of similar experiments on  $D_2 + Ag(111)^{25,32}$ . The reason behind this improved overal performance of mGGA based DFs over GGA based DFs is that mGGA DFs also depend on the kinetic energy density  $\tau$ , which allows a DF to distinguish between regions of the electron density describing single (covalent), metallic, and weak bonds<sup>33</sup> via the dimensionless inhomogeneity parameter  $\alpha^{26,27,33}$ . This parameter has also been used in the construction of several other much used mGGA DFs, such as TPSS<sup>34</sup>, revTPSS<sup>35</sup>, RTPSS<sup>36</sup>, SCAN<sup>37,38</sup> and mBEEF<sup>39</sup>. Several groups have now reported good simultaneous descriptions of lattice constants and adsorption energies<sup>39–41</sup>, or, more generally, energetics and structure<sup>26,27,42,43</sup>, when using mGGA DFs. The MS-RPBEl DF has also shown some success in describing the  $O_2 + Al(111)$  system<sup>16</sup>.

In Chapter 5 we also identified non-local correlation as a key ingredient for a DF that can describe dissociative chemisorption of  $H_2$  ( $D_2$ ) with chemical accuracy on multiple metals<sup>15</sup> and not just on different crystal faces of the same metal<sup>44,45</sup>, which had previously only been demonstrated for reactions of  $CH_4$  with metal surfaces, i.e.  $Ni(111)^{46}$  and  $Pt(111)^{47}$ . Here we combine the three previously developed MS mGGA DFs with rVV10<sup>48</sup> non-local correlation in order to obtain the MS-PBEl-rVV10, MS-B86bl-rVV10 and MS-RPBEl-rVV10 DFs, and we will evaluate their performance for the  $H_2 + Cu(111)$ , Ag(111), Au(111) and Pt(111) systems. The three original MS mGGA DFs<sup>25</sup> which we combine with rVV10<sup>48</sup> non-local correlation show no van der Waals interactions for  $H_2$  interacting with transition metals<sup>15</sup>, which is the best case scenario to complement a semi-local exchange-correlation functional with (r)VV10 non-local correlation according to Vydrov et al.<sup>49</sup>.

The PESs we computed with the three new DFs are subsequently used in quasi-classical trajectory (QCT) calculations. In the dynamics calculations we use the Born-Oppenheimer static surface (BOSS) model, which is known to work well for activated  $H_2$  dissociation on cold metals<sup>50–54</sup>. Calculations that incorporate surface motion show that the impact of surface atom motion (phonons) can be neglected due to the effect on the reaction probability being small for the low surface temperature experiments considered here<sup>20,22,52,55</sup>. It is also justified to neglect the effect of electron-hole pair excitation on the reaction

 $H_2 + Cu(111), D_2 + Ag(111), H_2 + Au(111) \text{ and } D_2 + Pt(111)$ 

probability, as its effect on sticking has previously been shown to be small in calculations on  $H_2 + Cu(111)^{56-58}$ ,  $Ag(111)^{59-61}$ , and  $Ru(0001)^{62}$ . Previous research has also shown that for highly activated dissociation of  $H_2$  on cold metals the difference between quantum dynamics (QD) and QCT calculations is marginal<sup>15,63,64</sup> (see also Chapter 4), and there is also some evidence that the same observation holds for the non-activated reaction of  $D_2 + Pt(111)$  for all but the lowest translational energies<sup>14,65</sup>. Since our dynamical model is best suited to molecular beam dissociative chemisorption experiments, we will mainly compare to this kind of experiment<sup>29–32,66,67</sup> to assess the quality of the obtained DFs. These experiments have been performed for  $H_2 + Cu(111)^{29-31}$ ,  $Ag(111)^{32}$  and  $Pt(111)^{66-68}$ .

Additionally we will also compare to the associative desorption experiments that are available for the  $H_2$  ( $D_2$ ) +  $Au(111)^{69}$  and  $Ag(111)^{70,71}$  systems as in Chapter 5, by comparing the measured  $E_0(\nu, J)$  parameters characterizing the measurements with calculated  $E_{1/2}(\nu, J)$  parameters<sup>15</sup> assuming detailed balance. Given that the DFs developed here are too reactive with respect to the  $H_2(D_2) + Cu(111)$  system (as will be shown below) we will omit such an analysis for the recent associative desorption experiments<sup>72</sup> for this system here. For the  $H_2 + Cu(111)$  system it is known that the effect of surface motion cannot readily be ignored for specific observables at high surface temperature<sup>53</sup>  $(T_s)$ , and this may hold for the  $H_2 + Au(111)$  and Ag(111) systems as well. Therefore it is difficult to assess the quality of the developed DFs when using the BOSS model in comparing to high surface temperature experiments<sup>69,72</sup>. as will be done below. We note that it is also possible to simulate associative desorption directly by running trajectories starting around the transition state using Metropolis sampling of the initial conditions<sup>73–77</sup>, and that this has also been done for  $H_2$  and  $D_2$  desorbing from Cu(111). There are some limitations regarding these calculations: in earlier work<sup>74,75</sup> a PES that is an approximate fit<sup>78</sup> to unconverged DFT calculations<sup>79</sup> was used. The statistical accuracy of the later work<sup>77</sup> is limited by the number of ab initio molecular dynamics (AIMD) trajectories that have been calculated.

The van der Waals well geometries obtained from our DFT calculations will be compared to experimental results, which are mostly obtained from analysis of selective adsorption experiments  $^{80-90}$ . In these experiments, an increase or a dip is observed in a peak associated with a rotational (rotationally mediated selective adsorption, RMSA<sup>80</sup>) transition or in a peak for a diffractive (corrugation mediated selective adsorption, CMSA<sup>91,92</sup>) transition if the translational energy passes through a value that overlaps with the energy difference between two hindered rotational or parallel translational metastable states, respectively. The  $\rm H_2$  molecule is then trapped in the final state in the van der Waals well close

to the surface<sup>82,87</sup>. The resonance energies can then be used to reconstruct the shape of the potential and thus to determine the van der Waals well depths and geometries. Concerning the systems investigated here, studies using experiments to analyze the van der Waals interaction have been performed for  $H_2 + Cu(111)^{89,90}$ ,  $Ag(111)^{83,84,86}$ ,  $Au(111)^{90}$ , and  $Pt(111)^{80-82,93}$ .

#### 6.2 Methodology

#### 6.2.1 Coordinate system

In the dynamics calculations we use the BOSS model<sup>13</sup>, meaning that we make the Born-Oppenheimer approximation and keep the surface atoms fixed at their ideal lattice positions. We only take into account the six degrees of freedom (DOF) of the  $H_2$  molecule (see figure 6.1a). We use molecular coordinates in which the center of mass (COM) coordinates X, Y describe the lateral position of the molecule, and Z describes the molecule surface distance. The remaining DOFs are the  $H_2$  bond length r, the polar angle  $\theta$  and the azimuth  $\phi$  defining the orientation of the molecule relative to the surface (see figure 6.1a). The geometry of the (111) face of an fcc metal together with its high symmetry sites is shown in relation to the coordinate system used in figure 6.1b.

### 6.2.2 Combining Made Simple meta-GGA exhcange-correlation with rVV10 non-local correlation

The form of the rVV10<sup>48</sup> non-local correlation functional is similar to that of the Rutgers-Chalmers vdW-DFs<sup>38</sup>:

$$E_c^{\text{non-local}} = \int d\mathbf{r} n(\mathbf{r}) \left(\frac{\hbar}{2} \int d\mathbf{r}' \Phi(\mathbf{r}, \mathbf{r}') n(\mathbf{r}') + \beta\right). \tag{6.1}$$

Here  $n(\mathbf{r})$  is the electron density and  $\Phi(\mathbf{r},\mathbf{r}')$  is the kernel describing the density-density interactions<sup>38</sup>. The parameter  $\beta$  is not present in the vdW-DF1<sup>94</sup> and vdW-DF2<sup>95</sup> non-local correlation functionals and is here taken to be  $\beta = \frac{1}{32} \left(\frac{3}{b}\right)^{\frac{3}{4}}$  so as to ensure that  $E_c^{\text{non-local}}$  is zero for the homogeneous electron gas<sup>38</sup>. In using the full exchange-correlation functional named rVV10, most researchers we are aware of <sup>38,96,97</sup> now append the non-local correlation (NLC) rVV10 functional to the following semi-local functional (SLF)

$$E_{xc}^{VV10-SL} = E_{x}^{rPW86} + E_{c}^{PBE}. \tag{6.2} \label{eq:6.2}$$

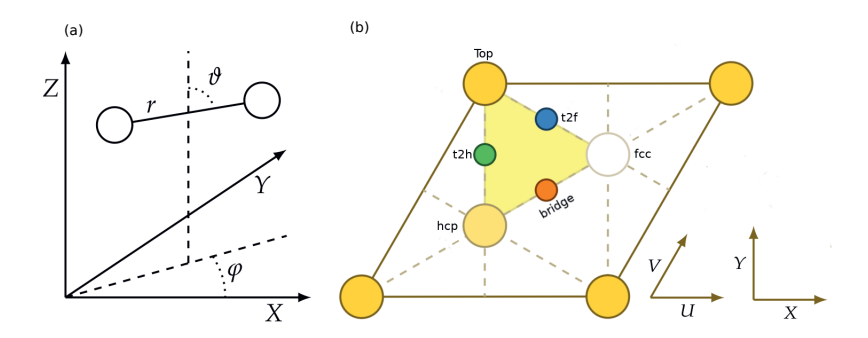


FIGURE 6.1: The COM coordinate system used for the description of the  $H_2$  ( $D_2$ ) molecule (a). The unit cell of a (111) face of a fcc metal together with the high symmetry sites as well as the relationship with the coordinate system chosen for  $H_2$  ( $D_2$ ) relative to the (111) surface (b). The origin of the COM coordinate system (X,Y,Z)=(0,0,0) is the center of a top atom. We define the polar angle and azimuth such that  $(\theta=90^\circ,\phi=0^\circ)$  corresponds to molecules parallel to the surface pointing along the X (or equivalent U) direction. The hcp and fcc hollow sites correspond to metal atoms in the second and third layer. Note that the colored triangle marks the irreducible wedge of the (111) unit cell.

Here,  $E_x^{PW86}$  is the exchange part of a refitted version of the PW86 functional<sup>98</sup>, and  $E_c^{PBE}$  is the PBE correlation functional<sup>99</sup>. In implementing the full rVV10 functional, DFT codes like Quantum Espresso<sup>100,101</sup> and Q-Chem<sup>102</sup> also append the NLC functional defined by Eq. 6.1 to the SLF defined by Eq. 6.2. Eq. 6.2 also defines the semi-local exchange correlation functional to which Vydrov et al.<sup>49</sup> appended their NLC VV10 functional to in order to obtain the full exchange correlation functional now referred to as the VV10 functional. Sabatini et al.<sup>48</sup> obtained the NLC rVV10 functional of (Eq. 6.1) by making a minor change to the NLC VV10 functional<sup>49</sup> in a clever way to make it amenable to efficient evaluation by the algorithm due to Róman-Pérez and Soler 103 that can also be used to speed up the evaluation of the vdW-DF1 and vdW-DF2 density functionals of the Lundqvist-Langreth group<sup>94,95</sup>. To reproduce the original VV10 results as closely as possible, Sabatini et al. 48 changed one of the empirical parameters in the NLC rVV10 functional, i.e., the b-parameter, from the original VV10 value of 5.96 to the rVV10 value of 6.37. Here, the b parameter can be used to control the damping of the kernel at short range, while the other empirical parameter in VV10 and rVV10, C, can be used to obtain good values for the  $C_6$  dispersion coefficients describing the long-range van der Waals interaction. The C parameter is taken the same<sup>48</sup> in the NLC rVV10 as in the NLC VV10 functional<sup>49</sup>.

We note that there is some ambiguity associated with the SLF Sabatini et al.  $^{48}$  originally appended their NLC rVV10 functional to. In a sentence saying that they were "following the original VV10 functional definition", they provided an equation for the full rVV10 functional in which the SLF to which the NLC rVV10 functional was appended would be given by

$$E_{xc}^{vdW-DF2} = E_x^{rPW86} + E_c^{LDA}. (6.3)$$

The equation they presented suggested that in their SLF PBE correlation was replaced with correlation from the local density approximation (where Sabatini et al.<sup>48</sup> state they used the functional as parameterized by Perdew and Wang<sup>104</sup>). This SLF happens to be the same as the one used with the non-local vdW-DF2 functional to obtain the full vdW-DF2 functional<sup>95</sup>. Regarding the SLF originally used, we think the equation provided by Sabatini et al.<sup>48</sup> contained a misprint, and that they in fact used the expression of Eq. 6.2 instead. Our reason for stating this is that the energies they present for the S22 database<sup>105</sup> in Table 1 of their Supporting material to Ref.<sup>48</sup>, which they computed with their rVV10 functional but using the b parameter from the original VV10 functional, were in excellent agreement with the original VV10 results computed by Vydrov et al.<sup>49</sup>. We believe that this would not have been

$$H_2 + Cu(111), D_2 + Ag(111), H_2 + Au(111) \text{ and } D_2 + Pt(111)$$

the case had Sabatini et al.<sup>48</sup> used Eq. 6.3 as Vydrov et al.<sup>49</sup> certainly used Eq. 6.2; the difference between the PBE and LDA semi-local contributions should have been too large to allow for the small differences obtained between the rVV10 with b = 5.9 and VV10 results that were obtained in practice[48]. Even more importantly, the rVV10 results obtained by Peng et al.<sup>38</sup>, who used Eq. 2 for the SLF, for the S22 database<sup>105</sup> as provided in table 4 of their paper<sup>38</sup> closely reproduce the rVV10 results of Sabatini et al.<sup>48</sup> as provided in table 1 of their supporting material[48]. Once, again, this would not have been the case had these teams used different SLFs appended to the NLF rVV10 DF.

More importantly to the purpose of the present work than the exact expression of the full rVV10 functional, the flexibility built in to the NLC rVV10 functional through the adjustable b parameter allows it to be used in combination with a number of exchange-correlation functionals, including mGGA functionals like the SCAN functional<sup>37</sup> and the B97M functional incorporated into the B97M-rV functional<sup>97</sup>. It is in this context that we use the NLC rVV10 functional, hoping that in this way we can obtain a good description of the long-range interaction, while hopefully keeping the medium-range interaction, which we think is reasonably described with the mGGA functionals<sup>25</sup> we will be testing as SLFs, intact, in the spirit of Peng et al.<sup>38</sup>. In this Chapter, the full exchange-correlation functional then takes the following form:

$$E_{xc}^{\text{MS-mGGA-rVV10}} = E_{x}^{\text{MS-mGGA}} + E_{c}^{\text{revTPSS}} + E_{c}^{\text{rVV10}}, \tag{6.4}$$

where  $E_c^{\text{revTPSS}}$  is the revTPSS<sup>35</sup> correlation functional that is used in the original semi-local MS mGGA DFs we developed<sup>25</sup>.  $E_x^{\text{MS-mGGA}}$  can be either of the three MS mGGA exchange functionals we developed previously<sup>25</sup> based on the MS formalism<sup>26</sup>. In this formalism one interpolates between two GGAs for two extreme scenarios, namely a single orbital system which describes covalent bonds  $(F_x^0(p;c))$  and one in which the bonding is metallic  $(F_x^1(p))^{25}$ . The exchange enhancement factor of a MS mGGA DF then becomes<sup>26</sup>:

$$F_r^{MS}(p,\alpha) = F_r^1(p) + f(\alpha)(F_r^0(p;c) - F_r^1(p)), \tag{6.5}$$

where  $p=s^2$  with s being the reduced gradient of the electron density<sup>26</sup>, and  $F_x^1(p)$  and  $F_x^0(p;c)$  are gradient enhancement factors that depend solely on p. The numerical parameter c is optimized to exactly reproduce the exchange energy of the hydrogen atom by cancelling the spurious self-interaction present in the Hartree energy in this atom<sup>26</sup>. For both  $F_x^1(p)$  and  $F_x^0(p;c)$  three expressions<sup>25</sup> have been used which are PBE-like<sup>99</sup>, RPBE-like<sup>106</sup> and B86b-like<sup>107</sup>, in the sense that we use the gradient enhancement expression of the PBE<sup>99</sup>, RPBE<sup>106</sup> and B86b<sup>107</sup> GGA DFs but with  $\mu = \frac{10}{81}$  as was done in

PBEsol<sup>28</sup>. The difference between  $F_x^1(p)$  and  $F_x^0(p;c)$  is that in the case of  $F_x^0(p;c)$  we replace  $\mu p$  by  $\mu p + c$  everywhere<sup>25</sup>, as done earlier in ref<sup>26</sup>. The interpolation between the two extreme cases then happens through a function of the inhomogeneity parameter  $f(\alpha)$ , with the inhomogeneity parameter being defined as:<sup>26,27</sup>

$$\alpha = \frac{\tau - \tau^W}{\tau^{\text{unif}}}.\tag{6.6}$$

Here,  $\tau^W$  is the Von Weizäcker kinetic energy, which is equal to the kinetic energy density associated with a single orbital electron density<sup>41</sup>, and  $\tau^{\text{unif}}$  is the kinetic energy of the homogeneous electron gas. Note that  $\alpha$  will approach unity as  $\tau \approx \tau^{\text{unif}}$  and  $\tau^W \ll \tau^{\text{unif}}$  for slowly varying electron densities, while  $\alpha$  approaches zero for densities found in covalent bonding for which  $\tau \approx \tau^{W41}$ . The expression for  $f(\alpha)$  can be found in Refs.<sup>25,26</sup>.

Above, we have already noted that the possibility to adapt the b parameter allows for flexibility in the combination of the NLC rVV10 functional with SLFs. In the past several strategies have been used to arrive at a good choice of b. In perhaps the most rigorous approach, in the original papers presenting the full  $VV10^{49}$  and  $rVV10^{48}$  functionals the b parameter was chosen to minimize the errors in the binding energies of weakly bonded dimers as present in the S22 database<sup>105</sup>. In a simplified procedure requiring fewer calculations, the b parameter has also been determined by demanding that calculations with the NLC rVV10 functional reproduce the Ar dimer energy curve determined with CCSD(T) calculations<sup>97</sup> as closely as possible<sup>38,48,96,97</sup>. In the development of functionals for specific purposes, the b parameter has also been fitted to more specific properties corresponding to these purposes. For instance, functionals have been developed that give good descriptions of layered materials by fitting the b parameter to obtain a good description of properties of these materials, after which the performance of the obtained functional is usually also tested on properties of other systems<sup>98,99</sup>. In the spirit of our SRP-DFT method, as described below we take an even more extreme approach to determining the bparameter.

The goal of the present paper is to investigate whether adding non-local rVV10 correlation to the MS mGGA functionals previously developed by us leads to functionals giving a better description of dissociative chemisorption of  $H_2$  on the noble metal surfaces Cu(111), Ag(111), Au(111) and Pt(111). With this goal in mind, we investigated how closely we could reproduce the van der Waals interaction for the system for which the most accurate experimental results are available for this interaction ( $H_2 + Cu(111)$ ), van der Waals well depths and geometries are available from RMSA<sup>80</sup> or CMSA<sup>91,92</sup> experiments on this system). An additional reason for our choice of strategy is that most general

 $H_2 + Cu(111)$ ,  $D_2 + Ag(111)$ ,  $H_2 + Au(111)$  and  $D_2 + Pt(111)$ 

purpose DFs (at the GGA or mGGA level) cannot describe the interaction of  $H_2$  with transition metal surfaces to within chemical accuracy (see for example figure 3.11 of Chapter 3 or figure 1a of Ref.<sup>13</sup>). Therefore closely reproducing reference data for gas phase dimers offers no guarantee that the obtained b value would be the best possible for  $H_2$  + transition metal systems (although we will see below that this strategy would have worked for our case). However, we do check that the b parameter we adopt by considering the long range attractive van der Waals interaction also yields a reasonably good description of the metal lattice constant for copper, which is a short-to-medium range interaction, to make sure that "the tail does not wag the dog"<sup>38</sup>.

Our tests on  $H_2 + Cu(111)$  were first done with the MS-PBEl-rVV10 DF (see figure 6.2). Adopting the b parameter of the original full rVV10 functional  $^{48}$ (b = 6.3) yields a good description of the van der Waals well depth and minimum geometry, while a still reasonable lattice constant is obtained for copper (see figure 6.2 and below). However, optimizing the b parameter for the MS-B86blrVV10 and MS-RPBEl-rVV10 functionals in this manner poses a dilemma. Using the small values of b suggested by a requirement of closely reproducing the  $H_2 + Cu(111)$  van der Waals interaction leads to an underestimation of the copper lattice constant that we deem unacceptable (see figures 6.3-6.4). This dilemma is illustrated in figures 6.3-6.4, in which the lattice constant, the van der Waals well depth and the position of the van der Waals minimum are shown as a function of b for the MS-B86bl-rVV10 and the MS-RPBEl-rVV10 DFs. In these figures and figure 6.2 the lattice constant has been recalculated for each value of b, after which the 6 layer metal slabs are relaxed accordingly, and the van der Waals curve is calculated for a geometry in which H<sub>2</sub> is parallel to the surface and above the top site. From figures S1-3 it is clear that reducing b yields smaller lattice constants and deeper van der Waals wells that are closer to the surface. Keeping these observations in mind, and noting that fitting the b parameters for the MS-PBEl-rVV10 DF to either the van der Waals well depth or the position of the minimum would have resulted in a value that is very similar to the original value of Sabatini et al.  $^{48}$  (b = 6.3), we simply chose to adopt this value for all three functionals.

Finally, we note that the original MS mGGA exchange-correlation functionals appear to meet the same criterion as the semi-local exchange-correlation functional used by Vydrov et al.<sup>49</sup> and Sabatini et al.<sup>48</sup>, i.e. that this functional does not yield an attractive long range interaction (see figure 5.3b of Chapter 5). As Vydrov et al.<sup>49</sup> point out: 'it is preferable to combine VV10 with a functional that gives no significant binding in van der Waals complexes'. As our SLFs meet this criterion, we are not surprised that these SLFs combined with the NLC rVV10 functional yield either a good (with MS-PBEl) or still reasonable

(with MS-B86bl or MS-RPBEl) description of the van der Waals interaction in  $H_2 + Cu(111)$  with the choice of the original value of the *b* parameter.

#### 6.2.3 Construction of the PESs

We use the corrugation reducing procedure (CRP)<sup>109</sup> to interpolate DFT results calculated on a grid in order to obtain a continuous representation of the PESs used in this work. Apart from using denser grids to improve the accuracy of the interpolated PESs our method is analogous to the one used by Wijzenbroek et al.<sup>110</sup>. In principle we use the grids reported in appendix 5.A of Chapter 5.

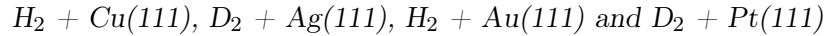
In Chapter 5 we have assessed the quality of the  $\rm H_2 + Cu(111)$  PES obtained using the B86SRP68-DF2 DF by using  $\sim \! 4900$  randomly sampled geometries of  $\rm H_2$  above the metal slab. Based on all the randomly sampled points taken together our CRP<sup>109</sup> fit had a root mean square (rms) error of 31 meV compared to the underlying electronic structure calculations. When only looking at the 3538 geometries that have an interaction energy of  $\rm H_2$  with the surface lower then 4 eV the rms error reduces to 8 meV ( $\sim 0.2$  kcal/mol). Since we use the same interpolation grids as in Chapter 5, we presume the accuracy of the obtained CRP PESs in this Chapter to be similar.

#### 6.2.4 Quasi-classical dynamics

We compute observables using the quasi-classical trajectory (QCT) method<sup>111</sup>. This means that we take into account the quantum mechanical energies of the impinging  $H_2$  and  $D_2$  molecules in their initial rovibrational states. The method used is described more fully in section 2.3.1 of Chapter 2. We integrate the equations of motion using the algorithm of Stoer et al.<sup>112</sup>.

In order to obtain reliable statistics we propagate 200,000 trajectories per energy point when simulating a molecular beam experiment, and 50,000 trajectories per energy point when calculating initial-state resolved reaction probabilities. Trajectories always start in the gas phase ( $Z_{\rm gas}=8{\rm \AA}$ ). When r becomes bigger than some critical value ( $r_c=2.2{\rm \AA}$ ) the trajectory is counted as reacted. If during the propagation Z becomes bigger than  $Z_{\rm gas}$  the trajectory is counted as scattered. In all QCT calculations we use a time step of dt=0.001 fs. The reaction probability  $P_r$  is then calculated by dividing the number of reacted trajectories  $N_r$  by the total number of trajectories  $N_{\rm total}$ 

$$P_r = \frac{N_r}{N_{\text{total}}}. (6.7)$$



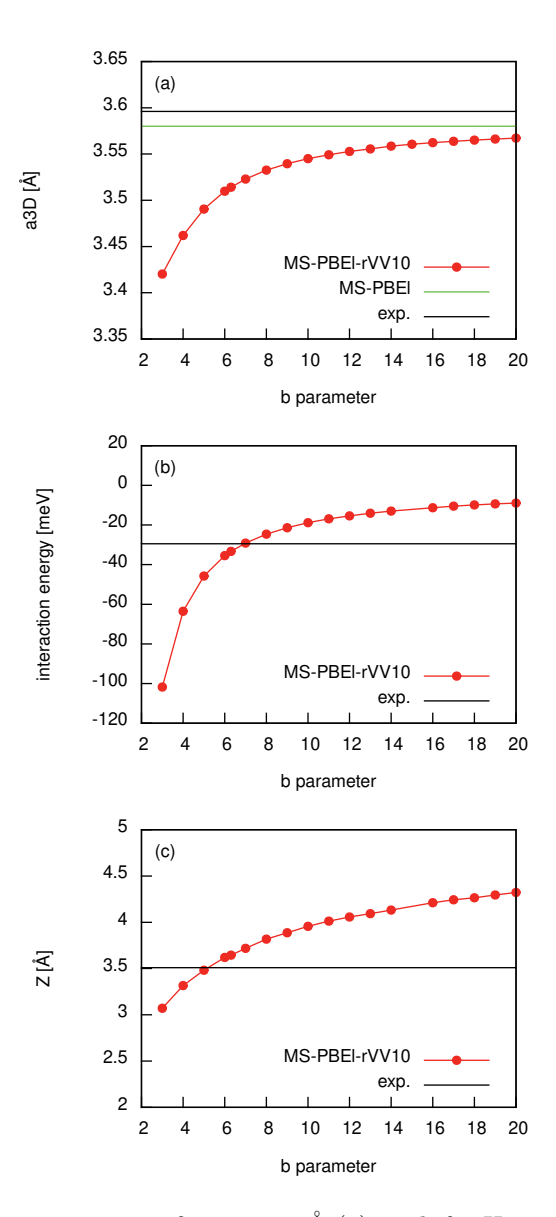


FIGURE 6.2: The lattice constant of copper in Å (a), and, for H<sub>2</sub> + Cu(111), the van der Waals well depth in meV (b) and the position of the van der Waals minimum in Å (c) are presented as calculated with the MS-PBEl-rVV10 DF. Calculated results are shown in red, experimental results are shown in black<sup>89,108</sup>. The green line in panel (a) shows the lattice constant obtained with the MS-PBEl DF<sup>25</sup>.

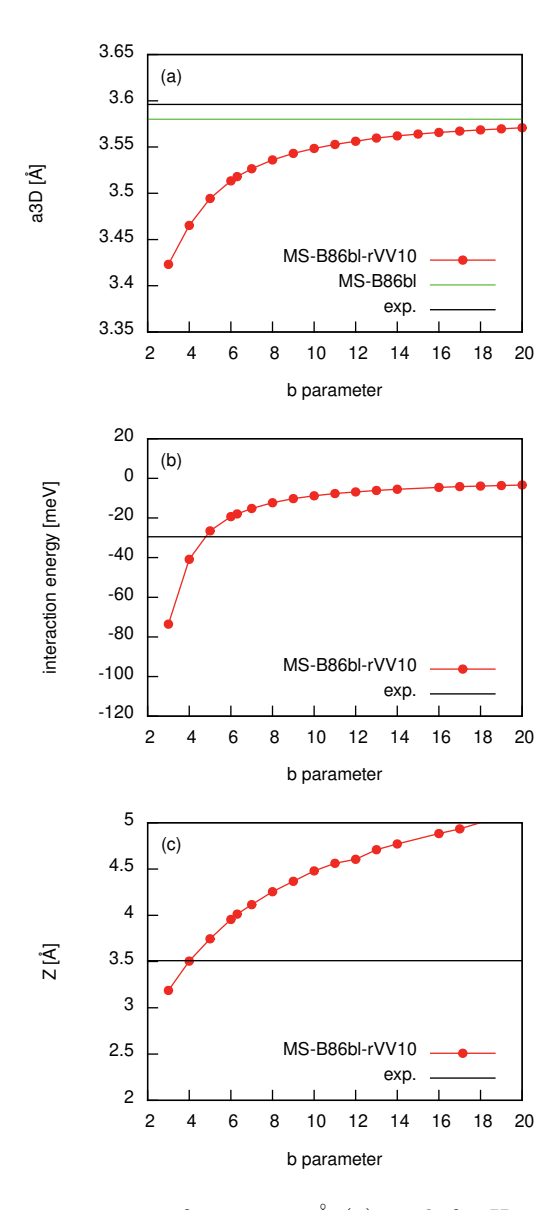
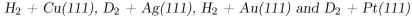


FIGURE 6.3: The lattice constant of copper in Å (a), and, for H<sub>2</sub> + Cu(111), the van der Waals well depth in meV (b) and the position of the van der Waals minimum in Å (c) are presented as calculated with the MS-B86bl-rVV10 DF. Calculated results are shown in red, experimental results are shown in black<sup>89,108</sup>. The green line in panel (a) shows the lattice constant obtained with the MS-B86bl DF<sup>25</sup>.



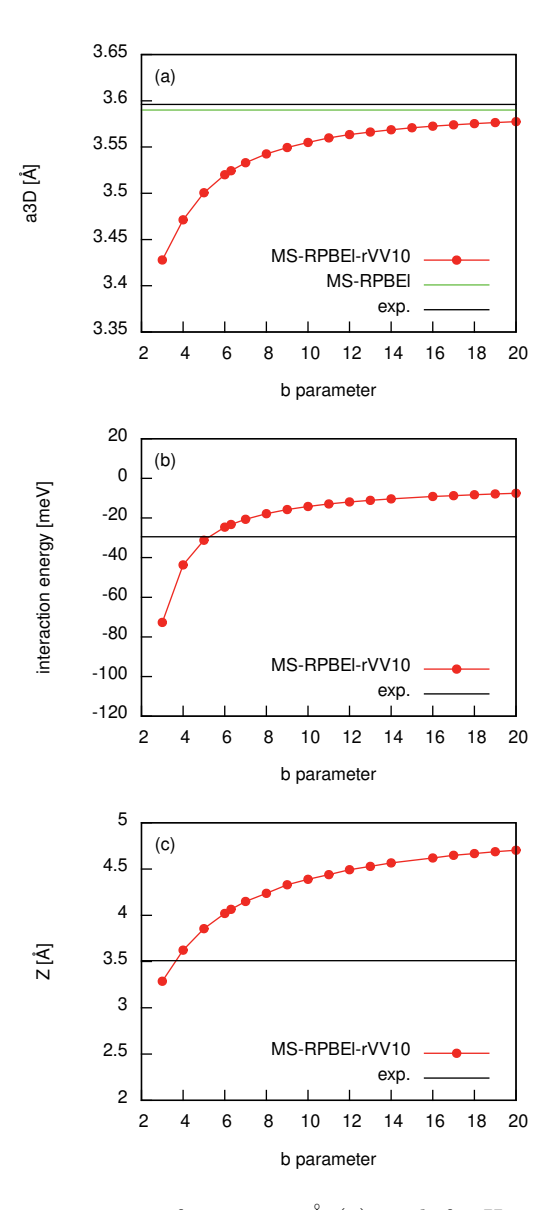


FIGURE 6.4: The lattice constant of copper in Å (a), and, for  $H_2 + Cu(111)$ , the van der Waals well depth in meV (b) and the position of the van der Waals minimum in Å (c) are presented as calculated with the MS-RPBEl-rVV10 DF. Calculated results are shown in red, experimental results are shown in black<sup>89,108</sup>. The green line in panel (a) shows the lattice constant obtained with the MS-RPBEl DF<sup>25</sup>.

#### 6.2.5 Computation of observables

#### Molecular beam sticking

In the molecular beams we simulate, the probability to find  $H_2$  with a velocity v in an interval v + dv and in a particular rovibrational state at a given nozzle temperature  $T_N$  can be described by:

$$P(v_0, \alpha, \nu, J, T_n)dv = \underbrace{Cv^3 e^{-(v-v_0)^2/\alpha^2} dv}_{P_{flux}(v, \alpha)} \times P_{int}(\nu, J, T_n)dv$$
 (6.8)

where C is a normalization constant,  $v_0$  is the stream velocity and  $\alpha$  is the width of the velocity distribution. With equation 6.8 the reactivity of each state can be weighted according to its Boltzmann weight as:

$$P_{int}(\nu, J, T_n) = \frac{g_N f(\nu, J, T_n)}{Z(T_n)}$$

$$\tag{6.9}$$

with

$$f(\nu, J, T_n) = (2J+1) \times e^{(-(E_{\nu,0} - E_{0,0})/k_B T_{vib})} \times e^{(-(E_{\nu,J} - E_{\nu,0})/k_B T_{rot})}.$$
(6.10)

Here, the factor  $g_N$  in equation 6.9 reflects the ortho/para ratio of hydrogen in the beam. For  $D_2$   $g_N = 2/3(1/3)$  for even (odd) values of J, while for  $H_2$   $g_N = 1/4(3/4)$  for even (odd) values of J.  $Z(T_n)$  is the partition function,  $k_B$  is the Boltzmann constant, and  $E_{\nu,J}$  is the energy of the rovibrational state characterized by the vibrational ( $\nu$ ) and rotational (J) quantum numbers. In equation 6.10 we take into account the rotational cooling of the  $H_2$  molecules due to the supersonic expansion by taking  $T_{rot} = 0.8 * T_n^{31}$ . Degeneracy averaged reaction probabilities are computed from fully initial-state resolved reaction probabilities as:

$$P_{\text{deg}}(E,\nu,J) = \sum_{m_J=0}^{J} (2 - \delta_{m_J 0}) \frac{P_r(E,\nu,J,m_J)}{2J+1},$$
(6.11)

where  $P_r(E, \nu, J, m_J)$  is the fully initial-state resolved reaction probability, with  $m_J$  being the magnetic rotational quantum number and  $E = \frac{1}{2}mv^2$  being the translational energy. Molecular beam sticking probabilities can then be computed as:

$$S_0(v_0, \alpha, T_N) = \sum_{\nu, J} \int P(v_0, \alpha, \nu, J, T_n) P_{\text{deg}}(E, \nu, J) d\nu.$$
 (6.12)

$$H_2 + Cu(111), D_2 + Ag(111), H_2 + Au(111) \text{ and } D_2 + Pt(111)$$

All parameters describing the molecular beams simulated in this work are listed in table 5.4 of Chapter 5. A more exhaustive description of how molecular beam sticking probabilities can be computed can be found in Ref.<sup>113</sup> The set of initial rovibrational states taken into account in the QCT calculations is listed in table 5.3 of Chapter 5.

#### Rovibrational state populations of H<sub>2</sub> and D<sub>2</sub> desorbing from Au(111)

The following expression is used to calculate state distributions of desorbing molecules:<sup>69</sup>

$$N(\nu, J) = \int_{0}^{E_{\max(\nu, J)}} P_{int}(\nu, J, T_S) \sqrt{E} \, e^{\left(-\frac{E}{k_B T_S}\right)} \, P_{\deg}(E, \nu, J) dE. \tag{6.13}$$

Here  $E_{\rm max}(\nu,J)$  is the maximum kinetic energy to which the experiment was sensitive<sup>69</sup> in the sense that  $P_{\rm deg}(E,\nu,J)$  could still be extracted reliably, and these parameters have been obtained in a private communication<sup>114</sup>.  $T_S$  is the surface temperature. The  $E_{\rm max}(\nu,J)$  parameters for  $H_2$  (D<sub>2</sub>) + Au(111) are plotted in figure 5.B.2 of Chapter 5. While Shuai et al.<sup>69</sup> integrated equation 6.13 up to 5 eV, we opt to integrate only until  $E_{\rm max}(\nu,J)$  since the error function expressions derived in Ref.<sup>69</sup> are only reliable up to  $E_{\rm max}(\nu,J)$  and can yield sticking probabilities substantially bigger than one for high translational energies. We integrate equation 6.13 by taking a right Riemann sum with a  $\Delta E$  of 0.2 meV. The  $N(\nu,J)$  populations are normalized to the total  $\nu=0$  population, as was done in Chapter 5. The ratios of populations we calculate are solely based on the rovibrational states shown in figure 6.12, i.e., we only go up to J=7 for  $H_2$  and J=9 for  $D_2$  as was done by Shuai et al.<sup>69</sup>.

# $E_{1/2}(\nu, J)$ parameters

In Chapter 5 we listed four possible methods to obtain  $E_{1/2}(\nu, J)$  parameters which can be used to compare to experimental  $E_0(\nu, J)$  parameters<sup>15</sup>. In this Chapter we only use method B2 to compare calculated  $E_{1/2}(\nu, J)$  parameters to measured  $E_0(\nu, J)$  parameters for the H<sub>2</sub> (D<sub>2</sub>) + Au(111) system. All four methods are discussed in Chapter 5, and we will only briefly discuss method B2 here.

When no measured sticking probabilities are available for the system of interest one may choose to normalize the extracted reaction probabilities with reference to theory<sup>69,72</sup>. In method B1 theory is compared to experiment by

extracting  $E_{1/2}(\nu, J)$  parameters using:

$$P_{deg}(E_{1/2}(\nu, J), \nu, J) = \frac{1}{2} A_{\nu, J}^{\text{B1}} = \frac{1}{2} P_{deg}(E_{\text{max}}(\nu, J), \nu, J).$$
 (6.14)

In other words, the  $E_{1/2}(\nu, J)$  parameter is the energy at which the degeneracy averaged reaction probability is equal to half the saturation value, which is taken equal to the reaction probability at the maximum kinetic energy to which the experiment was sensitive.

However, for  $H_2$  ( $D_2$ ) + Au(111) the  $E_{\rm max}(\nu,J)$  parameters are not large enough to reliably extract  $E_{1/2}(\nu,J)$  parameters<sup>15</sup>. In method B2 the measured  $E_0(\nu,J)$  and  $W_{\nu,J}$  values are therefore used to determine the  $A_{\nu,J}^{\rm B2}$  value at which the experimental reaction probability saturates according to the error function fit of the  $(\nu,J)$  rovibrational state<sup>15,69</sup>. Effectively, in method B2, we take the  $A_{\nu,J}^{\rm B1}$  value and scale it accordingly<sup>15</sup>:

$$A_{\nu,J}^{B2} = \frac{A_{\nu,J}^{B1}}{\frac{1}{2} + \frac{1}{2}erf\left(\frac{E_{\text{max}}(\nu,J) - E_0(\nu,J)}{W_{\nu,J}}\right)}$$
(6.15)

#### 6.2.6 Computational details

A user modified version 5.4.4 of the Vienna Ab Initio Simulation Package<sup>115–118</sup> (VASP) has been used for all plane wave periodic DFT electronic structure calculations. The modification of the computer package concerns the implementation of the mGGA DFs developed in Chapter 3 and this Chapter. In all calculations the standard projector augmented wave (PAW) potentials<sup>119</sup> are used. We use the rVV10<sup>48</sup> non-local correlation functional as implemented in VASP<sup>38</sup>, which is based on the vdW-DF1<sup>94,120,121</sup> implementation by Klimeš et al.<sup>122</sup>

All calculations are carried out using a plane wave cutoff energy of 600 eV together with smearing of 0.2 eV using the Methfessel-Paxton method of order one. All slabs consist of six layers, of which the bottom two layers are fixed at their ideal bulk interlayer distance. A 2×2 supercell is used for calculations of the PESs with a vacuum distance of 16 Å and a  $(11 \times 11 \times 1)\Gamma$ -centered k-point grid. Lattice constants have been calculated using four atom bulk unit cells and a  $(28 \times 28 \times 28)$  Monckhorst-Pack k-point grid, while slab relaxations were carried out using a  $(32 \times 32 \times 32)\Gamma$ -centered k-point grid together with a  $1\times 1$  supercell. For the molecule-metal surface calculations a convergence parameter of  $10^{-6}$  eV was used, and for the bulk lattice calculations, the slab relaxations

and the metal-atom calculations a convergence parameter of  $10^{-7}$  eV was used for the energy.

#### 6.3 Results and Discussion

#### 6.3.1 Metal properties

Table 6.1 shows the calculated lattice constants compared to zero-point energy corrected experimental results<sup>108</sup> for the three MS mGGA-rVV10 DFs tested in this work as well as the original three MS mGGA DFs. For the four metals investigated here we calculate lattice constants that are smaller than the zero-point energy corrected experimental results, although the agreement with experiment<sup>108</sup> is still reasonable. The underestimation of the experimental lattice constants for the three DFs developed here is, on average, comparable to the somewhat overestimation of the lattice constants for SRP DFs designed for the reaction of  $H_2$  ( $D_2$ ) on transition metals at the GGA level that include non-local correlation<sup>15</sup> (see table 5.5 of Chapter 5).

Table 6.2 shows the interlayer contractions for the top two layers (in %) for Cu(111), Ag(111), Au(111) and Pt(111). When combining our three MS mGGA DFs<sup>25</sup> with rVV10<sup>48</sup> non-local correlation we find that the relaxed six layer slabs tend to expand somewhat, in contrast to the results obtained when not using non-local correlation<sup>15,25</sup>. The description of the relaxed slabs is not as good as obtained with previously developed SRP DFs<sup>15</sup>, and with our mGGA DFs not using non-local correlation<sup>25</sup> (see table 6.2).

The three original MS mGGA DFs of Chapter 3 were developed to avoid having to compromise between a good description of the metal and a good description of the molecule-surface interaction<sup>17</sup>. It is therefore a somewhat disappointing result that when our three mGGA DFs are combined with non-local rVV10 correlation<sup>48</sup> this comes at the cost of a somewhat less good description of the metal. Tuning the b parameter in the implementation of rVV10 non-local correlation<sup>48</sup>, which modulates the repulsive part of the van der Waals description<sup>48</sup>, in order to obtain lattice constants closer to experiment unfortunately has the effect of removing the van der Waals wells in the PESs we calculate.

Including non-local correlation in a DF has a tendency to yield smaller lattice constants compared to DFs that do not include non-local correlation<sup>15,108</sup>. Our original MS mGGA DFs yield calculated lattice constants that are highly accurate<sup>25</sup>. Therefore combining them with non-local correlation, which tends to shrink the lattice constants, leads to too small calculated lattice constants.

|                        | Cı    | 1    | Ag    | g    | Aı    | 1    | P     | t    |
|------------------------|-------|------|-------|------|-------|------|-------|------|
|                        | Å     | %    | Å     | %    | Å     | %    | Å     | %    |
| $\exp^{108}$           | 3.596 |      | 4.062 |      | 4.062 |      | 3.913 |      |
| MS-PBEl <sup>25</sup>  | 3.580 | -0.4 | 4.090 | 0.7  | 4.084 | 0.5  | 3.906 | -0.2 |
| MS-PBEl-rVV10          | 3.514 | -2.2 | 4.003 | -1.4 | 4.034 | -0.7 | 3.879 | -0.9 |
| $MS-B86bl^{25}$        | 3.583 | -0.4 | 4.092 | 0.7  | 4.087 | 0.6  | 3.908 | -0.1 |
| MS-B86bl-rVV10         | 3.518 | -2.2 | 4.004 | -1.4 | 4.036 | -0.6 | 3.881 | -0.8 |
| MS-RPBEl <sup>25</sup> | 3.590 | -0.2 | 4.099 | 0.9  | 4.092 | 0.7  | 3.912 | 0    |
| MS-RPBEl-rVV10         | 3.524 | -2.0 | 4.008 | -1.3 | 4.040 | -0.5 | 3.884 | -0.7 |

Table 6.1: Calculated lattice constants in Å compared to to zero-point energy corrected experimental results<sup>108</sup>. Percentage deviations of the computed results from experimental results are also indicated.

We also observe that the interlayer distance between the top two layers of the relaxed six layer slabs tend to expand somewhat when using rVV10<sup>48</sup> non-local correlation (see table 6.2). When not using non-local correlation our three MS mGGA DFs produced interlayer distances between the top layers that were in line with experimental results 15,25. When using rVV10<sup>48</sup> nonlocal correlation together with our MS mGGA DFs our calculated interlayer distances of the top layer are still reasonable, although not as good as those obtained with GGA based SRP DFs that use vdW-DF1<sup>94</sup> or vdW-DF2<sup>95</sup> nonlocal correlation (see table 5.6 of Chapter 5). We speculate that the more accurate interlayer distances calculated when using  $vdW-DF1^{94}$  or  $vdW-DF2^{95}$ non-local correlation are due to the way in which the correlation part of the full exchange correlation functional is constructed. In the case of vdW-DF1<sup>94</sup> or vdW-DF2<sup>95</sup> the non-local correlation part is combined only with fully local LDA correlation. In the case of the MS mGGA-rVV10 functionals that we test here, the NLC rVV10 functional is combined with semi-local correlation instead (see Eq. 6.4 above). For calculating lattice constants and interlayer spacings of metals it might be better to combine the MS meta-GGA exchange functionals we investigate with correlation functionals based on LDA correlation and a non-local van der Waals correlation functional.

# 6.3.2 Static PES properties

Figure 6.5 shows van der Waals wells for  $H_2$  in a parallel ( $\phi = 0^{\circ}, \theta = 90^{\circ}$ ) and in the perpendicular ( $\theta = 0^{\circ}$ ) orientation above a top site for Cu(111) (a), Ag(111) (b), Au(111) (c) and Pt(111) (d). All van der Waals well geometries and well depths computed by us are tabulated in table 6.3, also comparing with experimental results that have been reported for  $H_2 + \text{Cu}(111)^{89,90}$ ,  $H_2 + \text{Ag}(111)^{84}$ ,  $H_2 + \text{Au}(111)^{90}$  and  $H_2 + \text{Pt}(111)^{81,93}$ . Note that we use the same b value (b = 6.3) for the three DFs that use rVV10<sup>48</sup> non-local correlation.

2.4%

3.5%

2.4%

MS-RPBEl-rVV10

|                        | Cu                          | Ag                            | Au            | Pt            |
|------------------------|-----------------------------|-------------------------------|---------------|---------------|
| exp.                   | $-1.0\%,^{123,124}, -0.7\%$ | $-2.5\%,^{126},^{126},^{127}$ | $1.5\%^{128}$ | $1.1\%^{129}$ |
| MS-PBEl <sup>25</sup>  | -1.0%                       | -0.4%                         | 1.0%          | 1.0%          |
| MS-PBEl-rVV10          | 1.5%                        | 2.3%                          | 3.5%          | 2.4%          |
| $MS-B86bl^{25}$        | -1.0%                       | -0.5%                         | 1.0%          | 1.0%          |
| MS-B86bl-rVV10         | 1.4%                        | 1.4%                          | 3.5%          | 2.3%          |
| MS-RPBEl <sup>25</sup> | -1.6%                       | -0.5%                         | 1.2%          | 1.1%          |

Table 6.2: Relaxations of the interlayer distance of the top two layers relative to the the bulk interlayer distance in %. Computed results are shown for six DFs and compared with experimental values.

1.6%

As noted in Chapter 5, for Cu(111) the experimental well depths are in good agreement. However, the position reported by Harten et al.<sup>90</sup> is somewhat closer to the surface. Ambiguities in the level assignments in the study of Andersson et al.<sup>88</sup> is the mostly likely reason for the van der Waals well being reported somewhat closer to the surface compared to the later measurements<sup>89</sup>. Andersson et al.<sup>89</sup> noted that their derived PES is also consistent with the earlier measurements<sup>88</sup>. As mentioned in Chapter 5, we suspect that reported van der Waals wells for  $H_2 + Ag(111)^{84}$  and  $H_2 + Au(111)^{90}$  might possibly be too close to the surface<sup>88</sup>.

The MS-PBEl-rVV10 DF performs best with respect to the van der Waals well interaction for all systems investigated. Highly accurate van der Waals well depths are obtained for both the highly activated systems and the non-activated  $\rm H_2 + Pt(111)$  system with this functional (see figure 6.5 and table 6.3). The agreement with the position of the minimum is also good for the system for which this is well-known, i.e.,  $\rm H_2 + Cu(111)$ . The agreement with the experimental well depth obtained with the MS-B86bl-rVV10 and MS-RPBEl-rVV10 DFs is reasonable. This agreement is not as good as obtained with the MS-PBEl-rVV10 DF, but the MS-RPBEl-rVV10 results agree better with the experimental results for the well depths for  $\rm H_2 + Ag(111)$  and  $\rm Au(111)$  than the results previously obtained with the vdW-DF1 functional (see table 6.3 and figures 6.5b and 6.5c). As discussed above, optimization of the b parameter to better reproduce the well depth obtained with the MS-B86bl-rVV10 and MS-RPBEl-rVV10 DFs would result in unacceptably small lattice constants.

When comparing the results it is clear that the MS-PBEl-rVV10 DF yields a better description of the H<sub>2</sub>-metal van der Waals wells investigated here than the vdW-DF1<sup>94</sup> and vdW-DF2<sup>95</sup> DFs, which is consistent with earlier work<sup>48</sup> on the binding energies of a subset of molecular configurations of the S22 data set<sup>105</sup> and the argon dimer<sup>48</sup>. However, we note that the previously

tested<sup>15</sup> B86SRP68-DF2 DF (which performed best of the vdW-DF1<sup>94</sup> and vdW-DF2<sup>95</sup> DFs tested in 5) shows a performance that is comparable to that of the MS-PBEl-rVV10 DF (table 6.3). We also note that the polarizability obtained for the H<sub>2</sub> molecule parallel and perpendicular to its molecular axis is similar for the MS-PBEl-rVV10 and vdW-DF2<sup>95</sup> DFs.

In principle the b parameter in the rVV10<sup>48</sup> non-local correlation functional could be tuned to match experimental observations of the van der Waals geometries in future work. However, decreasing the b parameter to obtain a van der Waals well geometry more in line with experiment would also lead to further decreased lattice constants thereby further worsening the agreement with experiment, and it would lead to lower dissociation barriers.

Tables 6.4-6.7 show barrier heights and geometries for  $H_2 + Cu(111)$ , Ag(111), Au(111) and Pt(111), respectively. For the activated systems the lateness of the barriers (values of r at which the barriers occur) is not influenced by the use of  $rVV10^{48}$  non-local correlation. However, for the bridge sites the barrier geometries do move to slightly higher Z values. Adding  $rVV10^{48}$  non-local correlation to our original three MS mGGA DFs yields barrier heights that are consistently lower by roughly 0.15-0.2 eV for the highly activated systems. For the barrier heights obtained with the current best SRP-DFs we refer the reader to Chapter 5.

For the non-activated  $\rm H_2 + Pt(111)$  system we also find that using rVV10<sup>48</sup> non-local correlation leads to lower barriers, by about 0.15 eV. However the picture is more complex since only three DFs show a double barrier structure for the t2b site, namely the MS-PBEl<sup>25</sup>, MS-B86bl<sup>25</sup> and MS-PBEl-rVV10 DFs. The DFs without non-local correlation do not show a double barrier structure for the t2h site, while the DFs that do use rVV10<sup>48</sup> non-local correlation do.

Note that observations on the van der Waals well depths and minimum positions extracted from RMSA<sup>80</sup> or CMSA<sup>91,92</sup> experiments usually represent averages taken over the sites in the surface unit cell. Checking for the site-dependence of the van der Waals interaction in  $H_2 + Cu(111)$ , as found by Lee et al.<sup>130</sup>, we see essentially no dependence of the van der Waals interaction on the site within the unit cell (see figure 6.6, which presents results for impact on three different sites obtained with the MS-PBEl-rVV10 DF). The site dependence found for the other systems and DFs treated here is similar to the results shown in figure 6.6 in that it is very small.

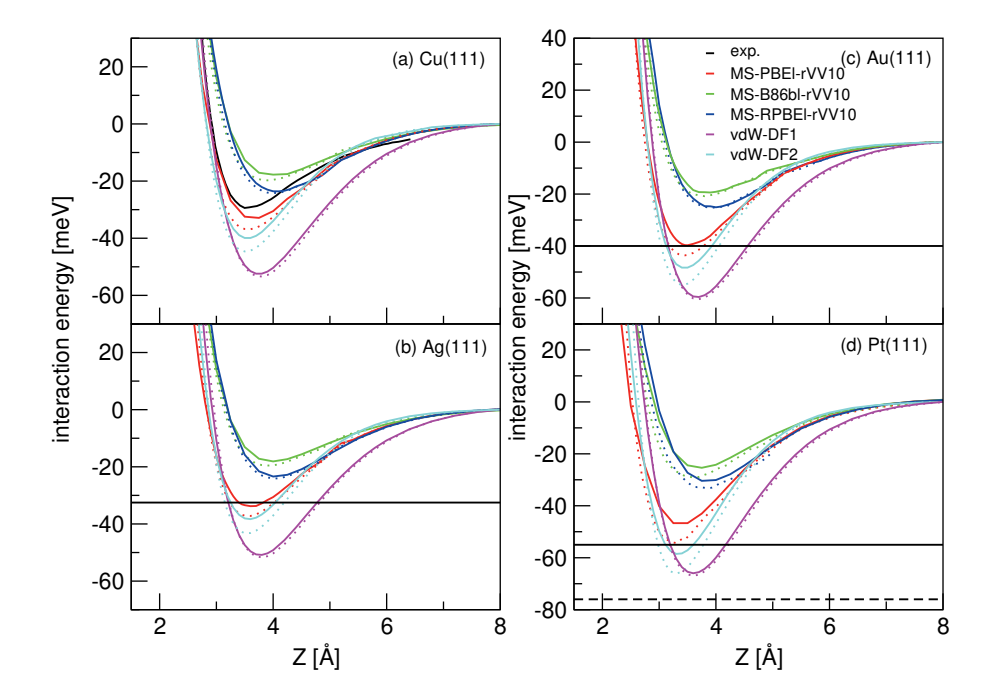


FIGURE 6.5: Van der Waals potential curves for  $H_2 + Cu(111)$  (a), Ag(111) (b), Au(111) (c) and Pt(111) (d). Solid lines represent a parallel orientation of  $H_2$  ( $\theta = 90^{\circ}$ ,  $\phi = 0^{\circ}$ ) and dotted lines a perpendicular orientation ( $\theta = 0^{\circ}$ ), both above a top site. Experimental results are shown in black for  $H_2 + Cu(111)^{89}$ ,  $H_2 + Ag(111)^{84}$ ,  $H_2 + Au(111)^{90}$  and  $H_2 + Pt(111)^{81,93}$ . In panels b and c the horizontal solid lines correspond to the experimental well depths. In panel d the dashed line corresponds to the result of Poelsema et al.<sup>93</sup> and the solid line corresponds to the result of Cowin et al.<sup>81</sup>. Results for five DFs are shown: MS-PBEl-rVV10 (red), MS-B86bl-rVV10 (green), MS-RPBEl-rVV10 (blue), vdW-DF1<sup>94</sup> (magenta) and vdW-DF2<sup>95</sup> (light blue).

| Cu(111)               | Z [Å]                  | $E_{vdW}$ [meV]        |
|-----------------------|------------------------|------------------------|
| exp.                  | $3.51^{89}, 2.71^{90}$ | $29.5^{89}, 22.2^{90}$ |
| MS-PBEl-rVV10         | 3.66                   | 33.1                   |
| MS-B86bl-rVV10        | 3.99                   | 18.2                   |
| MS-RPBEl-rVV10        | 4.05                   | 23.7                   |
| $vdW-DF1^{94}$        | 3.77                   | 52.4                   |
| $vdW-DF2^{95}$        | 3.58                   | 39.0                   |
| Ag(111)               |                        |                        |
| exp. <sup>84</sup>    | 1.98                   | 32.5                   |
| MS-PBEl-rVV10         | 3.66                   | 33.8                   |
| MS-B86bl-rVV10        | 4.02                   | 18.4                   |
| MS-RPBEl-rVV10        | 4.04                   | 23.4                   |
| $vdW-DF1^{94}$        | 3.77                   | 50.8                   |
| $vdW-DF2^{95}$        | 3.58                   | 38.3                   |
| Au(111)               |                        |                        |
| exp. <sup>90</sup>    | 2.2                    | 40.0                   |
| MS-PBEl-rVV10         | 3.48                   | 39.7                   |
| MS-B86bl-rVV10        | 3.90                   | 19.4                   |
| MS-RPBEl-rVV10        | 4.04                   | 25.2                   |
| $vdW-DF1^{94}$        | 3.68                   | 59.7                   |
| $vdW-DF2^{95}$        | 3.45                   | 48.5                   |
| Pt(111)               |                        |                        |
| exp.                  |                        | $55^{81}, 76^{93}$     |
| MS-PBEl-rVV10         | 3.35                   | 50.5                   |
| MS-B86bl-rVV10        | 3.30                   | 26.9                   |
| MS-RPBEl-rVV10        | 3.88                   | 32.3                   |
| $vdW-DF1^{94}$        | 3.61                   | 65.9                   |
| vdW-DF2 <sup>95</sup> | 3.36                   | 58.6                   |

Table 6.3: Van der Waals well depths and positions for Cu(111), Ag(111), Au(111) and Pt(111) for  $H_2$  in parallel orientation ( $\phi = 0^{\circ}, \theta = 90^{\circ}$ ) above a top site.

|                        |       | bridge         |       |       | t2b   |       |       | fcc            |       |
|------------------------|-------|----------------|-------|-------|-------|-------|-------|----------------|-------|
|                        | $E_b$ | $\mathbf{r}_b$ | $Z_b$ | $E_b$ | $r_b$ | $Z_b$ | $E_b$ | $\mathbf{r}_b$ | $Z_b$ |
| MS-PBEl <sup>25</sup>  | 0.629 | 1.002          | 1.198 | 0.847 | 1.350 | 1.390 | 0.988 | 1.339          | 1.267 |
| MS-PBEl-rVV10          | 0.459 | 0.985          | 1.240 | 0.665 | 1.328 | 1.400 | 0.815 | 1.331          | 1.285 |
| MS-B86bl <sup>25</sup> | 0.683 | 0.997          | 1.205 | 0.895 | 1.351 | 1.391 | 1.048 | 1.343          | 1.267 |
| MS-B86bl-rVV10         | 0.513 | 0.982          | 1.247 | 0.714 | 1.329 | 1.401 | 0.865 | 1.333          | 1.285 |
| MS-RPBEl <sup>25</sup> | 0.721 | 1.006          | 1.201 | 0.930 | 1.354 | 1.392 | 1.086 | 1.346          | 1.270 |
| MS-RPBEl-rVV10         | 0.549 | 0.985          | 1.247 | 0.747 | 1.329 | 1.403 | 0.899 | 1.334          | 1.286 |

TABLE 6.4: Barrier height for  $H_2$  reacting on Cu(111), for the bridge, t2b and fcc sites  $\phi = 0^{\circ}$  and  $\theta = 90^{\circ}$ . Barrier heights are in eV, and the barrier positions in Å.

|                        |       | bridge |       |       | t2b   |       |       | fcc   |       |
|------------------------|-------|--------|-------|-------|-------|-------|-------|-------|-------|
|                        | $E_b$ | $r_b$  | $Z_b$ | $E_b$ | $r_b$ | $Z_b$ | $E_b$ | $r_b$ | $Z_b$ |
| MS-PBEl <sup>25</sup>  | 1.288 | 1.230  | 1.116 | 1.534 | 1.508 | 1.493 | 1.601 | 1.556 | 1.315 |
| MS-PBEl-rVV10          | 1.082 | 1.224  | 1.157 | 1.328 | 1.486 | 1.506 | 1.392 | 1.553 | 1.345 |
| MS-B86bl <sup>25</sup> | 1.342 | 1.224  | 1.115 | 1.585 | 1.513 | 1.495 | 1.652 | 1.566 | 1.323 |
| MS-B86bl-rVV10         | 1.134 | 1.223  | 1.159 | 1.376 | 1.488 | 1.507 | 1.442 | 1.560 | 1.348 |
| MS-RPBEl-rVV10         | 1.171 | 1.226  | 1.161 | 1.410 | 1.489 | 1.508 | 1.479 | 1.560 | 1.349 |

TABLE 6.5: Barrier height for  $H_2$  reacting on Ag(111), for the bridge, t2b and fcc sites  $\phi = 0^{\circ}$  and  $\theta = 90^{\circ}$ . Barrier heights are in eV, and the barrier positions in Å.

|                        |       | bridge         |       |       | t2b            |       |       | fcc            |       |
|------------------------|-------|----------------|-------|-------|----------------|-------|-------|----------------|-------|
|                        | $E_b$ | $\mathbf{r}_b$ | $Z_b$ | $E_b$ | $\mathbf{r}_b$ | $Z_b$ | $E_b$ | $\mathbf{r}_b$ | $Z_b$ |
| MS-PBEl <sup>25</sup>  | 1.432 | 1.144          | 1.127 | 1.301 | 1.433          | 1.466 | 1.350 | 1.203          | 1.276 |
| MS-PBEl-rVV10          | 1.251 | 1.148          | 1.159 | 1.139 | 1.425          | 1.475 | 1.172 | 1.216          | 1.299 |
| MS-B86bl <sup>25</sup> | 1.481 | 1.142          | 1.130 | 1.355 | 1.438          | 1.467 | 1.402 | 1.204          | 1.276 |
| MS-B86bl-rVV10         | 1.302 | 1.147          | 1.162 | 1.192 | 1.427          | 1.476 | 1.224 | 1.216          | 1.299 |
| MS-RPBEl-rVV10         | 1.336 | 1.147          | 1.163 | 1.226 | 1.436          | 1.476 | 1.258 | 1.219          | 1.302 |

Table 6.6: Barrier height for  $H_2$  reacting on Au(111), for the bridge, t2b and fcc sites  $\phi = 0^{\circ}$  and  $\theta = 90^{\circ}$ . Barrier heights are in eV, and the barrier positions in Å.

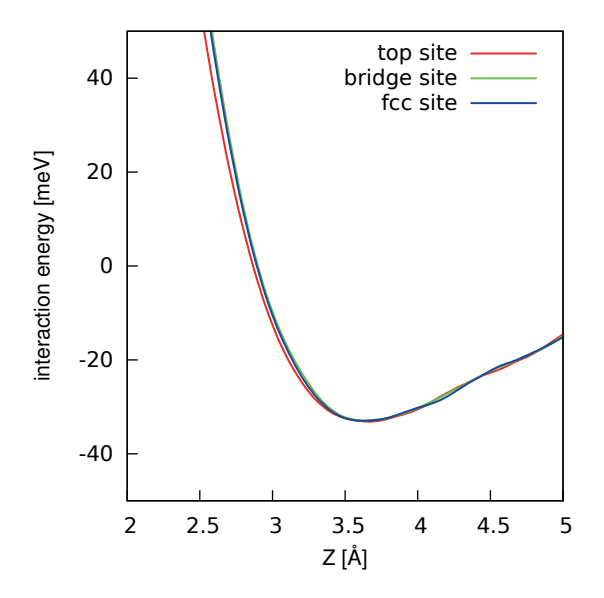


FIGURE 6.6: Van der Waals potential curves for  $H_2$  ( $\theta = 90^{\circ}$ ,  $\phi = 0^{\circ}$ ) above Cu(111) for impact on the top, bridge and fcc sites for the MS-PBEl-rVV10 density functional.

|                 |                | t2b early |       |                | t2b late         |                  |                | bridge |       | -              | 2h early |       |                | t2h late |       |
|-----------------|----------------|-----------|-------|----------------|------------------|------------------|----------------|--------|-------|----------------|----------|-------|----------------|----------|-------|
|                 | $\mathbf{E}_b$ | $r_b$     | $Z_b$ | $\mathbb{E}_b$ | $\mathbf{r}_{b}$ | $\mathbf{Z}_{b}$ | $\mathbf{E}_b$ | $r_b$  | $Z_b$ | $\mathbb{E}_b$ | $r_b$    | $Z_b$ | $\mathbb{E}_b$ | $r_b$    | $Z_b$ |
| $MS-PBE1^{25}$  | 0.145          | 992.0     | 2.205 | -0.035         | 1.096            | 1.529            | 0.616          | 0.838  | 1.599 | 0.339          | 0.800    | 1.840 |                |          |       |
| MS-PBEl-rVV10   | 0.008          | 0.763     | 2.326 | -0.211         | 1.087            | 1.538            | 0.445          | 0.837  | 1.634 | 0.180          | 0.828    | 1.809 | 0.217          | 1.195    | 1.525 |
| $MS-B86bl^{25}$ | 0.194          | 894.0     | 2.189 | 0.016          | 1.085            | 1.534            | 0.667          | 0.839  | 1.602 | 0.392          | 0.802    | 1.836 |                |          |       |
| MS-B86bl-rVV10  | 0.056          | 0.763     | 2.313 |                |                  |                  | 0.493          | 0.836  | 1.633 | 0.235          | 0.820    | 1.846 | 0.263          | 1.205    | 1.525 |
| MS-RPBEl-rVV10  | 0.071          | 694.0     | 2.230 |                |                  |                  | 0.521          | 0.841  | 1.624 | 0.261          | 0.830    | 1.805 | 0.319          | 1.211    | 1.526 |
|                 |                |           |       |                |                  |                  |                |        |       |                |          |       |                |          |       |

 $\phi=0^\circ$  and  $\theta=90^\circ$ , and for the t2h site  $\phi=120^\circ$ . Barrier heights are in eV, and the barrier positions in Å. For the t2b and t2h geometry data is presented for the early Table 6.7: Barrier heights for H<sub>2</sub> reacting on Pt(111), for the bridge and t2b sites and the late geometry when relevant.

### 6.3.3 Molecular beam sticking

#### Molecular beam sticking of $H_2$ ( $D_2$ ) + Cu(111)

Molecular beam sticking probabilities for  $H_2$  ( $D_2$ ) + Cu(111) for six sets of molecular beam experiments are shown in figure 6.7 for the three MS mGGA-rVV10 DFs tested in this work and for the MS-B86bl and PBE DFs<sup>25</sup>. The parameters describing the molecular beam experiments<sup>29–31</sup> are tabulated in table 5.4 of Chapter 5. Adding rVV10<sup>48</sup> non-local correlation to our three original mGGA DFs leads to higher sticking probabilities that are too high compared to experiment, as could be expected from its effect on the barrier heights (see table 6.4). MS-PBEl-rVV10, MS-B86bl-rVV10 and MS-RPBEl-rVV10 all overestimate the sticking probability and are not chemically accurate for this system. Given that the original three MS mGGA DFs were all chemically accurate for this system<sup>25</sup> this is a somewhat disappointing result.

#### Molecular beam sticking of $D_2 + Ag(111)$

Figure 6.8 shows sticking probabilities computed from simulations of molecular beams of  $D_2$  reacting on Ag(111) in comparison with experimental results<sup>32</sup>. Cottrell et al.<sup>32</sup> have reported molecular beam parameters that are symmetric with respect to the average collision energy. We consider these symmetric molecular beam parameters to be somewhat unphysical, as discussed in previous work from our group<sup>64</sup>. Therefore we opted to use the molecular beam parameters of pure  $D_2$  reacting on Cu(111) reported by Auerbach and coworkers<sup>29</sup> (see table 5.4), which likewise describe beams that are narrow in translational energy, in our simulations.

MAD values are computed by calculating the mean distance along the incidence energy axis from the calculated sticking probability to the cubic spline interpolated experimental results. We consider DFs that yield a MAD value smaller than 1 kcal/mol (4.2 kJ/mol) to be chemically accurate <sup>131</sup>. Figure 6.8 shows that all three DFs can be considered chemically accurate for this system, with the MS-PBEl-rVV10 DF performing best with a MAD of 1.0 kJ/mol and the MS-RPBE-rVV10 DF performing worst with a still good MAD value of 2.0 kJ/mol. Here we note that the distance between the computed and the measured  $S_0$  tends to increase with increasing translational energy.

This is the first time that we achieve a chemically accurate description of the  $D_2 + Ag(111)$  system. GGA based DFs with and without non-local correlation as well as the three original MS mGGA DFs have not been able to yield a chemically accurate description of this system <sup>15,25,64</sup>. The improved description of the sticking probability for this system is strictly due to the lowering of the

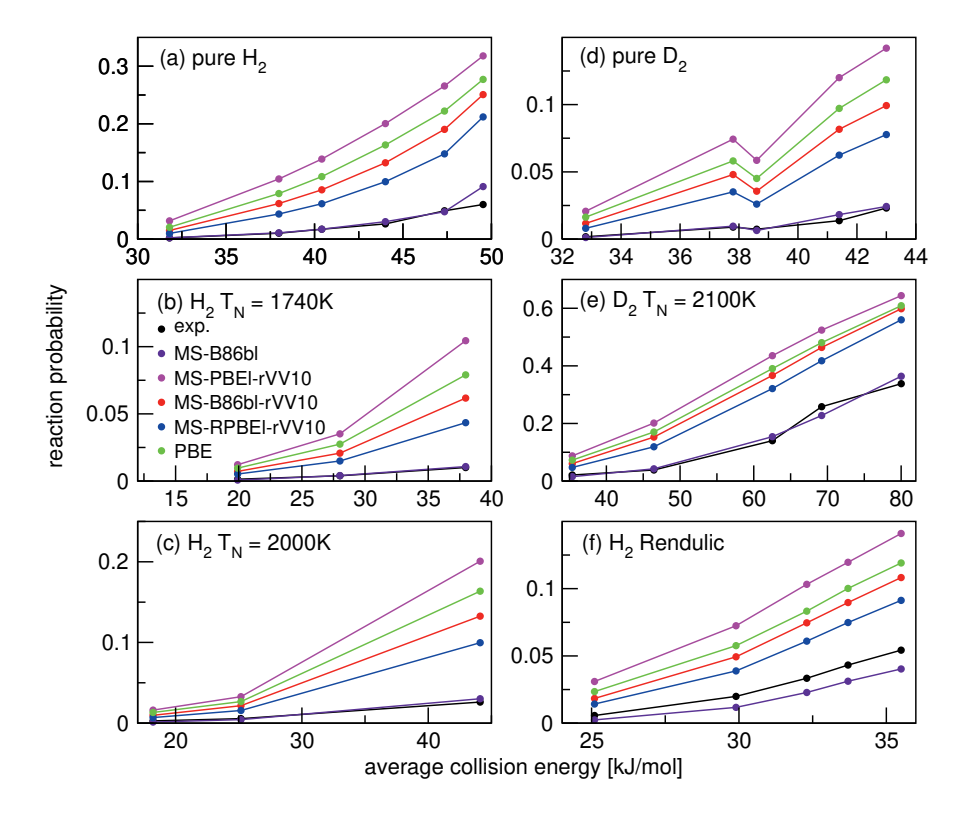


FIGURE 6.7: Molecular beam sticking probabilities for  $H_2$  and  $D_2$  reacting on Cu(111) for six sets of molecular beam experiments, as computed using the QCT method with the MS-B86bl<sup>25</sup> (purple), MS-PBEl-rVV10 (magenta), MS-B86bl-rVV10 (red), MS-RPBEl-rVV10 (blue) and PBE (green) DFs. Experimental results are shown in black<sup>29-31</sup>.

barrier to reaction. Barrier geometries of the MS mGGA DFs that use non-local  $\rm rVV10^{48}$  correlation are very similar to the barrier geometries of the original MS mGGA DFs (see table 6.5).

As we discussed in previous work from our group<sup>15,64</sup> and Chapter 5, assessing the the quality of the theoretical description of this system is difficult due to the lack of well defined molecular beam parameters<sup>64</sup>. Additional experiments would allow us to improve the description of this system<sup>15</sup>.

### Molecular beam sticking of $D_2 + Pt(111)$

Figure 6.9 shows calculations on  $D_2 + Pt(111)$  for two sets of molecular beam experiments<sup>66,67</sup>. Note that this is a non-activated system of which the original MS mGGA DFs gave a rather poor description<sup>15</sup> (see Chapter 5). Here we find that the MS-B86bl-rVV10 DF (figures 6.9b,e) yields the best results for both experiments, with a MAD of 2.7 kJ/mol for the experiment of Luntz et al.<sup>66</sup> and a MAD of 2.0 kJ/mol for the experiments of Cao et al.<sup>67</sup>. This may be compared to the MAD values of 1.1 kJ/mol for the experiment of Luntz et al.<sup>66</sup> and of 1.9 kJ/mol for the experiment of Cao et al.<sup>67</sup> that were obtained with the PBE $\alpha$ 57-DF2 DF<sup>14</sup>.

In general the three MS mGGA-rVV10 DFs treated here are either in good agreement with experiment for the lower translational energies (MS-PBEl-rVV10) or for the higher translational energies (MS-B86bl-rVV10 and MS-RPBE-rVV10). The reason for this is that the MS-PBEl-rVV10 DF is the DF yielding the lowest early t2b barrier to reaction (see table 6.7), which allows it to describe the experiment correctly at the lowest translational energies. The other two mGGA-rVV10 DFs exhibit a higher early t2b barrier, leading to a worse description of the experiments 66,67 at low translational energies. Overal the slope of the calculated sticking probability curve of the MS-PBEl-rVV10 DF is too steep, just right for the MS-B86bl-rVV10 DF, and somewhat too gentle for the MS-RPBEl-rVV10 DF.

Previous work from our group has indicated that the experiments of Luntz et al.<sup>66</sup> and Cao et al.<sup>67</sup> are in good agreement with each other for the lower incidence energies but somewhat diverge for the higher incidence energies<sup>132</sup>. The possible causes for this divergence are discussed in Ref.<sup>132</sup>, where it was remarked that at high incidence energies the reaction probabilities of Cao et al.<sup>67</sup> are most likely somewhat underestimated compared to the results of Luntz et al.<sup>66</sup>. Note that a small increase of reactivity at the higher translational energies for the experiments of Cao et al.<sup>67</sup> could improve the agreement with experiment for the MS-B86bl-rVV10 DF. However, this system is still best

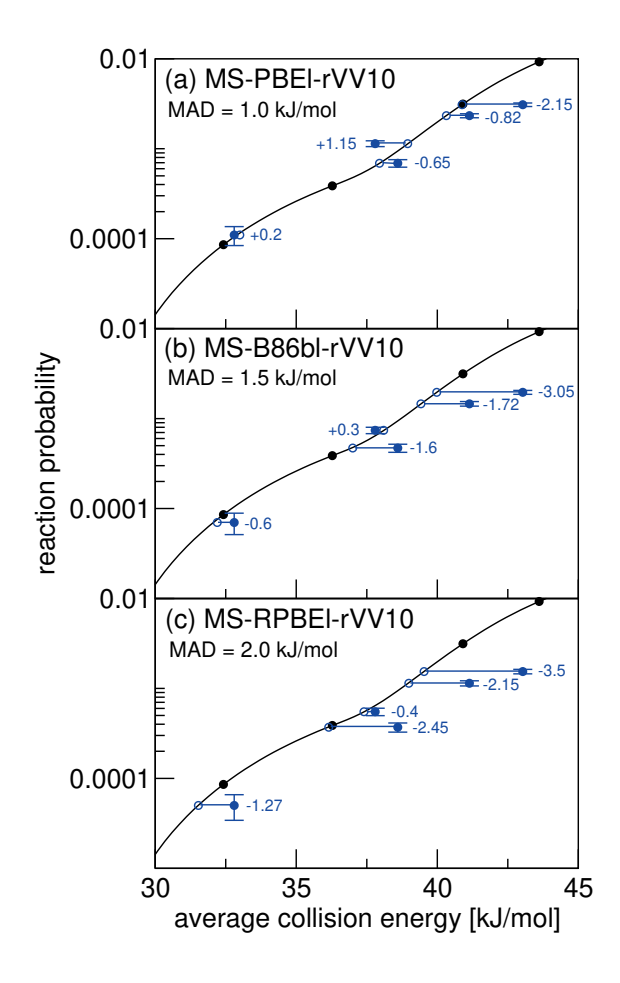
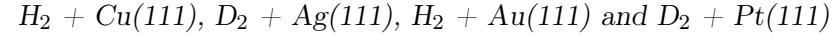


FIGURE 6.8: Molecular beam sticking probability as a function of the average incidence energy for  $D_2$  reacting on Ag(111). Experiment is shown in black<sup>32</sup>. QCT results are shown in blue for the following DFs: MS-PBEl-rVV10 (a), MS-B86bl-rVV10 (b) and MS-RPBEl-rVV10 (c). The values next to each data point denote the shift along the translational energy axis from the computed reaction probability to the interpolated experimental reaction probability curve in kJ/mol.



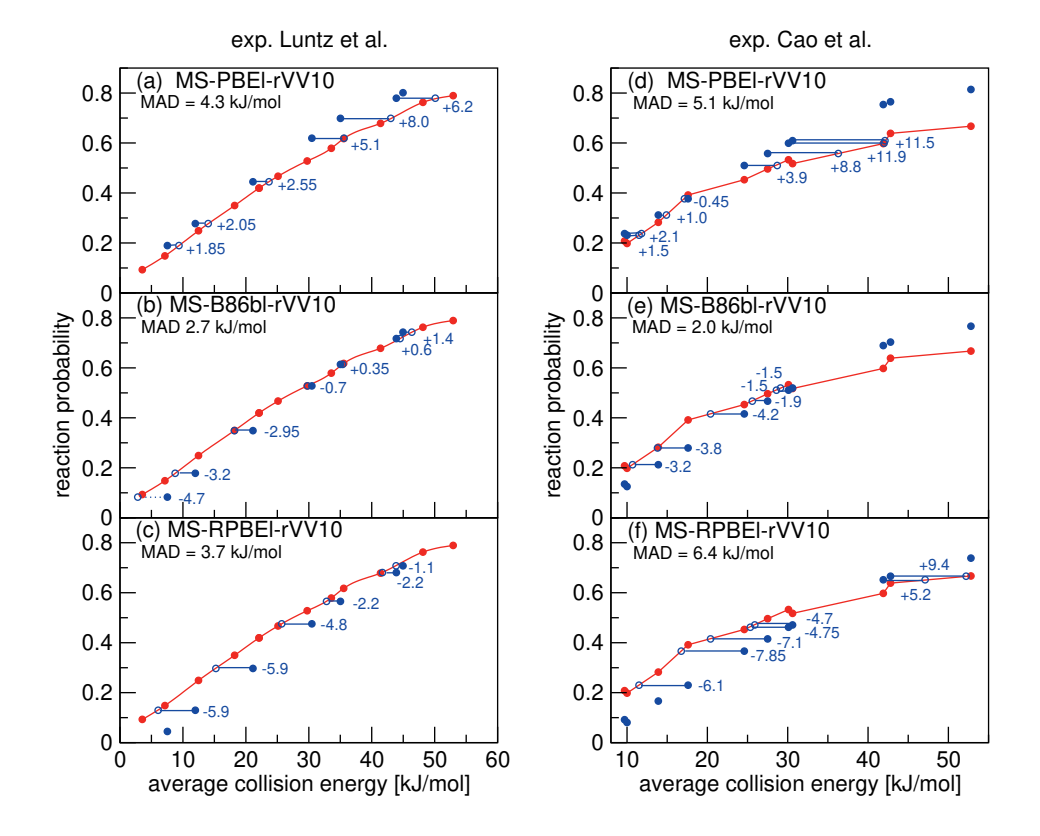


FIGURE 6.9: Molecular beam sticking probabilities for  $D_2$  reacting on Pt(111) for the MS-PBEl-rVV10 (a,d), MS-B86bl-rVV10 (b,e) and MS-RPBEl-rVV10 (c,f) DFs. Experimental results are shown in red<sup>66,67</sup>, QCT results in blue. The values next to each data point denote the shift along the translational energy axis from the computed reaction probability to the interpolated experimental reaction probability, curves in kJ/mol.

described with the GGA based SRP DF that was specifically designed for this system  $^{14,132}$ .

# 6.3.4 Associative desorption

# 3.4.1 Initial-state resolved reaction probabilities Ag(111)

Figure 6.10 shows degeneracy averaged initial-state resolved reaction probabilities for  $H_2$  and  $D_2$  reacting on Ag(111). A comparison is made to reaction probabilities extracted from associative desorption experiments assuming detailed balance<sup>70,71</sup>. Note that the experimental degeneracy averaged reaction

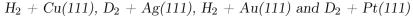
probabilities were not normalized but simply assumed to saturate at one, which makes it hard to make a comparison with experiment. The translational energy in figure 6.10 refers to the translational energy of the desorbing molecules which is measured by time-of-flight techniques<sup>70,71</sup>.

From figure 6.10 it can be seen that the three MS mGGA-rVV10 DFs somewhat overestimate the degeneracy averaged reaction probabilities for D<sub>2</sub> for most energies (figure 6.10a,b), but that the agreement with experiment is very good for H<sub>2</sub> (figure 6.10c). In previous work<sup>25</sup> the MS-PBEl DF was shown to perform better than other GGA based DFs mainly due to MS-PBEl exhibiting slightly earlier barriers. The barrier geometries of the three MS mGGA-rVV10 DFs we present here are very similar to the barrier geometries of the three original MS mGGA DFs<sup>25</sup>. Therefore we can say safely that the increased reactivity obtained with the mGGA-rVV10 DFs developed here is due to their barriers to reaction being somewhat lower and not to a change in barrier geometry (see table 6.5).

#### $E_{1/2}(\nu, J)$ parameters Au(111)

Figure 6.11 shows a comparison of measured<sup>69</sup>  $E_0(\nu, J)$  parameters to  $E_{1/2}(\nu, J)$  parameters calculated using method B2<sup>15</sup>. Table 6.8 shows the accompanying MAD and mean signed deviations (MSD) values. We note that the experiment was performed at a surface temperature of 1063 K<sup>69</sup>, while the calculations have been performed using the BOSS model. Furthermore, incorporating surface motion in the dynamics calculations would lead to a broadening of the reaction probability curves<sup>22,51,52,55</sup>. In view of the procedure used to calculate  $E_{1/2}(\nu, J)$  parameters, an increase of reactivity at low translational energies has the potential to lower the  $E_{1/2}(\nu, J)$  parameters<sup>15</sup>. We also note that our calculations have been carried out employing an unreconstructed Au(111) surface. Mapping out a full PES of H<sub>2</sub> interacting with reconstructed Au(111) is currently extremely hard to do if not impossible, due to the large unit cell size<sup>15</sup>. Earlier work in our group<sup>133</sup> has shown that dynamical barrier heights of reconstructed Au(111) are roughly 50 meV higher compared to unreconstructed Au(111), which would lead to slightly higher computed  $E_{1/2}(\nu, J)$  parameters<sup>15</sup>.

Even though all three developed MS mGGA DFs overestimate the measured  $E_0(\nu, J)$  parameters, it is clear from table 6.8 that MS-PBEl-rVV10 achieves chemical accuracy here for H<sub>2</sub>, and is just 1 meV shy of chemical accuracy (43 meV) for D<sub>2</sub>. The MAD values of all three newly developed DFs are similar to the MAD values of PBE (46 meV for H<sub>2</sub> and 58 meV for D<sub>2</sub>)<sup>15</sup>. Previously we have found that the original mGGA DFs as well as various GGA based SRP DFs that include non-local correlation overestimate the experimental  $E_0(\nu, J)$ 



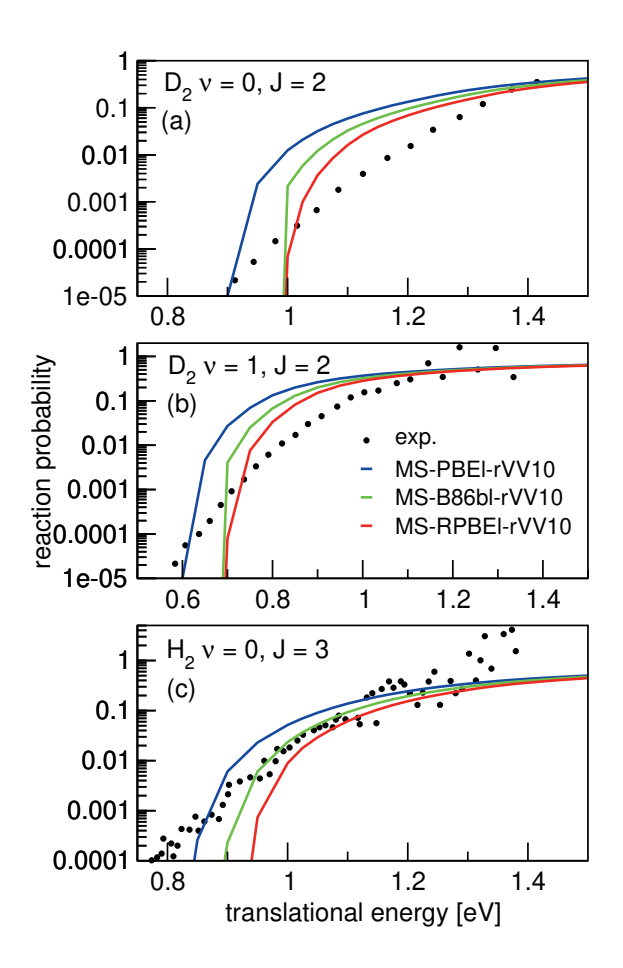


FIGURE 6.10: Initial-state selected reaction probabilities  $P_{deg}(E, \nu, J)$  computed for H<sub>2</sub> (D<sub>2</sub>) + Ag(111) using the MS-PBEl-rVV10 (blue), MS-B86bl-rVV10 (green) and MS-RPBEl-rVV10 (red) DFs as a function of translational energy are shown, comparing with values extracted from associative desorption experiments<sup>70,71</sup>. Results are shown for D<sub>2</sub> ( $\nu = 0, J = 2$ ) (a), D<sub>2</sub> ( $\nu = 1, J = 2$ ) (b), and H<sub>2</sub> ( $\nu = 0, J = 3$ ) (c).

parameters by roughly 0.1 eV<sup>15</sup> (see figure 5.17 of Chapter 5). Furthermore, all three developed mGGA DFs reproduce the J dependence of the  $E_0(\nu, J)$  parameters quite well. As discussed in Chapter 5, this suggests that the reactivities of the individual rovibrational states are well described relative to one another, as long as states are considered within the same vibrational level. Given the uncertainties involved in using method B2 to calculate  $E_{1/2}(\nu, J)$  parameters, we obtain excellent results using our three newly developed MS mGGA-rVV10 DFs.

Previously reported experiments implied that the recombination of H<sub>2</sub> on Au(111) is coupled to the electronic degrees of freedom of the metal<sup>134–137</sup>. Currently we cannot disentangle the effects of ehp excitation, surface motion and surface reconstruction. In Chapter 5 we discussed how a combined analysis of a molecular beam dissociative chemisorption experiment on a reasonably cold surface (if available) and calculations on a reconstructed Au(111) surface, together with the associative desorption experiment of Shuai et al.<sup>69</sup> could in principle be used to obtain a fingerprint of ehp excitation. Additionally, if a molecular beam dissociative chemisorption experiment were to become available, this would allow us to assess if the absolute reactivity computed with the new mGGA-rVV10 DFs and shown here is accurate<sup>15</sup>.

#### Rovibrational state populations of $H_2$ and $D_2$ desorbing from Au(111)

Rovibrational state populations for  $H_2$  and  $D_2$  desorbing from Au(111) are shown in figure 6.12. Here we plot  $ln[N/g_N(2J+1)]$  versus the rotational energy, with N being the total population for each  $(\nu, J)$  state and  $g_N(2J+1)$  being the statistical weight for rotational level  $J^{69}$ . In such a plot a Boltzmann distribution will appear as a straight line<sup>69</sup>. Shuai et al.<sup>69</sup> have used an upper integration limit of 5 eV. Since the error function fits of the experiment are only reliable below  $E_{\text{max}}(\nu, J)$ , we opt to use  $E_{\text{max}}(\nu, J)$  as the upper integration limit, as we did in Chapter 5. Note that we use the same normalization procedure as in Chapter 5. The solid line represents a Boltzman distribution at the surface temperature of 1063 K used in the experiment<sup>69</sup>.

For molecules in the vibrational ground state it can be seen that the rotationally excited molecules lie above the line set by the Boltzmann distributions. The experimental results lie on a gentler slope then the Boltzmann distributions, indicating that rotationally excited molecules are more likely to adsorb<sup>69</sup>. Similarly, the results for vibrationally excited molecules lie on a line with a gentler slope than shown by the Boltzmann distributions. Additionally the results for vibrationally excited molecules lie substantially above the line of Boltzmann

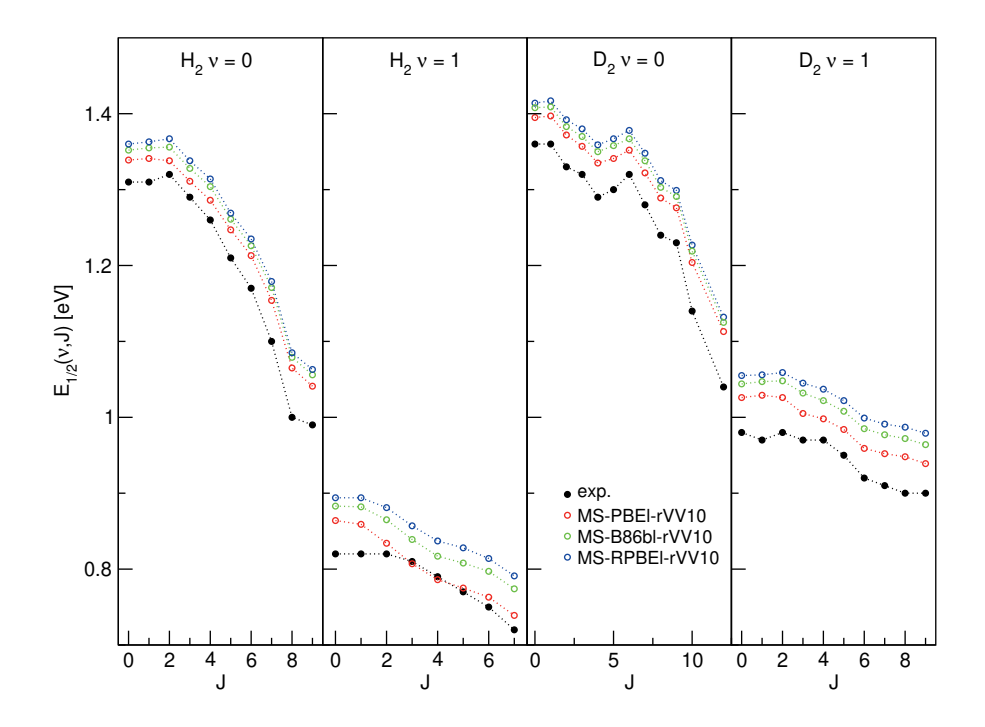


FIGURE 6.11:  $E_{1/2}(\nu,J)$  parameters as a function of J obtained using method B2 for H<sub>2</sub> and D<sub>2</sub> reacting on Au(111). Experimental values are shown in black<sup>69</sup>. Red circles represent the MS-PBEl-rVV10 values, green circles the MS-B86bl-rVV10 values and blue circles the MS-RPBEl-rVV10 values.

| total $\nu = 0$ 1 0.106 0.104 0.029 0.038 0.131 0.139 0.131 | _                         | чыр (еv) на | -2        | MF    | MAD (ev)               | $L_2$     | M      | SD (ev) 1 | 72        |
|---|---------------------------|-------------|-----------|-------|------------------------|-----------|--------|-----------|-----------|
| 0.106 0.104 (<br>0.029 0.038 (<br>0.139 0.131 (             | $v = 1 \mid \text{total}$ | $\nu = 0$   | $\nu = 1$ | total | $\nu = 0 \mid \nu = 1$ | $\nu = 1$ | total  | $\nu = 0$ | $\nu = 1$ |
| 0.029 0.038 (<br>0.139 0.131 (                              | 0.107 -0.106              | -0.104      | -0.107    | 0.092 | 0.084                  | 0.100     | -0.084 | -0.056    | -0.112    |
| 0.139 0.131 (   | 0.018   -0.028            | -0.038      | -0.016    | 0.044 | 0.045                  | 0.042     | -0.044 | -0.045    | -0.042    |
|   | 0.150 -0.139              | -0.131      | -0.150    | 0.112 | 0.100                  | 0.127     | -0.112 | -0.100    | -0.128    |
| MS-B86b-rVV10   0.050   0.053   0.046                       | 0.046   -0.050            | -0.053      | -0.046    | 0.061 | 0.059                  | 0.065     | -0.061 | -0.059    | -0.065    |
| MS-RPBE-rVV10 0.062 0.061 0.062                             | 0.062 -0.062              | -0.061      | -0.062    | 0.073 | 0.068                  | 0.078     | -0.073 | -0.068    | -0.078    |

TABLE 6.8: Mean absolute and mean signed deviations for the theoretical  $E_{1/2}(\nu,J)$  parameters compared to experimental  $E_0(\nu,J)$  values for  $\mathrm{Au}(111)^{69}$ .

|                        | $H_2$ | $D_2$ |
|------------------------|-------|-------|
| exp. <sup>69</sup>     | 0.552 | 0.424 |
| MS-PBEl <sup>25</sup>  | 0.178 | 0.387 |
| MS-PBEl-rVV10          | 0.175 | 0.377 |
| MS-B86bl <sup>25</sup> | 0.176 | 0.379 |
| MS-B86bl-rVV10         | 0.193 | 0.365 |
| MS-RPBEl-rVV10         | 0.180 | 0.366 |

Table 6.9: The ratio of  $\nu = 1 : \nu = 0$  molecules desorbing from Au(111) as measured in experiments<sup>69</sup> and computed with the MS-PBEl<sup>25</sup>, MS-PBEl-rVV10, MS-B86bl<sup>25</sup>, MS-B86bl-rVV10 and MS-RPBEl-rVV10 DFs.

distributions, thereby indicating that vibrationally excited molecules are more likely to adsorb<sup>69</sup>.

Table 6.9 shows the  $\nu = 1$ :  $\nu = 0$  ratio of desorbing molecules, these ratios are calculated using the same rovibrational states as shown in figure 6.12. Note that the difference between the experimental values shown in table 6.9 and those reported by Shuai et al.<sup>69</sup> is due to using  $E_{\text{max}}(\nu, J)$  as the upper integration limit.

From figure 6.12 it is clear that the differences between all DFs shown is minimal, and that the agreement between theory and experiment is best for  $D_2$ . As was already reported by Shuai et al.<sup>69</sup>, the theoretical ratios computed with different DFs for  $H_2$  are much lower than the experimental ratio. In Chapter 5 we speculated that his difference might be resolved by including surface motion in our dynamics calculations because the experimental time-of-flight distributions are much broader compared to the theoretical ones<sup>69</sup>.

It is clear that adding non-local correlation to the MS mGGA DFs has little effect on the  $\nu=1:\nu=0$  ratio of desorbing molecules. GGA based DFs yielded slightly better ratios for D<sub>2</sub> desorbing from Au(111)<sup>15</sup>. However, also these DFs predicted desorption ratios for H<sub>2</sub> that were much too low.

The fact that mGGA based DFs yield somewhat lower  $\nu=1:\nu=0$  ratios than the GGA based DFs<sup>15</sup> can be explained by the barriers to reaction predicted by the mGGA DFs being somewhat earlier. This allows the  $\nu=0$  population too grow somewhat relative to the  $\nu=1$  population, which would lower the  $\nu=1:\nu=0$  ratios.

# 6.3.5 Transferability

Previous work from our group has shown that semi-local DFs designed for the reaction of H<sub>2</sub> and D<sub>2</sub> dissociating on transition metals may be transferable

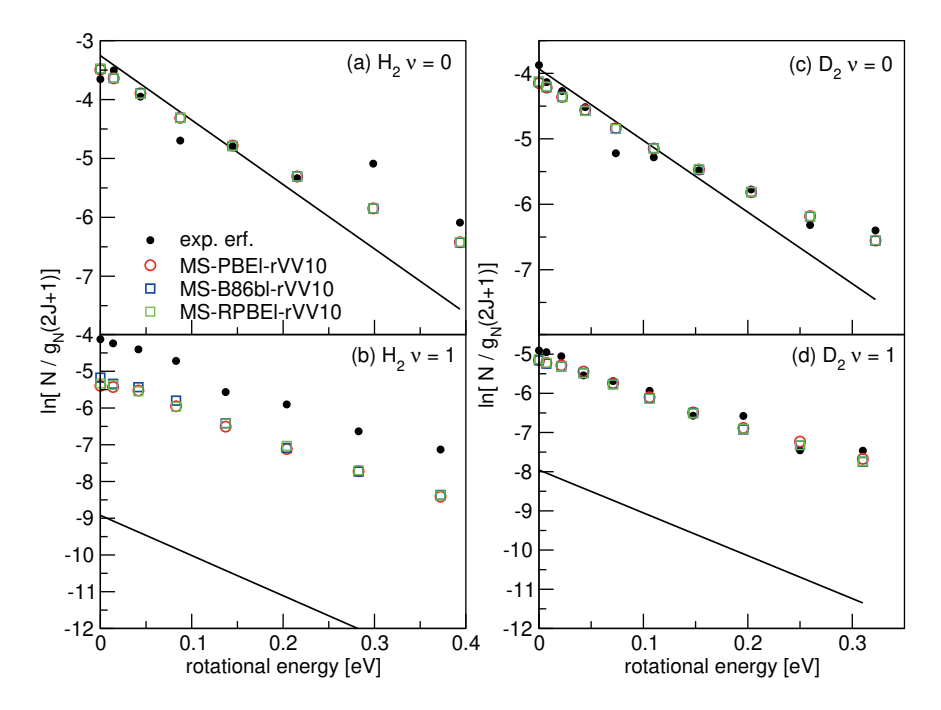


FIGURE 6.12: Rovibrational state populations of  $H_2$  and  $D_2$  desorbing from Au(111) are shown versus the rotational energy. Experimental results are shown in black<sup>69</sup>, theoretical results are shown for MS-PBEl-rVV10 (red), MS-B86bl-rVV10 (blue) and MS-RPBEl-rVV10 (green) DF. The straight lines represent Boltzmann distributions for the surface temperature of the experiment.

reacting on  $Pt(111)^{47}$ .

between different crystal faces of the same metal<sup>44,45</sup>, but until quite recently transferability between systems in which  $H_2$  interacts with different metals had not yet been observed<sup>64,138</sup>. In Chapter 5 we have shown that non-local correlation is a key ingredient in obtaining SRP DFs for the reaction of  $H_2$  and  $D_2$  on transition metals that show this type of transferability, by showing that a DF that we designed to describe the activated reaction of  $H_2 + Cu(111)$  can also describe the reaction of  $D_2 + Pt(111)$  and vice versa<sup>15</sup>. Earlier, transferability

of SRP-DFs between systems in which a molecule interacts with surfaces of different metals has only been reported for CH<sub>4</sub> reaction on Ni(111)<sup>46</sup> and CH<sub>4</sub>

In our calculations we employ the BOSS model and thus neglect any surface temperature effects, and it is known that the BOSS model works well for activated  $\rm H_2$  dissociation on cold metals<sup>20,50–52,54</sup>. Given that associative desorption experiments necessitate high surface temperatures<sup>69,72</sup> it is difficult to asses the quality of the DFs we developed here for the  $\rm H_2$  (D<sub>2</sub>) + Au(111) system, due to the absence of molecular beam sticking experiments for this system.

Here we show that the MS-PBEl-rVV10, MS-B86bl-rVV10 and MS-RPBEl-rVV10 DFs can describe molecular beam sticking experiments on  $D_2 + Ag(111)$  to within chemical accuracy (see figure 6.8), and that the MS-B86bl-rVV10 DF can also describe the  $D_2 + Pt(111)$  molecular beam sticking experiments of Luntz et al.<sup>66</sup> and Cao et al.<sup>67</sup> to within chemical accuracy (see figure 6.9). In the case of the  $H_2$  ( $D_2$ ) + Au(111) system the MS-PBEl-rVV10 DF yields very good results with respect to the calculated  $E_{1/2}(\nu, J)$  parameters. To the best of our knowledge this is the first time that an observable of the reaction of  $H_2$  ( $D_2$ ) on Au(111) that requires dynamics calculations is described with chemical accuracy. However, uncertainties remain for this system with respect to the effects of surface temperature, surface reconstruction and ehp excitation<sup>15</sup>.

Thus there now exist two groups of transferable (SRP) DFs for the reaction of  $H_2$  ( $D_2$ ) with transition metal surfaces. The first group consists of GGA based SRP DFs that use vdW-DF2<sup>95</sup> non-local correlation (B86SRP68-DF2<sup>15</sup> and PBE $\alpha$ 57-DF2<sup>14</sup>), which can describe the  $H_2$  ( $D_2$ ) + Cu(111) and  $D_2$  + Pt(111) reactions to within chemical accuracy. The second group consists of the MS mGGA DFs that use rVV10<sup>48</sup> non-local correlation developed here, which can describe the  $D_2$  + Ag(111) and  $D_2$  + Pt(111) systems with chemical accuracy. Of course there is also the non-conclusive evidence that suggests that the MS-PBEl-rVV10 DF can describe the associative desorption of  $H_2$  from Au(111) to within chemical accuracy.

Presently we cannot say which features of a PES are most important, apart from the lowest barrier to reaction. Experiments that probe different parts of 6.4. Conclusion 265

a PES, like vibrationally or rotationally inelastic scattering, where the latter process depends on the anisotropy of the PES, are few and far between  $^{139,140}$ . In general we see that the MS mGGA based DFs have somewhat earlier barriers for highly activated systems than the GGA based SRP DFs, while for the non-activated  $D_2 + Pt(111)$  system the barrier geometries of the MS mGGA based DFs that include rVV10<sup>48</sup> non-local correlation are very similar to the barrier geometries of GGA based SRP DFs that include vdW-DF2<sup>95</sup> non-local correlation. At the moment we cannot say which type of barrier geometry is more in line with reality.

If the suggested chemical accuracy in the description of  $H_2 + Au(111)$  holds in confrontation with experiment, then one could argue that the mGGA based DFs that include rVV10<sup>48</sup> non-local correlation are an improvement over the previously developed GGA based SRP DFs that include vdW-DF2<sup>95</sup> non-local correlation: in this case the MS mGGA-rVV10 based DFs can describe three systems with chemical accuracy, compared to two systems for the GGA based SRP DFs<sup>15</sup> developed in Chapter 5. This would indicate that climbing Jacob's ladder leads to a more universal description of the reaction of  $H_2$  on transition metal surfaces.

### 6.4 Conclusion

We have combined our three previously developed MS-PBEl, MS-B86bl and MS-RPBEl mGGA DFs with rVV10 non-local correlation to obtain the MS-PBEl-rVV10, MS-B86bl-rVV10 and MS-RPBEl-rVV10 DFs. We find that all three developed DFs can describe the molecular beam sticking experiments on dissociative chemisorption of D<sub>2</sub> on Ag(111) with chemical accuracy. We also find that the MS-B86bl-rVV10 DF can describe two sets of molecular beam sticking experiments on dissociative chemisorption of D<sub>2</sub> on Pt(111) with chemical accuracy. Additionally, by calculating  $E_{1/2}(\nu, J)$  parameters for the reaction of H<sub>2</sub> on Au(111) and comparing these to experimental  $E_0(\nu, J)$  parameters for state-selective associative desorption we obtain chemical accuracy with the MS-PBEl-rVV10 DF. Assessing the performance of the three developed MS mGGA-rVV10 DFs for the H<sub>2</sub> (D<sub>2</sub>) + Au(111) system is however difficult due to the lack of well characterized molecular beam sticking experiments of H<sub>2</sub> (D<sub>2</sub>) on Au(111) and the lack of calculations that use a reconstructed Au(111) surface and incorporate ehp excitation.

Of the three developed MS mGGA-rVV10 DFs, MS-PBEl-rVV10 performs excellently for the known van der Waals well geometries. The MS-PBEl-rVV10 DF also maintains the improvements generally observed for mGGA-rVV10

DFs relative to GGA-vdW-DF2 DFs in this regard. The MS-B86bl-rVV10 and MS-RPBEl-rVV10 DFs yield van der Waals wells that are too shallow.

In a comparison to state-selected experiments on associative desorption of  $H_2$  ( $D_2$ ) from Ag(111) we observe excellent agreement with experiment in the case of  $H_2$ , for all three developed DFs. For  $H_2$  all three developed DFs show improvement over the three original MS mGGA DFs and over the best GGA based SRP DFs that include vdW-DF2 non-local correlation. The associative desorption experiments on  $D_2$  desorbing from Ag(111) were less well described.

With respect to the molecular beam sticking probabilities of  $H_2$  ( $D_2$ ) + Cu(111) the three developed DFs yield sticking probabilities in line with sticking probabilities predicted by the PBE DF, which are too high. This in contrast to the highly accurate sticking probabilities obtained when using the original three MS mGGA DFs.

The three original MS mGGA DFs give a description of the metal that is comparable to that obtained with the PBEsol DF. Unfortunately, adding rVV10 non-local correlation comes at the cost of a worse description of the metal. In general we see lattice constants that are smaller than the zero-point energy corrected experimental results. However, in general the underestimation of the calculated lattice constants is still smaller than the overestimation of calculated lattice constants obtained with the current best SRP DFs that include vdW-DF2 non-local correlation. The three developed MS mGGA-rVV10 DFs predict interlayer distances between the top two layers that are too large compared to experimental observations.

The three MS mGGA DFs that have been combined in this work with rVV10 non-local correlation were not fitted to reproduce particular experiments, nor has the b parameter present in rVV10 been re-optimized. Our results show that, overall, ascending Jacob's ladder from the GGA plus non-local correlation rung to the mGGA plus non-local correlation rung leads to somewhat more accurate results for dissociative chemisorption of  $H_2$  ( $D_2$ ) on noble metals, although the metals themselves are described less accurately than with the MS mGGA DFs without non-local van der Waals correlation, and the improvement does not hold for the well studied  $H_2$  + Cu(111) system.

### References

(1) Smeets, E. W. F.; Kroes, G.-J. Performance of made-simple meta-GGA functionals with rVV10 non-local correlation for  $H_2 + Cu(111)$ ,  $D_2 + Ag(111)$ ,  $H_2 + Au(111)$  and  $D_2 + Pt(111)$ . J. Phys. Chem. C **2021**, DOI:  $10.1021/acs.jpcc\ 0c11034$ .

- (2) Wolcott, C. A.; Medford, A. J.; Studt, F.; Campbell, C. T. Degree of rate control approach to computational catalyst screening. *J. Catal.* **2015**, *330*, 197–207.
- (3) Sabbe, M. K.; Reyniers, M.-F.; Reuter, K. First-principles kinetic modeling in heterogeneous catalysis: an industrial perspective on best-practice, gaps and needs. *Catal. Sci. Technol.* **2012**, *2*, 2010–2024.
- (4) Ertl, G. Reactions at surfaces: from atoms to complexity (Nobel lecture). *Angew. Chem. Int. Ed.* **2008**, *47*, 3524–3535.
- (5) Noyori, R. Synthesizing our future. Nat. Chem. 2009, 1, 5–6.
- (6) Ertl, G. Primary steps in catalytic synthesis of ammonia. *J. Vac. Sci. Technol.* **1983**, *1*, 1247–1253.
- (7) Waugh, K. Methanol synthesis. Catal. Today 1992, 15, 51–75.
- (8) Grabow, L.; Mavrikakis, M. Mechanism of methanol synthesis on Cu through CO<sub>2</sub> and CO hydrogenation. *Acs Catalysis* **2011**, *1*, 365–384.
- (9) Behrens, M.; Studt, F.; Kasatkin, I.; Kühl, S.; Hävecker, M.; Abild-Pedersen, F.; Zander, S.; Girgsdies, F.; Kurr, P.; Kniep, B.-L., et al. The active site of methanol synthesis over Cu/ZnO/Al<sub>2</sub>O<sub>3</sub> industrial catalysts. *Science* **2012**, *336*, 893–897.
- (10) Kroes, G.-J. Toward a database of chemically accurate barrier heights for reactions of molecules with metal surfaces. J. Phys. Chem lett. 2015, 6, 4106–4114.
- (11) Stegelmann, C.; Andreasen, A.; Campbell, C. T. Degree of rate control: how much the energies of intermediates and transition states control rates. J. Am. Chem. Soc. 2009, 131, 8077–8082.
- (12) Park, G. B.; Kitsopoulos, T. N.; Borodin, D.; Golibrzuch, K.; Neugebohren, J.; Auerbach, D. J.; Campbell, C. T.; Wodtke, A. M. The kinetics of elementary thermal reactions in heterogeneous catalysis. *Nature Rev. Chem.* **2019**, *3*, 723–732.
- (13) Díaz, C.; Pijper, E.; Olsen, R.; Busnengo, H.; Auerbach, D.; Kroes, G. Chemically accurate simulation of a prototypical surface reaction: H<sub>2</sub> dissociation on Cu(111). *Science* **2009**, *326*, 832–834.

- (14) Ghassemi, E. N.; Wijzenbroek, M.; Somers, M. F.; Kroes, G.-J. Chemically accurate simulation of dissociative chemisorption of D<sub>2</sub> on Pt(111). Chem. Phys. Lett. 2017, 683, 329–335.
- (15) Smeets, E. W. F.; Kroes, G.-J. Designing new SRP density functionals including non-local vdW-DF2 correlation for H<sub>2</sub> + Cu(111) and their transferability to H<sub>2</sub> + Ag(111), Au(111) and Pt(111). *Phys. Chem. Chem. Phys.* **2021**, 23, 7875–7901.
- (16) Gerrits, N.; Smeets, E. W. F.; Vuckovic, S.; Powell, A. D.; Doblhoff-Dier, K.; Kroes, G.-J. Density functional theory for molecule-metal surface reactions: When does the generalized gradient approximation get it right, and what to do if it does not. J. Phys. Chem. Lett, 2020, 11, 10552–10560.
- (17) Schimka, L.; Harl, J.; Stroppa, A.; Grüneis, A.; Marsman, M.; Mittendorfer, F.; Kresse, G. Accurate surface and adsorption energies from many-body perturbation theory. *Nature materials* **2010**, *9*, 741–744.
- (18) Haas, P.; Tran, F.; Blaha, P.; Schwarz, K. Construction of an optimal GGA functional for molecules and solids. *Phys. Rev. B* **2011**, *83*, 205117.
- (19) Peverati, R.; Truhlar, D. G. Exchange–correlation functional with good accuracy for both structural and energetic properties while depending only on the density and its gradient. *J. Chem. Theory Comput.* **2012**, 8, 2310–2319.
- (20) Nattino, F.; Díaz, C.; Jackson, B.; Kroes, G.-J. Effect of surface motion on the rotational quadrupole alignment parameter of D<sub>2</sub> reacting on Cu(111). Phys. Rev. Lett. 2012, 108, 236104.
- (21) Marashdeh, A.; Casolo, S.; Sementa, L.; Zacharias, H.; Kroes, G.-J. Surface temperature effects on dissociative chemisorption of H<sub>2</sub> on Cu(100). *J. Phys. Chem. C* **2013**, *117*, 8851–8863.
- (22) Mondal, A.; Wijzenbroek, M.; Bonfanti, M.; Díaz, C.; Kroes, G.-J. Thermal lattice expansion effect on reactive scattering of  $H_2$  from Cu(111) at  $T_s=925$  K. J. Phys. Chem. A **2013**, 117, 8770–8781.
- (23) Tiwari, A. K.; Nave, S.; Jackson, B. Methane dissociation on Ni(111): A new understanding of the lattice effect. *Phys. Rev. Lett.* **2009**, *103*, 253201.
- (24) Tiwari, A. K.; Nave, S.; Jackson, B. The temperature dependence of methane dissociation on Ni(111) and Pt(111): mixed quantum-classical studies of the lattice response. *J. Chem. Phys.* **2010**, *132*, 134702.

(25) Smeets, E. W. F.; Voss, J.; Kroes, G.-J. Specific reaction parameter density functional based on the meta-generalized gradient approximation: application to  $H_2 + Cu(111)$  and  $H_2 + Ag(111)$ . J. Phys. Chem. A **2019**, 123, 5395–5406.

- (26) Sun, J.; Xiao, B.; Ruzsinszky, A. Communication: Effect of the orbital-overlap dependence in the meta generalized gradient approximation. *J. Chem. Phys.* **2012**, *137*, 051101.
- (27) Sun, J.; Haunschild, R.; Xiao, B.; Bulik, I. W.; Scuseria, G. E.; Perdew, J. P. Semilocal and hybrid meta-generalized gradient approximations based on the understanding of the kinetic-energy-density dependence. *J. Chem. Phys.* **2013**, *138*, 044113.
- (28) Perdew, J. P.; Ruzsinszky, A.; Csonka, G. I.; Vydrov, O. A.; Scuseria, G. E.; Constantin, L. A.; Zhou, X.; Burke, K. Restoring the density-gradient expansion for exchange in solids and surfaces. *Phys. Rev. Lett.* 2008, 100, 136406.
- (29) Michelsen, H.; Rettner, C.; Auerbach, D.; Zare, R. Effect of rotation on the translational and vibrational energy dependence of the dissociative adsorption of D<sub>2</sub> on Cu(111). *J. Chem. Phys.* **1993**, *98*, 8294–8307.
- (30) Berger, H.; Leisch, M.; Winkler, A.; Rendulic, K. A search for vibrational contributions to the activated adsorption of H<sub>2</sub> on copper. *Chem. Phys. Lett.* **1990**, *175*, 425–428.
- (31) Rettner, C.; Michelsen, H.; Auerbach, D. Quantum-state-specific dynamics of the dissociative adsorption and associative desorption of H<sub>2</sub> at a Cu(111) surface. *J. Chem. Phys.* **1995**, *102*, 4625–4641.
- (32) Cottrell, C.; Carter, R.; Nesbitt, A.; Samson, P.; Hodgson, A. Vibrational state dependence of D<sub>2</sub> dissociation on Ag(111). *J. Chem. Phys.* **1997**, 106, 4714–4722.
- (33) Sun, J.; Xiao, B.; Fang, Y.; Haunschild, R.; Hao, P.; Ruzsinszky, A.; Csonka, G. I.; Scuseria, G. E.; Perdew, J. P. Density functionals that recognize covalent, metallic, and weak bonds. *Phys. Rev. Lett.* **2013**, 111, 106401.
- (34) Tao, J.; Perdew, J. P.; Staroverov, V. N.; Scuseria, G. E. Climbing the density functional ladder: Nonempirical meta-generalized gradient approximation designed for molecules and solids. *Phys. Rev. Lett.* **2003**, *91*, 146401.

- (35) Perdew, J. P.; Ruzsinszky, A.; Csonka, G. I.; Constantin, L. A.; Sun, J. Workhorse semilocal density functional for condensed matter physics and quantum chemistry. *Phys. Rev. Lett.* **2009**, *103*, 026403.
- (36) Garza, A. J.; Bell, A. T.; Head-Gordon, M. Nonempirical meta-generalized gradient approximations for modeling chemisorption at metal surfaces. J. Chem. Theory Comput. 2018, 14, 3083–3090.
- (37) Sun, J.; Ruzsinszky, A.; Perdew, J. P. Strongly constrained and appropriately normed semilocal density functional. *Phys. Rev. Lett.* **2015**, 115, 036402.
- (38) Peng, H.; Yang, Z.-H.; Perdew, J. P.; Sun, J. Versatile van der Waals density functional based on a meta-generalized gradient approximation. *Phys. Rev. X* **2016**, *6*, 041005.
- (39) Wellendorff, J.; Lundgaard, K. T.; Jacobsen, K. W.; Bligaard, T. mBEEF: An accurate semi-local Bayesian error estimation density functional. *J. Chem. Phys.* **2014**, *140*, 144107.
- (40) Lundgaard, K. T.; Wellendorff, J.; Voss, J.; Jacobsen, K. W.; Bligaard, T. mBEEF-vdW: Robust fitting of error estimation density functionals. Phys. Rev. B 2016, 93, 235162.
- (41) Sun, J.; Marsman, M.; Ruzsinszky, A.; Kresse, G.; Perdew, J. P. Improved lattice constants, surface energies, and CO desorption energies from a semilocal density functional. *Phys. Rev. B* **2011**, *83*, 121410.
- (42) Sun, J.; Perdew, J. P.; Ruzsinszky, A. Semilocal density functional obeying a strongly tightened bound for exchange. *Proc. Nat. Ac. Sci.* **2015**, *112*, 685–689.
- (43) Peverati, R.; Truhlar, D. G. An improved and broadly accurate local approximation to the exchange-correlation density functional: The MN12-L functional for electronic structure calculations in chemistry and physics. *Phys. Chem. Chem. Phys.* **2012**, *14*, 13171–13174.
- (44) Ghassemi, E. N.; Smeets, E. W. F.; Somers, M. F.; Kroes, G.-J.; Groot, I. M.; Juurlink, L. B.; Füchsel, G. Transferability of the specific reaction parameter density functional for H<sub>2</sub> + Pt(111) to H<sub>2</sub> + Pt(211). *J. Phys. Chem. C* **2019**, *123*, 2973–2986.
- (45) Sementa, L.; Wijzenbroek, M.; Van Kolck, B.; Somers, M.; Al-Halabi, A.; Busnengo, H. F.; Olsen, R.; Kroes, G.-J.; Rutkowski, M.; Thewes, C., et al. Reactive scattering of H<sub>2</sub> from Cu(100): comparison of dynamics calculations based on the specific reaction parameter approach to density functional theory with experiment. J. Chem. Phys. **2013**, 138, 044708.

(46) Nattino, F.; Migliorini, D.; Kroes, G.-J.; Dombrowski, E.; High, E. A.; Killelea, D. R.; Utz, A. L. Chemically accurate simulation of a polyatomic molecule-metal surface reaction. *J. Phys. Chem. Lett.* **2016**, 7, 2402–2406.

- (47) Migliorini, D.; Chadwick, H.; Nattino, F.; Gutiérrez-González, A.; Dombrowski, E.; High, E. A.; Guo, H.; Utz, A. L.; Jackson, B.; Beck, R. D., et al. Surface reaction barriometry: methane dissociation on flat and stepped transition-metal surfaces. J. Phys. Chem. Lett. 2017, 8, 4177–4182.
- (48) Sabatini, R.; Gorni, T.; De Gironcoli, S. Nonlocal van der Waals density functional made simple and efficient. *Phys. Rev. B* **2013**, *87*, 041108.
- (49) Vydrov, O. A.; Van Voorhis, T. Nonlocal van der Waals density functional: The simpler the better. *J. Chem. Phys.* **2010**, *133*, 244103.
- (50) Díaz, C.; Olsen, R. A.; Auerbach, D. J.; Kroes, G.-J. Six-dimensional dynamics study of reactive and non reactive scattering of H<sub>2</sub> from Cu(111) using a chemically accurate potential energy surface. *Phys. Chem. Chem. Phys.* 2010, 12, 6499–519.
- (51) Wijzenbroek, M.; Somers, M. F. Static surface temperature effects on the dissociation of H<sub>2</sub> and D<sub>2</sub> on Cu(111). *J. Chem. Phys.* **2012**, *137*, 054703.
- (52) Spiering, P.; Wijzenbroek, M.; Somers, M. An improved static corrugation model. *J. Chem. Phys.* **2018**, *149*, 234702.
- (53) Nattino, F.; Genova, A.; Guijt, M.; Muzas, A. S.; Díaz, C.; Auerbach, D. J.; Kroes, G.-J. Dissociation and recombination of D<sub>2</sub> on Cu(111): Ab initio molecular dynamics calculations and improved analysis of desorption experiments. J. Chem. Phys. 2014, 141, 124705.
- (54) Kroes, G.-J.; Díaz, C. Quantum and classical dynamics of reactive scattering of H<sub>2</sub> from metal surfaces. *Chem. Soc. Rev.* **2016**, *45*, 3658–3700.
- (55) Bonfanti, M.; Somers, M. F.; Díaz, C.; Busnengo, H. F.; Kroes, G.-J. 7D quantum dynamics of H<sub>2</sub> scattering from Cu(111): the accuracy of the phonon sudden approximation. Z. Phys. Chem. **2013**, 227, 1397–1420.
- (56) Spiering, P.; Meyer, J. Testing electronic friction models: vibrational de-excitation in scattering of H<sub>2</sub> and D<sub>2</sub> from Cu(111). *J. Phys. Chem. Lett.* **2018**, *9*, 1803–1808.

- (57) Muzas, A. S.; Juaristi, J. I.; Alducin, M.; Díez Muiño, R.; Kroes, G.-J.; Díaz, C. Vibrational deexcitation and rotational excitation of H<sub>2</sub> and D<sub>2</sub> scattered from Cu(111): adiabatic versus non-adiabatic dynamics. J. Chem. Phys. 2012, 137, 064707.
- (58) Luntz, A. C.; Persson, M. How adiabatic is activated adsorption/associative desorption? *The Journal of chemical physics* **2005**, *123*, 074704.
- (59) Maurer, R. J.; Zhang, Y.; Guo, H.; Jiang, B. Hot electron effects during reactive scattering of H<sub>2</sub> from Ag(111): assessing the sensitivity to initial conditions, coupling magnitude, and electronic temperature. *Faraday Discuss.* **2019**, 214, 105–121.
- (60) Zhang, Y.; Maurer, R. J.; Guo, H.; Jiang, B. Hot-electron effects during reactive scattering of H<sub>2</sub> from Ag(111): the interplay between modespecific electronic friction and the potential energy landscape. *Chem.* Sci. 2019, 10, 1089–1097.
- (61) Maurer, R. J.; Jiang, B.; Guo, H.; Tully, J. C. Mode specific electronic friction in dissociative chemisorption on metal surfaces: H 2 on Ag (111). *Physical review letters* 2017, 118, 256001.
- (62) Füchsel, G.; Schimka, S.; Saalfrank, P. On the role of electronic friction for dissociative adsorption and scattering of hydrogen molecules at a Ru(0001) surface. J. Phys. Chem. A 2013, 117, 8761–8769.
- (63) Füchsel, G.; Cao, K.; Er, S.; Smeets, E. W. F.; Kleyn, A. W.; Juurlink, L. B. F.; Kroes, G.-J. Anomalous dependence of the reactivity on the presence of steps: dissociation of D<sub>2</sub> on Cu(211). *J. Phys. Chem. Lett.* 2018, 9, 170–175.
- (64) Nour Ghassemi, E.; Somers, M.; Kroes, G.-J. Test of the transferability of the specific reaction parameter functional for H<sub>2</sub>+ Cu(111) to D<sub>2</sub> + Ag(111). J. Phys. Chem. C **2018**, 122, 22939–22952.
- (65) Crespos, C.; Collins, M. A.; Pijper, E.; Kroes, G.-J. Multi-dimensional potential energy surface determination by modified Shepard interpolation for a molecule–surface reaction: H<sub>2</sub> + Pt(111). *Chem. Phys. Lett.* **2003**, *376*, 566–575.
- (66) Luntz, A.; Brown, J.; Williams, M. Molecular beam studies of H<sub>2</sub> and D<sub>2</sub> dissociative chemisorption on Pt(111). J. Chem. Phys. 1990, 93, 5240–5246.
- (67) Cao, K.; Füchsel, G.; Kleyn, A. W.; Juurlink, L. B. Hydrogen adsorption and desorption from Cu(111) and Cu(211). *Phys. Chem. Chem. Phys.* **2018**, *20*, 22477–22488.

(68) Samson, P.; Nesbitt, A.; Koel, B. E.; Hodgson, A. Deuterium dissociation on ordered Sn/Pt(111) surface alloys. J. Chem. Phys. 1998, 109, 3255– 3264.

- (69) Shuai, Q.; Kaufmann, S.; Auerbach, D. J.; Schwarzer, D.; Wodtke, A. M. Evidence for electron-hole pair excitation in the associative desorption of H<sub>2</sub> and D<sub>2</sub> from Au(111). J. Phys. Chem. Lett. 2017, 8, 1657–1663.
- (70) Murphy, M.; Hodgson, A. Translational energy release in the recombinative desorption of H<sub>2</sub> from Ag(111). Surf. Sci. **1997**, 390, 29–34.
- (71) Murphy, M.; Hodgson, A. Role of surface thermal motion in the dissociative chemisorption and recombinative desorption of D<sub>2</sub> on Ag(111). *Phys. Rev. Lett.* **1997**, *78*, 4458–4461.
- (72) Kaufmann, S.; Shuai, Q.; Auerbach, D. J.; Schwarzer, D.; Wodtke, A. M. Associative desorption of hydrogen isotopologues from copper surfaces: characterization of two reaction mechanisms. J. Chem. Phys. 2018, 148, 194703.
- (73) Perrier, A.; Bonnet, L.; Liotard, D.; Rayez, J.-C. On the dynamics of H<sub>2</sub> desorbing from a Pt(111) surface. Surf. Sci. **2005**, 581, 189–198.
- (74) Perrier, A.; Bonnet, L.; Rayez, J.-C. Dynamical study of H<sub>2</sub> and D<sub>2</sub> desorbing from a Cu(111) surface. *J. Phys. Chem. A* **2006**, *110*, 1608–1617.
- (75) Perrier, A.; Bonnet, L.; Rayez, J.-C. Statisticodynamical approach of final state distributions in associative desorptions. *J. Chem. Phys.* **2006**, 124, 194701.
- (76) Díaz, C.; Perrier, A.; Kroes, G. Associative desorption of N<sub>2</sub> from Ru(0001): a computational study. *Chem. Phys. Lett.* **2007**, 434, 231–236.
- (77) Galparsoro, O.; Kaufmann, S.; Auerbach, D. J.; Kandratsenka, A.; Wodtke, A. M. First principles rates for surface chemistry employing exact transition state theory: application to recombinative desorption of hydrogen from Cu(111). Phys. Chem. Chem. Phys. 2020, 22, 17532– 17539.
- (78) Dai, J.; Zhang, J. Z. Quantum adsorption dynamics of a diatomic molecule on surface: four-dimensional fixed-site model for H<sub>2</sub> on Cu(111). J. Chem. Phys. **1995**, 102, 6280–6289.
- (79) Hammer, B.; Scheffler, M.; Jacobsen, K. W.; Nørskov, J. K. Multidimensional potential energy surface for H<sub>2</sub> dissociation over Cu(111). *Phys. Rev. Lett.* 1994, 73, 1400–1403.

- (80) Cowin, J. P.; Yu, C.-F.; Sibener, S. J.; Hurst, J. E. Bound level resonances in rotationally inelastic HD/Pt (111) surface scattering. *The Journal of Chemical Physics* **1981**, *75*, 1033–1034.
- (81) Cowin, J. P.; Yu, C.-F.; Sibener, S. J.; Wharton, L. HD scattering from Pt(111): rotational excitation probabilities. *J. Chem. Phys.* **1983**, *79*, 3537–3549.
- (82) Cowin, J. P.; Yu, C.-F.; Wharton, L. HD scattering from Pt(111): Rotationally mediated selective adsorption. Surf. Sci. 1985, 161, 221–233.
- (83) Yu, C.-F.; Hogg, C. S.; Cowin, J. P.; Whaley, K. B.; Light, J. C.; Sibener, S. J. Rotationally mediated selective adsorption as a probe of isotropic and anisotropic molecule—surface interaction potentials: HD (J)/Ag(111). Israel J. Chem. 1982, 22, 305–314.
- (84) Yu, C.-f.; Whaley, K. B.; Hogg, C. S.; Sibener, S. J. Investigation of the spatially isotropic component of the laterally averaged molecular hydrogen/Ag(111) physisorption potential. J. Chem. Phys. 1985, 83, 4217–4234.
- (85) Perreau, J.; Lapujoulade, J. Selective adsorption of He, H<sub>2</sub> on copper surfaces. Surf. Sci. 1982, 122, 341–354.
- (86) Yu, C.-f.; Whaley, K. B.; Hogg, C. S.; Sibener, S. J. Selective Adsorption Resonances in the Scattering of n-H<sub>2</sub> p-H<sub>2</sub> n-D<sub>2</sub> and o-D<sub>2</sub> from Ag(111). *Phys. Rev. Lett.* **1983**, *51*, 2210.
- (87) Kaufhold, A.; Toennies, J. P. An optical potential for rotationally mediated selective adsorption (Feshbach) resonances in scattering of molecules from smooth crystal surfaces. *Surf. Sci.* **1986**, *173*, 320–336.
- (88) Andersson, S.; Wilzén, L.; Persson, M. Physisorption interaction of H<sub>2</sub> with noble-metal surfaces: A new H<sub>2</sub>-Cu potential. *Phys. Rev. B* **1988**, 38, 2967.
- (89) Andersson, S.; Persson, M. Sticking in the physisorption well: influence of surface structure. *Phys. Rev. Lett.* **1993**, *70*, 202.
- (90) Harten, U.; Toennies, J. P.; Wöll, C. Molecular beam translational spectroscopy of physisorption bound states of molecules on metal surfaces.
  I. HD on Cu(111) and Au(111) single crystal surfaces. J. Chem. Phys. 1986, 85, 2249–2258.
- (91) Lennard-Jones, J. E.; Devonshire, A. F. Diffraction and selective adsorption of atoms at crystal surfaces. *Nature* **1936**, *137*, 1069–1070.

References 275

(92) Hoinkes, H.; Wilsch, H. In *Helium Atom Scattering from Surfaces*; Springer: 1992, pp 113–172.

- (93) Poelsema, B.; Lenz, K.; Comsa, G. The dissociative adsorption of hydrogen on defect-free Pt(111). *J. Phys. Condens. Matter* **2010**, *22*, 304006.
- (94) Dion, M.; Rydberg, H.; Schröder, E.; Langreth, D. C.; Lundqvist, B. I. Van der Waals density functional for general geometries. *Phys. Rev. Lett.* **2004**, *92*, 246401.
- (95) Lee, K.; Murray, É. D.; Kong, L.; Lundqvist, B. I.; Langreth, D. C. Higher-accuracy van der Waals density functional. *Phys. Rev. B* **2010**, 82, 081101.
- (96) Mardirossian, N.; Head-Gordon, M. Thirty years of density functional theory in computational chemistry: an overview and extensive assessment of 200 density functionals. *Mol. Phys.* **2017**, *115*, 2315–2372.
- (97) Mardirossian, N.; Ruiz Pestana, L.; Womack, J. C.; Skylaris, C.-K.; Head-Gordon, T.; Head-Gordon, M. Use of the rVV10 nonlocal correlation functional in the B97M-V density functional: Defining B97M-rV and related functionals. J. Phys. Chem. Lett. 2017, 8, 35–40.
- (98) Murray, É. D.; Lee, K.; Langreth, D. C. Investigation of exchange energy density functional accuracy for interacting molecules. *J. Chem. Theor. Comput.* **2009**, *5*, 2754–2762.
- (99) Perdew, J. P.; Burke, K.; Ernzerhof, M. Generalized gradient approximation made simple. *Phys. Rev. Lett.* **1996**, *77*, 3865–3868.
- (100) Giannozzi, P.; Baroni, S.; Bonini, N.; Calandra, M.; Car, R.; Cavazzoni, C.; Ceresoli, D.; Chiarotti, G. L.; Cococcioni, M.; Dabo, I., et al. QUANTUM ESPRESSO: a modular and open-source software project for quantum simulations of materials. *J. Phys. Condens. Matt.* **2009**, 21, 395502.
- (101) Giannozzi, P.; Andreussi, O.; Brumme, T.; Bunau, O.; Nardelli, M. B.; Calandra, M.; Car, R.; Cavazzoni, C.; Ceresoli, D.; Cococcioni, M., et al. Advanced capabilities for materials modelling with Quantum ESPRESSO. J. Phys. Condens. Matt. 2017, 29, 465901.
- (102) Shao, Y.; Gan, Z.; Epifanovsky, E.; Gilbert, A. T.; Wormit, M.; Kussmann, J.; Lange, A. W.; Behn, A.; Deng, J.; Feng, X., et al. Advances in molecular quantum chemistry contained in the Q-Chem 4 program package. *Mol. Phys.* **2015**, *113*, 184–215.

- (103) Román-Pérez, G.; Soler, J. M. Efficient implementation of a van der Waals density functional: application to double-wall carbon nanotubes. *Phys. Rev. Lett.* 2009, 103, 096102.
- (104) Perdew, J. P.; Wang, Y. Pair-distribution function and its coupling-constant average for the spin-polarized electron gas. *Phys. Rev. B* **1992**, 46, 12947.
- (105) Jurečka, P.; Šponer, J.; Černy, J.; Hobza, P. Benchmark database of accurate (MP2 and CCSD (T) complete basis set limit) interaction energies of small model complexes, DNA base pairs, and amino acid pairs. *Phys. Chem. Chem. Phys.* **2006**, *8*, 1985–1993.
- (106) Hammer, B. H. L. B.; Hansen, L. B.; Nørskov, J. K. Improved adsorption energetics within density-functional theory using revised Perdew-Burke-Ernzerhof functionals. *Phys. Rev. B* 1999, 59, 7413–7421.
- (107) Becke, A. D. On the large-gradient behavior of the density functional exchange energy. J. Chem. Phys. 1986, 85, 7184–7187.
- (108) Haas, P.; Tran, F.; Blaha, P. Calculation of the lattice constant of solids with semilocal functionals. *Phys. Rev. B* **2009**, *79*, 085104.
- (109) Busnengo, H.; Salin, A.; Dong, W. Representation of the 6D potential energy surface for a diatomic molecule near a solid surface. *J. Chem. Phys.* **2000**, *112*, 7641–7651.
- (110) Wijzenbroek, M.; Klein, D. M.; Smits, B.; Somers, M. F.; Kroes, G.-J. Performance of a non-local van der Waals density functional on the dissociation of H<sub>2</sub> on metal surfaces. *J. Phys. Chem. A* **2015**, *119*, 12146–12158.
- (111) Raff, L. M.; Karplus, M. Theoretical investigations of reactive collisions in molecular beams: K+CH<sub>3</sub>I and related systems. *J. Chem. Phys.* **1966**, 44, 1212–1229.
- (112) Stoer, J.; Bulirsch, R., Introduction to numerical analysis; Springer Science & Business Media, New York: 2013; Vol. 12.
- (113) Füchsel, G.; del Cueto, M.; Díaz, C.; Kroes, G.-J. Enigmatic HCl + Au(111) reaction: a puzzle for theory and experiment. *J. Phys. Chem.* C 2016, 120, 25760–25779.
- (114) Kaufmann, S. personal communication.
- (115) Kresse, G.; Hafner, J. Ab initio molecular-dynamics simulation of the liquid-metal–amorphous-semiconductor transition in germanium. *Phys. Rev. B* **1994**, *49*, 14251–14269.

References 277

(116) Kresse, G.; Hafner, J. Ab initio molecular dynamics for liquid metals. *Phys. Rev. B* **1993**, *47*, 558–561.

- (117) Kresse, G.; Furthmüller, J. Efficient iterative schemes for ab initio totalenergy calculations using a plane-wave basis set. *Phys. Rev. B* **1996**, 54, 11169–11186.
- (118) Kresse, G.; Furthmüller, J. Efficiency of ab-initio total energy calculations for metals and semiconductors using a plane-wave basis set. *Comput. Mater. Sci.* **1996**, *6*, 15–50.
- (119) Blöchl, P. E. Projector augmented-wave method. *Phys. Rev. B* **1994**, 50, 17953–17979.
- (120) Klimeš, J. ř.; Bowler, D. R.; Michaelides, A. Van der Waals density functionals applied to solids. *Phys. Rev. B* **2011**, *83*, 195131.
- (121) Román-Pérez, G.; Soler, J. M. Efficient implementation of a Van der Waals density functional: application to double-wall carbon nanotubes. *Phys. Rev. Lett.* **2009**, *103*, 096102.
- (122) Klimeš, J.; Bowler, D. R.; Michaelides, A. Chemical accuracy for the van der Waals density functional. *J. Phys. Condens. Matter* **2009**, *22*, 022201.
- (123) Chae, K.; Lu, H.; Gustafsson, T. Medium-energy ion-scattering study of the temperature dependence of the structure of Cu(111). *Phys. Rev.* B **1996**, *54*, 14082.
- (124) Okazawa, T.; Takeuchi, F.; Kido, Y. Enhanced and correlated thermal vibrations of Cu(111) and Ni(111) surfaces. *Physical Review B* **2005**, 72, 075408.
- (125) Lindgren, S.; Walldén, L.; Rundgren, J.; Westrin, P. Low-energy electron diffraction from Cu(111): subthreshold effect and energy-dependent inner potential; surface relaxation and metric distances between spectra. *Phys. Rev. B* **1984**, *29*, 576–588.
- (126) Statiris, P.; Lu, H.; Gustafsson, T. Temperature dependent sign reversal of the surface contraction of Ag(111). *Phys. Rev. Lett.* **1994**, *72*, 3574–3577.
- (127) Soares, E.; Leatherman, G.; Diehl, R.; Van Hove, M. Low-energy electron diffraction study of the thermal expansion of Ag(111). *Surf. Sci.* **2000**, 468, 129–136.
- (128) Nichols, R.; Nouar, T.; Lucas, C.; Haiss, W.; Hofer, W. Surface relaxation and surface stress of Au(111). Surf. Sci. 2002, 513, 263–271.

- (129) Adams, D. L.; Nielsen, H.; Van Hove, M. A. Quantitative analysis of low-energy-electron diffraction: application to Pt(111). *Phys. Rev. B* **1979**, *20*, 4789.
- (130) Lee, K.; Berland, K.; Yoon, M.; Andersson, S.; Schröder, E.; Hyldgaard, P.; Lundqvist, B. I. Benchmarking van der Waals density functionals with experimental data: potential-energy curves for H<sub>2</sub> molecules on Cu(111),(100) and (110) surfaces. J. Phys. Condens. Matter 2012, 24, 424213.
- (131) Kroes, G.-J. Frontiers in surface scattering simulations. *Science* **2008**, 321, 794–797.
- (132) Ghassemi, E. N.; Somers, M. F.; Kroes, G.-J. Assessment of two problems of specific reaction parameter density functional theory: sticking and diffraction of H<sub>2</sub> on Pt(111). J. Phys. Chem. C 2019, 123, 10406-10418.
- (133) Wijzenbroek, M.; Helstone, D.; Meyer, J.; Kroes, G.-J. Dynamics of H<sub>2</sub> dissociation on the close-packed (111) surface of the noblest metal: H<sub>2</sub> + Au(111). J. Chem. Phys. **2016**, 145, 144701.
- (134) Mukherjee, S.; Libisch, F.; Large, N.; Neumann, O.; Brown, L. V.; Cheng, J.; Lassiter, J. B.; Carter, E. A.; Nordlander, P.; Halas, N. J. Hot electrons do the impossible: plasmon-induced dissociation of H<sub>2</sub> on Au. Nano lett. 2012, 13, 240–247.
- (135) Hasselbrink, E. Non-adiabaticity in surface chemical reactions. Surf. Sci. 2009, 603, 1564–1570.
- (136) Schindler, B.; Diesing, D.; Hasselbrink, E. Electronic excitations induced by hydrogen surface chemical reactions on gold. *J. Chem. Phys.* **2011**, 134, 034705.
- (137) Schindler, B.; Diesing, D.; Hasselbrink, E. Electronically nonadiabatic processes in the interaction of H with a Au surface revealed using MIM junctions: the temperature dependence. J. Phys. Chem. C 2013, 117, 6337–6345.
- (138) Tchakoua, T.; Smeets, E. W. F.; Somers, M.; Kroes, G.-J. Toward a specific reaction parameter density functional for  $H_2 + Ni(111)$ : comparison of theory with molecular beam sticking experiments. *J. Phys. Chem. C* **2019**, *123*, 20420–20433.
- (139) Hou, H.; Gulding, S.; Rettner, C.; Wodtke, A.; Auerbach, D. The stereodynamics of a gas-surface reaction. *Science* **1997**, *277*, 80–82.

References 279

(140) Hodgson, A.; Samson, P.; Wight, A.; Cottrell, C. Rotational excitation and vibrational relaxation of  $H_2$  ( $\nu = 1$ , J = 0) Scattered from Cu(111). *Phys. Rev. Lett.* **1997**, 78, 963–966.

## Samenvatting: Ontwikkeling van zeer nauwkeurige dichtheidsfunctionalen voor de dissociatie van H<sub>2</sub> aan overgangsmetaaloppervlakken

De chemie van kleine moleculen die reageren aan oppervlakken maakt een onmisbaar deel uit van ons dagelijks leven. Denk hierbij bijvoorbeeld aan de productie van plastics en andere alledaagse materialen, de productie van ammoniak die zeer belangrijk is voor het bereiden van kunstmest, de katalysator in de uitlaat van de auto die de schadelijke uitstoot van het verbrandingsproces aanzienlijk vermindert, of het stoomhervormingsproces waarmee methaan  $(CH_4)$  en water omgezet kan worden in koolstofdioxide  $(CO_2)$  en waterstof  $(H_2)$ . Reacties tussen gassen en oppervlakken komen ook voor in de natuur. Bij het roesten van een stuk ijzer in een vochtige omgeving reageert zuurstof  $(O_2)$  uit de lucht met het metaal oppervlak. Al deze voorbeelden behelzen de reactie van een gas met een oppervlak, en zijn een voorbeeld van heterogene katalyse.

In de meest simpele chemische reactie botsen twee reactanten op elkaar met genoeg energie om de energetische barrière voor hun reactie te overwinnen om vervolgens één of meerdere producten te vormen. Een katalysator is een deelnemer aan de reactie die tijdens de reactie niet wordt verbruikt. Een katalysator maakt een alternatief reactiemechanisme mogelijk dat wellicht gecompliceerder maar wel energetisch voordeliger is. In het algemeen stabiliseert een katalysator de overgangstoestand van het reactiecomplex dat wordt gevormd door de reactanten die bij elkaar komen op de katalysator. Hierdoor wordt de energetische barrière van de reactie verlaagd en wordt het verbreken van bestaande en vormen van nieuwe chemische banden makkelijker. Na de reactie bewegen de gevormde producten weg van de katalysator waardoor de katalysator aan een nieuwe katalytische cyclus kan beginnen. Het verlagen van de energetische

barrière versnelt niet alleen de reactie. Het zorgt er er ook voor dat de reactie kan plaatsvinden bij een lagere druk of temperatuur, wat de kosten van het uitvoeren van een dergelijk proces mogelijk kan verlagen.

In een heterogeen gekatalyseerde reactie bevinden de deelnemende reactanten en katalysator zich in een verschillende aggregatietoestand. In een homogeen gekatalyseerde reactie bevinden de deelnemende reactanten en katalysator zich in dezelfde aggregatietoestand. Een ander belangrijk type van gekatalyseerde reacties is biologische katalyse, waarbij eiwitten functioneren als zeer gespecialiseerde katalysatoren voor vrijwel alle biochemische reacties die aan de basis staan van het leven zoals we dat nu kennen.

Een heterogeen gekatalyseerde reactie bestaat vrijwel nooit uit slechts één enkele reactiestap. Een chemische reactie die plaatsheeft aan een katalytisch oppervlak kan beschreven worden als een complex proces dat bestaat uit meerdere elementaire reactiestappen. Een voorbeeld van zo een proces is het adsorberen van een molecuul op het katalystisch oppervlak en diffuseert naar een reactieplaats om vervolgens te dissociëren. In dit voorbeeld maakte het molecuul de volgende elementaire reactie stappen mee: adsorptie, diffusie naar een reactieplaats, en dissociatie bij een reactieplaats. In 2007 heeft Ertl de Nobelprijs voor de chemie gewonnen voor het experimenteel onderzoeken van elementaire reactiestappen bij heterogeen gekatalyseerde reacties.

De elementaire reactiestappen binnen de heterogene katalyse vormen een complex netwerk van reacties. De belangrijkste stappen in zo een netwerk worden de snelheidsbepalende stappen genoemd. Idealiter begint de theoretische beschrijving van een complex reactienetwerk met het berekenen van 'chemisch nauwkeurige' barrièrehoogtes voor elementaire reactiestappen. Binnen de heterogene katalyse is de snelheidsbepalende stap vaak de dissociatieve chemisorptie van een molecuul op een oppervlak. Het berekenen van chemisch nauwkeurige barrièrehoogtes voor snelheidsbepalende elementaire reactiestappen zodat de reactiesnelheid van het gehele netwerk in kaart gebracht kan worden is een complexe taak die niet alleen rekening moet houden met de elektronische structuur van de reactant en het katalytisch oppervlak, maar ook met dynamische effecten zoals de aanloop van een molecuul naar de overgangstoestand, de interne bewegingen van het molecuul, en de thermische beweging van oppervlakte atomen.

Metaaloppervlakken vormen een groep van zeer effectieve katalysatoren voor de reactie van kleine moleculen zoals H<sub>2</sub>. De elektronen van een metaal zijn overwegend gedelocaliseerd terwijl de elektronen van moleculen meer gelocaliseerd zijn rond de atoomkernen van het moleculen. Dat de elektronen van een metaaloppervlak banden vormen, waarvan sommige dicht bij het Fermi niveau liggen, maakt het mogelijk voor het metaaloppervlak om elektronen

te doneren of te accepteren van het molecuul zonder (vrijwel) enige energie. Deze mogelijkheid tot elektronuitwisseling is wat metaaloppervlakken tot goede katalysatoren maakt.

Het onderzoek dat wordt besproken in dit proefschrift betreft de reactie van H<sub>2</sub> aan metaaloppervlakken. De dissociatie van H<sub>2</sub> is ook relevant voor de industriële productie van methanol uit CO<sub>2</sub> met behulp van een Cu/ZnO/Al<sub>2</sub>O<sub>3</sub> katalysator, omdat in dit proces de dissociatie van H<sub>2</sub> de snelheidsbepalende stap is. H<sub>2</sub> dissociatie aan overgangsmetaaloppervlakken is ook een belangrijke stap bij hydrogenatie katalyse, waarbij onverzadigde banden van organische moleculen worden gehydrogeneerd. Hoewel de basale elementaire reactiestappen van H<sub>2</sub> dissociatie en hydrogenatie lang geleden zijn opgehelderd door Horiuti en Polanyi zijn er nog vele open vragen en onderzoeksmogelijkheden met betrekking tot de efficiëntie, selectiviteit, het ontwerp van katalytische deeltjes, en de geometrie van een oppervlak.

De kinetiek van  $H_2$  dissociatie, recombinatieve desorptie en vertrooiïng wordt experimenteel vooral bestudeerd onder ultrahoogvacuüm. Reactiewaarschijnlijkheidscurves als functie van de translatie energie kunnen verkregen worden uit moleculaire bundel experimenten. Informatie over het effect van de initiële rovibrationele toestand en de orientatie van het moleculaire prichte van het oppervlak op de reactiewaarschijnlijkheid kan verkregen worden uit associatieve desorptie-experimenten. Moleculaire bundel experimenten waarbij  $H_2$  verstrooit aan het oppervlak kunnen eindtoestand-opgehelderde informatie opleveren over vibrationele excitatie, rotationeel (in)elastische verstrooiïng, en rotationeel elastische en vibrationeel inelastische verstrooiïng.

Om de voorspellingskracht van de theorie met betrekking tot de katalytische activiteit van overgangsmetaaloppervlakken voor de reactie van kleine moleculen te vergroten is het nodig om op een fundamenteel niveau te begrijpen op welke manier overgangsmetaaloppervlakken de potentiële energie van moleculen beïnvloeden. De elementaire reactiestappen van een molecuul dat reageert aan een oppervlak kunnen experimenteel bestudeerd worden met behulp van technieken die controle uitoefenen over de verschillende vrijheidsgraden van het molecuul. Het onderzoek in dit proefschrift richt zich hoofdzakelijk op beschrijving en simulatie van supersonische moleculaire bundel- en associatieve-desorptie experimenten. Momenteel bestaan er geen ab initio methodes die chemisch nauwkeurige molecuul-metaaloppervlak interactie-energieën en barrièrehoogtes kunnen berekenen. In de afwezigheid van dergelijke methoden die de interactie van moleculen met metalen kunnen beschrijven is het noodzakelijk berekende barrières te valideren aan de hand van experimenten. Helaas is de barrièrehoogte geen direct meetbare grootheid. Een alternatieve manier om berekende barrièrehoogtes te valideren is het gebruik van dynamische methodieken (zoals de

quasi-klassieke baan (QKB) methode of quantum dynamica (QD)) om grootheden te berekenen die wél meetbaar zijn, zoals de reactiewaarschijn lijkheid als functie van de translatie-energie.

Bereking van de interactie-energie van een molecuul met een overgangsmetaaloppervlak geschiedt binnen het kader van dit proefschrift met behulp van dichtheidsfunctionaaltheorie (DFT). Hierbij worden dichtheidsfunctionalen (DFen) gebruikt op het niveau van de gegeneraliseerde gradiënt benadering (GGB) of de meta-gegeneraliseerde gradiënt benadering (meta-GGB) om potentiële energie-oppervlakken (PEOen) voor de interactie van moleculen met metaaloppervlakken uit te rekenen. Recent is de specifieke reactieparameter aanpak voor DFT (SRP-DFT) toegepast om tot een chemisch nauwkeurige beschrijving van de interactie van moleculen met metaaloppervlakken te komen. Binnen de SRP-DFT aanpak is het gebruikelijk dat één enkele parameter in de DF op empirische wijze wordt aangepast opdat een experiment gereproduceerd kan worden, waarbij dat experiment zeer gevoelig is voor de hoogte van de barrière van het specifieke systeem dat beschouwd wordt. De kwaliteit van de verkregen kandidaat specifieke reactieparameter dichtheidsfunctionaal (SRP-DF) wordt geborgd door te verifiëren dat de kandidaat SRP-DF ook gebruikt kan worden om andere experimenten aan het zelfde systeem te reproduceren dan slechts het systeem waaraan de SRP-DF was gefit. Deze SRP-DFT aanpak heeft vooralsnog chemisch nauwkeurige barrièrehoogtes opgeleverd voor de dissociatieve chemisorptie van H<sub>2</sub> op Cu(111), Cu(100) en Pt(111), alsook voor de dissociatieve chemisorptie van  $CH_4$  op Ni(111), Pt(111) en Pt(211).

Het hoofddoel van dit proefschrift is de verbetering van de theoretische beschrijving van de reactive verstrooiïng van H<sub>2</sub> aan verschillende overgangsmetaaloppervlakken, zoals Cu(111), Cu(211), Ag(111), Au(111) en Pt(111). Het basisvertrekpunt voor elke theoretische beschrijving van de interactie van H<sub>2</sub> met overgangsmetaaloppervlakken zal hierbij altijd de tijdsafhankelijke Schrödingervergelijking zijn, met inachtneming van de Born-Oppenheimer benadering (BOB). In het bijzonder betreft het hier het verkleinen van de discrepantie tussen de theorie en het experiment met betrekking tot de beschrijving van de reactiewaarschijnlijkheid én toestand-specifieke reactiedynamica doormiddel van de ontwikkeling van zeer nauwkeurige DFen.

Het doel van **Hoofdstuk 3** is de ontwikkeling van meta-GGB DFen gebaseerd op de 'made simple' (MS) aanpak. DFen op het niveau van de meta-GGB hebben de potentie om tegelijkertijd een chemisch nauwkeurige beschrijving van het metaaloppervlak én de interactie van een molecuul met een metaaloppervlak te geven. Hiertoe zijn drie DFen ontwikkeld, namelijk de MS-PBEl, MS-B86bl en de MS-RPBEl DFen. De 'l' staat hier voor 'like', om

aan te duiden dat deze drie DFen zijn gebaseerd op de PBE, B86b en RPBE DFen maar een andere  $\mu$  waarde gebruiken. Binnen de MS aanpak om een DF op het niveau van de meta-GGB te maken wordt een functie van de kinetische energiedichtheid gebruikt waardoor de DF onderscheid kan maken tussen metallische of covalente binding in een bepaalde regio van de coördinaatruimte. De drie nieuwe MS meta-GGB DFen voorspellen roosterconstantes die in zeer goede overeenstemming zijn met nulpuntsenergie-gecorrigeerde experimentele resultaten. Ook zijn de voorspelde afstanden tussen bovenste twee lagen van de Cu(111) en Ag(111) oppervlakken in goede overeenstemming met experimentele resultaten. De prestaties van de drie nieuwe MS meta-GGB DFen bleken in overeenstemming met de voorspellingen van de PBEsol DF, een DF die specifiek ontworpen is voor vaste stoffen. De verkregen barrièrehoogtes voor H<sub>2</sub> + Cu(111) komen ook goed overeen met met de oorspronkelijke SRP-DF waarde voor  $H_2 + Cu(111)$ . Nog belangrijker is de chemisch nauwkeurige overeenkomst van de met de QKB methode verkregen reactiewaarschijnlijkheidscurves met de experimenten van Auerbach en collega's en Rettner en collega's. De reactiewaarschijnlijkheidscurves berekend met de MS-PBEl en MS-B86bl DFen komen bovendien ook beter overeen met experimentele observaties voor D<sub>2</sub> + Ag(111) dan de resultaten verkregen met de SRP48 GGB DF, die ontworpen is voor  $H_2 + Cu(111)$ . Ook is goede overeenstemming bereikt voor initiëletoestand geselecteerde reactiewaarschijnlijkheden die berekend zijn voor H<sub>2</sub> en  $D_2 + Ag(111)$  en de initiële-toestand geselecteerde reactiewaarschijnlijkheden die verkregen zijn uit de associatieve desorptie-experimenten van Hodgson en collega's aan dit systeem. De behaalde resultaten tonen aan dat het mogelijk is om niet-empirische SG meta-GGB DFen te maken voor  $H_2 + Cu(111)$  en  $H_2 + Ag(111)$  die dissociatieve chemisorptie even nauwkeurig beschrijven als de voorgaande semi-empirische DFen op het niveau van de GGB, terwijl zij tegelijkertijd een nauwkeurigere beschrijving geven van het metaalrooster.

In **Hoofdstuk 4** wordt gekeken naar hoe de getrapte eenheidscel van Cu(211) van invloed is op de dynamica van  $H_2$  dat botst met Cu(211), en of die dynamica nog wel beschreven kan worden met quasi-klassieke methoden. Hiertoe is een gehele moleculaire bundelsimulatie gedaan met de QD methode waarvoor een groot aantal tijdsafhankelijke golfpakket (TAGP) berekeningen zijn uitgevoerd om geheel initiële-toestand-specifieke reactiewaarschijnlijkheidscurves te verkrijgen voor all rovibrationele toestanden die redelijkerwijs relevant zijn voor de gesimuleerde moleculaire bundel experimenten. Het belangrijkste resultaat is dat de reactie van  $H_2$  aan Cu(211) goed beschreven kan worden met de QKB methode. Dit is zeker het geval bij moleculaire bundelsimulaties waarbij gemiddeld wordt over een groot aantal rovibrationele toestanden en een

brede snelheidsverdeling. Er blijven echter wel kleine verschillen bestaan tussen de QD en QKB methode, met name voor de afhankelijkheid van de reactie van de orientatie van H<sub>2</sub> ten opzichte van het oppervlak. De QD methode voorspelt een iets grotere afhankelijkheid van de reactiewaarschijnlijkheid voor de orientatie van H<sub>2</sub> dan de QKB methode voor laaggelegen rotatietoestanden. Een vergelijking met recente associatieve desorptie-experimenten en directe dynamica berekeningen suggereert dat het het meenemen van het effect van thermische beweging van oppervlakte atomen op de reactiewaarschijnlijkheid binnen chemische nauwkeurigheid valt, zelfs voor hoge oppervlaktetemperaturen. In contrast met theoretische en experimentele resultaten voor de reactie van D<sub>2</sub> met Cu(111) en Cu(100) bij een lage translatie-energie valt de scherpe neergang van de rotationele quadrupooloriëntatieparameter op voor vibrationeel aageslagen moleculen. Deze neergang kan toegeschreven worden aan het specifieke reactiemechanisme van rotationeel inelastische vergroting. De resultaten tonen aan dat het Cu(211) oppervlak zich onderscheidt van de Cu(111)terrassen en Cu(100) traptredes waaruit het bestaat, en dus niet kan worden worden beschreven als een som van zijn onderdelen met betrekkking tot de oriëntatie-afhankelijke reactiedynamica.

In **Hoofdstuk 5** worden nieuwe SRP-DFen ontwikkeld op het niveau van de GGB die niet-lokale vdW-DF2 correlatie gebruiken voor het  $H_2 + Cu(111)$ systeem, namelijk de B86SRP68-DF2 en SRPsol63-DF2 DFen. De overdraagbaarheid van deze DFen naar de  $H_2 + Ag(111)$ , Au(111) en Pt(111) systemen wordt ook onderzocht. De nieuw ontwikkelde DFen beschrijven de reactie van  $H_2$  aan Cu(111) met chemische nauwkeurigheid, en, voor zover dat dit kan worden vastgesteld, vebeteren de overdraagbaarheid naar andere systemen ten opzichte van de eerder gerapporteerde SRP48 en MS-B86bl SRP-DFen. Twee SRP-DFen die niet-lokale correlatie gebruiken, namelijk de B86SRP68-DF2 en PBE $\alpha$ 57-DF2 DFen, blijken overdraagbaar van het zeer geäctiveerde late barrière  $H_2 + Cu(111)$  systeem naar het zwak geactiveerde vroege barrière  $H_2 + Pt(111)$  systeem en vice versa. Dit resultaat kon niet bereikt worden met SRP-DFen op GGB of meta-GGB niveau die geen niet-lokale correlatie gebruiken. Het beoordelen van de overdraagbaarheid van de geteste en ontwikkelde SRP-DFen naar  $H_2 + Ag(111)$  en  $H_2 + Au(111)$  wordt bemoeilijkt door het gebrek aan nauwkeurig beschreven moleculaire bundelexperimenten voor  $H_2 + Ag(111)$  en het algehele gebrek daarvan voor  $H_2 + Au(111)$ . Een gedetailleerde analyse van associatieve desorptie-experimenten aan Cu(111) suggereert dat voor een nauwkeurige berekening van  $E_{1/2}(\nu, J)$  parameters een verbetering van het dynamisch model noodzakelijk is. Mogelijk maakt het beschrijven van de vrijheidsgraden van het oppervlak het mogelijk het gat te

dichten tussen de excellente beschrijving van dissociatieve chemisorptie en de goede beschrijving van associatieve desorptie, voor moleculen in de vibrationele grondtoestand. Elke overgebleven discrepantie in voorspelde reactiviteit tussen gesimuleerde associatieve desorptie en dissociatieve chemisorptie die overblijft nadat is rekening gehouden met de beweging van oppervlakte atomen kan dan hoogstwaarschijnlijk worden toegeschreven aan elektron-gat paar (egp) excitaties. Het gebrek aan additionele experimenten aan  $H_2 + Au(111)$ , in het bijzonder een nauwkeurig beschreven moleculaire bundel experiment, zorgt er momenteel voor dat het niet mogelijk is de effecten van oppervlaktereconstructie, oppervlaktetemperatuur, en egp excitatie te ontwarren. Ook is een volledige moleculaire bundelsimulatie uitgevoerd voor  $H_2 + Cu(111)$  met de QD methode waarbij de B86SRP68-DF2 DF is gebruikt, welke de best presterende DF voor dit systeem is en welke ook een goede beschrijving geeft van de Van der Waalskrachten in dit systeem. Op de keper beschouwd kan het  $H_2 + Cu(111)$ systeem zeer goed beschreven worden met quasi-klassieke methoden wanneer naar reactiewaarschijnlijkheden van moleculaire bundels of naar reactiewaarschiinlijkheden die gemiddeld zijn over het magnetische rotationele kwantumgetal.

Het doel van Hoofdstuk 6 is combineren van de in Hoofdstuk 3 ontwikkelde MS meta-GGB DFen met rVV10 niet-lokale correlatie om de MS-PBEl-rVV10, MS-B86bl-rVV10 en MS-RPBEl-rVV10 DFen te verkrijgen. Alle drie de nieuwe DFen beschrijven moleculaire bundelexperimenten aan D<sub>2</sub> + Ag(111) met chemische nauwkeurigheid, en de MS-B86bl-rVV10 beschrijft ook twee sets aan moleculaire bundel experimenten aan  $D_2 + Pt(111)$  met chemische nauwkeurigheid. Uit een vergelijking tussen berekende  $E_{1/2}(\nu, J)$ parameters voor  $H_2$  ( $D_2$ ) + Au(111) en experimentele  $E_0(\nu, J)$  parameters blijkt dat chemische nauwkeurigheid wordt bereikt met de MS-PBEl-rVV10 DF. Het beoordelen van de prestaties van de drie nieuwe DFen voor H<sub>2</sub> (D<sub>2</sub>) + Au(111) is echter moeilijk door de afwezigheid van een nauwkeurig beschreven moleculaire bundelexperiment en berekeningen met een gereconstrueerd Au(111) oppervlak waarbij de beweging van oppvervlakte atomen wordt meegenomen. Van de drie nieuwe DFen geeft de MS-PBEl-rVV10 excellente resultaten met betrekking tot bekende Van der Waals geometrieën, terwijl de MS-B86blrVV10 en MS-RPBEl-rVV10 DFen Van der Waals putten geven die ietwat te ondiep zijn. In een vergelijking met initiële-toestand-geselecteerde experimenten voor  $H_2(D_2) + Ag(111)$  blijkt dat een zeer goede overeenstemming met de experimenten wordt bereikt voor alle drie de DFen voor H<sub>2</sub>. Met betrekking tot moleculaire bundelreactiewaarschijnlijkheden voor het  $H_2 + Cu(111)$  system voorspellen alle drie de DFen een reactiewaarschijnlijkheid overeenkomstig met de PBE DF, welke te hoog is. De drie originele MS meta-GGB DFen

gaven een beschrijving van het metaal die vergelijkbaar was met die van de PBEsol DF. Hier wordt gevonden dat het combineren van deze drie DFen met rVV10 niet-lokale correlatie zorgt voor een iets minder goede beschrijving van het metaal. Over het algemeen worden de roosterconstantes iets kleiner dan nulpuntsenergie-gecorrigeerde experimentele resultaten. De drie ontwikkelde DFen voorspellen ook dat de afstand tussen de bovenste twee lagen van het metaal lichtelijk uitzetten, in tegenstelling tot experimentele resultaten. De verkregen resultaten laten zien dat een sport stijgen op Jakob's ladder steeds nauwkeurigere resultaten oplevert voor de meeste gas-oppervlakte systemen voor de interactie van  $H_2$  ( $D_2$ ) met overgangsmetaaloppervlakken.

## Curriculum vitae

Egidius Wilhelmus François Smeets is geboren op 21 mei 1989 te Sittard. In 2007 heeft hij zijn gymnasiumdiploma behaald aan de Trevianum scholengroep, tevens te Sittard. In datzelfde jaar is hij begonnen aan de bachelorstudie "Natuurkunde" aan de Universiteit Leiden. Twee jaar later is hij, in 2009, overgestapt naar de bachelorstudie "Molecular Science and Technology" aan de Universiteit Leiden en de Technische Universiteit Delft. Na deze studie in 2015 met succes te hebben afgerond, is hij aan de masterstudie "Chemistry" aan de Universiteit Leiden begonnen. Als onderdeel van deze studie heeft hij een onderzoeksstage gedaan bij de groep Theoretische Chemie van prof. dr. Geert-Jan Kroes, waar hij begeleid is door dr. Gernot Füchsel. In 2017 heeft hij zijn masterstudie afgerond, waarna hij in datzelfde jaar is begonnen als promovendus in dezelfde groep, in het Leids Instituut voor Chemisch onderzoek.

## List of publications

- Füchsel, G.; Cao, K.; Er, S.; Smeets, E. W. F.; Kleyn, A. W.; Juurlink, L. B. F.; Kroes, G.-J. Anomalous dependence of the reactivity on the presence of steps: dissociation of D<sub>2</sub> on Cu(211). *J. Phys. Chem. Lett.* **2018**, *9*, 170–175
- Ghassemi, E. N.; Smeets, E. W. F.; Somers, M. F.; Kroes, G.-J.; Groot, I. M.; Juurlink, L. B.; Füchsel, G. Transferability of the specific reaction parameter density functional for H<sub>2</sub> + Pt(111) to H<sub>2</sub> + Pt(211). J. Phys. Chem. C 2019, 123, 2973–2986
- Smeets, E. W. F.; Voss, J.; Kroes, G.-J. Specific reaction parameter density functional based on the meta-generalized gradient approximation: application to H<sub>2</sub> + Cu(111) and H<sub>2</sub> + Ag(111). J. Phys. Chem. A 2019, 123, 5395-5406
- Smeets, E. W. F.; Füchsel, G.; Kroes, G.-J. Quantum dynamics of dissociative chemisorption of H<sub>2</sub> on the Stepped Cu(211) Surface. *J. Phys. Chem. C* **2019**, *123*, 23049–23063
- Tchakoua, T.; Smeets, E. W. F.; Somers, M.; Kroes, G.-J. Toward a specific reaction parameter density functional for H<sub>2</sub> + Ni(111): comparison of theory with molecular beam sticking experiments. *J. Phys. Chem. C* 2019, 123, 20420–20433
- Gerrits, N.; Geweke, J.; Smeets, E. W. F.; Voss, J.; Wodtke, A. M.; Kroes, G.-J. Closing the Gap Between Experiment and Theory: Reactive Scattering of HCl from Au(111). J. Phys. Chem. C 2020, 124, 15944–15960

- Gerrits, N.; Smeets, E. W. F.; Vuckovic, S.; Powell, A. D.; Doblhoff-Dier, K.; Kroes, G.-J. Density functional theory for molecule–metal surface reactions: When does the generalized gradient approximation get it right, and what to do if it does not. J. Phys. Chem. Lett, 2020, 11, 10552–10560
- Smeets, E. W. F.; Kroes, G.-J. Designing new SRP density functionals including non-local vdW-DF2 correlation for H<sub>2</sub> + Cu(111) and their transferability to H<sub>2</sub> + Ag(111), Au(111) and Pt(111). *Phys. Chem. Chem. Phys.* **2021**, 23, 7875–7901
- Smeets, E. W. F.; Kroes, G.-J. Performance of made-simple meta-GGA functionals with rVV10 non-local correlation for  $H_2$  + Cu(111),  $D_2$  + Ag(111),  $H_2$  + Au(111) and  $D_2$  + Pt(111). J. Phys. Chem. C **2021**, DOI:  $10.1021/acs.jpcc\ 0c11034$